Infrared Studies of Hydrocarbons on an Alumina Supported Nickel Catalyst.

Ian C. Wilcock

A thesis submitted for the degree of Doctor of Philosophy.

University of Edinburgh.

1992

Abstract

The work described in this thesis concerns the adsorption and decomposition of small hydrocarbon molecules on the surface of an alumina supported nickel catalyst.

The catalyst was prepared using a co-precipitation method and contained 25% nickel by weight. Temperature programmed reduction revealed that reduction at over 550°C in hydrogen was necessary in order to fully reduce the catalyst. Nickel surface area measurements were performed using hydrogen chemisorption and nitrous oxide decomposition, revealing an area of 30→45m^2/g. X ray diffraction and transmission electron microscopy showed an average nickel particle diameter of 13nm. Total catalyst surface area was measured by nitrogen adsorption at -196°C, giving a value of 250m^2/g for the as prepared catalyst.

Infrared studies were performed using a combination of Diffuse Reflectance Infrared Fourier Transform Spectroscopy (DRIFTS), with a standard Spectratech cell, and transmission infrared spectroscopy, with a home made infrared cell. A passivation procedure was developed so that pre-reduced catalyst could be transferred to the infrared cells and re-reduced *in situ* at 300°C.

The adsorption and reaction of the two simple alkenes, ethene and propene were investigated at temperatures between 25 and 300°C. The room temperature surface chemistry of both molecules was dominated by the initial formation of alkylidyne species, ethylidyne (CCH_3) from ethene and propylidyne (CCH_2CH_3) from propene. The ethylidyne formed from ethene decayed to surface methyl (CH_3) and C_4 containing species. These were hydrogenated to methane and butane respectively. Ethylidyne itself was stable to hydrogenation. Methane was the only product released during temperature programming of the sample up to 300°C in helium. Propylidyne formed from propene decayed to ethylidyne, methyl and other C_3 and C_6 containing carbonaceous deposits. Hydrogenation produced methane and propane, leaving propylidyne and ethylidyne. Temperature programming of these species in helium produced only methane, and heating in hydrogen produced a small quantity of hexane in addition.

After ethene adsorption, only 77% of the carbon deposited could be removed during re-reduction. Temperature programmed oxidation removed all of the carbon but substantial re-oxidation of the nickel catalyst occurred.

I certify that, unless otherwise stated, the work presented in this thesis was performed by myself in the Chemistry Department of the University of Edinburgh and at the Billingham Catalysis Research Centre of ICI Chemicals and Polymers Plc.

Ian C. Wilcock

Some of the work presented here has been published previously as;

Holmes,P.D.; McDougall, G.S.; Wilcock, I.C. and Waugh, K.C.
Catalysis Today **9** 15 (1991).

Acknowledgments

Firstly I would like to thank my two supervisors, Gordon McDougall at Edinburgh University for his encouragement and advice, and Ken Waugh of ICI for showing me the industrial side of research.

I would also like to thank Roni Brown, without whose technical expertise this work would not have been possible, and Clive Werrett for showing me the ropes at ICI.

I am also grateful to Stewart and John in the mechanical workshop, the glassblower and the staff of the electronics workshop for help with equipment construction and maintenance.

In addition I would like to mention friends and colleagues in the catalysis group: Anne, Hilary, Philip, Mushtaq, Brian, Peter and Graeme, as well as the 'zeolite boys': Gordon, Keith, Jim and Alister.

Finally, I would like to express my thanks to the SERC and ICI Chemicals and Polymers Plc. for financial support through the CASE studentship scheme.

For Mum and Dad . . . .

Table of Contents.

CHAPTER 1

Introduction.

The Oxford English Dictionary defines a catalyst as 'a substance that, without itself undergoing change, aids a chemical change in other substances', illustrating how the word has come into everyday use. This definition, almost a century old now, was proposed in 1894 by Ostwald [1], and remains as the simplest and clearest statement. Catalysis, the effect produced by a catalyst, was first used by Berzelius in 1836 [2], as a term to describe the ability of some metals, possessing a 'catalytic force', to decompose ammonia. Prior to this, one of the earliest observations of catalytic behaviour in metals was the discovery by Priestley that copper and silver could dehydrogenate alcohols [3]. Whilst the foundations of catalytic studies are comparatively old, it is really only since World War II that the most significant advances in the field have occurred. In this sense catalytic chemistry is still in its relative youth.

Catalysis can take several forms, and is usually divided into two distinct types; homogeneous and heterogeneous catalysis. Homogeneous catalysis is the name given to catalysis when the reactants, products and catalyst are all in the same phase, usually all liquids. In heterogeneous catalysis the catalyst and reactants are in different phases, generally gaseous reactants and products, reacting over a solid catalyst, either a metal or non-metal. The interface between them is the catalyst surface and consequently the study of this form of catalysis is the study of molecules on surfaces. Only catalysis involving the gas/solid interface will be considered in this thesis.

Metals that are active for catalysis occur mainly in Groups 8, 9, 10 and 11 (VIII and IB) of the transition metals in the periodic table. Metal catalysts can be divided into two groups, those that contain only metal e.g. metal films, metal powders, wires etc., and those that contain two components or more, at least one of which is a metal e.g. nickel mixed with alumina. Non metals can be classified into insulators or semiconductors, and include various metal oxides, sulphides and acids active for catalysis. Metals tend to be efficient for hydrogen addition or abstraction reactions and generally poor at adding or removing oxygen. Insulators, such as alumina, tend to be good at dehydrogenation but poor at oxidation or hydrogenation. Semiconductors are generally good at catalysing oxidation-reduction processes, but poor at hydrogenation.

An example of the above processes is the reaction of ethanol over nickel and over alumina [4]. Nickel tends to dehydrogenate the C_2H_5OH (Reaction 1.1),

$$C_2H_5OH \rightarrow CH_3CHO + H_2 \qquad \text{Reaction 1.1}$$

Alumina will dehydrate the same molecule although in different ways above and below 300°C. Above 300°C, the reaction proceeds to ethene (Reaction 1.2), whilst below this temperature diethyl ether is the major product (Reaction 1.3).

$$C_2H_5OH \rightarrow C_2H_4 + H_2O \qquad \text{Reaction 1.2}$$

$$C_2H_5OH \rightarrow C_2H_5OC_2H_5 \qquad \text{Reaction 1.3}$$

Another definition of a catalyst, perhaps more accurate, is that of a substance that changes the rate of attainment of equilibrium of a reaction, without altering the overall free energy change i.e. the catalyst merely facilitates the progress of a reaction A to B without changing the overall equilibrium [5]. Whilst the original definition implies that the catalyst remains unchanged after reaction, in practice this may not always be true. Residual deposits may remain after a reaction, the catalyst may be eroded or 'leached' in some way, and metal particles may sinter during reaction. Hence the catalyst may be altered quite substantially, for example with a type of filamentous carbon deposit, the structure may be totally destroyed [6]. If volatile intermediates form, the catalyst may be 'dissolved' and precipitated in a different place.

Adsorption.

For a catalytic reaction to proceed, a necessary initial step is the adsorption of at least one of the reacting species onto the catalyst surface. Adsorption is possible because the atoms at the surface of a solid are not as fully coordinated as those in the bulk and hence possess a certain degree of unsaturation. Molecules approaching the surface are able to bond and remove this unsaturation to some extent. This adsorption results in a decrease in the free energy, ΔG, of the system. Since a molecule would also lose certain degrees of freedom on adsorption, a decrease in entropy, ΔS, is also expected. Using the relationship,

$$\Delta G = \Delta H - T\Delta S \qquad \text{Equation 1.1}$$

where ΔH is the enthalpy change on adsorption and T is the temperature (K), would imply that ΔH is negative, i.e. adsorption is always exothermic.

The exact nature of the bond between surface metal atoms (the adsorbent) and the adatom or molecule adsorbed on the surface (the adsorbate) depends on both of these components. Adsorption can be conveniently divided into two types; physical adsorption and chemical adsorption (usually referred to as physisorption and chemisorption respectively).

In principle physisorption can occur between all gases and liquids bonded to any surface. A weak Van der Waals' type bond forms, usually with the enthalpy change on physisorption, $\Delta H_p < 20$kJ/mol. Significant physisorption only occurs at around the boiling point of a liquid. Chemisorption involves the formation of new bonds of comparable strength to those that already exist within the incoming molecule and within the surface itself. Generally the enthalpy change on chemisorption, $\Delta H_c >> 20$kJ/mol. A central feature to the discussion of adsorption on solids is the use of the Lennard-Jones potential energy diagram [7]. This is a plot of potential energy *versus* reaction coordinate. A Lennard-Jones diagram (adapted from [8]), showing the energy changes in a typical molecule A_2 as it approaches a surface, is shown in Figure 1.1 below. The dissociation energy of the molecule is D and E is the activation energy needed to move from a physisorbed to a chemisorbed state.

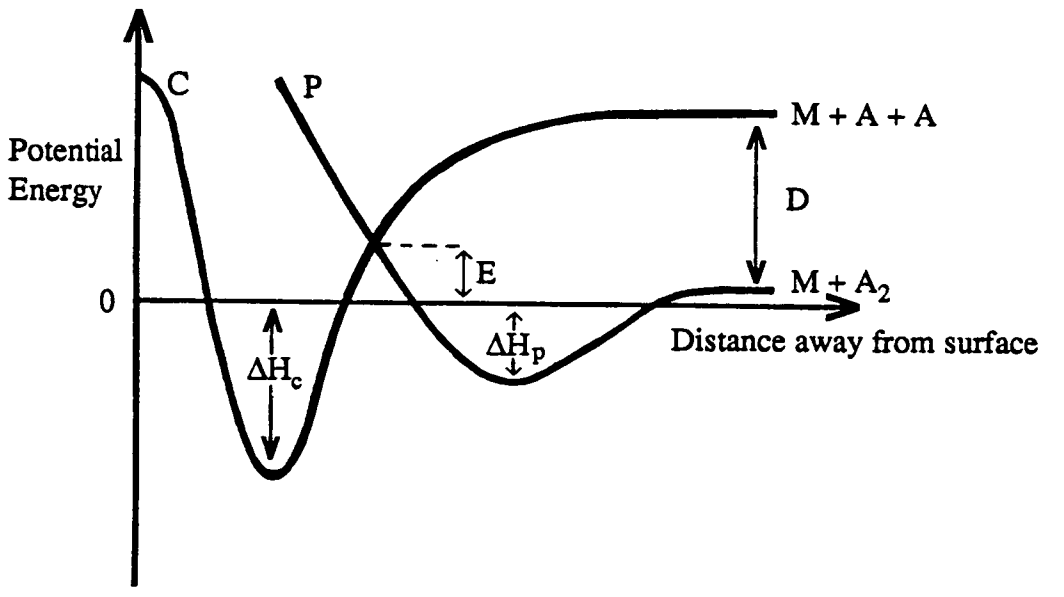

Figure 1.1 *Lennard-Jones potential energy diagram for physisorption (curve P) and chemisorption (curve C) of a typical molecule A_2.*

A schematic representation of physisorption and chemisorption of H_2 on nickel is shown in Figure 1.2 below;

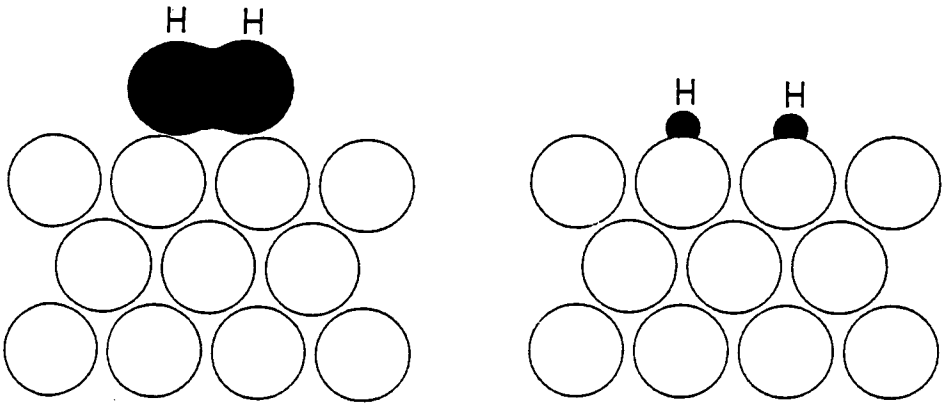

Figure 1.2 *Physisorption and chemisorption of H_2 on a metal surface.*

The hydrogen dissociates on chemisorbing to the nickel. Dissociative adsorption occurs on the more reactive surfaces and varies between adsorbates. Whilst adsorption is essential for catalysis and strong enough to give a high surface coverage of the reacting molecules, it must not be too strong so as to block the active sites, immobilising the reactants and thus prevent further reaction. Only a limited number of metals can achieve this balance between activity and adsorption which makes them useful catalysts. As an example, the rate of decomposition of methanoic (formic) acid;

$$HCOOH \rightarrow CO + H_2O \qquad \text{Reaction 1.4}$$

is examined for various metals, and plotted below in Figure 1.3. This is an example of a 'volcano' diagram, with the platinum metals having the fastest rate of decomposition of formic acid. Those metals to the right of the peak e.g. Ag and Au, adsorb methanoic acid too weakly, whilst those to the left e.g. W and Fe, adsorb too strongly, leaving the platinum metals with intermediate adsorption strength and hence the highest activity.

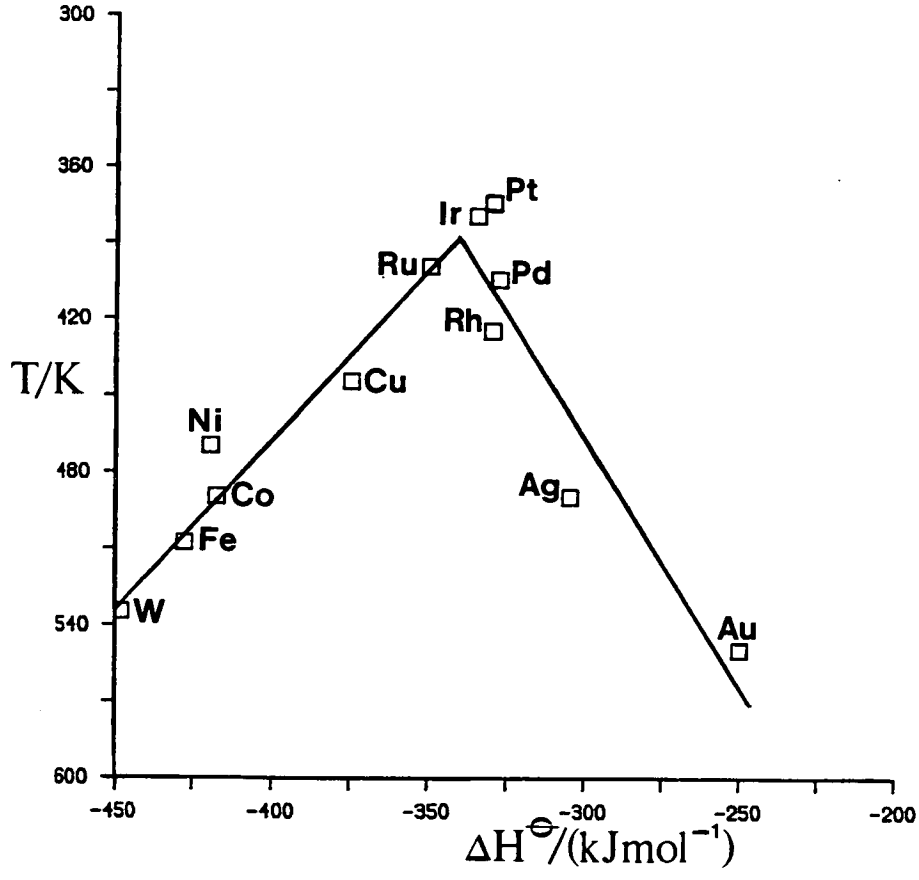

Figure 1.3 *The reaction temperature for a set rate of methanoic acid decomposition plotted against the stability of the corresponding metal methanoate (formate) species (ΔH) (adapted from* [13]).

Turning now to the energetics of the process, a catalyst works by reducing the activation energy barrier of a reaction (ΔE_g in Figure 1.4 below). For example, in the hydrogenation of ethene;

$$C_2H_4 + H_2 \rightarrow C_2H_6 \qquad \text{Reaction 1.5}$$

equilibrium is achieved in 30 minutes at 600°C without the use of a catalyst, but in 30 minutes at room temperature in the presence of a platinum catalyst [4]. The platinum catalyst provides a path through surface adsorbed intermediates (I), which have a lower energy of activation (ΔE_s) for formation than the corresponding gas phase free radicals (ΔE_g). There may be several different intermediate stages, not just one as illustrated. A further activation energy barrier to desorption (ΔE_{des}) of the products exists, so for the catalyst to be effective this must be low enough to achieve a reasonable rate of desorption i.e. the intermediates must not be too strongly adsorbed to the surface.

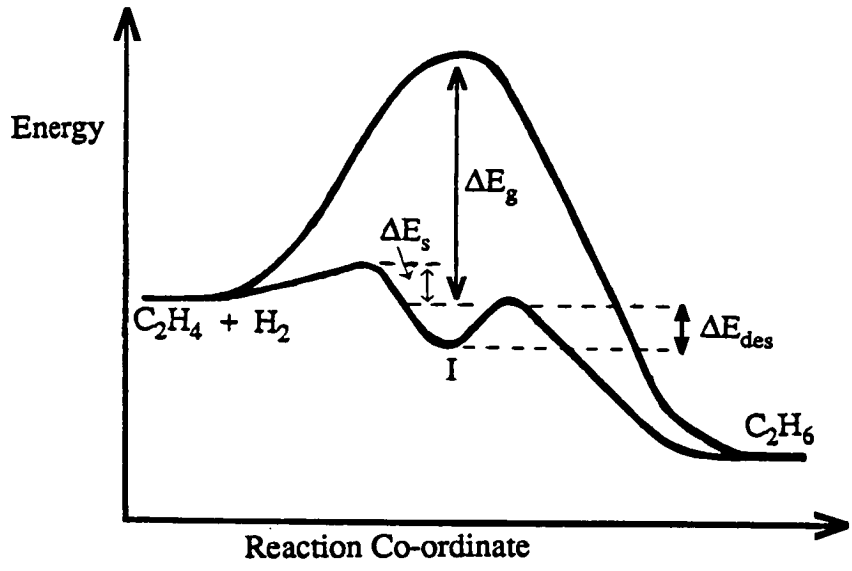

Figure 1.4 *Simplified potential energy diagram for the ethene hydrogenation reaction over platinum.*

Before a catalyst can be used for a reaction, generally the surface has to be 'activated' in some way. In the case of γ-alumina for example, this means removing water at high temperature. For metals, it generally means reduction of a metallic compound to the zero valent state of the metal e.g. $Ni^{2+} \rightarrow Ni$, with a suitable reductant such as hydrogen or carbon monoxide, generating active metal particles. Reduction behaviour is described in more detail in Chapter 3.

Nickel as a catalyst.

Nickel is a very important metal to industry. The vast majority of nickel consumption is in the production of stainless steels and other alloys such as copper-nickel coinage metal, nickel-iron thermal expansion alloys for bimetallic strips in switches, and steels for cryogenic use. Electroplating for corrosion resistance in chromium plate and battery production are also major nickel uses. A very minor use in terms of volume, quite out of proportion to its significance to industry and the world at large, is the use of nickel in catalysis. ICI's headquarters in London has front doors of nickel, perhaps indicating the importance of the metal to this company.

After Priestley's initial discoveries, very little work appeared on the heterogeneous catalysis of organic/metal systems during the nineteenth century. A milestone in catalysis occurred in 1897 with Sabatier's observations of catalytic hydrogenation [9]. Whilst attempting to synthesize $Ni(C_2H_4)_4$ in a similar manner to

Mond, Langer and Quinke's synthesis of nickel carbonyl, $Ni(CO)_4$, he noted that passing ethene over heated nickel produced ethane, rather than a volatile nickel compound. Mixing the ethene with hydrogen and then passing the mixture over the metal gave a greater yield of ethane. Sabatier found that nickel, cobalt, copper and iron all acted as hydrogenation catalysts, usually in the 160-250°C temperature range, with nickel being the most efficient. Alkenes (e.g. ethene, propene etc.) gave the corresponding alkanes. Alkynes also produced alkanes. Aromatic hydrocarbons (e.g. benzene, methylbenzenes etc.) gave the corresponding hexahydro derivatives. Carbon monoxide and carbon dioxide both gave methane. This led to the methanation process where 'syn gas', a CO/H_2 mixture, is converted to methane over a supported nickel catalyst, Reaction 1.6 below.

$$CO + 3H_2 \rightarrow CH_4 + H_2O \qquad \Delta H = -206 kJ/mol \qquad \text{Reaction 1.6}$$

The methane produced is usually known as Towns' gas or 'synthetic natural gas' (SNG). Hydrogenation of alkenes became commercially very important, particularly the hydrogenation of unsaturated fatty acids, which is still one of the main uses of nickel catalysts today. Sabatier was awarded a Nobel prize for his work on hydrogenation [10]. The hydrocarbon catalysis of nickel is described in more detail in Chapter 4.

Another important use of nickel catalysts is in steam reforming. Here hydrocarbons and steam react over the catalyst to produce a mixture of carbon oxides and hydrogen. Steam reforming of hydrocarbons is a major part in the overall process of producing hydrogen in industry. Other uses are for producing carbon monoxide and hydrogen mixtures for methanol synthesis, and for the production of methane rich mixtures formed from higher hydrocarbon streams, described above. The original technology was introduced in the 1930s to produce hydrogen for ammonia synthesis. The feedstock was 'off gas', a by-product of the oil industry containing a mixture of hydrogen, methane and light hydrocarbons. In principle, any hydrocarbon may be used and broken down to hydrogen and carbon oxides, although in practice there is a limit on carbon chain length with no feedstocks heavier than naptha (C_3-C_7) being used. The overall reaction is written as

$$CH_{2\alpha} + H_2O \rightarrow CO + (1+\alpha)H_2 \qquad \Delta H = +206 kJ/mol \ (\text{for } \alpha=2) \qquad \text{Reaction 1.7}$$

$$CO + H_2O \rightarrow CO_2 + H_2 \qquad \Delta H = -41 kJ/mol \qquad \text{Reaction 1.8}$$

The reaction scheme is strongly endothermic and temperatures of up to 1000°C and pressures of up to 50 bar are usually employed. During the 1950s, various naptha reforming processes were developed making use of supported nickel catalysts. With the advent of natural gas in the 1970s, this became the dominant feedstock, being much cleaner and more economic to process to synthesis gas than other hydrocarbons.

The steam reforming reaction is somewhat complex. The hydrocarbon feedstock undergoes both catalytic and thermal cracking over the catalyst, forming unsaturated intermediates. Steam reacts with these to give a mixture of carbon oxides and hydrogen. A simplified schematic diagram of the process is shown in Figure 1.5.

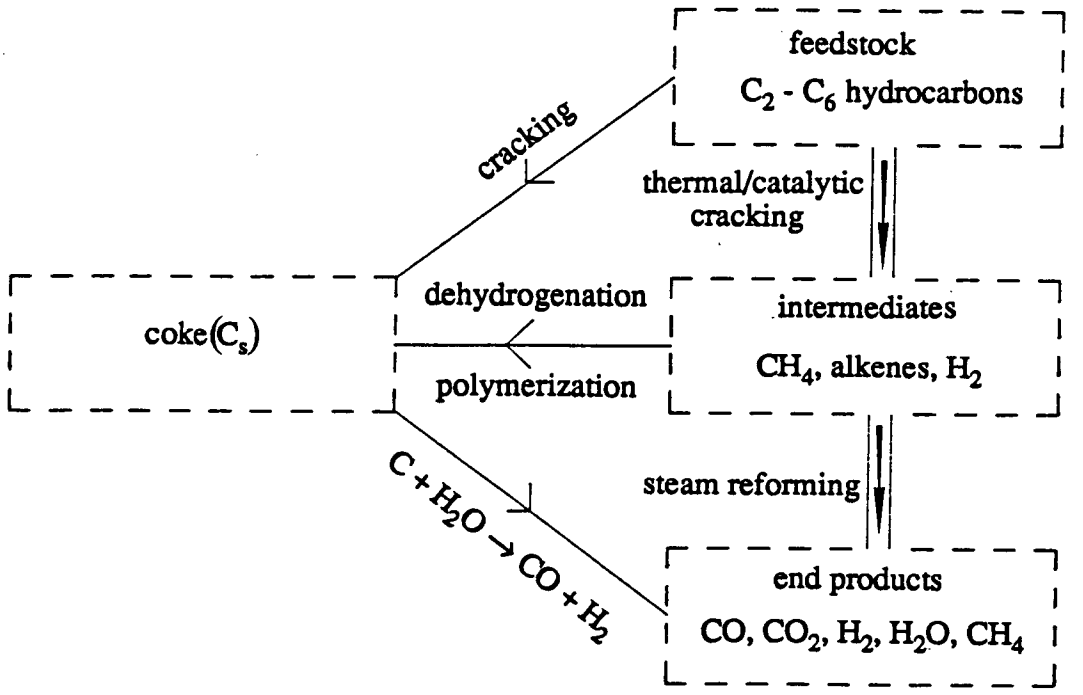

Figure 1.5 *A simplified schematic diagram of the process of steam reforming of natural gas (adapted from* [11]).

The high temperatures employed during reaction may lead to thermolysis, polymerisation and dehydrogenation side reactions resulting in the formation of coke deposits. This becomes more of a problem as the carbon content of the hydrocarbon feedstock increases, and this is one reason why molecules heavier than naptha are troublesome to process. The coke may block the active sites so the catalyst loses its activity and the reaction stops. This may lead to overheating in the reactor tubes since the endothermic reforming reaction is not removing the heat, and damage may result. The coke deposits cause the catalyst feed to expand, which can also lead to reactor

tube failure.

Several methods are employed to prevent the build up of coke during reaction. Examining Equation 1.7 it can be seen that thermodynamically, a carbon:steam ratio of 1:1 is all that is needed for the reaction to run. In practice higher ratios than this are used to prevent coke build up; 1:2.5 for methane reforming, and higher for naptha reforming. The lowest ratio possible is desirable in economic terms and hence if a technological breakthrough occurred preventing coke formation and allowing lower carbon:steam ratios to be used, there would be considerable economic benefit. At present, heavy feedstocks, low hydrocarbon:steam ratios and high catalyst loadings all contribute to the problem.

Nickel is as active for steam reforming as any metal apart from ruthenium, and over the years considerable effort has been made in developing commercial catalysts. Other metals, such as platinum, do not suffer from coke formation problems to the same extent. However since platinum is currently some 15,000 times more expensive per gramme than nickel, there are strong economic reasons for persisting with nickel and trying to understand and overcome the carbon and coke formation steps.

A convention has grown up that defines coke and carbon deposits according to their gas phase origin, although this is not always strictly adhered to. Carbon is defined as the C_s deposit laid down by carbon monoxide disproportionation i.e.

$$2\,CO \rightarrow C_s + CO_2 \qquad \text{Reaction 1.9}$$

Coke is defined as the C_s laid down by successive C-H bond scissions of hydrocarbons *via* highly unsaturated CH_x species.

$$C_nH_m \rightarrow nC + m/2H_2 \qquad \text{Reaction 1.10}$$

Consequently, studying the formation and decay of these CH_x intermediates can lead to a better understanding of the process of coke formation. It is this approach that I have taken in this thesis, by examining the adsorption of ethene and propene onto supported nickel and then following the thermal evolution of the surface species formed.

The thermolysis of hydrocarbon intermediates is catalysed by acid sites on the

alumina support of the catalyst. By alkali doping the catalyst, the number of these sites are reduced, and this is the most common method employed to prevent carbon build up. The alkali is either present as an alkaline support, such as calcium aluminate, or can be mixed with the catalyst by the addition of the hydroxide of an alkali metal, such as potash (potassium hydroxide). The alkali also catalyses two reactions which actually remove carbon/coke from the surface once it has formed;

$$C + CO_2 \rightarrow 2CO \qquad \text{Reaction 1.11}$$

$$C + H_2O \rightarrow CO + H_2 \qquad \text{Reaction 1.12}$$

Alkali doping increases the amount of water adsorbed onto the catalyst surface and hence increases the rate of steam reforming of hydrocarbon fragments, preventing them from undergoimg thermolysis/dehydrogenation to coke. However the overall activity of the catalyst is reduced as addition of alkali will generally result in a loss of catalyst surface area [12].

So far in this introduction, supported catalysts have been mentioned but not defined in any detail. Most metallic catalysts used in the laboratory and in commercial reactors consist of metal particles contained in the pores of a support material, usually a refractory inorganic oxide such as silica or alumina. Commercial catalysts have surface areas covering a large range. 'Low' area supports of 10 m^2/g and below, 'high' area supports, up to 100 m^2/g and 'very high' at up to 300 m^2/g and above. Metal particles are usually around 1-10nm in diameter. The support acts to reduce the sintering of the metal component, relative to that which would occur in a pure metal powder or film. This allows the catalyst to maintain a high metal surface area at high temperatures and hence a large number of active sites. The support then acts as a 'physical' spacer between metal crystallites. Accessibility of the catalyst surface to the reactants will be improved and the catalyst activity and selectivity may be modified in a beneficial manner if a support is employed. Heat generated during a reaction may be dissipated more easily. A nickel catalyst with an alumina support will be denoted as Ni/Al_2O_3.

Supported catalysts are, by their nature, complex in structure. Obtaining a full understanding of all the processes occurring on their surfaces is very difficult if not impossible. The metal particles themselves present a host of different crystalline sites to any reactant. Edge sites, plane sites, sites at steps and defects in the structure all have different free energies and symmetries associated with them. The support may

influence the adsorption of reactants, either directly or by some interaction with the metal phase, the so called 'metal-support interactions' [14].

1 The Use of Single Crystals.

Ultrapure single crystals of metals were developed as a consequence of the demand for purity by transistor manufacturers in the 1950s and 1960s. They soon provided a new angle from which to attack the problem of understanding surface catalysis. The development of ultra high vacuum technology as a result of huge space research programmes at around the same time, provided the opportunity to study clean, well defined surfaces of metals for the first time.

Without the complication of support effects and with the greatly simplified structure of the metal phase with a reduced number of types of adsorption sites, a great deal has been determined about the structural influence of catalysts on reactions by using single crystals. The adsorption surface can be fully characterised before, during and after reaction in a way that is impossible for supported catalysts. Contamination of a single crystal may be easily analysed, whereas this may not be so for a supported metal catalyst. These will inevitably contain some traces of the original metal compound i.e. they will generally not be fully reduced, and may also contain traces of hydrogen that remain after reduction. Single crystals have led to a better understanding of processes such as adsorption, surface reaction and desorption. New concepts such as surface reconstruction, surface relaxation and structured overlayers have been introduced into the catalytic world [16].

Metal atoms in crystals pack together in a variety of different ways. One of the more common packing arrangements is the face centred cubic (f.c.c.) structure. Nickel, palladium and platinum all have this structure. The exposed surface of a crystal is usually characterised by a set of coordinates known as the Miller indices, (x y z), which define the orientation of planes relative to the axes of the system. For an f.c.c. structure, there are three low index planes, i.e. three flat surface arrangements, that can exist. They are denoted as [111], [110] and [100] and are illustrated in Figure 1.6 below.

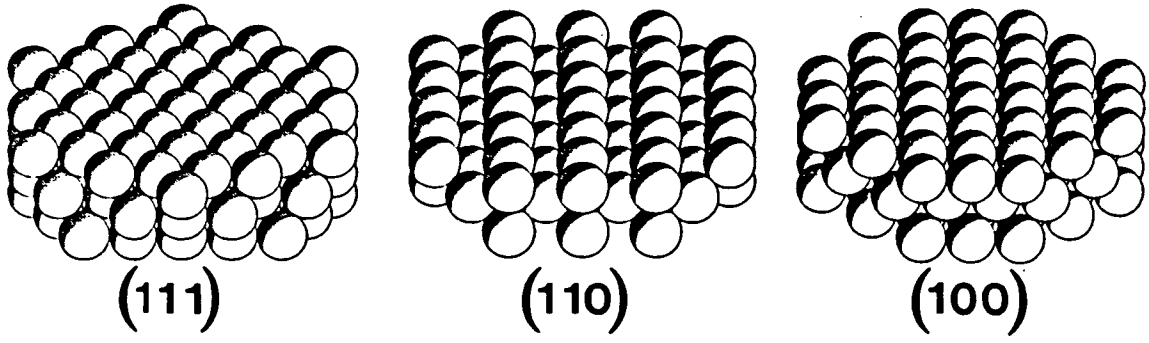

Figure 1.6 *The three low index planes of an f.c.c. metal.*

Many examples now exist in which a single crystal surface science approach has aided the understanding of supported catalysis. This is particularly true in the identification of adsorbed intermediate species and their bonding sites and surface arrangement. One early success for surface science was in the identification and characterisation of the ethylidyne species, CCH_3, illustrated in Figure 1.7 below.

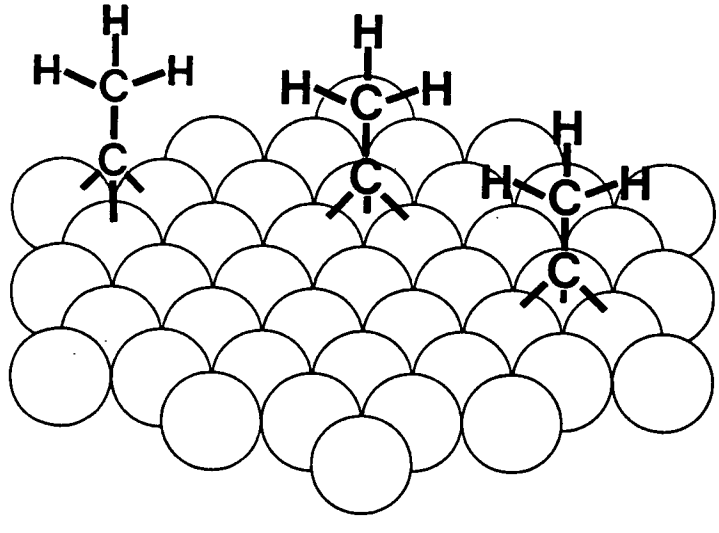

Figure 1.7 *Ethylidyne bonded to a (111)* plane of an f.c.c. metal.

The sequence of discoveries leading up to the identification of CCH_3 is outlined below. The basis of this work began with the work of Thomson and Webb [17]. They

suggested that on adsorption of C_2H_4 onto the catalyst, H transfer took place between the adsorbed C_2H_4 molecules, forming a C_2H_x species. Subsequently, in 1978 Ibach and Lehwald [18], using Electron Energy Loss Spectroscopy (EELS), revealed that a CH_3 containing species was present on the surface of a Pt(111) single crystal after adsorption of ethene at -70°C and warming to 25°C. They concluded that a $CHCH_3$ species had been formed.

Using Low Energy Electron Diffraction (LEED) intensity measurements, Somorjai *et al.* [19] showed that the C-C bond in the C_2H_x species was perpendicular to the platinum surface. Demuth was able to demonstrate that the composition of the C_2H_x species was C_2H_3 with the use of temperature programmed desorption [20]. Finally Skinner *et al.* [21] used a model organometallic compound, $(CH_3C)Co_3(CO)_9$ to demonstrate that the C_2H_x species formed on platinum was as illustrated in Figure 1.7. Taking infrared spectra of this model compound and examining the part of the spectrum with information about the CH_3C ligand, they showed that the same bands were also present in the original Ibach and Lehwald work, but modified by the surface selection rule in this case. Adsorption of an infrared active species onto a surface restricts the number of vibrations that can be observed, being restricted to those that involve a dipole change perpendicular to the surface. This is the 'metal surface selection rule', described in more detail in Chapter 2. Hence the work of Ibach and Lehwald was re-interpreted, proving entirely consistent with the ethylidyne, CCH_3 species.

Subsequently, ethylidyne has been observed on several more single crystal surfaces and also on supported metal catalysts (see Chapter 4 for more detail). Many more organometallic compounds have been employed in conjunction with single crystal studies allowing a large number of surface hydrocarbon species to be identified. These species have been named the 'surface organometallic zoo' [22]. A review by Sheppard of the vibrational spectroscopy of hydrocarbon species on single crystals was published in 1988 [23]. Again, this subject is considered in more detail in Chapter 4.

Supported metal catalysts are likely to possess a variety of metal adsorption sites and display several crystallographic planes in each particle. Van Hardeveld and Hartog [24] have shown that for a particle of an f.c.c. metal with a diameter greater than 5nm, (100) and (111) planes dominate the structure.

As the first sentence of this thesis illustrates, catalysis is essentially a kinetic phenomenon i.e. it is concerned about the rate of processes. This was emphasised by

Halpern, writing in 1978 [25];

> " Catalysis, by definition and significance, is *wholly* a kinetic phenomenon. However interesting may be the study of the physical and chemical properties of *species* involved in catalytic systems, it is only to the degree that the results of such studies can be related to the *rates* of catalytic processes that they are relevant to catalysis. "

Many surface science techniques can only be utilised in vacua of 10^{-6}mbar or better, whereas 'real' catalysis may occur at pressures of several atmospheres. This pressure difference, some 10 orders of magnitude, between these two methods of study has come to be known as the 'pressure gap' [33].

Initially, comparison of results between single crystal and supported catalyst experiments seemed puzzling. However, if the essential kinetic and thermodynamic parameters of a reaction are known, it is straightforward to extrapolate between the two. High pressure reactors for single crystals were developed for studying kinetics (e.g. [34]) and some techniques such as high pressure Reflection-Absorption Infrared Spectroscopy (RAIRS) [27] have been developed in order to 'bridge the pressure gap'.

Many studies now exist showing that similar rates of reaction can be obtained for reactions over both single crystals and supported metal catalysts. A good example is the hydrogenation of carbon monoxide to methane over nickel. Identical rates have been found for the reaction over supported nickel [28] and over two low index planes of nickel single crystals [26]. This in an example of a 'structure insensitive' reaction i.e. one in which the rate of reaction is independent of the nickel plane on which the reaction takes place. For 'structure sensitive' reactions, such as ammonia synthesis over iron, the rate of reaction varies with the iron single crystal face used [29]. The explanation of surface insensitivity may well lie in an adsorbate induced reconstruction of the surface structure of the catalyst during reaction [32].

The fact that so many experiments have yielded similar rates using both macroscopic single crystals and supported catalysts containing metal particles as small as 1nm in diameter, leads to the conclusion that metal support interactions may well be absent in the supported catalysts used for these studies. Single crystals, then, seem to be excellent model catalysts. Boudart concludes that,

> " . . . . work on single crystals provides the standards by which work on commercial catalysts can be assessed" [30].

Whilst catalysis is a kinetic phenomenon, and this underlying basis should not be

forgotten, a full understanding of rates of reaction cannot be achieved without knowledge of a reaction mechanism involving intermediate species. Indeed, kinetic data has not been enough to deduce reaction mechanisms in many cases [31]. Knowledge of reaction intermediates is necessary in order to correctly work back from kinetics to reaction mechanism.

2 Techniques for Studying Catalysis.

The chemistry of hydrocarbon catalysis involves a series of C-C and C-H bond scissions and constructions *via* surface intermediates in the evolution of reactants to products. A myriad of techniques is available in the catalytic chemists' tool kit to aid the goal of understanding the overall chemistry by identifying these intermediate species.

The essential aspect of a technique suitable for studying surface intermediates during reaction is that something must be put into the system, to interrogate it, in order to get some information out. This is illustrated well in the Propst diagram [35] below;

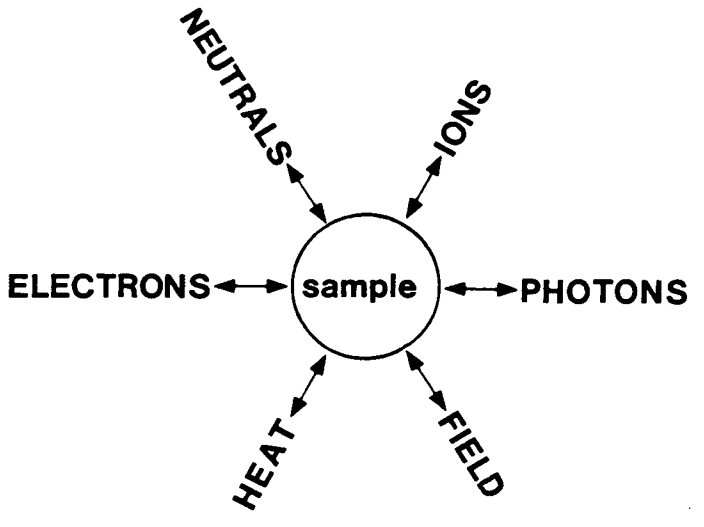

Figure 1.8 *The Propst diagram. The circle at the centre represents the catalyst sample. Ingoing arrows are the incoming probes, outgoing arrows carry the information about the sample.*

Each possible combination of incoming and outgoing arrows would seem to constitute a possible technique, making 36 possible combinations. Many of these techniques do exist and certainly all of the possibilities have been attempted. There are many duplicates, such as for photons in and electrons out, where the photons may

be either ultraviolet {making ultraviolet Photoelectron spectroscopy (UPS)} or X-rays {making X-ray Photoelectron spectroscopy (XPS)}. In both cases electrons are emitted and analysed.

Some of the more common techniques relevant to catalysis are listed in Table 1.1 below;

Table 1.1 Some Common Catalytic Techniques.

In	Out	Technique
photons	photons	Infrared Spectroscopy
photons/field	photons	Solid-State Nuclear Magnetic Resonance
electrons	electrons	Auger Electron Spectroscopy (AES)
electrons	electrons	Low Energy Electron Diffraction (LEED)
electrons	electrons	Electron Energy Loss Spectroscopy (EELS)
electrons	electrons	Electron Microscopies; Transmission/Scanning/Scanning-Tunneling
photons	electrons	X-ray Photoelectron Spectroscopy (XPS)
photons	electrons	Ultraviolet Photoelectron Spectroscopy (UPS)
heat	neutrals	Thermal Desorption Spectroscopy (TDS)
ions	ions	Secondary Ion Mass Spectrometry (SIMS)

A whole arsenal of instrumental techniques [15] has become available, from electron spectroscopies to X-ray and infrared probes, to study adsorption of molecules on surfaces. Work of this nature has come to be known as 'surface science'. The polycrystalline, or possibly amorphous structure of supported catalysts, and their generally poor electrical conductivity, renders many of these 'surface science' techniques of little use for this kind of work e.g. Low Energy Electron Diffraction (LEED) and Electron Energy Loss Spectroscopy (EELS). However, many techniques developed for surface science have found a use in heterogeneous catalysis e.g. X-ray Photoelectron Spectroscopy (XPS). Obviously with such a vast range of techniques it would be impractical to review all of them in this context. Many reviews and books exist (e.g. [36], [37]). A few techniques of relevance to this thesis are discussed below.

Perhaps the most widely used technique in surface chemistry is that of infrared

spectroscopy, and it forms the basis of later chapters in this thesis. Referring to the Propst diagram, this is a photon in and photon out technique. Infrared photons interact with the surface species, either in a transmission, reflection or diffuse reflectance mode of set-up. Some frequencies of photon will be absorbed, whilst most will be unaffected and proceed out of the system.

The frequencies that are absorbed each correspond to the natural vibrational frequency of chemical bonds. Each type of bond in a compound has its own specific vibrational frequency or 'group frequency'. By examining the absorption bands in an infrared spectrum, direct information about the type of bonds present in a compound can be obtained. As has already been explained, when infrared spectroscopy is applied to surfaces, an additional 'metal surface selection rule' comes into play. This restricts the number of vibrations that are infrared active and considerably helps in assignment of bands in the infrared spectrum. The application of infrared spectroscopy *via* various different techniques, as well as the theory of interaction will be discussed in more detail in Chapter 2.

The ease of application and versatility, allied to the many types of material that can be studied has made infrared spectroscopy probably the most widely used spectroscopic technique in catalysis. Single crystals may be studied in ultra high vacuum, and at the other extreme, supported metal catalysts can be studied during high pressure and temperature reaction. To be observable in infrared spectroscopy, an intermediate species must have a lifetime of a least the scan time for collection of one infrared spectrum, $\approx$ 0.5s in the case of a $4cm^{-1}$ resolution spectrum on a Digilab FTS-40 Spectrometer. There is no way of proving that species observed in an infrared spectrum are real reaction intermediates or simply 'spectator species'. However, if the transient response of a surface species parallels that of the gas phase product evolution, it can be reasonably assumed that the surface species is an intermediate in the process [38].

Like infrared spectroscopy, thermal desorption is another of the standard workhorses used in surface studies today. Unlike infrared spectroscopy, thermal desorption is a destructive technique. It simply involves heating the sample and examining the gas that desorbs from the surface, i.e. adsorbate-adsorbent bonds are broken. Various techniques such as mass spectrometry and gas chromatography can be used to identify and quantify the molecules that desorb. As well as this quantitative data, kinetic information can be derived from the rate of desorption. A linear heating rate is generally employed. Thermal desorption studies of H_2 desorption from

Ni/Al_2O_3 are described in Chapter 3. A review of thermal desorption methods was published in 1983 [39].

In this thesis, both of these techniques are used to study the adsorption and desorption of C_2H_4 and C_3H_6 on an alumina supported nickel catalyst.

CHAPTER 2

Infrared Spectroscopy-Theory and Practice.

Infrared spectroscopy is a subset of a larger class of spectroscopy, that of vibrational spectroscopy. Probably the earliest use of infrared spectroscopy to study adsorbed gases on solids was in 1911 by Coblentz [40]. Surface hydroxyl groups bonded to oxides were examined in the near infrared region of the spectrum (10000-4000cm^{-1}), using transmission absorption spectroscopy. Not until the 1950s were the instrumental problems associated with the study of supported metal catalysts overcome. Eischens and Pliskin [41] were then able to make the first studies of adsorption on heterogeneous catalysts in the more useful mid-infrared region (4000-400cm^{-1}). Since that time, the use of infrared spectroscopy for studying adsorption has become widespread.

1 The Physical Basis of Infrared Spectroscopy.

Chemical bonds are essentially electrostatic interactions between positively charged nuclei and negatively charged electrons that surround them. Bond vibrations are displacements of these atoms over potential energy surfaces, leading to distortions in the distribution of charge in the molecule. These electrical distortions can be resolved into a dipole change (and higher terms, quadrupoles etc.) within the molecule as it vibrates. The frequency of the oscillation of the electric charge is governed by the normal vibrational modes of the system.

The electric vector of electromagnetic radiation of the same frequency can undergo resonant energy transfer with this molecular dipole. The intensity (I) of a vibrational infrared band is shown in the 'golden rule' expression, Equation 2.1 below;

$$I = | < \psi_i^{||} | \mu_i . E | \psi_i^{|} > |^2 \qquad \text{Equation 2.1}$$

where $\psi_i^{|}$ and $\psi_i^{||}$ are vibrational wave functions of the ith mode.
E is the electric field acting on the vibrating bond.
μ_i is the dipole moment.

The oscillator is raised from one eigenstate, or energy level υ to another, $\upsilon + 1$ with the quantum energy of the radiation $h\nu$, which is equal to the quantum energy of the oscillator $h\omega$. The frequency of radiation able to interact with molecular vibrations occurs in the 'mid-infrared' region of the spectrum (between 10^{11} and 10^{13} Hz, 30-3000cm^{-1}). The frequencies of radiation that are absorbed appear as absorption bands in an infrared spectrum. Only vibrations that produce a dipole change are able to interact and absorb radiation energy from the infrared beam.

Oscillating dipoles may only absorb radiation and change vibrational quantum number by one i.e. go from $\upsilon=0$ to $\upsilon=1$, or $\upsilon=1$ to $\upsilon=2$. In practice, only the $\upsilon=0$ level has significant population at room temperature for transitions >1000cm^{-1}, and so $\upsilon=0$ to $\upsilon=1$ is the dominant absorption for any specific bond. This is known as the fundamental vibrational selection rule. This classical view of infrared absorption remains valid when a quantum mechanical approach is taken.

In order to determine what vibrations of a molecule may be give rise to a dipole change and therefore be infrared active, reference to the symmetry of a molecule is required. Each molecule may be associated with a specific 'point group' which describes the symmetry of the molecule in terms of reflections, inversions, rotations and rotation-reflections [42]. Each vibration of a molecule can then be characterised by a specific symmetry species by reference to the 'character table' for each point group.

The number of possible vibrations that a molecule can possess is restricted. In the gas phase, a species with N atoms possesses 3N degrees of freedom. For a non linear species, three of these are rotations and three are translations, leaving 3N-6 possible vibrations. For linear molecules, there are 3N-5 vibrations since only 2 degrees of rotational freedom are needed for a full description.

In gas phase ethene, a six atom non linear molecule, there should be 12 possible vibrations. The 12 normal modes of ethene are illustrated in Figure 2.1 below.

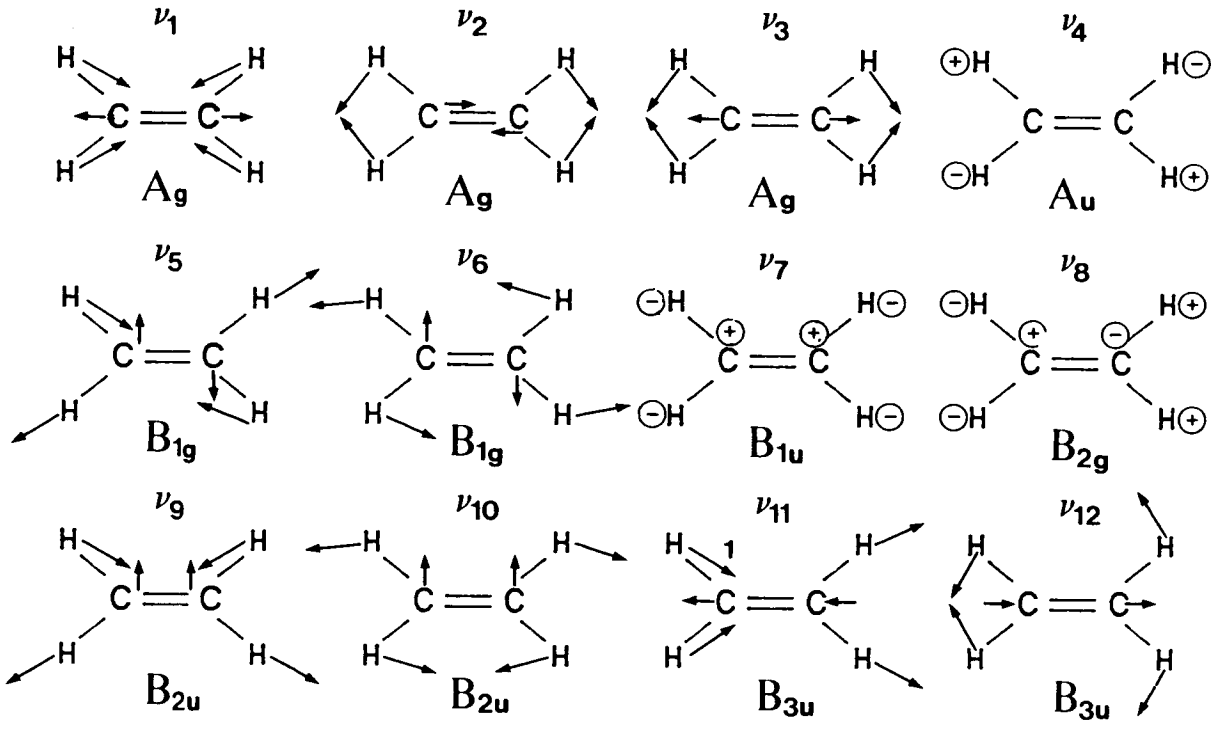

Figure 2.1 *The 12 normal vibrations of gas phase C_2H_4* [44].

Ethene belongs to the D_{2h} symmetry point group, and knowing this allows the number of infrared active vibrations to be determined. By examining the D_{2h} point group character table, the vibrations that involve displacement along either the x, y or z axes can identified. These will be the infrared active modes. For ethene, these turn out to be only those with an irreducible representation of the B_n type, ν_7, ν_9 - ν_{12}. In the CH stretching region of the spectrum they are ν_9 at 3105.5cm^{-1} and ν_{11} at 2989.5cm^{-1}, whilst ν_7 at 949cm^{-1}, ν_{10} at 995cm^{-1} and ν_{12} at 1443.5cm^{-1} are CH deformation modes. It is worth noting that in the gas phase, the νCC stretching mode is totally symmetric (A type) and thus cannot be observed with infrared spectroscopy.

On adsorption of a gas phase species onto a solid, the number of atoms in the whole system increases by 3N, where N is the number of atoms in the solid. If the species is weakly bonded, and the frequency corresponding to translational motion is low compared to kT, diffusion of the species will be significant. Hence the two degrees of freedom corresponding to motion parallel to the surface continue as translations and the 3N-6 vibrations of this species are little changed. If the molecule

remains intact, the vibrational modes of the molecule will remain similar to the original ones.

If strong chemisorption results, the molecules may be translationally hindered by a strong restoring force and these movements are converted to a vibration of the species against the surface. These are known as 'frustrated' translations and rotations. With very strong chemisorption, strong coupling to the internal vibrations of the adsorbed species become so involved with the internal vibrations of the solid lattice that they must be regarded as one entity, with an additional 3N vibrational degrees of freedom added after chemisorption. A good example of this are the OH groups on the surface of a silica crystal, where there is considerable interaction between the O-H and Si-O vibrations.

When light atoms such as H, C and N are bonded to heavy atoms such as transition metals, only weak coupling occurs between the vibrations of the metal lattice and the internal vibrations of the adsorbed species. This is due to the frequency mismatch between the phonon energies in the solid and the intramolecular frequencies of an adsorbed species e.g. C-H stretches are $\approx 3000 cm^{-1}$, Ni-C stretches are $\approx 400 cm^{-1}$ and Ni-Ni stretches at $\approx 200 cm^{-1}$. Consequently the internal vibrations of the individual adsorbed species exist in a more meaningful way.

When molecules adsorb onto a surface the symmetry of the structures formed will generally be lowered from that in the gas phase. Surface species may only possess symmetry planes and rotations perpendicular to the surface as symmetry elements. This limits them to only 10 point groups of the C_n and C_{nv} series, C_1, C_2, C_3, C_4, C_6, C_s, C_{2v}, C_{3v}, C_{4v} and C_{6v} [43]. The vibrations in a species can be analysed once the point group of a species is known, giving an indication of their infrared activity. However, if the incoming molecule has dissociatively adsorbed or reacted in some way, the resulting structures may bear little resemblance to the original gas phase species. More clues are needed to help in the identification of surface structures in this situation.

One of the most fruitful aids to identification is to examine the extensive literature of infrared band assignments that has been generated over the years. Vibrations can be divided up into 'group frequencies', allowing conclusions to be drawn about the position and type of vibrations in infrared spectra. Some group frequencies for gas phase hydrocarbon species are shown in Table 2.1 below.

Table 2.1 Group Frequencies of Some Hydrocarbon Vibrations [45].

Vibration	cm^{-1}	Description	Vibration	cm^{-1}	Description
≡C—H	3300	'acetylenic' C-H stretch	C=C (H, H)	1410	CH_2 in plane deformation
C=C (H)	3020	'olefinic' C-H stretch	—C(H)(H)H ⊖	1375	symmetric CH_3 deformation
—C(H)(H)H	2960	asymmetric CH_3 stretch	C(H)(H)	1465	CH_2 deformation
C(H)(H)	2925	asymmetric CH_2 stretch	—C(H)(H)H ⊕	1450	asymmetric CH_3 deformation
—C(H)(H)H	2870	symmetric CH_3 stretch	C=C (H⊕, H⊕)	890	out of plane deformation
C(H)(H)	2850	symmetric CH_2 stretch	—C=C—	1650	C=C stretch

Another useful aid to identification of unknown surface species is the use of organometallic compounds as models for adsorbate structures, as mentioned in the introduction. Many of these compounds contain clusters of metal atoms with a variety of surrounding hydrocarbon ligands. Infrared spectra of them can lead to direct assignment of the vibrations of the hydrocarbon ligands in question, provided there is no interference with the absorption bands of other ligands. This is usually the case, as the other ligands tend to be CO and are therefore well away from CH bands in the

spectrum. It has been found that many hydrocarbon ligands in organometallic compounds do indeed have similar frequencies to their surface relatives [46]. As discussed below, as a consequence of the metal-surface selection rule (MSSR), only vibrations of a species that have a component of dipole change perpendicular to the surface can be observed with infrared spectroscopy. Such vibrations are generally totally symmetric modes. This in itself is another aid to the identification of surface species, because a degree of simplification is introduced by a reduction in the number of observable bands. Although there may be 3N localised vibrational modes associated with an isolated adsorbed molecule, many will not be observed, either because they are not inherently infrared active, or because infrared active asymmetric modes are quenched by the MSSR.

2.1 The Metal-Surface Selection Rule.

The origin of the MSSR lies in the property of metals, distinguishing them from dielectrics, of the conduction of electricity. As electromagnetic radiation approaches a metal, the electric field vector (E) is able to polarize the electrons in the metal's conduction band and also the dipoles of adsorbed molecules. Electromagnetic theory indicates that at a boundary i.e. at the metal surface, the tangential component of E (parallel to the surface) must be continuous across the boundary. Most metals are excellent conductors at infrared frequencies and so approximate to the requirement that the E field inside a perfect conductor must be zero. Combining these two conditions implies that the component of the E field parallel to the surface must be zero. In other words, electromagnetic radiation impinging on a metal is unable to excite vibrations in oscillating dipoles that are parallel to the surface. Therefore, only vibrations perpendicular to the surface are able to absorb infrared energy. Looking at this in a slightly different way, the electric vector perpendicular to the surface generates a standing wave within the metal, which will have a node at the surface. Standing waves are not generated parallel to the surface as the electrons are able to move to neutralise this applied field and damp the incoming wave. The end result is that only vibrations that produce an oscillating dipole perpendicular to the surface can absorb incoming infrared radiation. In practice this is usually for totally symmetric vibrations of adsorbed species.

A schematic diagram of the damping of parallel vibrations and amplification of perpendicular vibrations is illustrated in Figure 2.2 below,

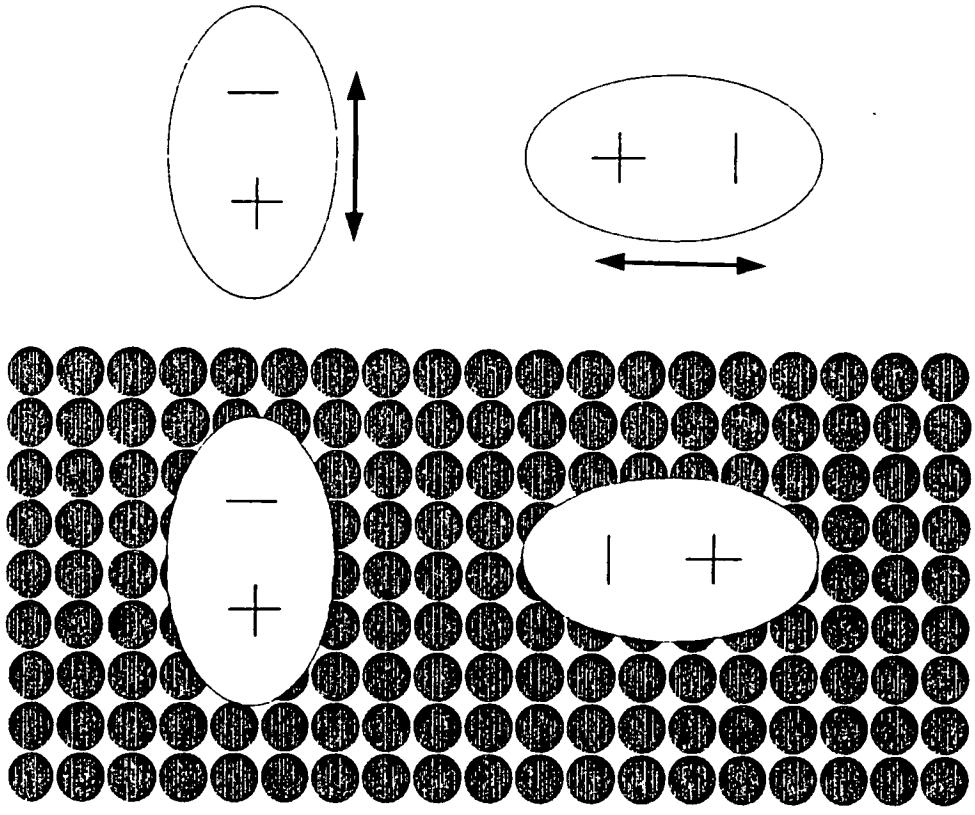

Figure 2.2 *Perpendicular vibration (left) and parallel vibration (right).*

The electric field vector does not decrease to zero abruptly at the boundary of a metal, but decays exponentially within the bulk. If the penetration depth of the E field is defined as the depth where its intensity has dropped by 1/e, it turns out that for most metals this depth is about 10-20nm [47]. If this is the determining factor in the establishment of the MSSR, then it should break down with particles that are smaller than this. However it appears that the metal surface selection rule does apply for particles smaller than this [47] and that the decay of the electric field vector within a metal is the wrong way to describe this phenomenon.

Another argument begins with defining the electric field perpendicular to the surface of a small metal particle as E_r (the radial component) and the parallel field as E_t (the tangential component). The integrated intensity should be then E^2. The ratio of these two intensities is therefore proportional to E_t^2 / E_r^2. Averaged over a whole particle E_t^2 / E_r^2 becomes the surface ratio SR. For the MSSR to work, SR must be zero. This would only be so if E_t^2 is zero, because the parallel oscillations have been

suppressed.

Using a classical Maxwellian approach, it can be shown that in order to consider the static field at the surface of a sphere, only potential theory need be considered [48]. This gives E outside a spherical metal particle of radius r as,

$$E(r,\theta) = E_0 \left[r - \left(\frac{\bar{n}^2 - 1}{\bar{n} + 2} \right) \frac{r_0^3}{r^2} \right] \cos\theta \qquad \text{Equation 2.2}$$

where E_0 is the amplitude of the incident plane wave.
θ is the angle measure of E_0.
$\bar{n}$ is the refractive index, n - ik.
r_0 is the radius of the spherical particle.

Differentiating Equation 2.2 gives E_t and E_r. Because $SR = E_t^2 / E_r^2$ this gives;

$$SR = 2 \left| \frac{1 - \left(\frac{\bar{n}^2 - 1}{\bar{n}^2 + 2} \right) \left(\frac{r_0}{r_0 + d} \right)^3}{1 + 2 \left(\frac{\bar{n}^2 - 1}{\bar{n}^2 + 2} \right) \left(\frac{r_0}{r_0 + d} \right)^3} \right|^2 \qquad \text{Equation 2.3}$$

where d is the distance from the sphere.

Using this equation for copper ($\bar{n}$ = 3-i30), over the distance at which chemisorption normally occurs, say 0.2-0.3nm from the surface, SR appears to remain zero for particles down to a diameter of about 1 to 1.5nm. Smaller particles are not able to bend the field lines enough over this chemisorption distance so that they are normal to the surface. The catalyst used in this thesis has nickel particles in the range 10 to 15nm and so it can be assumed that this is well within the regime of relevance of the MSSR. Consequently, all infrared spectral assignments can be made with this in mind. A pictorial way of representing the field lines surrounding a metal particle is shown in Figure 2.3 below,

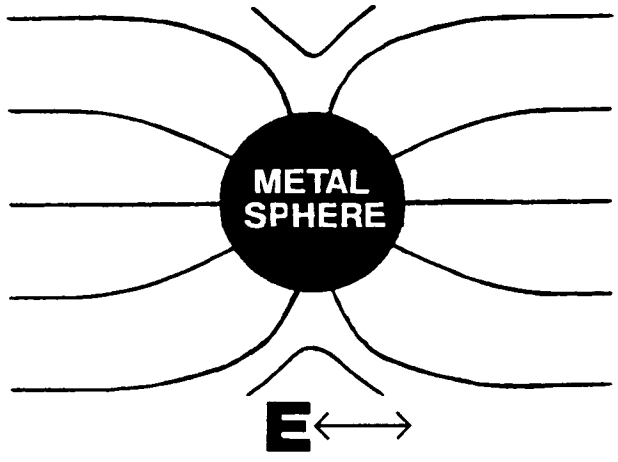

Figure 2.3 *Representation of the bending of electric field lines into a metal sphere placed into a uniform electric field. The lines are perpendicular as they enter the surface of a metal* [47].

The size of the support particles in the catalyst is generally much larger than the metal particles that they support. As discussed in Chapter 3, the support particles of the Ni/Al_2O_3 catalyst used in this thesis have an average diameter of 6μm when reduced, several orders of magnitude larger than the 12nm metal particles that they support. Radiation in the mid-infrared region has a wavelength of between 2.5μm ($4000cm^{-1}$) and 25μm ($400cm^{-1}$), of similar dimensions to the support particles.

2.1.1 The Interaction of Light with Powders.

Incoming radiation may interact with a powdered catalyst in four main ways ; absorption, reflection, transmission and chemical change. The first two always occur to some extent, transmission only occurs with matter that is transparent to the specific radiation wavelength and chemical change occurs only in special circumstances such as photo-chemical reactions.

The Ni/Al_2O_3 catalyst is opaque in the visible region, and has variable colour. On preparation it is pale green. When calcined it becomes grey. On reduction, the catalyst turns totally black.

The green nature of the as-prepared sample is due to the hexa-aquo ion of nickel(II), $[Ni(H_2O)_6]^{2+}$. Most common nickel salts are green because of the

octahedral field acting in this ion, absorbing light in the orange (605-595nm) region.

On calcination, the hexa-aquo ion dehydrates, forming a black compound, probably a mixture of NiO and βNiO(OH). This mixture is totally absorbing and should appear black. It has a grey tint because, although absorbing, the small particles are in the region of significant Rayleigh scattering (see Equation 2.15). Some white light is scattered from the top surface of the catalyst, and consequently appears grey. The as-prepared catalyst appears pale green because some Rayleigh scattering also occurs here, mixing the green with white. If particles were smaller they would appear in their 'true colours' as they would be out of the region of significant scattering of white light.

On reduction, the catalyst becomes black. Evidently scattering of light is no longer important, the material is totally absorbing. Whilst metals are usually totally reflecting, a special situation may exist when small particles of a metal interact with light. At some point, highly reflecting and shiny metals become totally absorbing and therefore black. This effect is due to the 'spongy' surface structure of a collection of metal particles meaning that the majority of light entering the powder is reflected into the body of the sample and absorbed [49]. At all states of the catalyst, the support particles of alumina are transparent to visible radiation, and only contribute to scattering.

Such transparent and translucent materials allow light to pass straight through, apart from some absorption losses. In the infrared region, some materials such as metal halide salts are transmitting over a wide range of wavelengths, making them suitable for windows in infrared equipment. A characteristic 'cut-off' frequency at low wavenumber may be associated with these materials, below which the material is absorbing due to intense metal-X absorption bands (X=oxide, halide etc.). For alumina this is usually at $\approx 1100 cm^{-1}$, and for silica $\approx 1300 cm^{-1}$. Figure 2.4 below shows the transmittance of several materials over the mid infrared region.

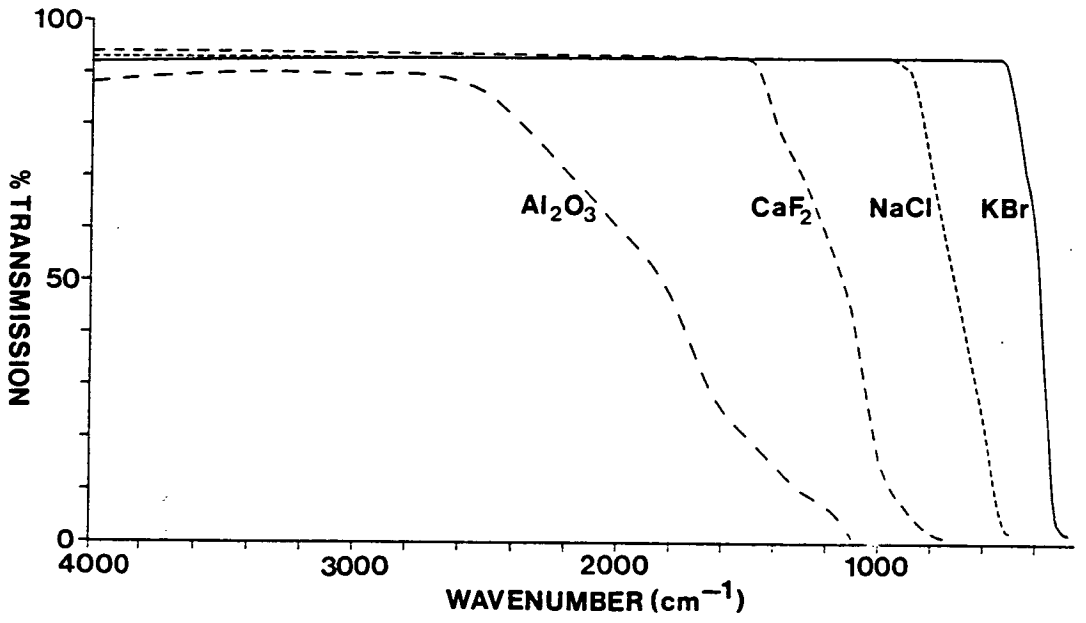

Figure 2.4 *Infrared transmittance of Al_2O_3, CaF_2,* NaCl and KBr (4000-400cm^{-1}.)

Two types of reflection of radiation can occur from surfaces. Reflection from mirror like surfaces where the angle of incidence equals the angle of reflection, is known is this context as direct, geometrical or regular Fresnel reflection, obeying Fresnel's Law. When light interacts with a powder, Fresnel reflection from the top surface of the powder is generally known as specular reflection. The randomly oriented particles produce both regular Fresnel reflection from parallel surfaces and diffuse Fresnel reflection from particles whose surfaces are not parallel to the surface of the macroscopic sample.

Light reflected from a mat surface is called diffuse reflection. The radiation has generally entered the material and undergone reflection, refraction, scattering and absorption to a varying degree, before re-emerging as diffuse reflectance. Unlike specular reflection, the diffuse reflectance from a perfectly mat surface is distributed isotropically in all directions. This would make it appear equally bright in all directions. Such a surface is known as a uniformly diffuse reflector or sometimes a 'Lambert reflector', because it obeys the Lambert Cosine Law of Emission [49]. Whether reflection from a particular surface is diffuse or specular depends on the nature of the material and the orientation of the particles in a powder.

Metals are inherently specular reflectors, radiation may not enter the bulk. Most materials reflect both specularly and diffusely to some extent, and this is usually

known as mixed reflection. Reflection from the alumina support of the catalyst will possess significant components of both. Whilst the diffusely reflected component interacts with the support and consequently suffers absorption losses and is influenced by the infrared 'cut-off', specular reflection is not significantly affected by absorption and is therefore referred to as the residual ray or reststrahlen.

Figure 2.5 below shows a variety of optical processes that can occur when a beam of radiation interacts with a powder.

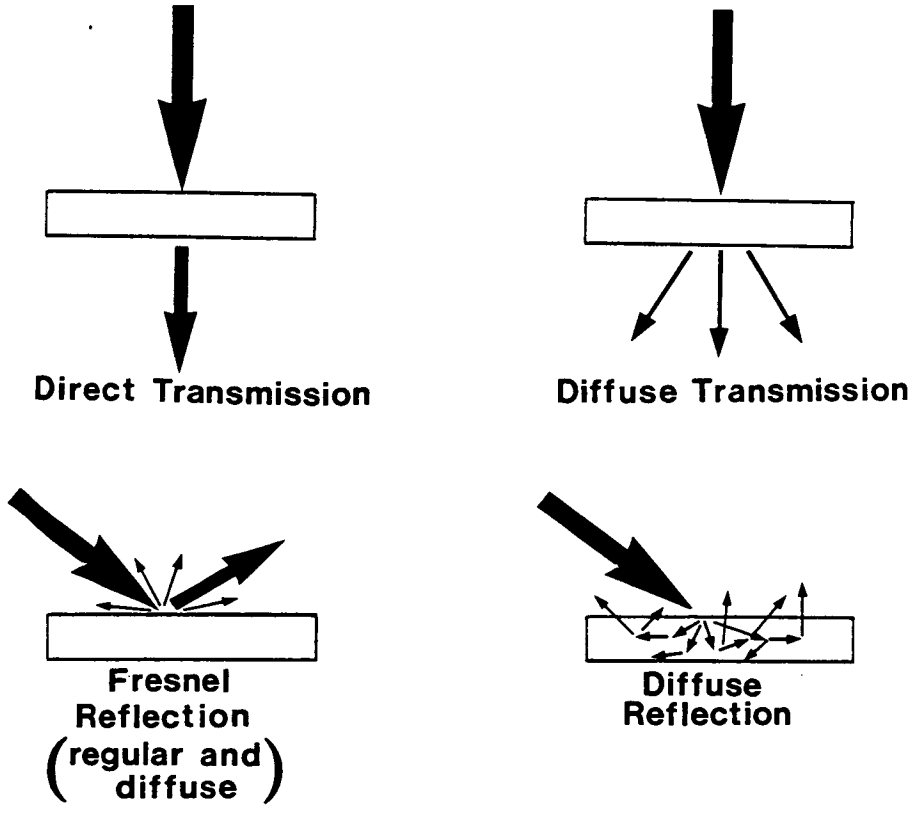

Figure 2.5 *Possible pathways for outgoing radiation after interacting with a powdered sample, such as a catalyst.*

The exact nature of the interaction of radiation with powdered materials is quite complex. It is very difficult to predict which of the absorption, reflection and transmission processes will occur. The nature of the particles, their size, shape, orientation and packing density all affect the interaction processes. Some general conclusions can be drawn.

Mie scattering of radiation from a particle will occur when the particle is about the same size or larger than the incident infrared

wavelength. Strictly speaking scattering by this theory is restricted to single scattering events from isotropic spheres at a large separation from each other [50], although it is still useful in explaining the behaviour of a large conglomerate of particles [51]. The nature of the surface of the support particles determines the nature of the reflection since the metal phase of the catalyst exists in particles too small to interfere with the radiation except to produce local perturbations in the E vector. If the support consists of large crystals, specular reflection is more likely as the particles present large surfaces to the incoming radiation. A way of defining the difference between diffuse reflection and specular reflection is the fact that light that is specularly reflected undergoes only one interaction with the sample, a reflection from the top surface of the sample. Diffusely reflected radiation undergoes *at least* two interactions which may be reflections, refractions or diffractions, before re-emerging from the sample.

Infrared spectra of adsorbates on catalysts may be collected with a variety of optical arrangements. Traditionally a transmission mode has been employed, looking at the extent of radiation absorption by the catalyst in the infrared beam, giving Transmission-Absorption Infrared Spectroscopy. More recently, powdered catalysts have been studied by looking at the diffusely reflected component of the radiation, giving Diffuse Reflectance Spectroscopy. Both of these techniques are discussed below.

2.2 Collection of Data.

2.2.1 Transmission Infrared Spectroscopy.

Two types of transmission of infrared radiation through a sample are possible. Direct transmission (sometimes miscalled 'specular transmission') refers to light transmitted without any scattering e.g. by clear glass. Diffuse transmission happens when scattering occurs in a translucent medium. As we have already seen, metals will not transmit radiation, whereas dielectrics will. The basis of the transmission experiment is to allow the interaction of the radiation with the metal and the adsorbed species, the remainder passing straight through the sample. Reflection losses, both specular and diffuse, must be minimised with this mode of collection. Transmission would be impossible through an all metal sample, so another function of the support is to allow transmission of the radiation that has not been absorbed by the sample and adsorbed molecules.

A schematic diagram of the transmission process is shown below in Figure 2.6.

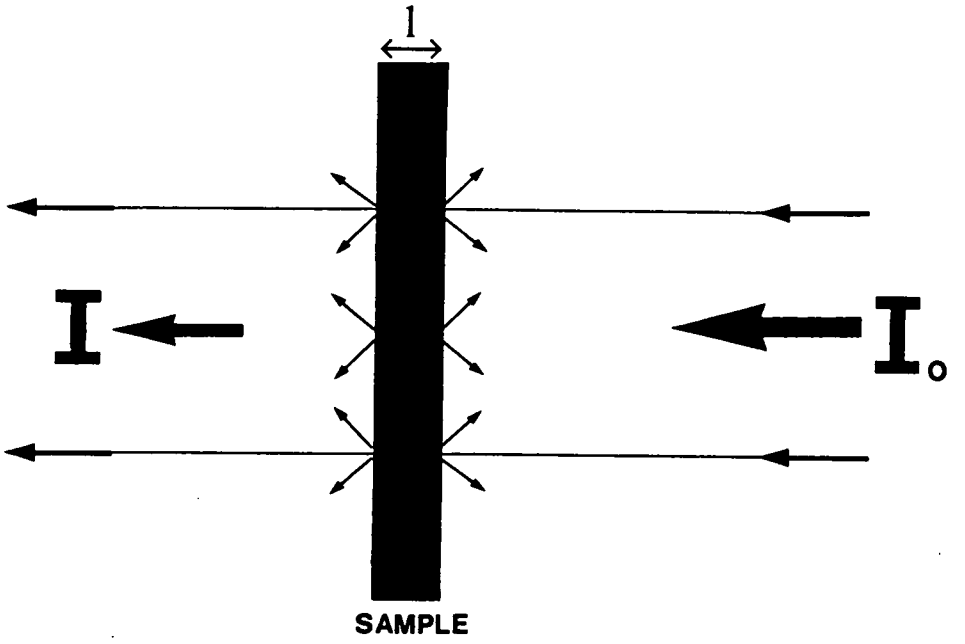

Figure 2.6 *Schematic diagram of the transmission of radiation through a catalyst sample. I_0 is the incident intensity, I the transmitted intensity and l is the path length through the sample.*

The beam will undergo a series of different losses in intensity from I_0 to I. Some reflection will occur from the front face of the sample. Within the sample, some absorption of the beam will take place, both by the support and the adsorbed molecules. It is this latter term that is of interest. Some diffuse transmission will also occur, spreading the beam out over a solid angle on leaving the sample. The effect of these losses will be dependent on how large a solid angle the infrared collection optics cover.

The transmittance, $T(\bar{\nu})$, and the optical density, or absorbance $A(\bar{\nu})$, both at a given wavenumber, $\bar{\nu}$, are defined as,

$$T(\bar{\nu}) = \frac{I(\bar{\nu})}{I_0(\bar{\nu})} \qquad \text{Equation 2.4}$$

$$A(\bar{\nu}) = \log_{10}\left(\frac{I_0(\bar{\nu})}{I(\bar{\nu})}\right) \qquad \text{Equation 2.5}$$

Another term sometimes used is the absorptance, $(1-T(\bar{\nu}))$, the signal due to the

absorbing sample. The molar extinction coefficient is given by the Beer-Lambert Law;

$$\varepsilon = \frac{1}{cl} \log\left(\frac{I_0(\bar{\nu})}{I(\bar{\nu})}\right) \qquad \text{Equation 2.6}$$

where c is the concentration of the absorbing molecules.
l is the path length through the sample.

or written in terms of transmittance,

$$T(\bar{\nu}) = \exp[\, -\varepsilon\, c\, l\,] \qquad \text{Equation 2.7}$$

The attenuation of the beam, $+\varepsilon cl$, is known as the absorbance, $A(\bar{\nu})$. Thus the concentration c of absorbing molecules is related to the log of the intensity, allowing quantitative conclusions to be drawn from the Beer-Lambert Law. The absorbance of the beam is the sum of the sample absorbance and the absorbance due to the adsorbed species. The catalyst discs used here had a typical sample thickness of 0.5mm. This reduced the transmitted signal, integrated over the whole range of frequencies, by around 70% from I_0=7V to I=2V. The absorbance of the adsorbed species is much smaller and is superimposed on this loss.

For catalysts, the integrated absorbance, A, is usually used rather than the absorbance at band maximum. The derivation of A is formulated below [52],

$$A = A(\bar{\nu})\, d\nu$$

$$= \int_{\bar{\nu}_1}^{\bar{\nu}_2} \ln\left(\frac{I_0(\bar{\nu})}{I(\bar{\nu})}\right) d\nu \qquad \text{Equation 2.8}$$

But $A = \bar{\varepsilon}\, c\, l$ where $\bar{\varepsilon}$ is the integrated absorption coefficient.

The spectrum of adsorbed species (A_c) is the total absorbance (A) minus the absorbance of the sample, (A_s),

$$A = A_s - A_c$$

$$= \int_{\bar{\nu}_1}^{\bar{\nu}_2} \ln\left(\frac{I_c(\bar{\nu})}{I(\bar{\nu})}\right) d\bar{\nu} \qquad \text{Equation 2.9}$$

$$= \varepsilon_a \, c \, l$$

where I_c is the intensity of the transmitted beam through the catalyst *without* adsorbed species.
ε_a is the integrated absorption coefficient for the adsorbate.

Whilst the absorption coefficient of the catalyst, ε_c, is independent of the sample thickness and is a constant, ε_a for adsorbates may vary with the concentration of the adsorbed species. An example of this is the adsorption of CO on Ru/SiO_2. Here, ε_{CO} is constant at low coverage of CO, and decreases as the coverage increases. This is due to adsorbate-adsorbate interactions between adjacent CO molecules at high coverage [52]

The sample illustrated in Figure 2.6 is a self supporting disc placed perpendicular to the beam of infrared radiation. This is the usual method of sample preparation, the powdered sample being pressed into a disc under a pressure of several tons. This is often experimentally tedious. Other methods of sample preparation can be used, such as spray drying samples onto grids and plates (see section 2.1.2). However, it is known that scattering losses increase when the catalyst is in a loosely held form [53]. The scattering coefficient, s, decreases as loosely held powders are compressed, and hence the amount of light transmitted increases. Scattering is discussed in more detail in section 2.1.2.

2.2.2 Review of Cell Designs.

Since the earliest infrared cell design of Eischens and Pliskin [54], a myriad of different designs have been developed, with a variety of features. The Eischens' cell had a main body of silica, with CaF_2 infrared transmitting windows. The catalyst was pressed onto another CaF_2 plate, and the cell could reach a maximum temperature of 800°C *in situ*. The path length for the infrared radiation was of the order of 20cm. A list of some more recent designs, by no means exhaustive, appears below in Table 2.2, together with some design features.

Table 2.2 Transmission Cell Characteristics.

maximum temperature *in situ*	>600°C	**this cell**, [55], [59], [64], [69], [73].
	500-600°C	[60], [66]- [68], [75], [81].
	400-500°C	[57], [58], [61], [62], [74], [77], [78].
	300-400°C	[65], [70]- [72], [76].
	200-300°C	[56], [63], [79], [80].
cryogenic operation		[55], [56], [67], [72], [75], [76], [81].
linear temperature programming	≤1°C/s	**this cell**, [55], [57], [58], [61], [64], [71], [74], [75].
	≥1°C/s	**this cell**, [55].
window materials	Al_2O_3	[61].
	CaF_2	**this cell**, [55]- [59], [63]- [65], [69]- [72], [76], [80], [81].
	ZnS	[66].
	SiO_2	[58]
	KBr	[60], [62], [67], [78].
	ZnSe	[79].
	CsI	[68], [73].
	NaCl	**this cell.**
	IRTRAN 2	[74].
	Silicon	[75].
cell body	steel	**this cell**, [55]- [57], [59]- [62], [64]- [72], [74]- [81].
	silica	[58], [63], [73].
sample preparation	wafer -self supporting	[57]- [67], [69]- [73], [75], [77]- [81].
	powdered	[55], [56], [68], [76].
	wafer pressed into grid	**this cell**, [74].
mode of operation	U.H.V.	**this cell**, [55], [56], [59], [60], [66], [72]- [74], [76], [77].
	vacuum	[58], [63], [78].
	gas flow	**this cell**, [57], [59], [61], [66]- [71], [79]- [81].
	high pressure	[57], [59], [62], [64], [65], [69], [80].
infrared path length	<1cm	[65], [69].
	1-2cm	[59], [62].
	2-3cm	**this cell**, [70], [71].
	3-4cm	[75], [78].
	4-5cm	[72], [74], [76], [80].
	>5cm	[55]- [58], [60], [62]- [64], [66], [67], [73], [77], [79], [81].
gas through catalyst		**this cell**, [57], [62], [68]- [72], [75].

A review of designs has been published recently [55], together with a cell design combining many desirable features as described above. This probably illustrates the 'state of the art' in transmission cell design. However, this cell does have a rather long infrared beam path through the cell (≈6cm). It is often useful to minimise this in order to reduce the interference generated by absorption bands of gas phase species, allowing a clearer view of the surface infrared bands. Also, this cell does not force the gas to flow through the catalyst, the gas flows across the sample, allowing it to escape around the edges.

In deciding what features were desirable for the cell used in this work, several factors were considered. Reduction of catalysts such as a Ni/Al_2O_3 material requires temperatures of up to 600°C (detailed in Chapter 3). If this is to take place *in situ*, together with a minimum infrared path length and under gas flow conditions, care has to be taken in order to reduce the potential damage to window material as a result of excessive heating. This can be achieved by using CaF_2 as the window material, which is relatively robust, having efficient cooling of the windows and by localising the effect of the catalyst heater as much as possible. Consequently, a system of preparing catalyst discs was developed involving pressing a tungsten mesh within the disc to act as a very localised heating element. This allows the cell to operate up to a temperature of 600°C under one atmosphere of gas, with the windows reaching 85°C and the cell body only 40°C. The localised heating means that there is minimal thermal lag between heater control and thermocouple measurements, and consequently linear temperature programming is easily achieved. Since the catalyst heating element is *in situ*, saturation of the infrared detector occurs, usually at temperatures of >400°C, because of the unmodulated infrared emission from the heating element. This makes collection of spectra at higher temperatures impossible.

Cell Construction.

The design and construction is illustrated in three diagrams. Figure 2.7 shows a plan view of the inside and outside of both flanges. Figure 2.8 shows an exploded view taken vertically through both flanges and Figure 2.9 a more detailed view of the sample holder construction.

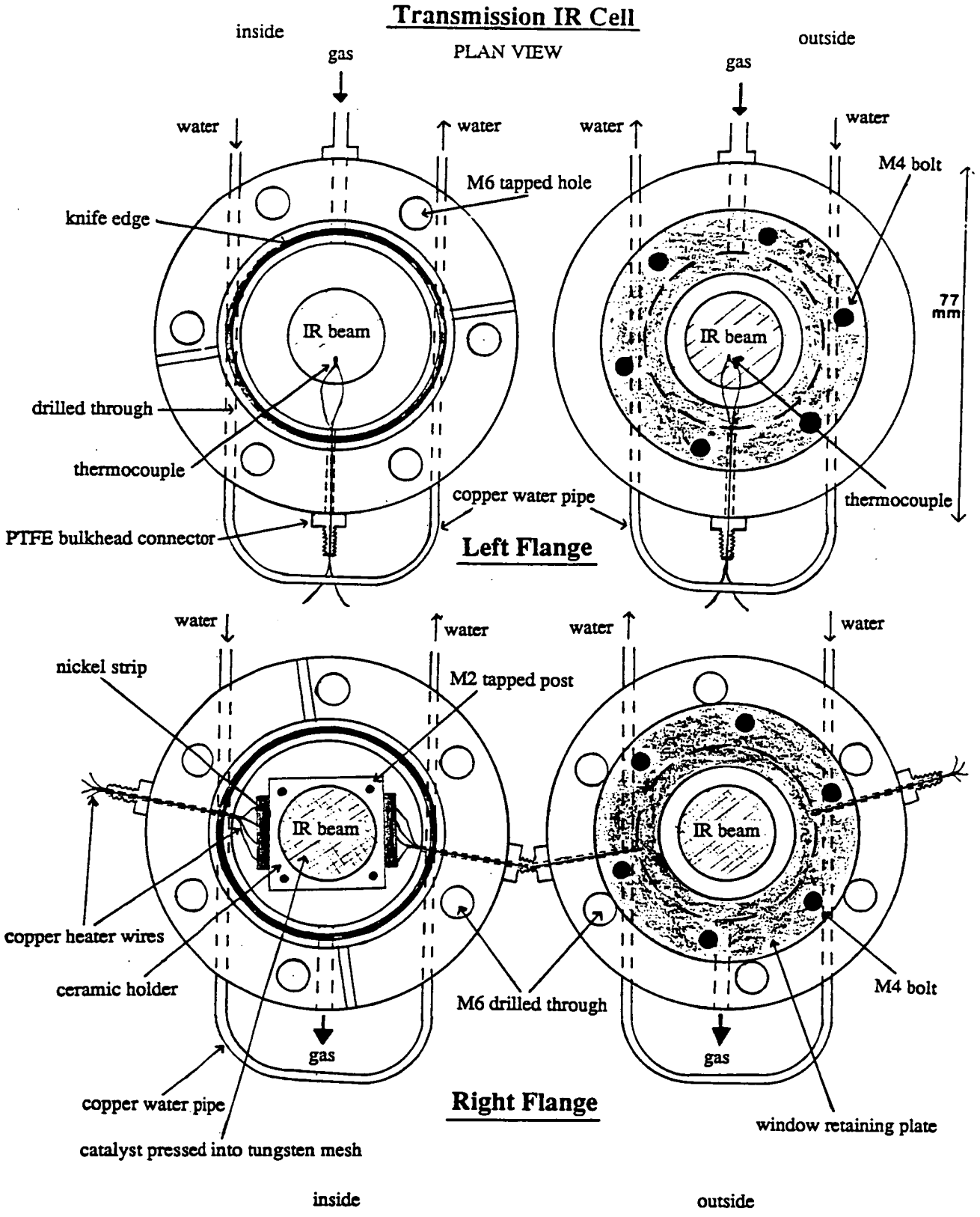

Figure 2.7 *Plan view of the inside and outside of both the flanges of the Transmission Infrared Cell used in this thesis.*

SIDE VIEW

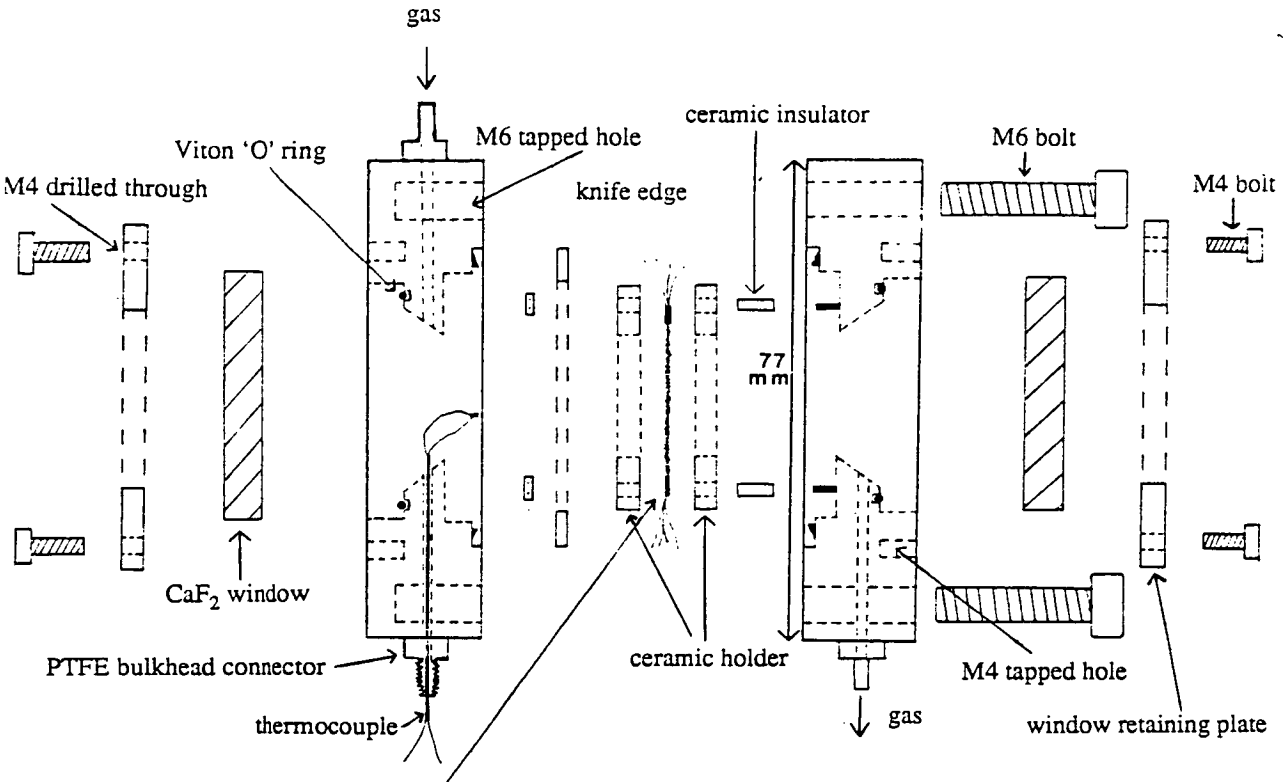

Transmission IR Cell

EXPLODED VIEW

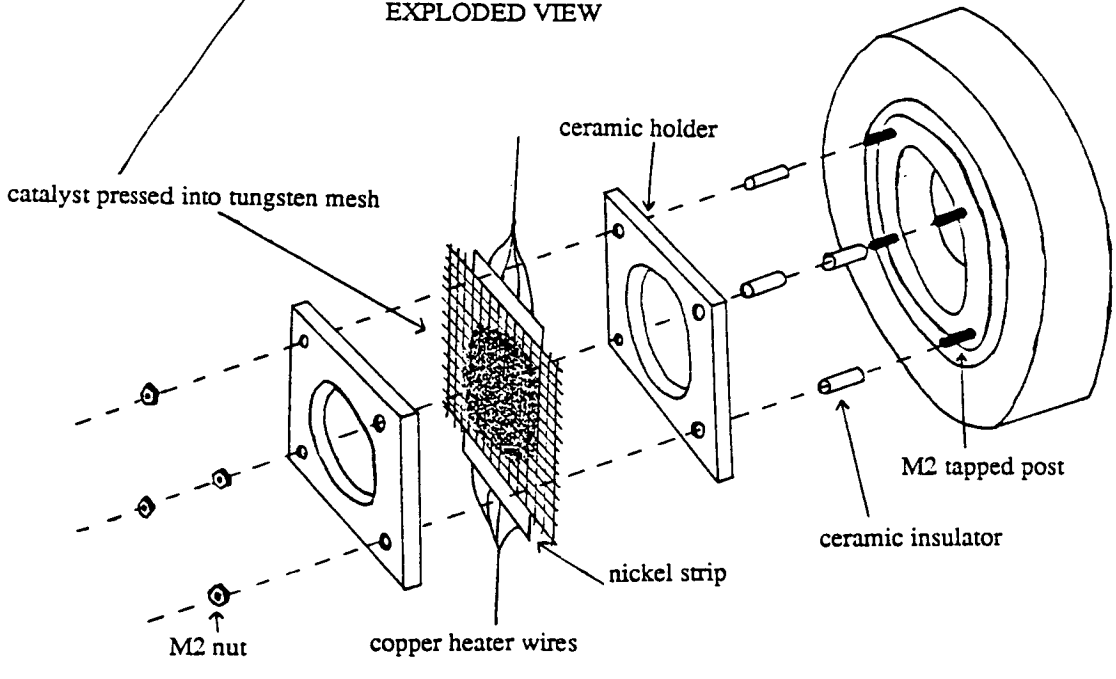

Figures 2.8 and 2.9 *Exploded views of the transmission cell from the side. Figure 2.9 is a more detailed view of the sample holder.*

The main body of the cell consists of two stainless steel machined flanges of 77mm diameter, sealed by a standard 38mm copper gasket. The windows, CaF_2 or NaCl, are 38 x 6mm discs (Buck Scientific), fitting into machined grooves on the outside of both flanges. Viton 'O' rings provide a seal for the windows, which are held in place by two brass retaining plates. CaF_2 would be used for high temperature operation, although NaCl or similar can be used for lower temperature operation and/or if a lower infrared cut-off frequency is required ($\approx$1000-cm^{-1} for CaF_2, $\approx$600cm^{-1} for NaCl). Cell cooling is effected by water pipes drilled through the main body, passing close to the window seals at two points.

The heater and thermocouple enter the cell through PTFE bulkhead connectors (Swagelok), inside ceramic tubes (Lodge Ceramics) for insulation, allowing leak free feedthough of wires from outside to inside. Gas enters and leaves the cell via brass bulkhead connectors and stainless steel tubing. The left hand flange of the cell contains the thermocouple and gas in, the right hand flange has the heater connections and gas out. The thermocouple is positioned so as to spring against the sample as the cell body is closed.

The catalyst disc is prepared by pressing 150mg of catalyst (75mg if pre-reduced catalyst is being used), into a 25 x 30 x 0.2mm tungsten wire mesh under a 10 ton pressure for 30 seconds. The heater wires, to which the mesh is now attached, consist of four 0.2mm copper wires, threaded inside the ceramic feedthrough, and then spot welded to two 20 x 5 x 0.25mm nickel strips for rigidity. The prepared tungsten mesh with the catalyst is then spot welded to the nickel strips, giving a resistance of 4ohms for the whole heater assembly when constructed. The catalyst disc is held between two ceramic plates (Lodge Ceramics), which have been cut to allow passage of the infrared beam through 20mm diameter holes and is secured to the body of the cell by threading onto four M2 posts in the right hand flange. The posts are insulated with ceramic tubes, and the whole assembly is kept in place with M2 nuts. When firmly held down the ceramic holder makes a partial seal to the cell body, forcing the gas through the catalyst sample and not across it and around the edges.

The operation of the cell described so far is for gas flow operation, using an inert carrier gas for transport of reactants and products. This cell is also capable of vacuum operation, down to 10^{-8}mbar. The same flow/vacuum system, with thermal conductivity and mass spectral analysis, is used for both transmission and diffuse reflectance studies, and is described in detail in Chapter 4.

It is theoretically possible to run the cell under gas pressures of greater than one

atmosphere. The maximum pressure that the cell windows can withstand is related to the unsupported diameter of the windows, their thickness and the strength of the window material. These are related by Equation 2.10 below [82],

$$P = \frac{2.37 \times 10^8 \cdot T^2 \cdot S}{R^2} \qquad \text{Equation 2.10}$$

S = Modulus of rupture (N/m^2)
R = Unsupported radius (m)
P = max. pressure differential (N/m^2)
T = Thickness of windows (m)

For CaF_2 windows, with an unsupported diameter of 30mm and with the modulus of rupture for CaF_2 equal to $3.65 \times 10^{-2} N/m^2$, a maximum differential pressure of 13 atmospheres can be withstood.

Optical arrangement.

The transmission cell sits inside the sample compartment of the FTS-40 spectrometer, with the optical arrangement shown below in Figure 2.10.

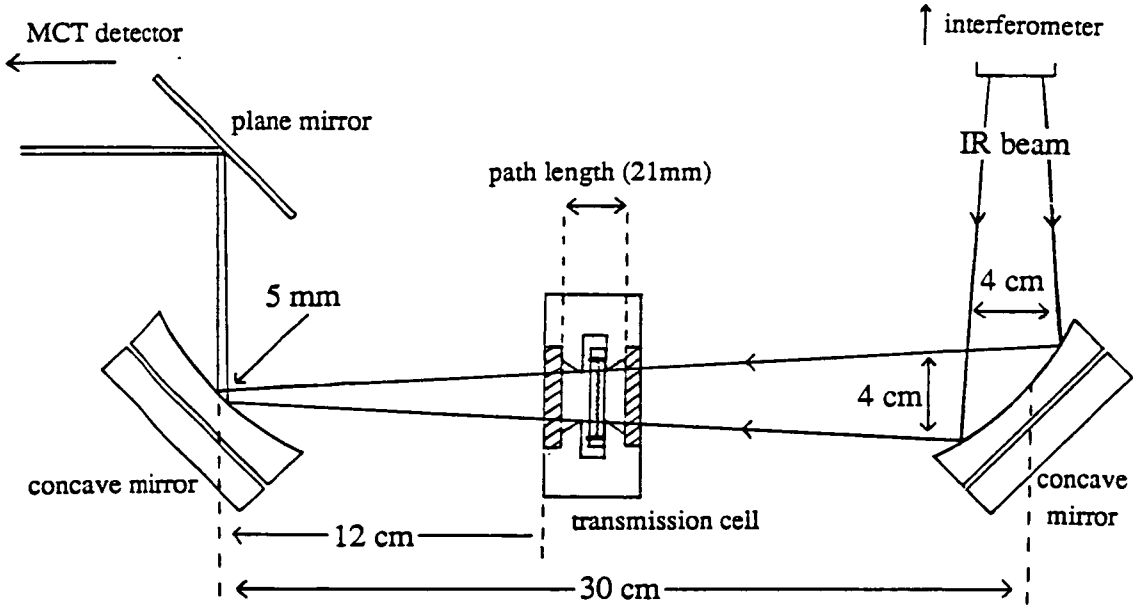

Figure 2.10 *Optical diagram of the transmission cell inside the FTS-40 sample compartment, showing the infrared beam profile.*

The infrared path length inside the cell is 21mm and the cell has a minimum aperture of 20mm. The area of catalyst exposed to the beam is $300mm^2$, giving 40mg of pre-reduced catalyst directly exposed to the radiation.

2.2.3 Diffuse Reflectance Spectroscopy.

Diffuse Reflectance.

Understanding the processes involved in diffuse reflection is of importance in several areas of study, such as the surface of paints, the quality of frosted glass and paper, the structure of coal, as well as the application of it to the study of catalysts [83]. Diffuse reflectance in the infrared is at best very weak. This is the principle reason that the technique of Diffuse Reflectance Spectroscopy (DRS) is much less commonly used for studying catalysis than Transmission Infrared Spectroscopy. The first use of DRS for catalysis was described by Kortüm and Delfs in 1964 [84] with a study of HCN and C_2H_4 adsorbed on metal oxides. In 1978, Fuller and Griffiths published a design of an infrared cell that allowed diffuse reflectance spectra to be measured at a resolution of 2-4cm^{-1} and with a high signal to noise ratio [85]. Since then, DRS has become a valuable tool for the study of adsorption systems ([86], [87] are some recent examples). When Fourier Transform spectrometers are employed, as they usually are, the acronym DRIFTS (Diffuse Reflectance Infrared Fourier Transform Spectroscopy) is used. The advantages of using Fourier Transform spectrometers is described later in this chapter.

The most widely used method of interpreting data from diffuse reflectance experiments, with a quantitative basis, is the Kubelka-Munk theory, published in 1931 [88]. This was in fact a re-discovery of an earlier theory developed by Schuster in 1905 [89]. The Kubelka-Munk (K-M) form is more convenient for analytical purposes and this is probably why it is used much more widely.

The K-M theory relies on a quantity, R_∞, the ratio of the diffuse reflectance from the sample with that of a non-absorbing powdered reference material, such as KBr, at 'infinite depth'. This is taken to mean the depth at which addition depth makes no difference to the diffuse reflectance signal. A function of R_∞, written $f(R_\infty)$, the Kubelka-Munk function, is related to R_∞ *via* Equation 2.11,

$$f(R_\infty) = \frac{(1 - R_\infty)^2}{2R_\infty} \qquad \text{Equation 2.11}$$

From the K-M theory it follows that

$$f(R_\infty) = \frac{k}{s} \qquad \text{Equation 2.12}$$

where k is the absorption coefficient.
s is the (elastic) scattering coefficient.

If the scattering is constant (i.e. independent of wavenumber), the absorption coefficient is related to the absorptivity, a, and concentration, c, as,

$$k = 2.303\ a\ c \qquad \text{Equation 2.13}$$

$$f(R_\infty) = \frac{2.303\ a\ c}{s} = k^{l}\ c \qquad \text{Equation 2.14}$$

In other words, at constant external conditions (wavelength, particle size, temperature etc.) the K-M function is proportional to the concentration c. A plot of $f(R_\infty)$ *versus* c should yield a straight line, passing through the origin. It should, then, be possible to employ Equation 2.13 for quantitative analysis in a similar manner to the way the Beer-Lambert Law is applied in transmission experiments. Most data stations supplied with FTIR spectrometers can produce plots in K-M units. A plot in K-M units resembles an absorbance plot, although the band intensities are different. Absorbance plots tend to emphasise weaker features, whilst K-M plots will generally exaggerate strong features relative to the weaker ones [90]. At higher analyte concentrations, s is not determined solely by the non-absorbing matrix, resulting in anomalous dispersion. Scattering is not isotropic for highly absorbing samples [91].

The K-M theory was developed for a situation when the active component to be studied is diluted in a non-absorbing medium, such as KBr. The situation is slightly different if a supported metal catalyst is to be studied. The support is not wholly non-absorbing, as we have seen, it has a characteristic 'cut-off' frequency, below which it becomes wholly absorbing. The application of K-M theory to supported metal catalysts appears to have at least two problems, that of scattering being dependent on wavenumber, which it is not if Rayleigh scattering dominates, and the fact that the support becomes absorbing below a 'cut off', and cannot therefore be regarded as a perfectly non-absorbing matrix. When catalysts are studied, the reference material and the sample material are simply the same catalyst, before and after gas adsorption. This is obviously a departure from the use a blank non-absorbing material as a reference.

Fuller and Griffiths [85] have studied the effect of particle size of KCl on the diffuse reflectance signal obtainable. The highest diffuse reflectance occurred at high wavenumbers with the smallest particles.

A theory that qualitatively describes the general behaviour of reflection from mat surfaces as a function of particle size and absorption coefficient has been produced by Vincent and Hunt [92]. The behaviour of absorption bands in a series of differently sized particles could be predicted with reference to the transmission spectrum of the sample and the reflectance spectrum of a polished sample. Large specular components in the collected signal produced asymmetric absorption bands in the resulting spectrum.

The K-M theory states that the band intensity of an absorption band is proportional to the sample concentration, only if it is measured with an 'infinite depth' of material. Fuller [93] has looked at the relationship between the sample depth and the resulting absorbance band intensity at 725cm^{-1} and 1450cm^{-1} of a 1% mixture of carbazole in KCl. As the sample depth was increased, the absorbance bands at first increased in intensity, coming to a maximum at 1.3mm for 1450cm^{-1} and 1.6mm for 725cm^{-1}. They then decreased slightly until a depth of around 3mm from where a constant value was found. The initial maximum is due to reflection from the base of the sample cup back up into the sample, allowing part of the radiation to interact with the sample twice. The maximum for the 725cm^{-1} band occurs at a lower sample depth than for the higher band at 1450cm^{-1}, as the lower frequency radiation penetrates more deeply into the sample. A sample depth of 3mm, as in the Spectratech cell used in the work in this thesis, should be sufficient to achieve 'infinite depth' at wavelengths down to the typical cut-off levels of support materials.

Whilst the K-M theory is an attempt to quantify the absorption of a band in a way that is linear with concentration, as has been seen the application of this to supported metal catalysts may not be totally successful. This conclusion has been reached by Brimmer and Griffiths [94]. Spectra plotted with K-M units will not necessarily be any more meaningful for quantitative analysis than the same data plotted as spectra in traditional absorbance units. Another problem is that Equation 2.11 runs into difficulty when negative absorption bands are encountered, when for instance, a specific species suddenly shifts or disappears on adsorption of another species.

For these reasons, absorbance units are used throughout this thesis for both diffuse reflectance and transmission infrared experiments. The plots are generated by ratioing single beam spectra of the catalyst sample before and after the introduction of the

species to be studied. Therefore, reference spectra from non-absorbing media are not used for work in this thesis. The use of KBr as a dilutant may actually have an effect on the chemistry of surface processes. Alkali metals are used as additives in catalysts precisely because they suppress specific reactions [95]. Chloride ions are a well known poison of many catalysts. So the inertness of the diluting media may be called into question.

Unfortunately, Yang *et al.* have concluded that specular reflection can only be removed with the use of a diluting, non absorbing medium [96]. The problems of specular reflection from the top layer of a sample have addressed by Messerschmidt [97], using a 'blocker' device designed to physically block the specular reflection. It consisted of a perpendicular razor blade touching the sample surface, allowing only radiation that had penetrated the sample to be collected, which should only consist of diffuse reflectance. In practice 90% of the diffuse reflectance was also blocked.

Another method for the elimination of specular reflection is employing the different polarisation characteristics of the diffuse and specular reflection. If plane polarised radiation is used as the source, specularly reflected light should retain the original plane polarisation, whilst the diffusely reflected component changes its state of polarisation. Thus, if measurements are made between crossed polarising sheets, in theory the specular reflection should be eliminated, whilst the diffusely reflected component should be partly transmitted. This effect has been demonstrated by Yang *et al.* [96], although complete removal of the specular reflection was not achieved. Consequently in spite of all efforts, a degree of specular reflection is expected to persist in studies using undiluted catalysts samples for DRS.

Hembree and Smyrl [98] conclude that unrejected specular reflectance is the primary source of deviation from behaviour predicted in the K-M theory. If specular reflectance occurs, a linear relationship with sample concentration cannot be assumed, except in the limit of very low concentration.

To conclude, work in this thesis will be presented using only absorptance plots and no attempt to interpret the resulting absorption bands in a quantitative way will be made.

2.2.4 Diffuse Reflection Equipment.

A number of commercially produced diffuse reflectance cells are available. A review of three of them has been published by Yang *et al* [96], comparing the ease of operation, radiation throughput and amount of specular reflection and how easily it could be distinguished from diffuse reflection. The essential function of any optical design for DRIFTS is to collect as efficiently as possible the diffusely reflected component of the radiation (which has interacted with the adsorbed molecules). The work in this thesis has been carried out using a Spectra-Tech diffuse reflectance accessory [99]. The optical layout is shown in Figure 2.11. A more detailed view of the sample cup and sealing cap is presented in Figure 2.12.

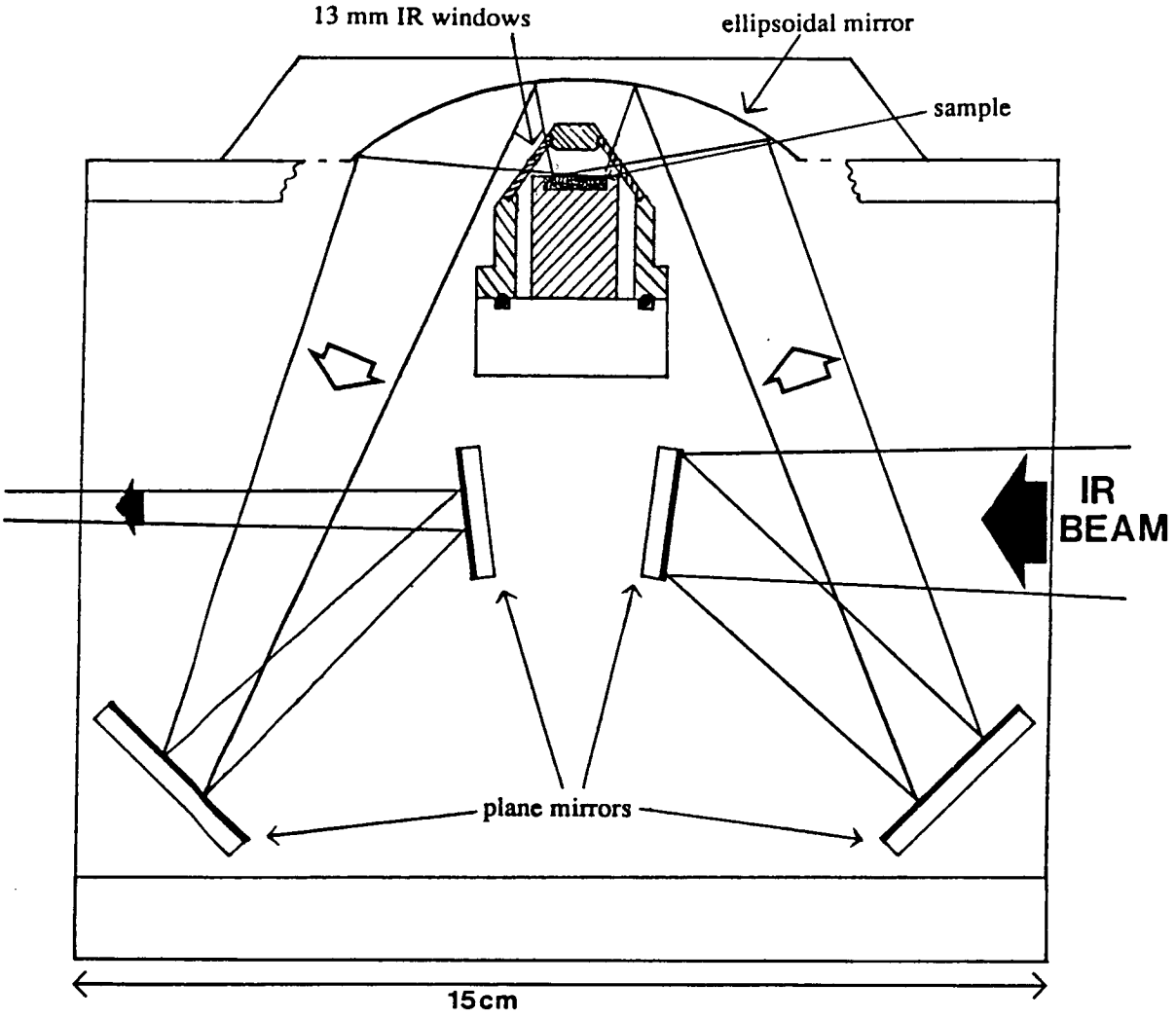

Figure 2.11 *Scale drawing of the optical layout of a Spectratech Diffuse Reflectance Accessory. The infrared source and interferometer are to the right and the detector optics to the left.*

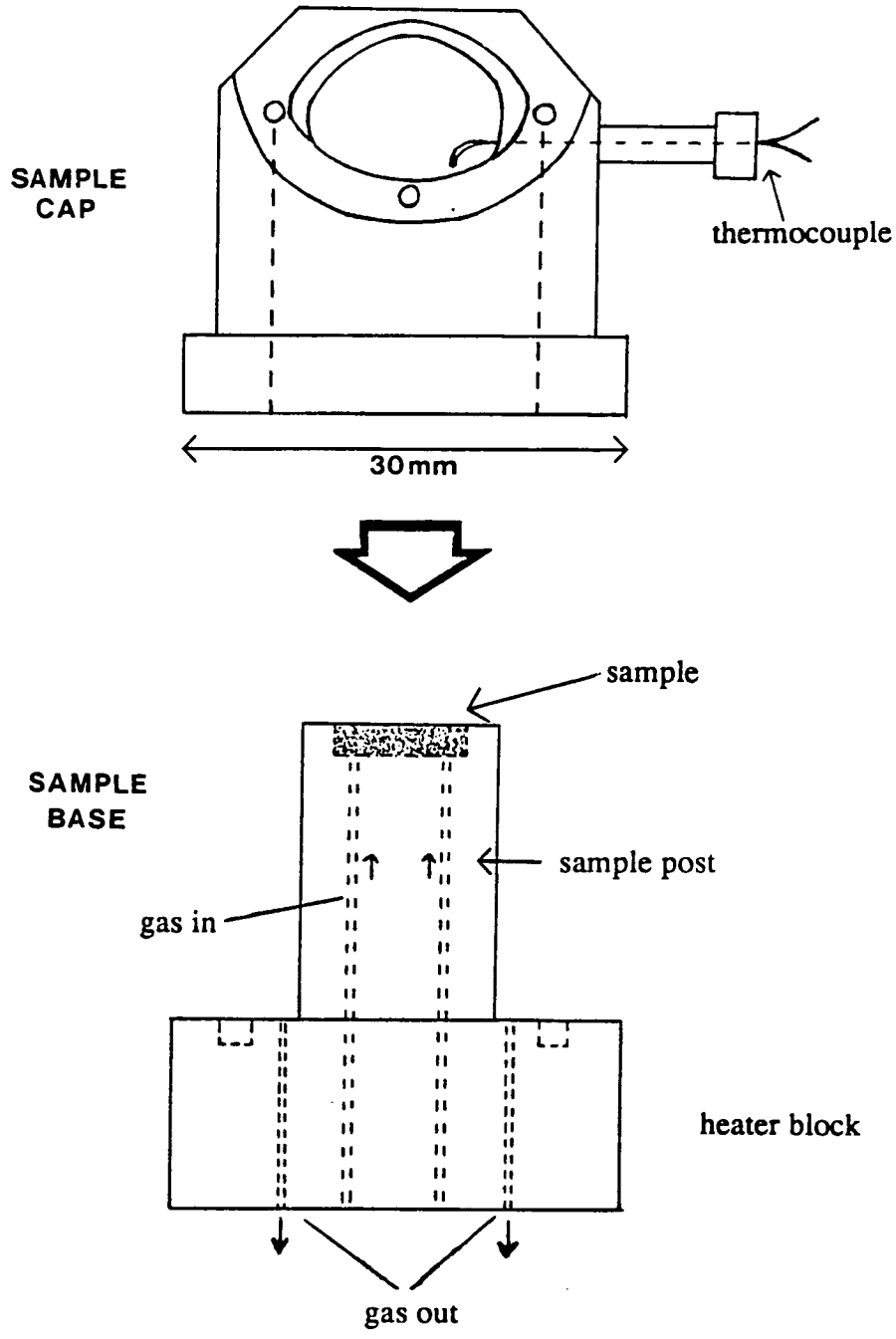

Figure 2.12 *Detail of the sample section of the diffuse reflectance cell, with the sample post and sealing cap. The thermocouple enters through a side arm in the cap.*

The whole assembly is designed to fit into the sample compartment of most commercially produced infrared spectrometers. Referring to Figure 2.11, the slightly converging infrared beam is guided *via* two plane mirrors onto the first ellipsoidal mirror above the sample. This focuses the beam onto the sample in the sample cup. The diffuse reflectance, plus some unwanted specular reflectance, is distributed essentially isotropically over the whole hemisphere above the sample. The second ellipsoidal mirror is set to capture as much of this as possible, although an estimated 90% is lost, less than 10% of the diffuse reflectance being captured at the optimum mirror positions. The outgoing beam remains slightly converging and proceeds *via* two more mirrors into the detector optics. This particular optical arrangement is known as an 'on axis' geometry in that the second ellipsoidal mirror is on the same axis as the first, as if it was set to receive regular Fresnel reflected radiation.

Referring to Figure 2.12, the catalyst sample is placed at the top of the sample post, which contains the heating element. The sample space has a depth of 3mm and diameter of 10mm, holding 40mg of pre-reduced Ni/Al_2O_3 catalyst. Gas can enter at the bottom of this space or at the base of the sample post. The cell is water cooled, and can be run at a maximum of 300°C (2A, 30V) without damage to the window materials and 'O' ring that seals the cap to the base. A BBC microcomputer provides a temperature programming facility, giving a linear heating rate from room temperature up to 300°C at up to 30°C/min. The sample temperature is measured using a thermocouple in the sample cap which becomes embedded in the sample as the cap is lowered onto the 'O' ring in the base. The whole sample block may be raised or lowered relative to the mirror assembly using a sprung screw mechanism.

The cell may be operated under vacuum or gas flow conditions. The same flow/vacuum system, coupled with thermal conductivity cell and mass spectrometer, is also used in conjunction with the transmission cell, the two being interchangeable. The system is described in more detail in Chapter 4.

2.3 Fourier Transform Spectrometry.

Until the advent of Fourier Transform Spectrometers in the 1970s, infrared spectrometry was predominantly carried out on dispersive double beam spectrometers. In these, a polychromatic beam of infrared radiation is dispersed with a diffraction grating after it has passed through the sample. A conventional intensity (I) *versus* wavelength (ν) spectrum is achieved by scanning along the dispersed beam, by rotating the diffraction grating. Each particular wavelength is selected by a

monochromator and directed as a narrow beam to the detector. The rest of the radiation is diffracted away without reaching the detector. Consequently only a small proportion of the radiation is detected at any one time.

An alternative method for obtaining a spectrum is with Fourier Transform Spectroscopy (FTS), using an interferometer instead of a diffraction grating. The principles of FTS have been described by several authors e.g. [100], [101]. In FTS all wavelengths of radiation are monitored simultaneously. This is known as 'multiplexing' and immediately introduces two advantages over dispersive instruments. Firstly, the speed of collection of a whole spectrum is improved to the order of 1s compared to minutes with dispersive instruments. Consequently, the signal to noise ratio possible in spectra is improved by several orders of magnitude by signal averaging and is known as Fellgett's advantage. Without the need for a monochromator with narrow slits, far more radiation may pass through a Fourier Transform instrument. The advantage of a higher throughput of infrared radiation is generally known as the Throughput or Jacquinot advantage.

Whereas a dispersive spectrometer produces a spectrum directly, an FT instrument records an interferogram, a variation of radiation intensity with time. Fourier transformation of this interferogram digitally demodulates it, producing the conventional intensity *versus* wavelength spectrum. In this context, this type of spectrum in known as a single beam spectrum. Ratioing a single beam spectrum of a sample against a background single beam produces the more familiar absorbance or transmittance plots. Interferograms are co-added by the spectrometer in order to increase the signal to noise level in the resultant spectra. The noise level in a spectrum is inversely proportional to the square root of the number of scans used i.e. noise $\propto 1/\sqrt{N}$.

A Digilab FTS-40 spectrometer [102] is used throughout this thesis. The optical bench is evacuable down to 10^{-2}mbar or better, including the sample compartment where the DRIFTS and transmission accessories are placed. This allows mis-cancellation features from gas phase species such as CO_2 and H_2O to be removed, without having to purge the surroundings with dry nitrogen or air.

A liquid nitrogen cooled Mercury Cadmium Telluride (MCT) photoconductive infrared detector was used, sensitive over the 4000-650cm^{-1} wavelength range. D.C. signal from thermal emission from the sample at high temperature tends to decrease the sensitivity of MCT detectors. This may affect the intensity of absorption bands during temperature programmed studies. Triglycine sulphate (TGS) detectors

do not suffer from this problem but are relatively insensitive compared to the MCT. Although the spectrometer could work at a resolution of up to $0.05cm^{-1}$, a standard of $4cm^{-1}$ was adopted for the infrared studies throughout this thesis.

A single beam spectrum is a spectrum of the radiation reaching the detector, and is the sum of the individual characteristics of the infrared source, the transfer optics, the catalyst sample, the atmosphere within the spectrometer and the response of the detector. Figure 2.13 shows a blank single beam, illustrating the sum of the source and detector characteristics, without passing through an infrared accessory. The KBr optics have little effect on the beam, as the KBr cut-off is below the detector's own sensitivity cut-off. As Figure 2.13 illustrates, the interference of gas phase bands such as H_2O and CO_2 has been successfully removed by evacuating the spectrometer. The maximum intensity of detected radiation is at $1300cm^{-1}$.

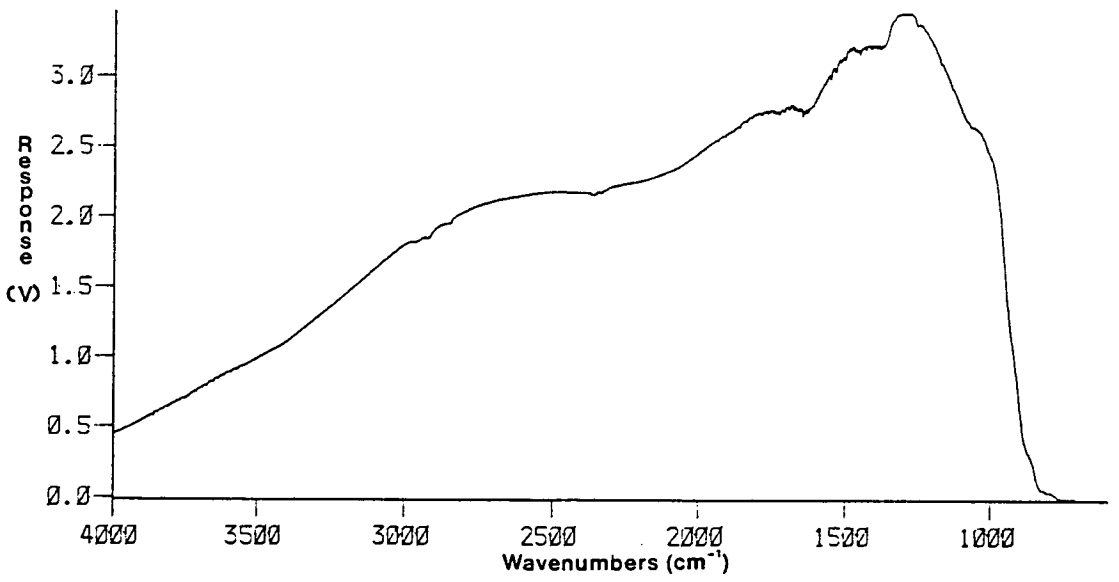

Figure 2.13 *Single beam of the source and detector characteristics, without passing through an infrared cell with the sample. Gas phase bands have been effectively removed by evacuating the spectrometer.*

2.4 Diffuse Reflectance or Transmission ?

The same Ni/Al_2O_3 catalyst has been studied with both DRIFTS and transmission and the two techniques are compared and contrasted below.

Scattering, or specular reflection, should be avoided with both techniques. It is a function of both the particle size and the difference in refractive index between the sample and the surrounding medium. The amount of radiation scattered by a particle decreases as the difference in refractive index between the particle and the surrounding medium decreases. Consequently an isolated particle in a vacuum or gaseous environment will scatter the most. As discussed earlier, compressing powders reduces scattering. Rayleigh scattering is defined by Equation 2.15 below,

$$S \propto d_p^3 (\bar{\nu})^4 \qquad \text{Equation 2.15}$$

where d_p is the particle diameter.
$\bar{\nu}$ is the radiation wavenumber.

Scattering is therefore more severe for larger particles and at higher wavenumber of radiation. It appears that for particles larger than 5μm that Rayleigh scattering is significant and adds to the apparent absorption coefficient of the catalyst. It is therefore advisable to work with particles of a smaller diameter than this for both Transmission Infrared Spectroscopy and DRIFTS. In DRIFTS, the specular reflection has been reflected only from the top surface of the sample and will have had less opportunity to interact with the sample than the diffusely reflected component, and consequently holds much less information. Since it has not passed through the alumina catalyst support, it will not have been affected by the absorbance of the support below the 'cut-off' frequency at $1100cm^{-1}$. The degree of specular reflection may be assessed by examining a single beam spectrum of the sample for significant intensity below the 'cut-off'. Materials of high refractive index will suffer more from specular reflection, as defined by Fresnel's Laws of Reflection.

In transmission, all reflectances will in general not be collected by the detector optics, and so specular reflectance losses are a problem only in that they add to the general absorption losses of the sample and reduce infrared throughput. Hence, measures to avoid reflection losses should be taken in both techniques.

2.5 Sample Preparation.

The exact nature of the sample often dictates which of the two technique is to be used. The method of sample preparation varies between the two techniques and has an important effect on the degree of reflection losses.

For transmission infrared spectroscopy, as previously discussed, the pressed disc method is widely used to produce self supporting wafers of the material to be studied. Not all materials lend themselves to easy pressing of discs, making the process often experimentally tedious. The high pressures usually employed can cause physical change to some samples. Phase changes in zeolites such as silicalite have been reported [103], and pressing of silane modified silica has caused the hydrolysis of methoxy groups for Blitz *et al.* [104]. DRIFTS was preferred in both of these cases.

Another important problem in pressed disc techniques is the effect of sample thickness and density on the dynamics of gas adsorption and reaction. Gas usually penetrates into a sample *via* diffusion. If the gas flows through the sample, the rate of delivery of the reactants is governed by convection. If a particular species reacts rapidly and the flow rate is low, this may lead to an uneven reactant concentration profile across the disc. The infrared beam will tend to average out this uneven distribution across the disc. Loosely held powders have a much higher diffusion rate of gases and consequently do not tend to suffer from concentration gradients to the same extent. Therefore DRIFTS may be more suitable for accurately studying reaction rates.

Very little sample preparation is required for DRIFTS once the particles are small enough to prevent significant scattering losses. A large number of powdered materials may be studied *in situ*, giving a considerable advantage over transmission using pressed discs in this aspect. Powdered samples may be used in transmission as well. A thin layer of a sample may be spread onto an infrared transparent window such as CaF_2, NaCl, etc., often *via* a spray-dry technique [55]. If the particle sizes are small enough then scattering losses may be minimal, although there may be a significant degree of diffuse transmission, not all of which will be collected by the detector optics. There is also the possibility, as with the use of KBr as a diluting medium in DRIFTS, that the salt windows may chemically interact with the sample in some way.

As has been described, some samples are unsuitable for pressing as discs and are studied with DRIFTS. In contrast same materials do not possess a sufficiently mat surface to generate significant diffuse reflectance for DRIFTS, and are studied in

transmission. Very often a material suitable for DRIFTS may not be for transmission and *vice versa*. Many materials, such as the Ni/Al_2O_3 catalyst used here, are suitable for both techniques.

2.6 Single Beam Profiles.

Single beam spectra of Ni/Al_2O_3 in transmission and diffuse reflectance are shown in Figure 2.14 A and B respectively.

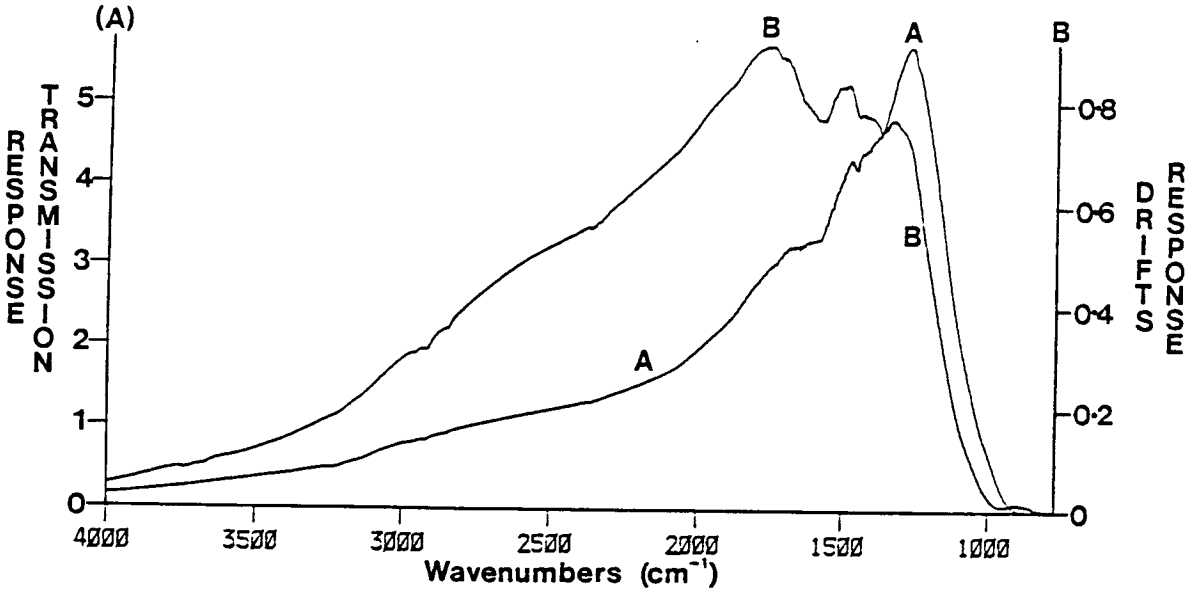

Figure 2.14 *Single beam spectra of Ni/Al_2O_3 in A) transmission and B) diffuse reflectance. Both spectra consist of 250 co-added interferograms.*

These spectra show the sum of the source/detector characteristics and the absorption/scattering properties of the sample. By ratioing against a blank single beam of the source/detector characteristics without the sample (Figure 2.13), the true effect of the sample in attenuating the beam in both collection modes is revealed. Figure 2.15 A and B illustrates this.

Figure 2.15 *Transmittance spectra of the Ni/Al_2O_3 in A) transmission and B) diffuse reflection, using the blank single beam, Figure 2.13 as a background spectrum.*

The different shapes of the single beams can be explained as follows [105]. In the transmission spectrum, the signal is composed of both the direct and the diffuse transmission. Scattering will in general not be detected. In DRIFTS, the diffusely scattered radiation is detected. Consequently, a substance that scatters will show a relatively greater intensity in a single beam spectrum from a DRIFTS experiment, than from a transmission experiment. This is evident in Figure 2.15 A and B where between 4000cm^{-1} and 1400cm^{-1}, B is at all times higher than A. Below 1400cm^{-1} and towards the cut-off of 1100-1000cm^{-1}, the transmission signal is higher than that from DRIFTS. This is due to the absorbance effect of the support as the diffusely reflected component will in general have a longer path length through the catalyst and will consequently be more effected by the absorbance. Scattering is weaker at these lower wavelengths (Equation 2.15), so the transmission spectrum (A) is less attenuated than the DRIFTS one.

The cut-off frequency is 50cm^{-1} higher in DRIFTS compared to transmission. This effect is due to 'anomalous dispersion' where intense fundamental absorption bands (i.e. Al-O) cause rapid variations in the refractive index with wavenumber close to their maximum. This is generally known as the Christiansen effect [106]. At some point above the maximum of the Al-O absorption, a refractive index of 1 will be

presented to incoming radiation. Consequently as there is no refractive index change from the surrounding gas to the alumina particle, there can be no diffuse reflection, the radiation must be transmitted. So whilst the DRIFTS signal falls to zero, there is a momentary increase in transmittance, allowing the transmitted signal to remain at a higher level than DRIFTS close to the Al-O absorption maximum. In DRIFTS, this has the effect of producing a cut-off at higher wavenumbers than in transmission. At wavenumbers below the absorption maximum, no radiation may be transmitted, so the transmission signal remains zero. An increase in the refractive index, allows specular reflection to reappear without the diffuse reflectance. These effects are more marked for silica supports [107].

Signal to Noise Levels in Absorbance Spectra.

The transmitted signal level in the transmission experiments, integrated over the whole wavelength range, was usually ≈6V, contrasting to ≈1V as the corresponding level in DRIFTS. This 6 fold signal intensity advantage allows spectra to be recorded with a lower noise level than in DRIFTS, for the same number of scans.

Figure 2.16 A and B and Figure 2.17 A and B are absorbance plots produced on adsorption of ethene onto Ni/Al_2O_3. Each consists of 30 co-added scans ratioed against a background of 250 scans. Figure 2.16 A and B are the CH stretching regions (3200-2700cm^{-1}) in transmission and DRIFTS respectively. Figure 2.17 A and B are the corresponding CH deformation regions (1600-1080cm^{-1}) for these two techniques.

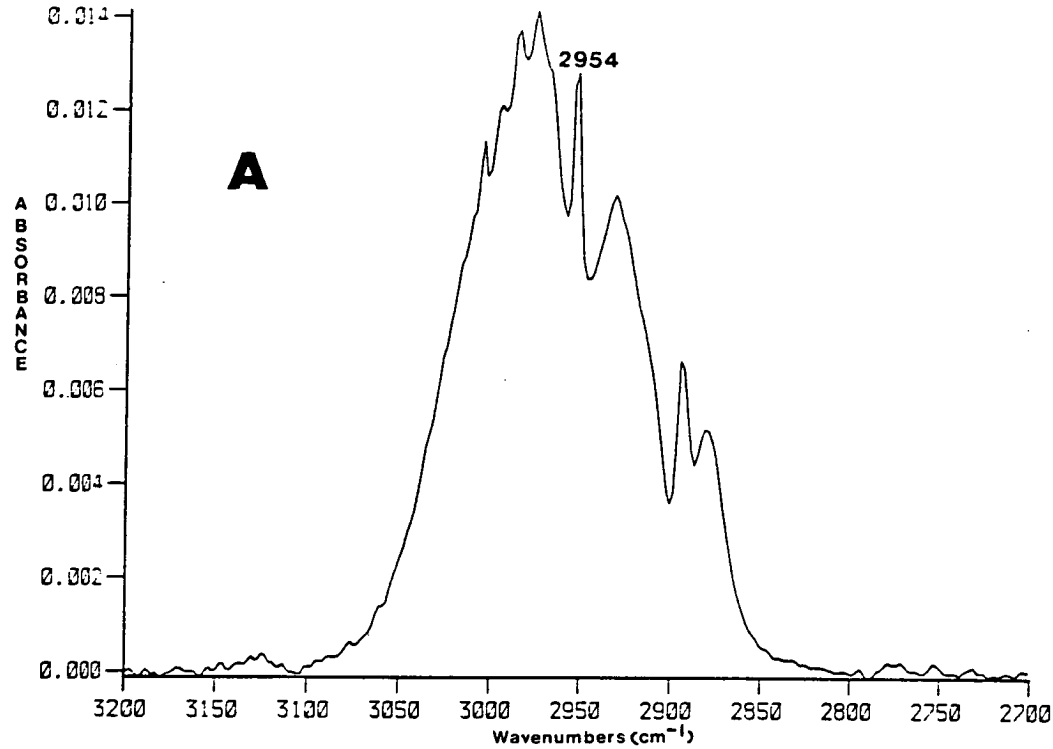

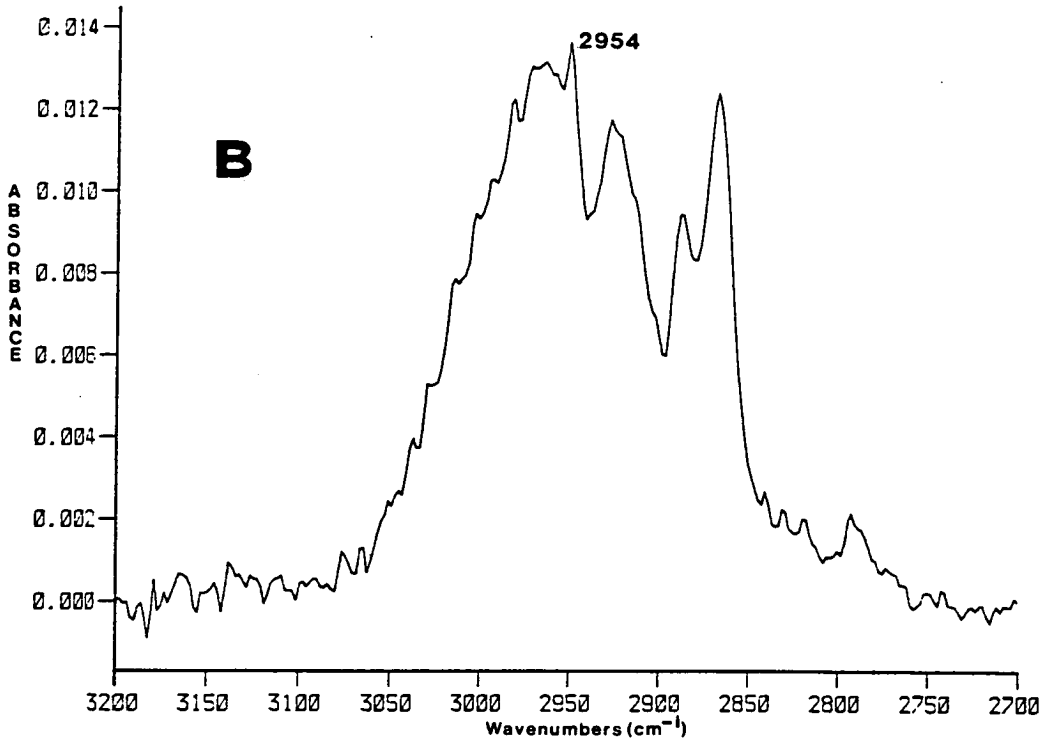

Figure 2.16 *Ethene adsorption on Ni/Al_2O_3, plotted from 3200-2700cm^{-1}, the CH stretching region. A) is measured in transmission and B) in DRIFTS.*

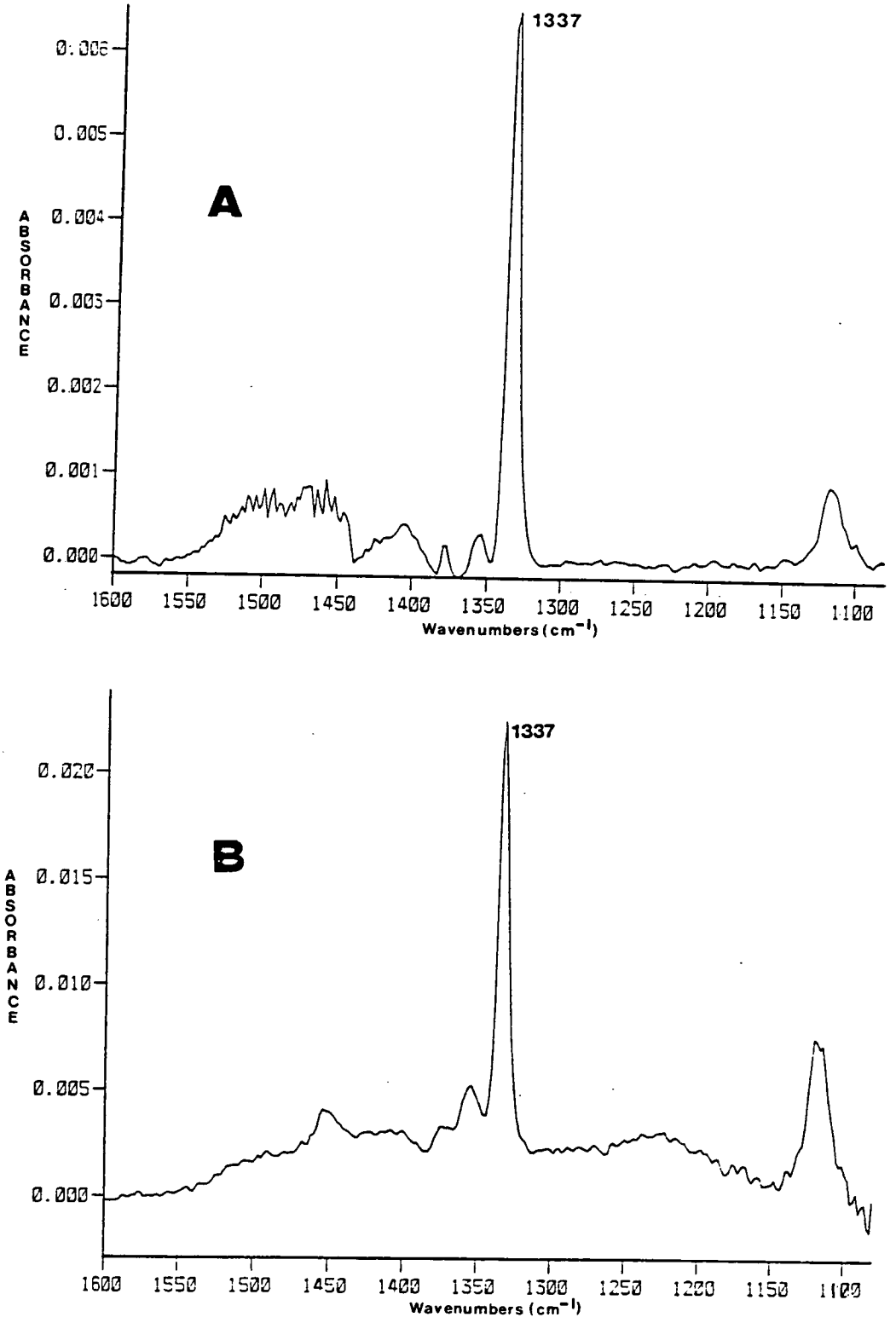

Figure 2.17 *Ethene adsorption on Ni/Al_2O_3, plotted from 1600-1080cm^{-1}, the CH deformation region. A) is measured in transmission and B) in DRIFTS.*

The peak to peak noise levels in Figure 2.16 are 0.0002 and 0.0005 absorbance units for the transmission and DRIFTS experiments respectively. In the CH deformation region, Figure 2.17 A and B, the transmission spectrum has a much lower noise of 0.00005 absorbance units, compared to 0.0005 for DRIFTS. This can be explained with reference to Figure 2.14. Whilst the integrated intensity may be 6 times greater in transmission, this is averaged over the whole wavelength range. Between 1600 and 1100cm^{-1}, the transmission single beam has relatively greater intensity than the DRIFTS signal, (6V c.f. 0.6), explaining the 10 fold noise advantage. In the 3200-2700cm^{-1} region, the DRIFTS signal increases its intensity level relative to the transmission signal, (0.4 c.f. 0.8), allowing it to approach within two times the noise level of the transmission experiment. Therefore transmission is relatively better for observing CH deformations, whereas DRIFTS is approximately the same in both.

The signal levels in each experiment are the height of the absorption bands in the spectra. The 1337cm^{-1} band has an intensity of 0.007 absorbance units in transmission and 0.02 in the DRIFTS spectrum, in Figure 2.17 A and B respectively. The 2954cm^{-1} bands have a similar intensity of 0.014 absorbance units for both. The 1337cm^{-1} band is due to the CH_3 deformation of the ethylidyne species and the 2954cm^{-1} band the ν_5CH stretch of ethane evolved by the hydrogenation of ethene. Looking at these two bands gives an indication of the sensitivity of the two techniques for observation of surface species and gas phase species respectively.

The mass of pre-reduced catalyst samples in the infrared beam is about the same in both techniques. The DRIFTS cell holds 40mg and the assumption is that all the catalyst is sampled by the beam. In the transmission cell, 75mg of catalyst is usually used for a disc, although only the central section of it, 40mg is exposed to the infrared beam. Therefore the number of adsorption sites available to incoming molecules is approximately the same in both. 40% of this is nickel (if pre-reduced catalyst is used), with a nickel surface area of 20m^2/g, giving 1.3 x 10^{17} metal adsorption sites in the infrared beam in both cells[1]. Therefore the concentration of molecules should be the same in both techniques.

The signal level in the transmission experiment is governed by the Beer-Lambert

[1]assuming majority (111) surface orientation, with 1.8 x 10^{19}Ni atoms/m^2.

Law, and in the limit of low concentration, the signal is proportional to concentration. In DRIFTS, as we have seen, quantitative analysis is difficult, although in low concentration, the signal is proportional to $\sqrt{c}$ [109]. Therefore at low concentration of adsorbates, DRIFTS has a sensitivity advantage over transmission.

The ratio of signal levels can be equated to the ratio of concentrations *via* Equation 2.16,

$$\frac{A_T}{A_{DR}} = \frac{C_T}{\sqrt{C_{DR}}} \qquad \text{Equation 2.16}$$

For the 1337cm^{-1} band, the absorbance value is three times greater in DRIFTS compared with transmission. Substituting into Equation 2.16,

$$\frac{A_T}{A_{DR}} = \frac{1}{3}$$

$$= \frac{C_T}{\sqrt{C_{DR}}}$$

$$\therefore C_{DR} = 9\,C_T^2 \qquad \text{Equation 2.17}$$

This implies that the infrared beam has sampled a larger number of molecules in the DRIFTS spectrum compared to the transmission spectrum. Since the concentration of surface ethylidyne species is the same, this must mean that the path length of the radiation through the catalyst is longer in DRIFTS, allowing three times the absorption. The path length through the wafer in the transmission cell is about 0.5mm, implying that the path length is more than this in the DRIFTS cell, at least 1.5mm if the path length is proportional to absorbance. The sample depth in the DRIFTS cell is 3mm, which is considered 'infinite depth'. The gives a possible maximum infrared path length of greater than 6mm.

The 2954cm^{-1} gas phase ethane band has a similar signal level in both spectra as shown in Figure 2.16. This probably indicates that the infrared beam has passed through an identical amount of gas in both cells since the catalyst sample has

undergone the same treatment, the number of reactant sites is the same and the amount of ethene injected is identical in both. The path length through the gas space in the transmission cell, i.e. not the catalyst wafer, is 21mm. The beam in the DRIFTS cell must pass through a similar amount of gas, and it has a path length of 12mm, from one window to the other *via* the top of the sample.

The signal to noise ratio (SNR), the absorptance strength of a band ratioed against the noise level in the spectrum, is 140 and 70 for the 1337cm^{-1} surface band and the 2954cm^{-1} gas phase band in transmission respectively. For these two regions in DRIFTS, the values are 40 and 20. These are all for 30 scan spectra. So while the infrared intensity is 6 or more times larger through the disc in the transmission cell than the DRIFTS signal, the SNR in the spectra is only about 3 times larger than DRIFTS in the CH deformation region. So DRIFTS shows excellent sensitivity for hydrocarbon species. Griffiths estimates that DRIFTS can be used for studying catalysts with a metal loading of as low as 0.01%, down to a coverage of 10^{-6} of a monolayer of adsorbed species [108]. Relatively more scans are needed than with transmission in order to generate spectra with sufficient SNR. This is essential for detection of adsorbates at low coverage and also useful in order to allow computer manipulation of spectra which may require spectra with a high SNR.

CHAPTER 3

Preparation and Characterisation of an Alumina Supported Nickel Catalyst.

Throughout this thesis a Ni/Al_2O_3 catalyst was studied. This chapter describes its preparation by co-precipitation, and characterisation with a host of techniques.

Before attempting adsorption studies, an idea of the physical nature of the catalyst is essential. Useful properties or characteristics of the catalyst may be listed as follows;

- The surface area of the metal component i.e. the nickel, giving the number of active sites.
- The total surface area of the catalyst, metal plus support.
- The average metal crystallite size and the support particle size.
- The overall composition of the catalyst, i.e. metal loading, Ni/Al ratio and the contaminant level.
- The reduction profile - how easy is the reduction of the catalyst?

The following techniques were used in the characterisation of the catalyst, listed in Table 3.1 below. Each will be discussed in the following text.

Table 3.1 Catalyst Characterisation Techniques.

Technique	Information
Chemisorption of H_2	Metal Surface Area
Reaction of N_2O	Metal Surface Area
N_2 Uptake at -196°C	Total Surface Area
X-Ray Diffraction	Phase Determination/Metal Particle Size
Electron Microscopy	Metal Particle Size
Optical Microscopy	Support Particle Size
Atomic Absorption Spectroscopy	Ni, Al and Na Concentration
Temperature Programmed Reduction	Reduction Profile

3.1 Preparation.

Supported metal catalysts are usually prepared by one of three methods : impregnation, co-precipitation or deposition [4]. Conventional wisdom indicates that the co-precipitation method tends to produce catalysts with the highest dispersion and therefore a large metal surface area [110]. Maximising the surface area is important in order to maximise the number of active sites in the infrared beam during an infrared experiment. Co-precipitated Ni/Al_2O_3 catalysts were first prepared in 1924 [113], and this method is today widely used for preparation of steam reforming and hydrogenation catalysts. In co-precipitation, the nickel compound and the alumina support are simultaneously precipitated from the same solution, instead of being prepared separately as in other preparation methods. Ross *et al.* [111] have reported that co-precipitated catalyst prepared with CO_3^{2-} as the dominant anion (as opposed to NO_3^{2-}, or Cl^-) have the highest activity. The catalyst used here was prepared by the *constant pH method* of co-precipitation, adapted from the work of Kruissink *et al.* [112], using sodium carbonate.

3.1.1 Experimental.

The outline procedure for the preparation of the catalyst is shown in Figure 3.1 below. Two solutions were prepared, one containing both 0.9M $Ni(NO_3)_2.6H_2O$ and 0.9M $Al(NO_3)_3.9H_2O$ and the other 1M Na_2CO_3, all in doubly de-ionized water. The suppliers and quoted purity of the chemicals used are listed in Appendix 1.

These two solutions, heated to 80°C were then simultaneously mixed at a rate that maintained the pH of the mixture at 7 throughout. Copious amounts of carbon dioxide were evolved, and an apple green precipitate was formed. The contents were left to age for 30 minutes, before filtering and washing with doubly de-ionized water at 40°C. The filtered precipitate was dried at 110°C for 15 hours in a ceramic crucible, producing a very fine pale green powder.

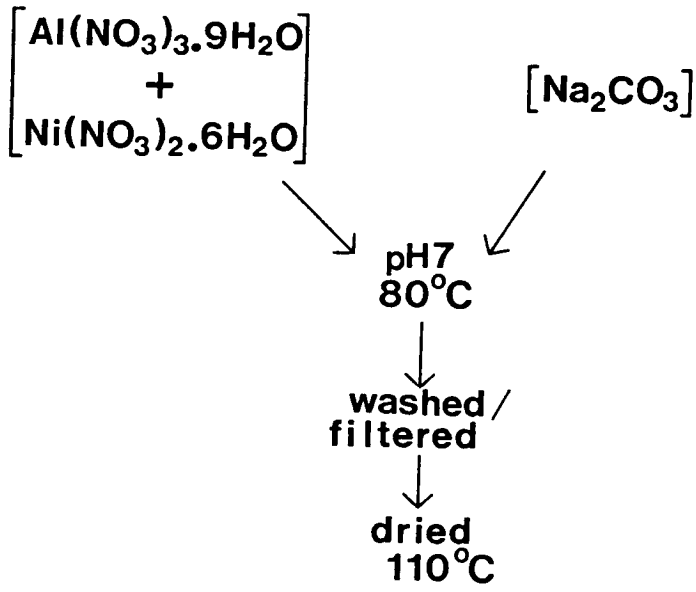

Figure 3.1 *Outline procedure for the preparation of Ni/Al_2O_3 via co-precipitation.*

3.1.2 X-ray Analysis.

X-Ray diffraction of the powdered as-prepared catalyst gives information about the different phases present. The results are illustrated in Figure 3.2A. A diffraction pattern from a calcined sample is shown in Figure 3.2B (see Section 3.2). Also shown in Figures 3.3 and 3.4 are diffraction patterns of some pure compounds, $Ni(NO_3)_2.6H_2O$, $Al(NO_3)_3.9H_2O$, Na_2CO_3, $Al(OH)_3$, α-Al_2O_3, $NiCO_3$, $Al_2(CO_3)_3$, NiO and a NiO/Ni_2O_3 mixture.

The broad peaks in Figure 3.2A indicates that the as-prepared catalyst is largely amorphous. The formation of a hydrocalcite type structure can be identified (broad peaks at $2\theta=10°$ and $2\theta=35°$), and possibly some $Ni(CO_3)$ and unreacted $Ni(NO_3)_2$. On calcination at 400°C as shown in Figure 3.2 B, these phases decompose, and only a semi-crystalline NiO phase can be identified in the XRD pattern. There is no evidence of crystalline alumina or aluminium hydroxide phases.

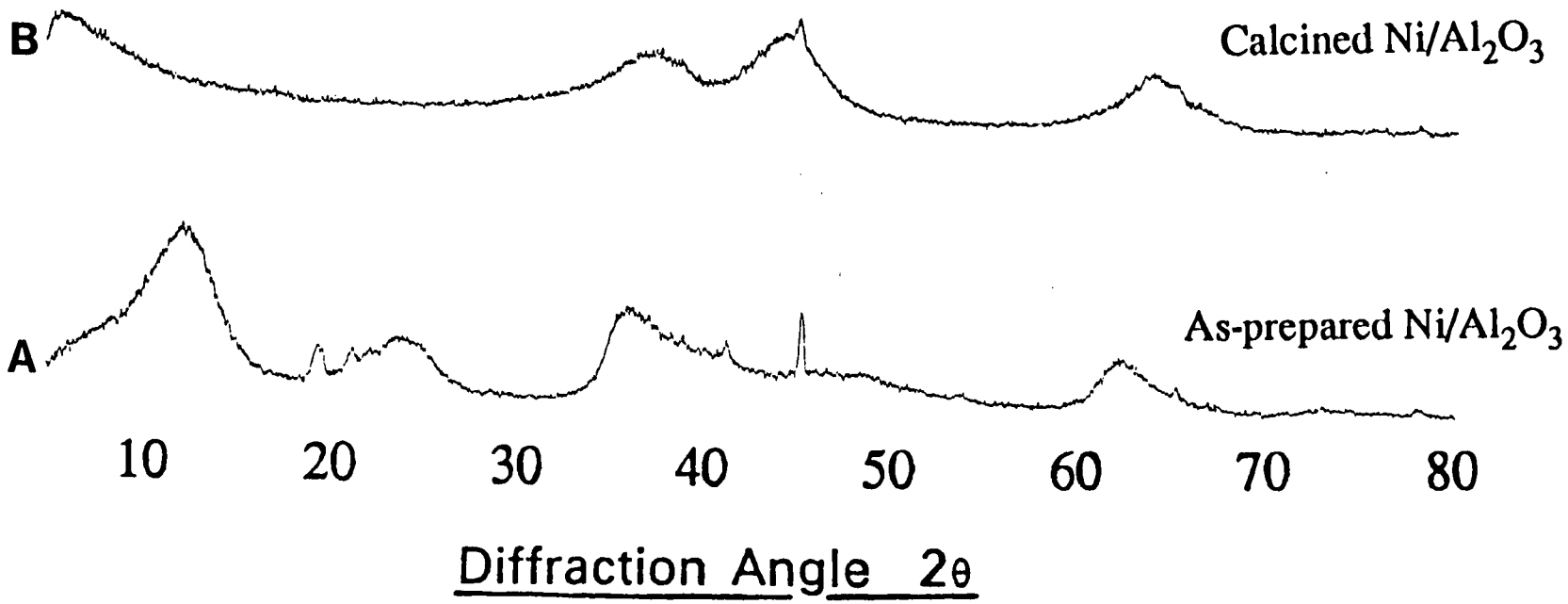

Figure 3.2 *X-Ray diffraction patterns of Ni/Al_2O_3 A) as-prepared and B) calcined.*

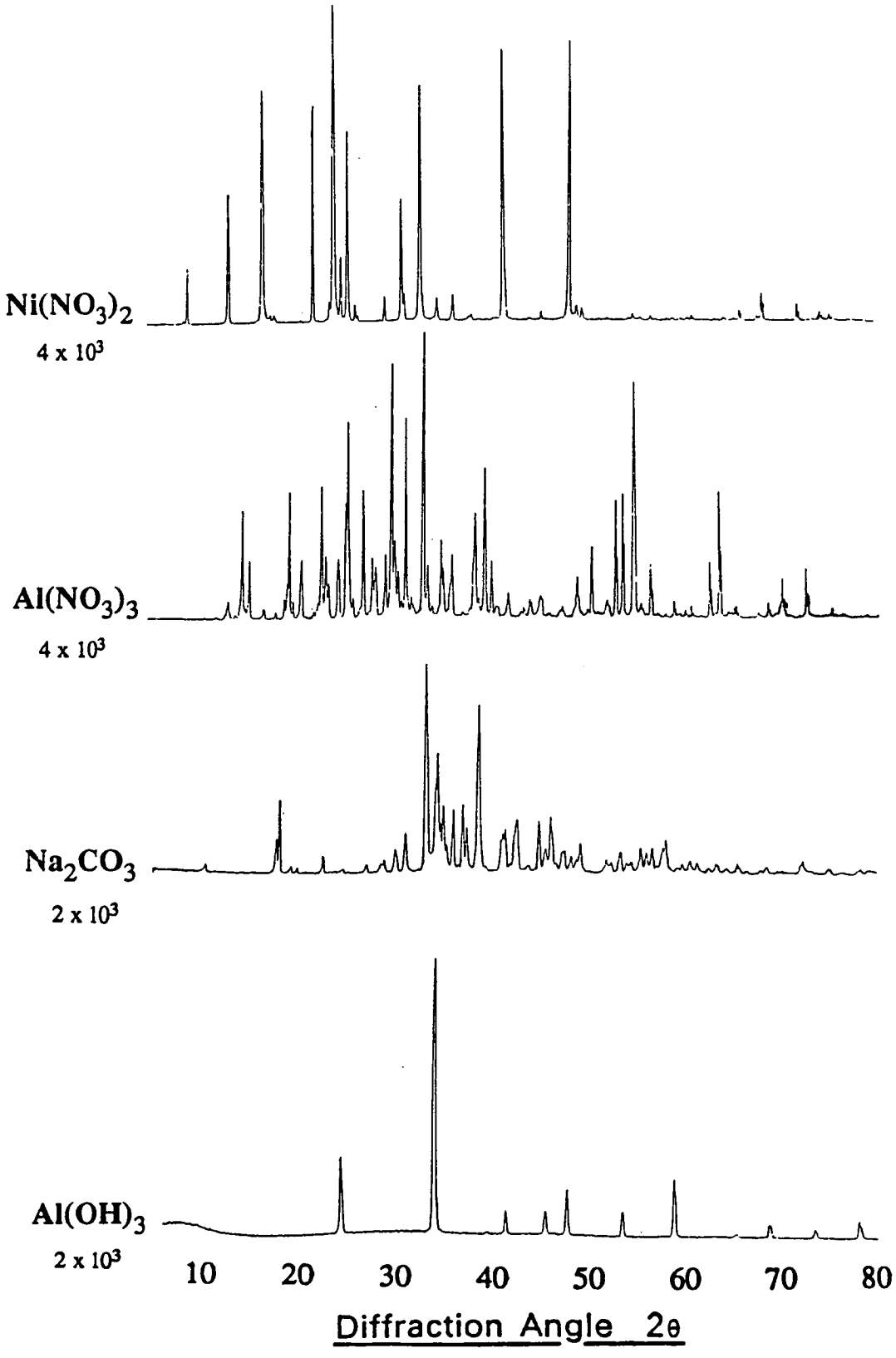

Figure 3.3 *X-Ray diffraction patterns of A) $Ni(NO_3)_2.6H_2O$, B) $Al(NO_3)_3.9H_2O$, C) Na_2CO_3 and D) $Al(OH)_3$*

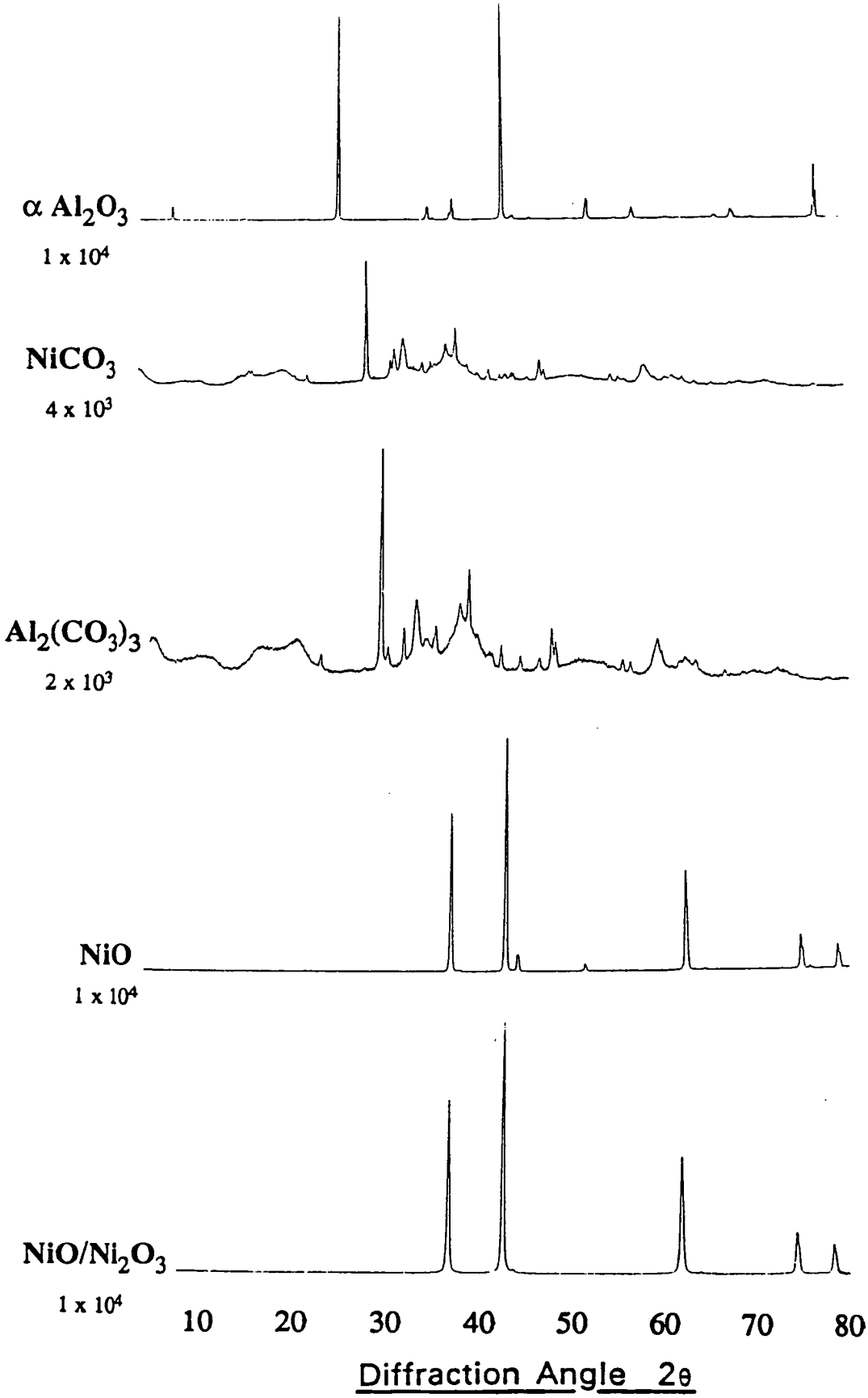

Figure 3.4 *X-Ray diffraction patterns of A) α-Al_2O_3, B) $NiCO_3$, C) $Al_2(CO_3)_3$, D) NiO and E) NiO/Ni_2O_3.*

3.1.3 Elemental Analysis.

By dissolving the catalyst in a suitable acid, the concentration of the ions Ni^{2+}, Al^{3+} and Na^{2+} can be determined using Atomic Absorption Spectroscopy, and therefore the overall make up of the catalyst can be deduced. Samples of as-prepared, calcined and reduced catalyst were dissolved in concentrated hydrochloric acid and the solutions analysed for Ni, Al and Na. Table 3.2 shows the concentration of Ni, Al and Na in the catalyst samples, converted into % by weight values. The Ni concentration was also determined using a traditional titration with ethylenediaminetetra-acetic acid (EDTA) [114]. Murexide ($C_8H_4N_5O_6NH_4$) was used to indicate the end-point of the titration.

Table 3.2 Elemental Analysis of Ni/Al_2O_3.

Sample	%Ni		%Al	%Na	Ni/Al
	AAS	EDTA	AAS	AAS	ratio
As-prepared	23.4	23.7	8.77	0.63	2.67
Calcined	37.0	31.0	12.2	0.59	3.03
Reduced	51.5	38.9	15.7	0.57	3.27

These results indicate that even after extensive washing, sodium remained as a significant contaminant. The %Ni and %Al increase on calcination and reduction because during calcination both water and CO_2 are evolved (see section 3.2) and oxygen is removed on reduction. The absolute amount of nickel and aluminium remains the same throughout, calcination and reduction merely concentrating it. Calcination and reduction seem to reduce the sodium level.

An average weight loss of 44% occurred on reduction of the as-prepared catalyst (see section 3.3), which should indicate that the nickel loading has increased from 23.5% to 50% by weight during reduction. This is in good agreement with the AAS results for the reduced catalyst above.

3.1.4 Discussion

The as-prepared catalyst is generally recognised to have a structure of a Feitknecht compound [115]. These materials have a 'double layer' structure, and have the general formula,

$$Ni_x^{2+}Al_y^{3+}(OH)^-_{2x+3y-2z}(CO_3^{2-})_z.nH_2O$$

This compound exists as 'Brucite' like layers of $[Ni_{1-a}^{2+}Al_a^{3+}(OH^-)_2]_n^{an+}$ with alternating metal and hydroxide levels. Generally x/y is between 1.5/1 and 4/1 in natural minerals. Table 3.2 indicates that x/y in the as-prepared catalyst is 2.67/1. Puxley *et al.* [115] believe this main nickel phase to have the approximate composition $Ni_6Al_2(OH)_6CO_3.4H_2O$. Ross *et al.* [111] conclude that for Ni/Al ratios outside the 2/1-3/1 range, the excess nickel or aluminium forms separate hydroxide phases.

3.2 Calcination.

Calcination is often used in pre-processing catalysts before reduction, in order to decompose nitrate and carbonate phases, generating oxides. Figure 3.2 B illustrates the XRD pattern of a sample of the Ni/Al_2O_3 catalyst calcined at 400°C in air for 2 hours. Poorly crystalline NiO seems to be formed, without evidence of any other crystalline phase.

The decomposition of a sample during calcination was followed using a mass spectrometer as the temperature was increased at 10°C/min. The apparatus used was the same as that used for all the temperature programmed studies in this chapter (see next section). Figure 3.5 illustrates the desorption products as a function of temperature. The solid line indicates the thermal conductivity change during calcination, the sum of all the desorption/adsorption processes occurring.

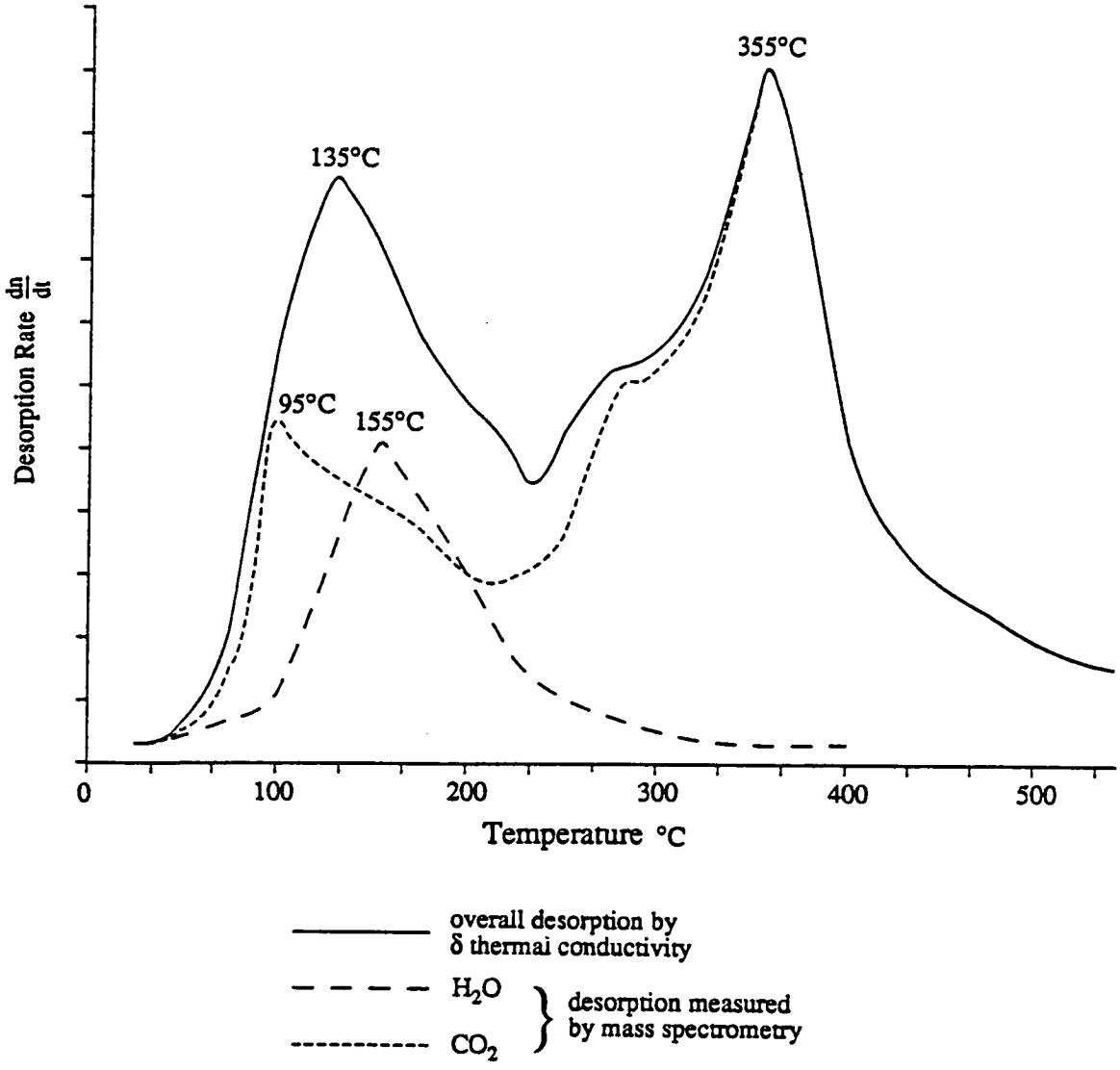

Figure 3.5 *Calcination of Ni/Al_2O_3. The desorption of CO_2 and H_2O as a function of temperature.*

Water has a broad desorption peak, with maximum rate at 155°C. CO_2 has two desorption peaks, a low temperature one at 95°C and a high temperature one at 355°C, with a lower temperature shoulder. It is apparent from Figure 3.5 that calcination at a temperature of at least 400°C is required for complete structure collapse to NiO. Water desorbing above 100°C can be considered as 'structural water' [112], removed from the interlayer in a double layer structure. The Brucite layer is totally destroyed with the decomposition of the carbonates, evolving CO_2 at a maximum rate at 355°C. The aluminium is thought to form an $Al(OH)_3$ phase (Boehmite) on calcination [111].

3.2.1 Simultaneous Thermal Analysis

Simultaneous Thermal Analysis (STA) is another way of examining the calcination process. Samples are heated at a linear rate in air and the mass, temperature and the differential of both of these are monitored. This allows mass loss as a function of temperature to be studied. The differential temperature trace indicates the extent of exothermicity of the calcination process. Experiments here were performed using a Stanton Redcroft Simultaneous Thermal Analyser, STA 780, interfaced to a BBC Microcomputer [116]. Figure 3.6 below illustrates the results of an STA experiment on 15mg of as-prepared Ni/Al_2O_3 heated at 10°C/min in air.

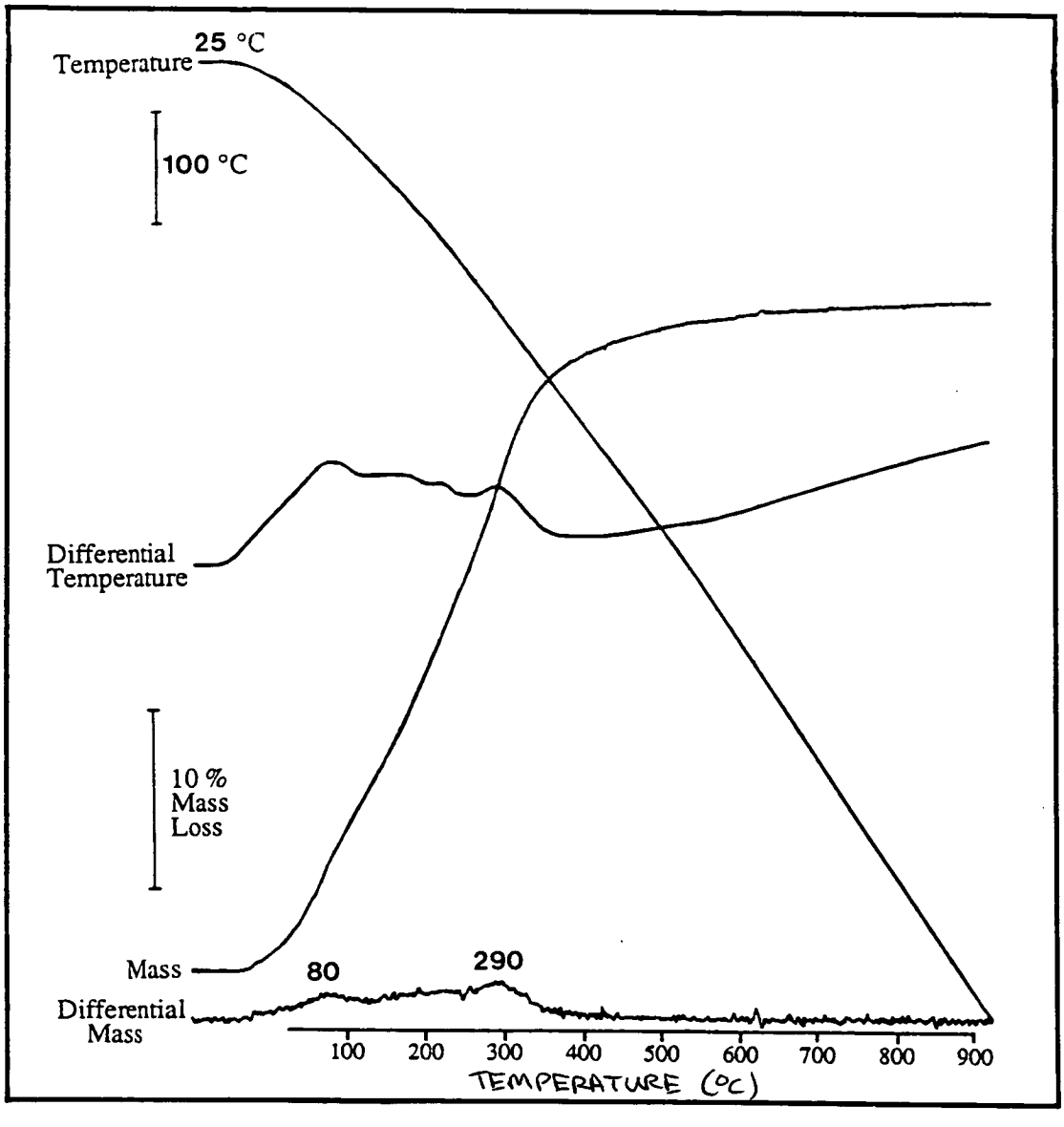

Figure 3.6 *Simultaneous Thermal Analysis of 15mg of as-prepared Ni/Al_2O_3 heated at 10°C/min.*

A gradual mass loss between 30°C and 300°C has occurred, with two peaks in the differential mass plot at 80°C and 290°C. A corresponding increase in temperature at the desorption points is indicated by the differential temperature trace. There is also a gradual rise in differential temperature above 500°C.

These results tie in well with the mass spectral results shown in Figure 3.5. The mass loss between 30°C and 300°C in Figure 3.6 can be attributed to a combination of CO_2 and H_2O desorption. The rise in the differential temperature trace at desorption points indicates that the collapse of the catalyst structure during calcination, forming NiO, is an exothermic process. The overall mass loss of 35% during the calcination process in Figure 3.6 also agrees with the increase in %Ni and %Al in the structure as measured by Atomic Absorption Spectroscopy (Table 3.2). The gradual rise in the differential temperature above 500°C, may be due to the onset of the $Al(OH)_3$ (boehmite)$\rightarrow\gamma$-Al_2O_3 phase transition [151], which would probably occur without any perceptible mass loss.

3.3 Reduction.

The active phase of the catalyst, the zero valent metal Ni(0), is generated by reduction of the Ni^{2+} with a suitable reductant, usually hydrogen. A relatively recent and convenient method of investigating reduction behaviour is *via* Temperature Programmed Reduction (T.P.R.) [117]. The method used here involves linearly temperature programming a catalyst sample in a flow of 5% hydrogen in argon. The hydrogen consumption rate is measured as a function of temperature by monitoring the hydrogen concentration after the gas has passed over the sample. This is done either by mass spectrometry or by measuring the change in thermal conductivity of the gas stream before and after the sample. Experiments here indicate that the latter technique is more sensitive than mass spectrometry when 5% hydrogen in argon is used, although the specificity attainable with mass spectrometry is lost.

3.3.1 Experimental.

The apparatus used here is shown schematically in Figure 3.7 below.

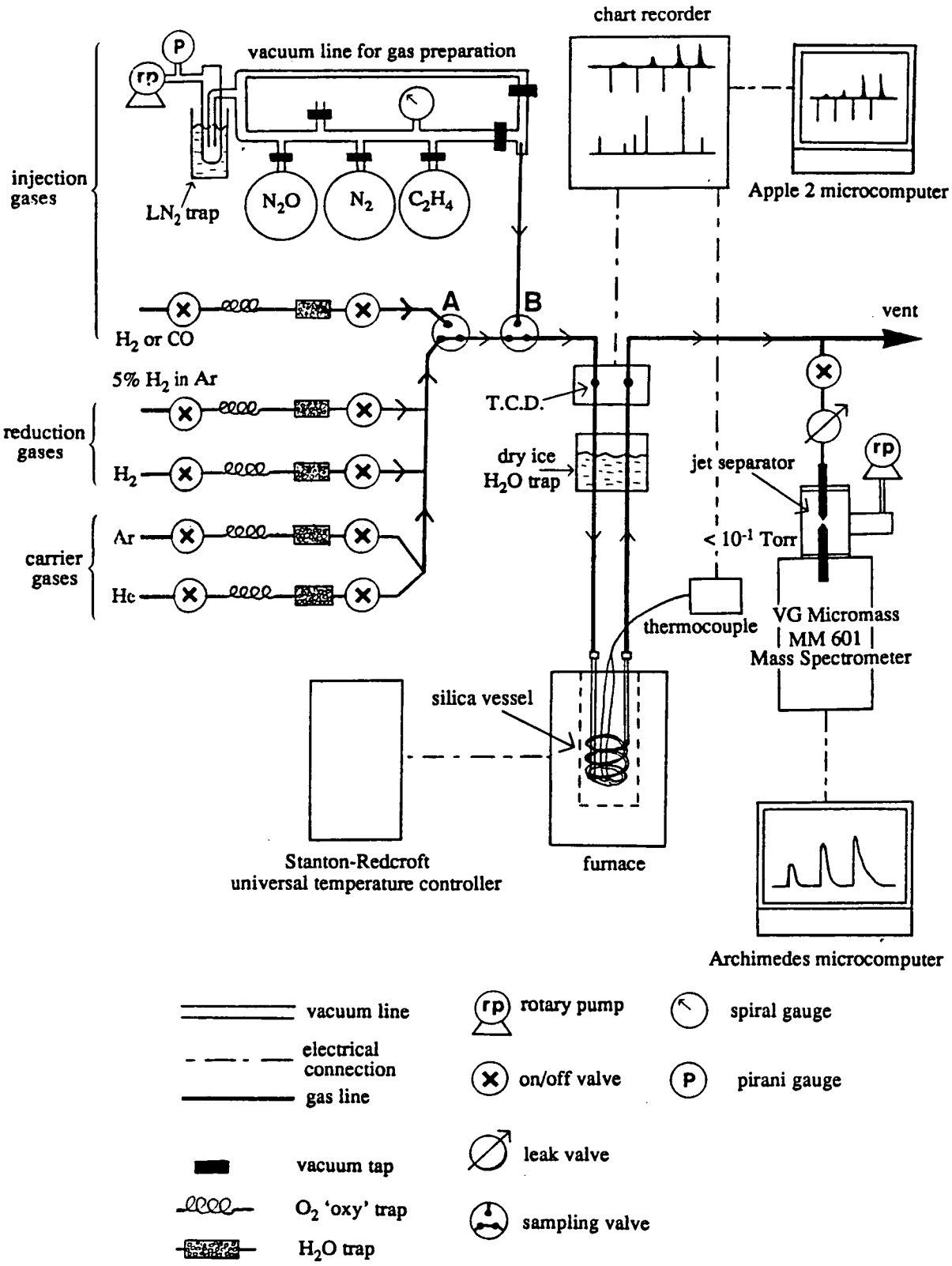

Figure 3.7 *Apparatus used for temperature programmed and pulsed reaction/chemisorption experiments.*

Gas flows from the left hand side, through one side of the thermal conductivity detector (TCD), over the sample and then through the other side of the cell and to vent. A silica vessel is used the hold the catalyst samples as it is capable of withstanding the high temperature reduction needed by nickel catalysts (often >600°C). A portion of the output may be sampled by the jet separator, which then supplies the VG MM601 mass spectrometer with a mass selected beam. The temperature of the vessel is controlled by a Stanton Redcroft temperature programmer which supplies a furnace that can be raised up to enclose the silica sample vessel. The thermal conductivity detector is of the thermistor bead type. Changes in thermal conductivity are recorded by an Apple II microcomputer, and mass spectrometer measurements by an Archimedes microcomputer. Both allow integration and manipulation of spectra. A glass vacuum line can be used for preparation of gases for injection into the carrier gas stream. The same apparatus is used for all temperature programmed studies, including TPR, temperature programmed desorption (TPD), temperature programmed oxidation (TPO) and temperature programmed surface reaction (TPSR). For reduction either hydrogen or 5% hydrogen in argon is used. For desorption studies, a carrier gas of helium or argon is used.

Results.

Figure 3.8A shows the TPR of the as-prepared catalyst, B) the calcined sample and C) a sample of the standard EURO-Ni catalyst [118] for comparison. Reduction profiles of $Al_2(CO_3)_3$, γ-Al_2O_3, SiO_2 and α-Al_2O_3 are shown in Figure 3.9 and a series of physically mixed systems, $Ni(NO_3)_2/SiO_2$, $NiCO_3/SiO_2$ and NiO/SiO_2 in Figure 3.10. These TPR experiments were performed with 'standard' conditions of 30mg of material, a flow rate of 20cm^3/min of 5% hydrogen in argon and a heating rate of 10°C/min. The effect of altering these conditions is discussed later. A dry ice trap is used to prevent any water from the reduction process or any desorption product from decomposition such as CO_2, from reaching the detector. Hence the TPR profile is purely a hydrogen consumption measurement.

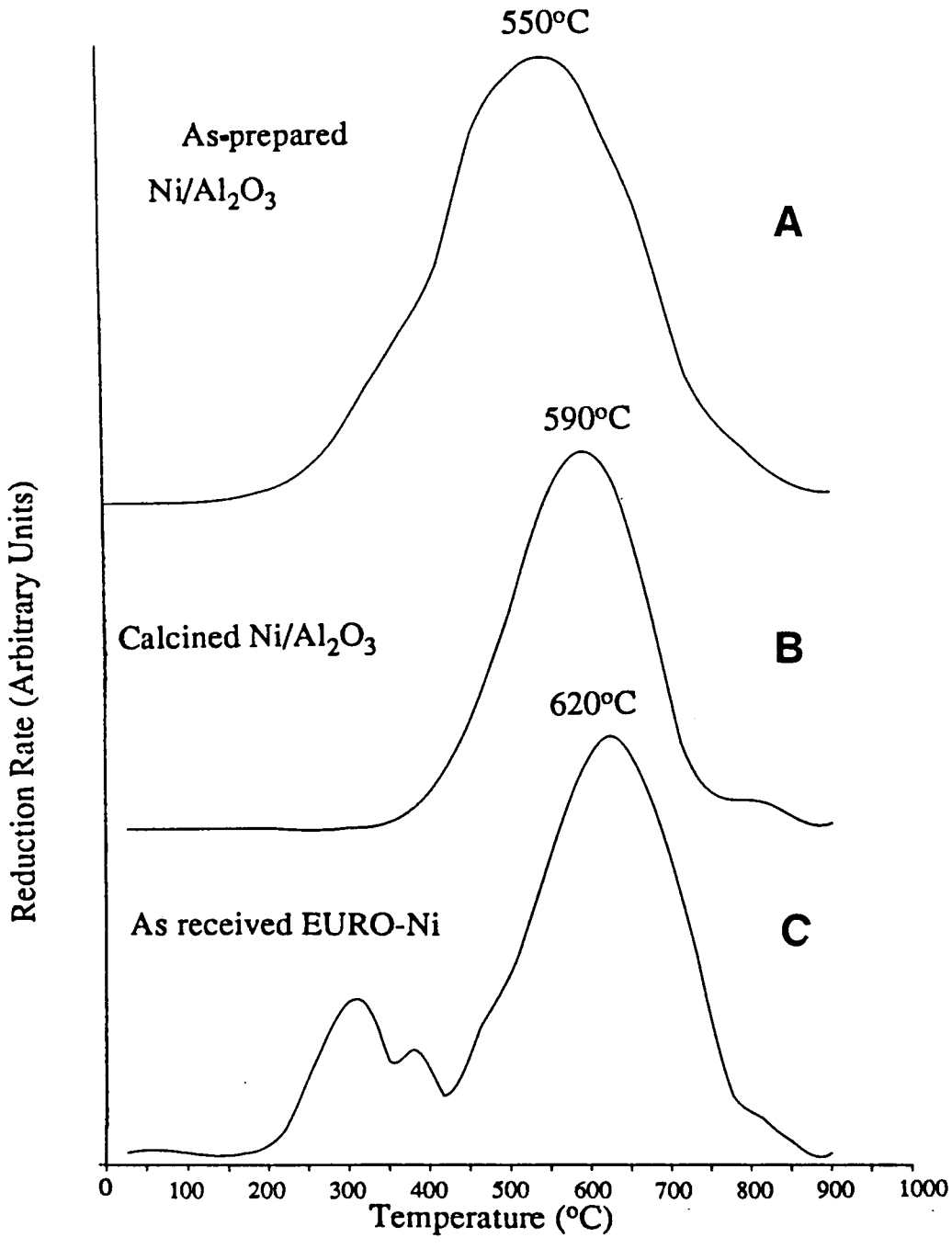

Figure 3.8 *TPR profiles of A) as-prepared Ni/Al_2O_3, B) calcined Ni/Al_2O_3 and C) as-received EURO-Ni.*

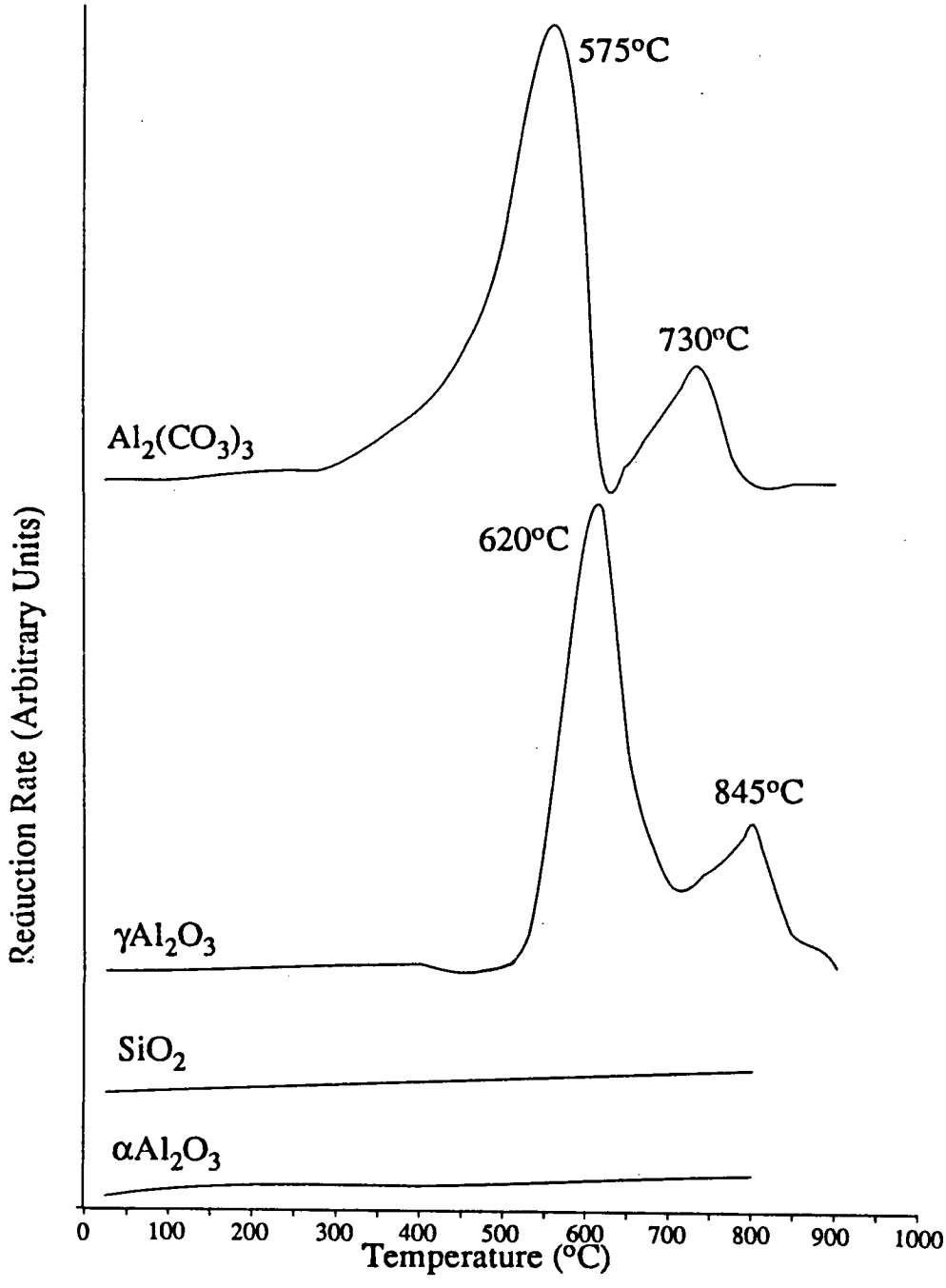

Figure 3.9 *TPR profiles of $Al_2(CO_3)_3$, γ-Al_2O_3, SiO_2 and α-Al_2O_3.*

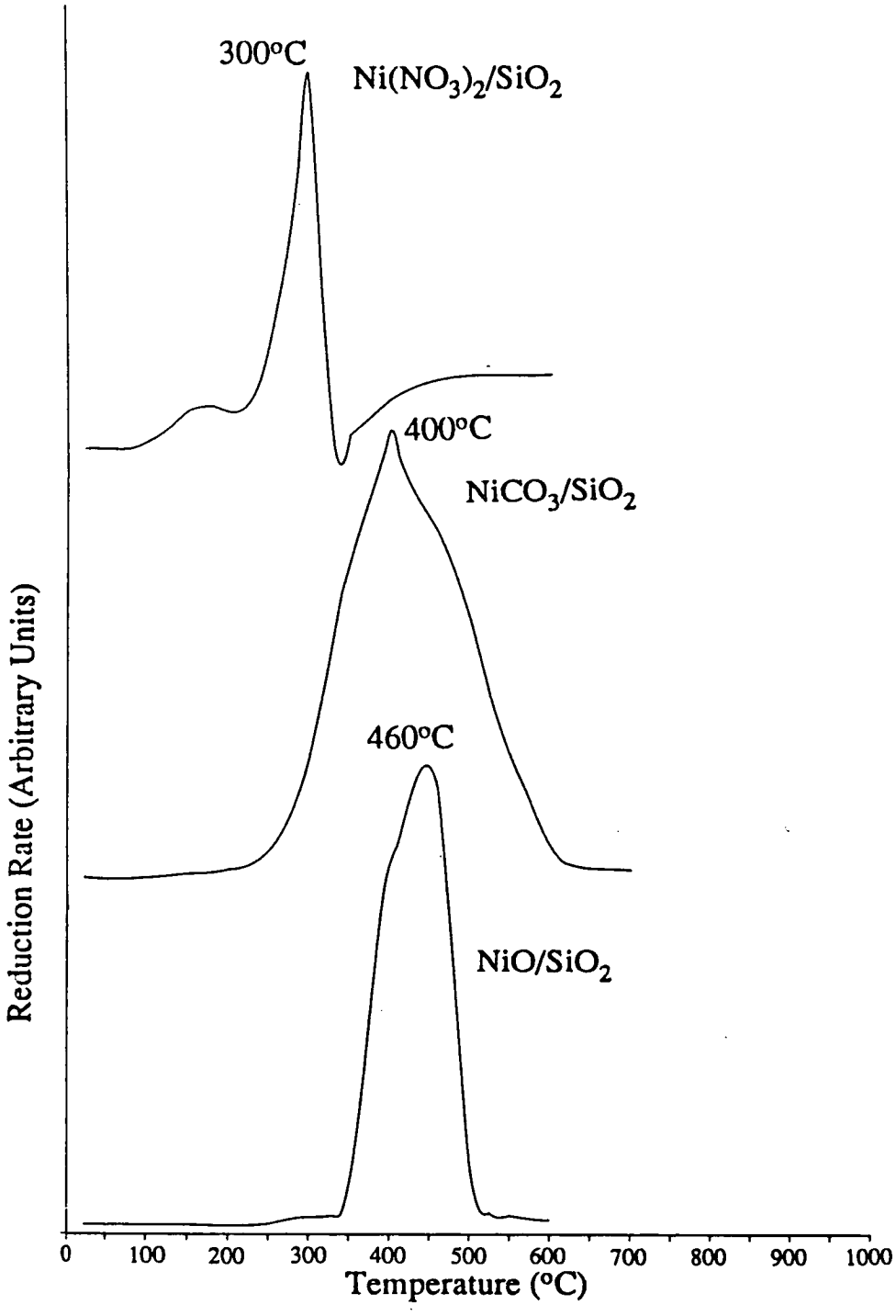

Figure 3.10 *TPR profiles of $Ni(NO_3)_2/SiO_2$, $NiCO_3/SiO_2$ and NiO/SiO_2.*

Discussion

The maximum rate of reduction occurs at 550°C for the as-prepared catalyst and is raised to 590°C on calcination. These peaks occur at a much higher temperature than for the NiO/SiO_2 (physically mixed) system, at 460°C, and also the mixtures of the other nickel compounds $Ni(NO_3)_2/SiO_2$ and $NiCO_3/SiO_2$ at 300°C and 400°C respectively. As illustrated in Figure 3.9, SiO_2 itself is not reducible in the temperature range of these experiments. γ-Al_2O_3 and $Al_2(CO_3)_3$ both show reduction behaviour, with maximum rate at 620°C and 575°C respectively.

The reduction activation energy may be obtained from Equation 3.01 below, using the temperature of maximum rate of reduction [119]. This is an application of Redhead's second order desorption equation [120].

$$\frac{E_r}{R\,T_m^2} - \frac{[H_2]\,A_r\,e^{-E_r/RT_m}}{\beta} = 0 \qquad \text{Equation 3.01}$$

where E_r is the reduction activation energy.
A_r is the reduction pre-exponential factor.
T_m is the temperature of maximum reduction rate.
β is the heating rate.
R is the Boltzmann constant.
$[H_2]$ is the gas phase concentration of hydrogen.

This gives values of 182.1 kJ/mol and 190.1kJ/mol for the 550°C and 590°C peaks of the as-prepared and calcined sample TPRs respectively. Both of these TPRs indicate that isolated nickel compounds do not exist and that the nickel must be inextricably linked with the aluminium in the structure. In the as-prepared sample the XRD pattern indicates that some unreacted $Ni(NO_3)_2$ and also some $NiCO_3$ exist, and since their reduction maxima are at 300°C, this may explain the broad shoulder to the lower temperature side of the reduction peak, Figure 3.8A. The majority of the nickel is held in a double layer structure and is evidently not reduced significantly until 550°C.

Calcining the as-prepared catalyst shifts the maximum up to 590°C. XRD indicates some poorly crystalline NiO, which should be reduced at 460°C (Figure 3.10). Whilst some of this may be accounted for in the broad reduction peak of the calcined sample, it seems that most of the Ni is not present as a facile NiO phase. Ross *et al.* [138] propose that two phases form on calcination at temperatures

greater than 350°C. One is rich in NiO, containing small amounts of Al^{3+}, the other rich in Al_2O_3 with a small proportion of Ni^{2+}. The results indicated here are in agreement with this theory, if the alumina phase is non crystalline and hence not observable in XRD. The presence of Al^{3+} within the NiO crystallites hinders reduction to some extent, forcing reduction maxima to higher temperature. The Al^{3+} ions are forced to segregate, allowing a pure nickel phase to form. Interestingly, on re-oxidation, a facile NiO phase is formed, without any Al^{3+} content [138]. This allows the re-reduction to take place at a lower temperature to that of the original reduction. The re-reduction of 'passivated' catalysts is discussed later as a method of producing reduced nickel *in situ* inside the DRIFTS apparatus.

The nickel in the alumina rich phase will be more difficult to reduce. The amount of nickel in this phase seems to be a function of the temperature at which calcination took place. Ross *et al.* [138] propose this phase to be nickel aluminate, $NiAl_2O_4$. More of the nickel is bound up here the higher the temperature used for calcination. In the catalyst used here, very little nickel is present in this alumina phase as the catalyst is essentially totally reducible as is described later. No evidence of an aluminate phase is seen in XRD experiments.

3.3.2 The Real TPR Profile.

Adsorption/Desorption Processes.

The hydrogen flowing through the catalyst during TPR reduces individual metal ions, lowering their valence state and hydrogen is consumed. The hydrogen may also adsorb onto reduced metal and then desorb into the carrier gas. In some situations, hydrogen may 'spillover' onto the support of a catalyst, only desorbing at a higher temperature [121]. These processes may lead to an apparent hydrogen consumption rate that differs from the true consumption of hydrogen solely for reduction.

Apparent hydrogen consumption can be written as the sum of the following processes [122].

Apparent hydrogen consumption = reduction $Ni^{2+} \rightarrow Ni(0)$
+ adsorption onto Ni(0)
+ spillover onto Al_2O_3
- desorption from Ni(0)
- desorption from Al_2O_3

If a second TPR is performed immediately after the initial one, then assuming that all the metal has been reduced (at least all that is reducible in the temperature range of

the experiment), no hydrogen consumption due to reduction processes will occur. Only apparent consumption due to the adsorption/desorption will lead to a signal during TPR.

With this in mind, a second TPR was performed on a reduced sample. There was no detectable signal change during this second experiment and consequently it can be safely assumed that under the conditions used for TPR here, the adsorption/desorption terms have little or no effect on the overall profile. Hence the TPR profiles shown are the 'real' ones.

Change in Reduction Variables.

Whilst TPR profiles are useful in investigating the reducibility of catalyst samples, a degree of caution needs to be applied when comparing results from different systems and laboratories. The exact shape of peaks and position of peak maxima may vary as a function of several experimental variables such as catalyst sample mass, the gas flow rate and temperature ramping rate. Examining Equation 3.01 reveals that both the hydrogen concentration term (flow rate) and the heating rate, β, have an effect on T_m. Figures 3.11, 3.12 and 3.13 show TPR profiles of as-prepared catalyst recorded as a function of different catalyst mass, gas flow rate and temperature ramping rate, with the other variables kept constant.

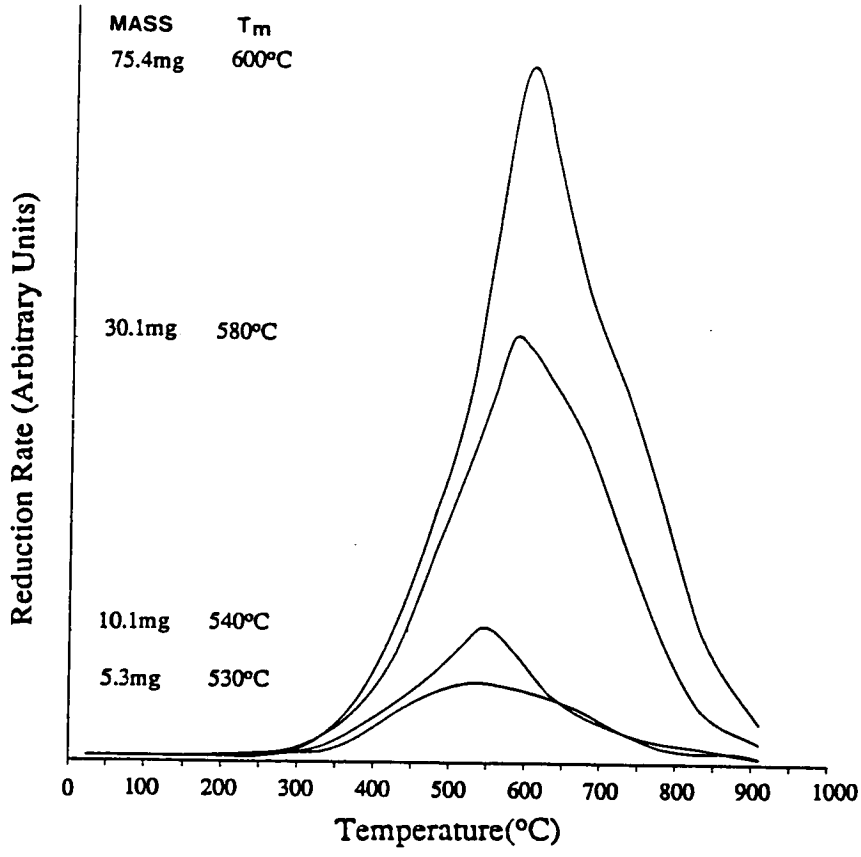

Figure 3.11 *TPR profiles recorded with various masses of catalyst sample. Hydrogen flow rate=10cm^3/min, heating rate=20°C/min.*

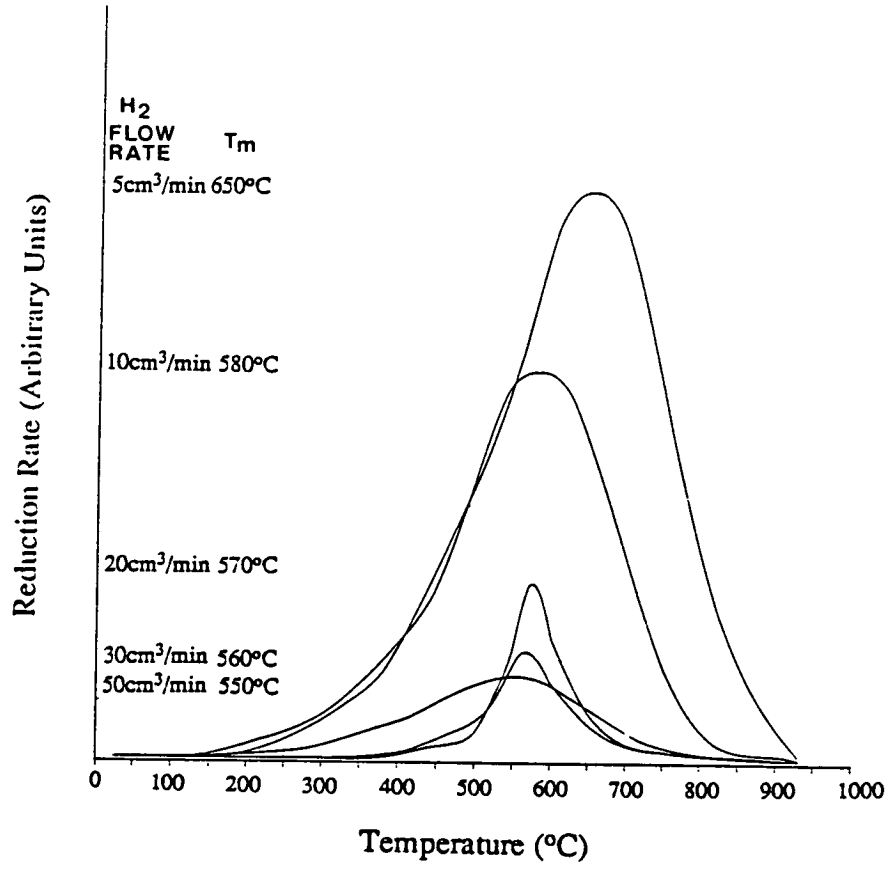

Figure 3.12 *TPR profiles recorded with various values of hydrogen flow rate. Catalyst mass=30mg, heating rate=20°C/min.*

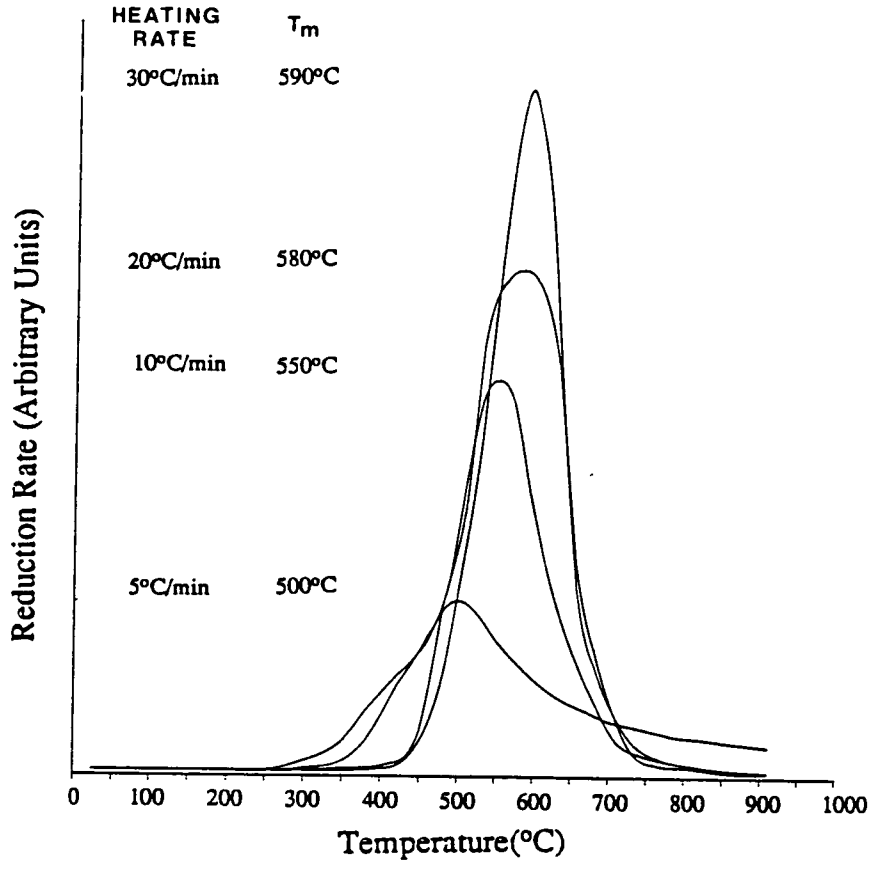

Figure 3.13 *TPR profiles recorded with various values of heating rate. Catalyst mass=30mg, hydrogen flow rate=10cm^3/min.*

It is immediately obvious that both the shape and position of the maximum rate of hydrogen consumption change as a function of all of these factors. In Figure 3.11 increasing the mass of catalyst, increases the temperature of maximum rate of reduction. This is not predicted in Equation 3.01, which appears to show that T_m is independent of catalyst mass. The shift in maxima is probably due to the rate limiting step in reduction, the hydrogen flow rate. The greater the catalyst mass means that correspondingly more hydrogen is consumed and the area under the TPR profile is therefore larger. If there is not enough hydrogen present at any one temperature, a significant hydrogen concentration gradient will occur across the catalyst sample, giving non homogeneous reduction. Reduction rate maxima will move to higher temperatures.

The same effect is apparent in both Figures 3.12 and 3.13. Increasing the flow rate of hydrogen lowers the peak maxima as does lowering the temperature ramping rate. Both of these effects are predicted in Equation 3.01. Flow theory shows that for a first order process, increasing the flow rate for a reactant consumed in the reaction results in a lowering of the degree of conversion, and consequently an increase in reactant concentration [123]. Changing the flow rate from $50cm^3/min$ to $10cm^3/min$ is predicted to move T_m from 550°C to 595°C (Equation 3.01). This is measured experimentally as a shift up to 580°C (Figure 3.12). A TPR profile with the lowest T_{max} should be generated when a high flow rate of hydrogen, low catalyst sample mass and low temperature ramping rate are used. Of these factors, the ramping rate is the most important. Such a TPR profile for this system is one with a maximum reduction rate at 500°C.

3.3.3 Assessing Degree of Reduction.

Achieving a fully reduced catalyst is important in order to not only maximise the reduced metal surface area, but also to remove any Ni^{2+} ions from the system which may alter the observed chemistry. The extent of reduction may be assessed in several ways. Firstly, if the reduced catalyst is subjected to pulses of oxygen at temperatures high enough to cause complete oxidation, then assuming that all the nickel is oxidised to NiO, a direct measurement of the total number of Ni(0) atoms may be made. Bartholomew and Farrauto [124] have used oxidation at 450°C to assess the percentage reduction. Secondly, by looking at the infrared spectra produced on adsorption of CO on the reduced catalyst, the position of bands at wavenumbers higher than gas phase CO (2143 cm^{-1}) immediately indicates unreduced Ni^{2+}. This can be used as a method of assessing whether unreduced nickel remains in the system.

Finally, by integrating the area under the TPR profiles, having first calibrated the system with a known amount of NiO, the hydrogen consumption can be evaluated, and since the nickel loading is known, the number of H_2 molecules needed to reduce the NiO phase in the calcined catalyst can be determined.

Oxidation at 450°C.

Using the apparatus illustrated in Figure 3.7, pulses of oxygen (1.25×10^{-5} moles O_2) were injected in the helium carrier gas and passed over the reduced and outgassed catalyst at 450°C. The total number of moles of oxygen used for oxidation was measured using the thermal conductivity detector.

Experimental.

53.7mg of as-prepared Ni/Al_2O_3 was reduced at 600°C until no further hydrogen consumption was measurable (after about 1 hr). The catalyst was then outgassed for 30 minutes in helium at the reduction temperature. 35 pulses were required in order to completely oxidise the Ni(0) to NiO. The peak areas were integrated, revealing that 1.125×10^{-4} moles of O_2 was consumed. Assuming only NiO was formed, this would imply that twice this number of Ni(0) atoms were present in the reduced catalyst, giving a nickel content of 24.6% in the as-prepared sample. This is approximately the same as the nickel content of the catalyst measured by AAS and EDTA titration (23.4% and 23.7% respectively). Therefore it seems that, within experimental error, all of the available nickel in the catalyst is reducible, as measured by the oxidation method.

3.3.4 Carbon Monoxide Infrared Study.

A DRIFTS study of CO adsorbed on the Ni/Al_2O_3 catalyst was performed using the apparatus described in Chapter 4. A 0.2μmol pulse of CO was injected into the helium stream and the build up of surface bands was examined as a function of time. Figure 3.14 illustrates infrared bands due to chemisorbed CO on the Ni/Al_2O_3. Table 3.3 shows the assignment of relevant CO infrared bands, adapted from [125].

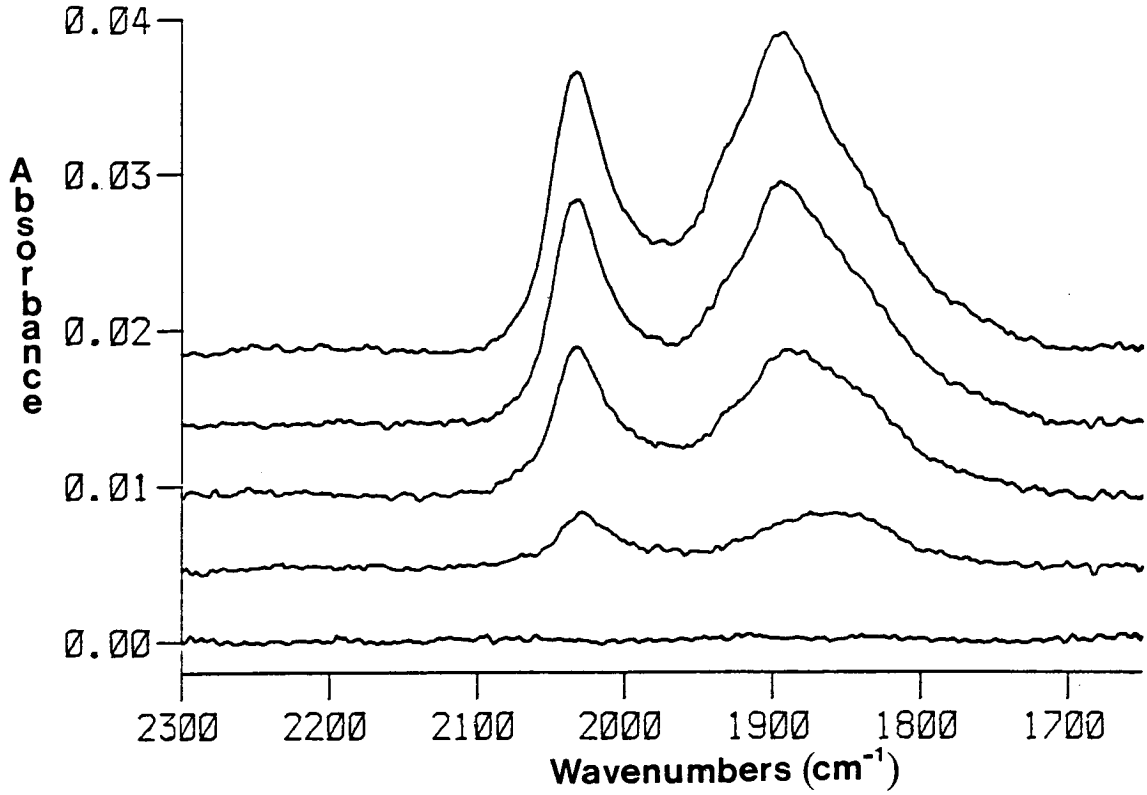

Figure 3.14 *DRIFTS spectra of CO adsorbed on Ni/Al_2O_3.*

Table 3.3 CO vibrational bands and assignment.

Infrared Frequency cm^{-1}		Species	Site
1960	Bridged	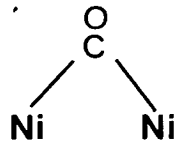	Poorly dispersed, crystalline Ni
2030 - 2050	Linear		Moderately dispersed Ni
2065 - 2090	Subcarbonyl	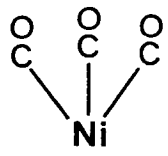	Well dispersed Ni
2195	Ni^{2+}	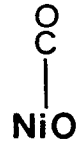	Partially reduced Ni

Discussion.

Immediately obvious in Figure 3.14 is the absence of intensity at *circa* 2195 cm^{-1}, indicating that there are not significant numbers of Ni^{2+} ions forming bonds with the CO. Increasing the size of the CO pulses and repeated exposure to CO failed to generate any absorbance features in this region. Consequently, as far as infrared spectroscopy is concerned, no unreduced nickel ions can be detected in the reduced sample. In fact Primet *et al.* [125] estimate that this 2195cm^{-1} band is only significant when the catalyst is less than 5% reduced. In this sense it may not be very useful for determining the extent of reduction. The bands at 2030cm^{-1} (linear species) and 1900cm^{-1} (bridged species) indicate that the nickel is present as relatively large crystallites.

Integration of TPR Profiles.

By integrating the area under the TPR profiles, Figure 3.8A and B, a measure of the hydrogen consumption per nickel atom in the catalyst can be obtained. Table 3.4 shows the integration figures for the as-prepared and calcined Ni/Al_2O_3.

Table 3.4 Integration of TPR profiles.

	As-prepared	Calcined
Apparent H_2 consumption	1.84×10^{20} molecules	1.15×10^{20} molecules
Catalyst Mass	28.3 mg	32.7 mg
Nickel loading	23.5 %	31 → 39 %
∴ H_2:Ni ratio (for reduction)	2.7 : 1	1.1 → 0.9 : 1

Discussion.

The calcined catalyst shows a 1:1 H_2:Ni ratio in hydrogen consumption, indicating that the reduction is predominantly from NiO. All the available nickel is reduced. Apparently much more hydrogen is consumed in the reduction of the as-prepared catalyst. The probable reason for this is that during the temperature programming, the catalyst will be decomposing as well as undergoing reduction. This would cause the evolution of CO_2 and H_2O. Whilst this will not increase the hydrogen consumption, the evolved gas will cause a greater change in thermal conductivity and contribute to the TPR peaks. TPR using a mass spectrometer should be able to resolve this problem.

3.4 Passivation.

As mentioned previously, the DRIFTS accessory is only capable of operating at temperatures up to 300°C. As the TPR profiles of Ni/Al_2O_3 illustrate, the as-prepared and calcined catalysts both require reduction at a temperature between 550°C and 600°C. Consequently a procedure involving the passivation of reduced catalysts allowing samples to be moved and re-reduced *in situ* inside the DRIFTS cell was developed. With careful passivation it should be possible to generate only a facile

NiO phase on the surface of the nickel crystallites which allows easy and complete re-reduction, without loss of metal surface area.

Nickel is a pyrophoric metal, exposure of a reduced sample to air causing it to rapidly catch fire and be deeply oxidised. Figure 3.15A illustrates a TPR profile of a reduced Ni/Al_2O_3 sample after catching fire. Total oxidation of the nickel has occurred, requiring re-reduction at a temperature in excess of 700°C. The intense heat has caused the nickel to react with the alumina support, probably generating the nickel aluminate phase discussed previously. It is this kind of behaviour that passivation seeks to prevent. Adsorption of another species onto the surface of a reduced sample may enable a purely superficial oxide coating to develop when exposed to air. This should both prevent further oxidation and also enable easy re-reduction.

Passivation of nickel catalysts with oxygen seems to be the most frequently used technique (e.g. [126], [127]). Steam has also been used [128]. In all cases, some degree of bulk oxidation was detected.

3.4.1 Experimental.

A series of different adsorbate systems were investigated, and the degree of passivation assessed using TPR after the reduced catalyst had been exposed to the adsorbate and then to air. Figure 3.15B and C illustrate the effect of passivation with $5\%O_2/He$ and H_2 respectively. Similarly Figure 3.16 shows the effect of passivation with A) CO, B) N_2O and C) C_2H_4, Figure 3.17 with A) CO_2 (without exposure to air), B) a 3:1 CO_2:C_2H_4 mixture and C) CO_2. Finally, Figure 3.18 shows passivation with A) a 1:1 C_2H_4:CO mixture, B) a 5:3 C_2H_4:CO mixture and C) a 3:1 C_2H_4:CO mixture. All of these passivations were performed at room temperature using the apparatus shown in Figure 3.7.

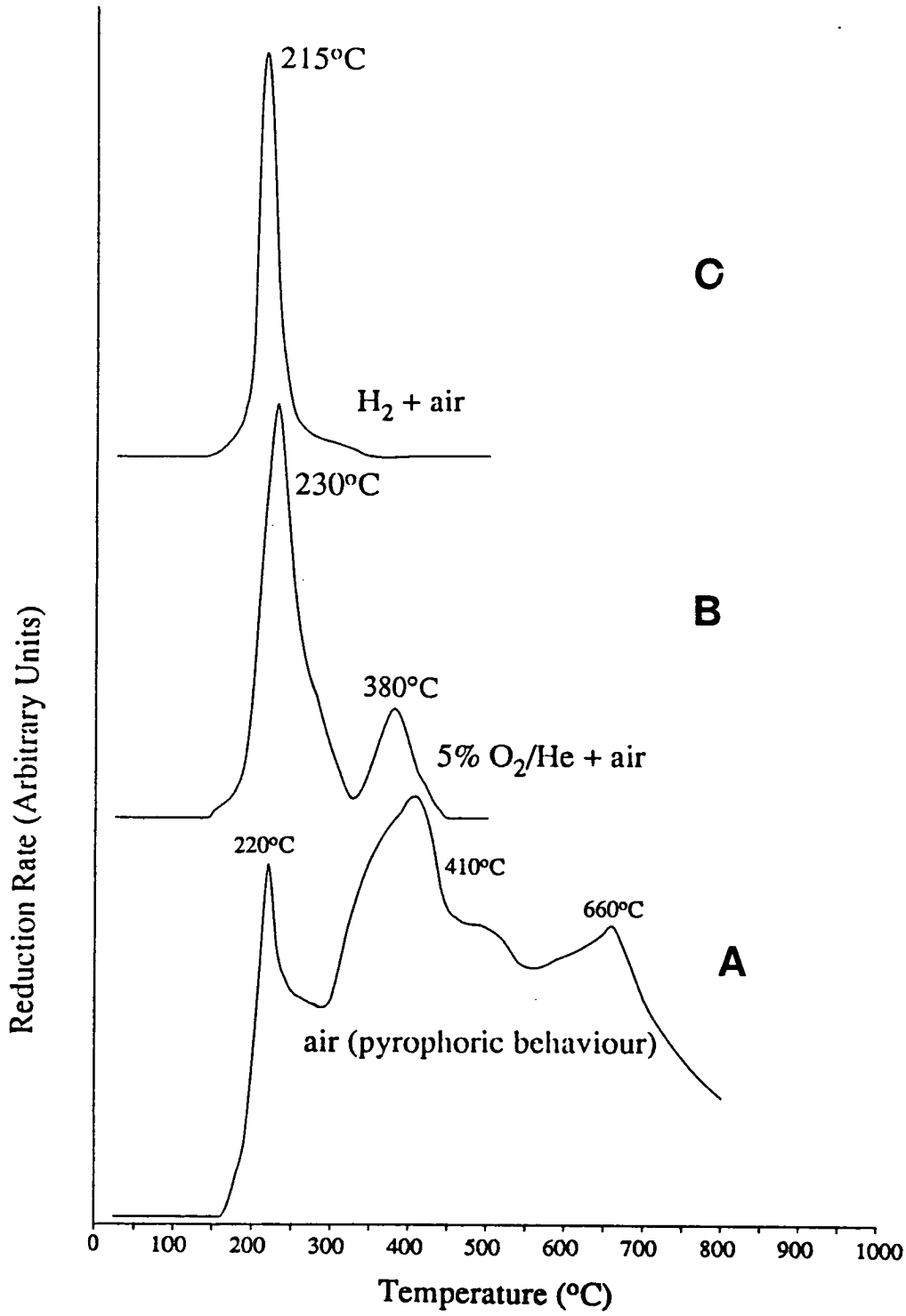

Figure 3.15 *TPR profiles after A) pyrophoric behaviour, B) passivation with 5%O_2/He and C) passivation with H_2.*

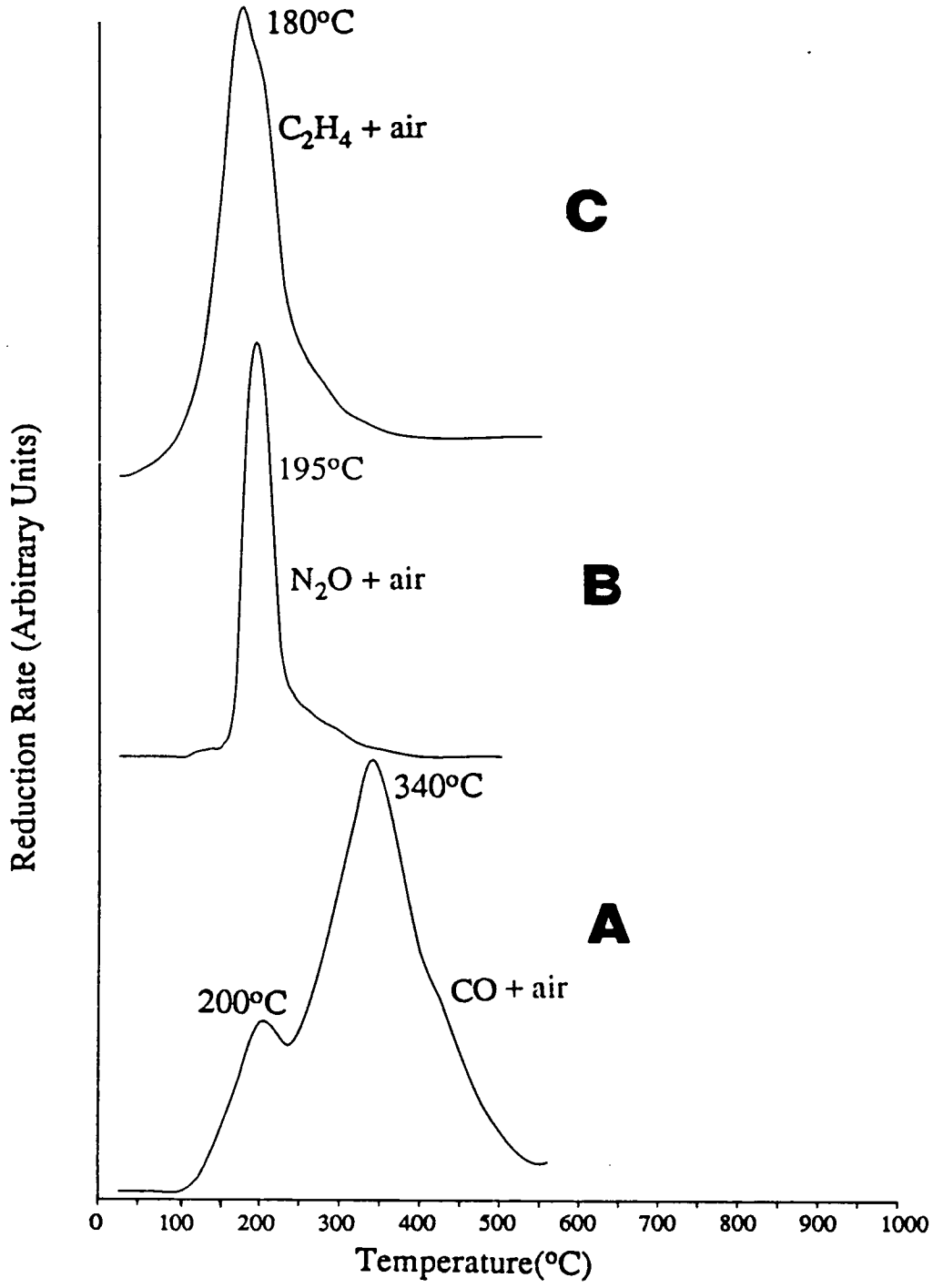

Figure 3.16 *TPR profiles after passivation with A) CO, B) N_2O and C) C_2H_4.*

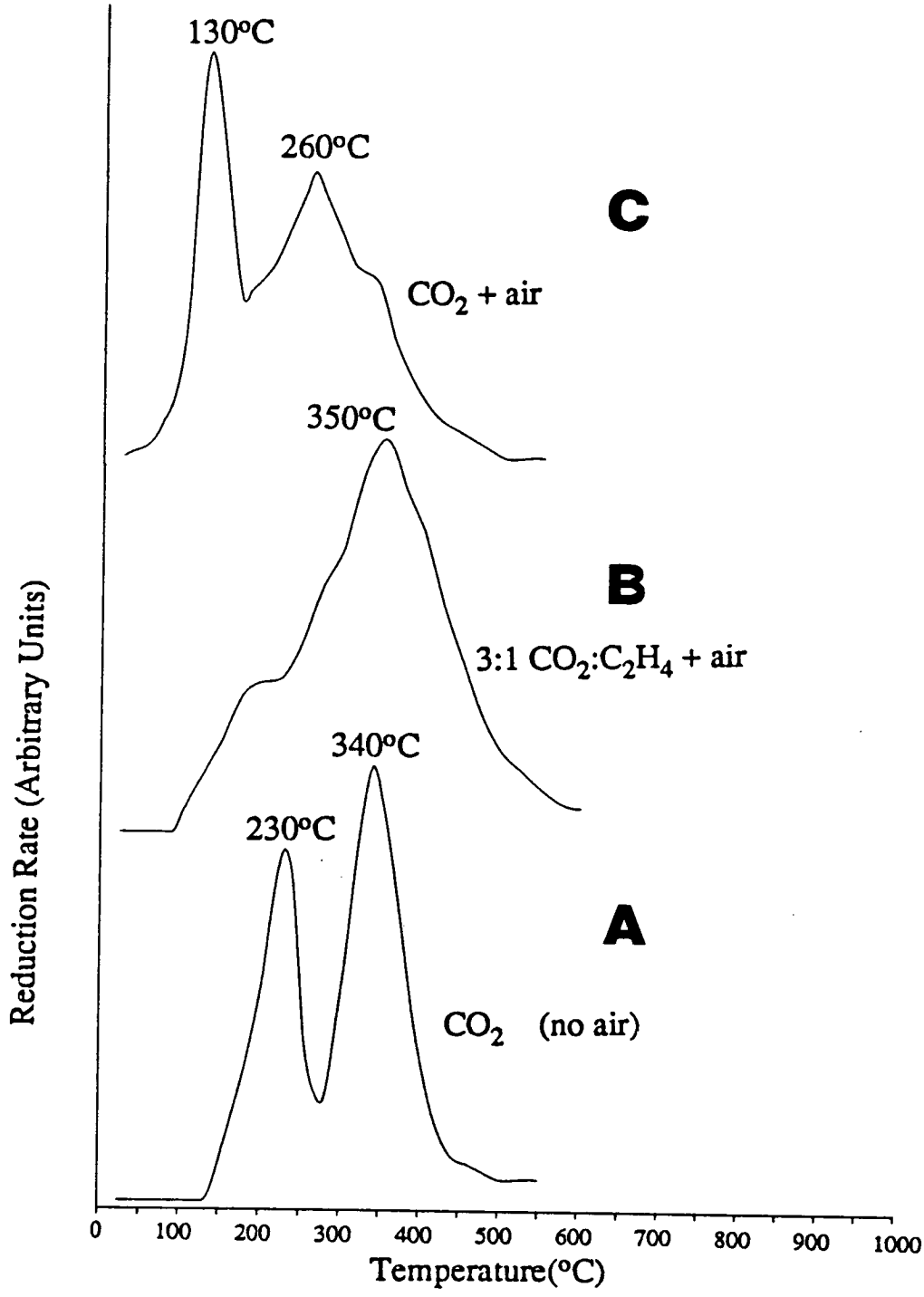

Figure 3.17 *TPR profiles after passivation with A) CO_2 (without exposure to air), B) a 3:1 CO_2:C_2H_4 mixture and C) CO_2.*

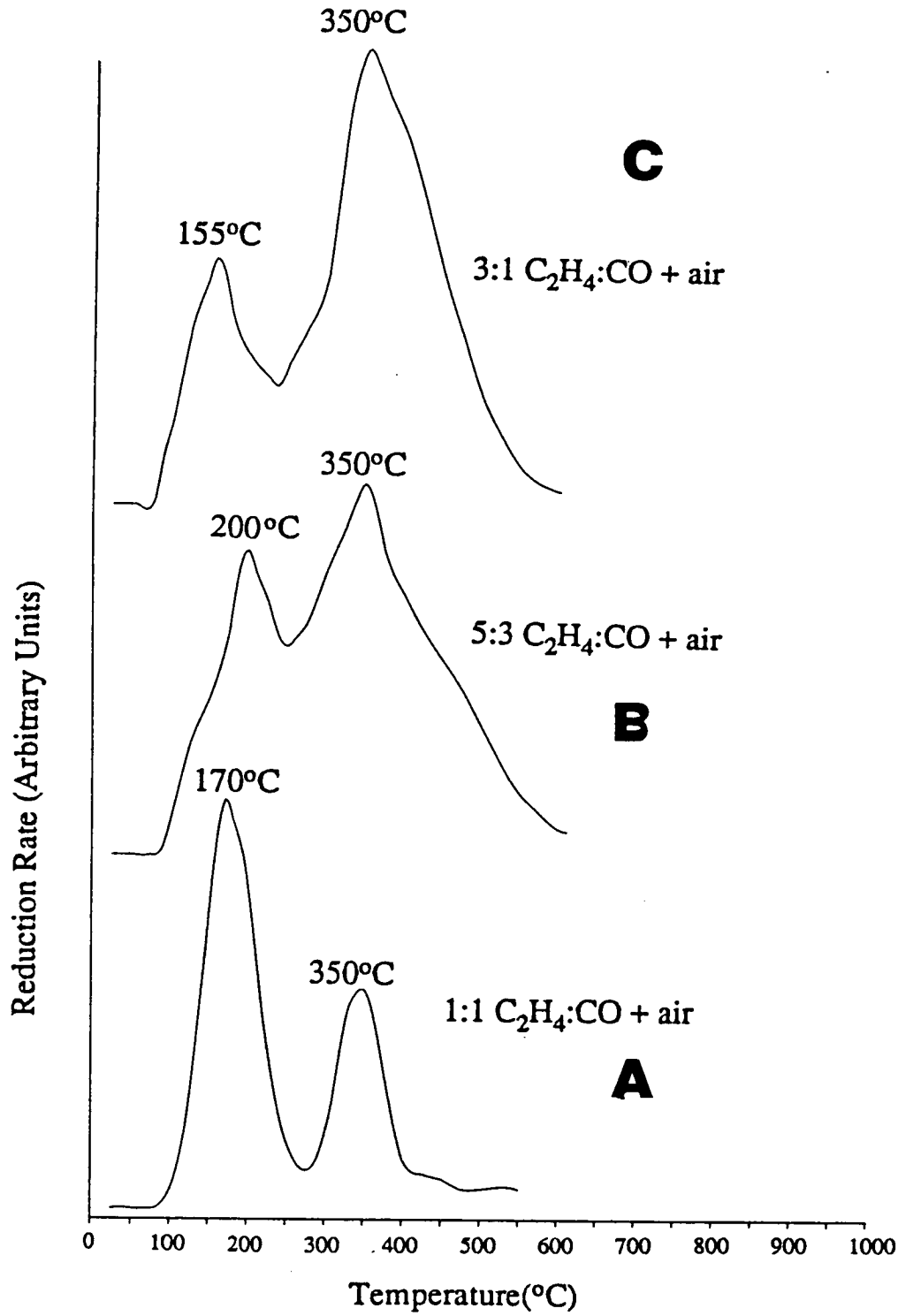

Figure 3.18 *TPR profiles after passivation with A) a 1:1 C_2H_4:CO mixture, B) a 5:3 C_2H_4:CO mixture and C) a 3:1 C_2H_4:CO mixture.*

The results are summarised in Table 3.5 below.

Table 3.5 Re-reduction temperatures after passivation.

Adsorbate	Maxima in TPR Profiles.
5% O_2/He	230°C and 380°C
H_2	215°C
CO	200°C and 340°C
N_2O	195°C
C_2H_4	180°C
3:1 CO_2:C_2H_4	350°C
CO_2	130°C and 260°C
1:1 C_2H_4:CO	170°C and 350°C
5:3 C_2H_4:CO	200°C and 350°C
3:1 C_2H_4:CO	155°C and 350°C

Only C_2H_4, N_2O, H_2 and CO_2 passivate the catalyst sufficiently to allow re-reduction at a temperature below 300°C after exposure to air. Of these, C_2H_4 seems to allow re-reduction at the lowest temperature. Integrating the area beneath the TPR profiles should give a measure of the extent of oxidation that has occurred, again assuming stoichiometric NiO has formed. Measurement of the nickel surface area after passivation and re-reduction will indicate how much of the original surface area remains.

The hydrogen consumption in TPR profiles for various adsorbate passivations is indicated below in Table 3.6. The original metal surface area before passivation (measured by H_2 pulsed chemisorption and described in the next section) was $28m^2/g$ in all of these experiments. The regenerated surface area, after re-reduction at 300°C, is shown in the third column. In the last column the ratio of the NiO re-reduced after passivation to the original number of surface atoms is displayed. This indicates the number of layers of oxide formed on passivation.

Table 3.6 Hydrogen consumption during re-reduction of passivated catalysts.

Passivation procedure	H_2 consumption (molecules)	Sample mass (mg)	Regenerated Nickel Area (m^2/g)	Layers of NiO formed
C_2H_4	4.08×10^{19}	33.7	18.2	2.4
H_2	1.96×10^{19}	32.4	18.4	1.18
	1.94×10^{19}	31.2	21.3	1.21
N_2O	6.04×10^{19}	39.1	20.8	3.07
	4.78×10^{19}	35.3	19.3	2.6
CO_2	5.27×10^{19}	39.1	17.1	2.6

None of these techniques was able to regenerate the original metal surface area of $28m^2/g$. The best situation was with hydrogen passivation before exposure to air, but even here 25% of the original surface area was lost. Just over one monolayer of oxide was formed. With N_2O, it appears that between 2 and 3 monolayers of NiO are formed on exposure to air. Hydrogen adsorption was adopted as the standard passivation procedure for the Ni/Al_2O_3 catalyst used here. The nickel surface area after re-reduction in the DRIFTS cell will fall to $20m^2/g$.

Recently, Gil *et al.* [129] report oxidation of 4 to 7 monolayers depth for passivation of a Ni/Al_2O_3 catalyst with oxygen, and loss of 15% of the original nickel surface area, even when the original conditions of reduction were applied. The maximum in TPR occurred at 500°C.

3.4.2 Effect of Successive Passivation.

As we have seen, at least 25% of the original nickel surface area is lost on passivation and re-reduction. All experiments so far have considered re-reduction of passivated freshly reduced catalyst samples. The effect of successive reductions, passivations and re-reductions was considered in a series of experiments illustrated below. Figure 3.19 shows the nickel surface area (measured by H_2 pulsed chemisorption) as a function of reduction cycle number. The sample was passivated with hydrogen flowing at $100cm^3/min$, before being exposed to air. Re-reduction was performed at 300°C in 100% H_2 flowing at $100cm^3/min$.

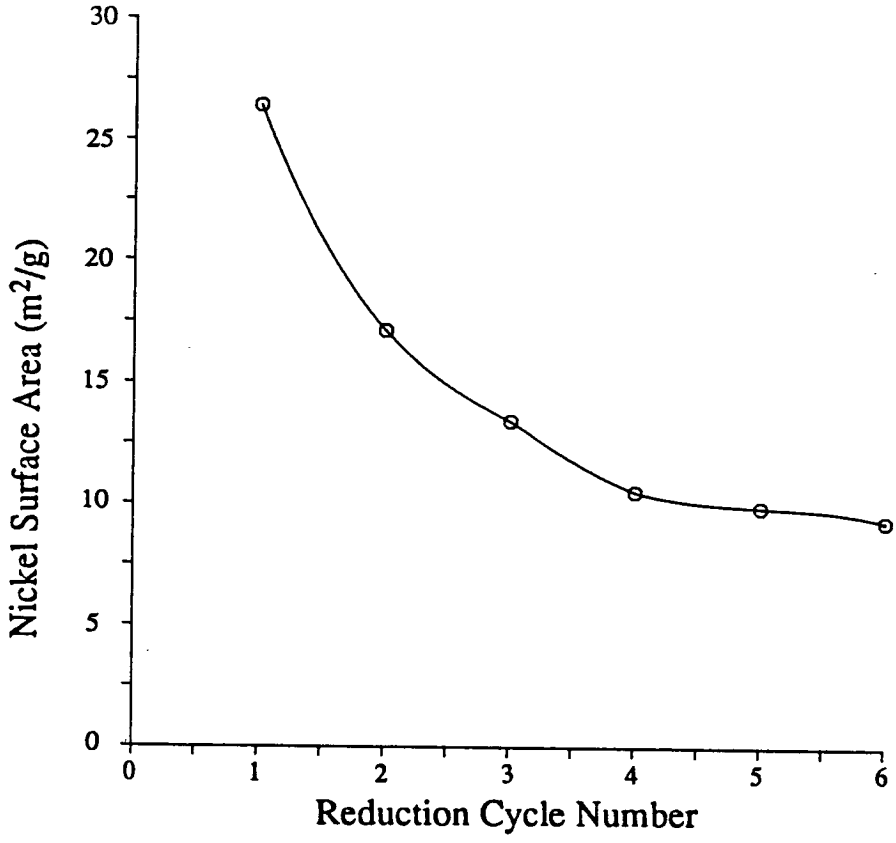

Figure 3.19 *Nickel surface area of Ni/Al_2O_3 during a series of reductions and passivations.*

The rate of decline of nickel surface area seems to slow as the number of reduction and passivation cycles increases. Initially 35% of nickel area is lost on passivation and re-reduction. The rate of loss slows after this, until less than 5% of nickel area is lost between the 5th and 6th reduction. This gradual loss in surface area can be ascribed to the sintering of nickel particles which occurs during each reduction. This is described in the next section.

3.5 Maximising the Nickel Surface Area.

The nickel surface area obtained after reduction is of fundamental importance in the study of catalysis. Although the rate of a reaction may not be a function of the metal surface area, in terms of infrared spectroscopy where only a fixed amount of catalyst may be studied *in situ*, a greater surface area means more active sites for adsorption, and consequently a greater number of adsorbed molecules in the infrared beam. This is an advantage when studying weakly absorbing infrared species as a large number of infrared absorbers can be packed into the beam.

Consequently, maximising the nickel surface area is an important goal. The relationship between temperature of reduction and subsequent nickel surface area is most important. Reduction at a low temperature may incompletely reduce the sample and so not generate all of the possible Ni(0) atoms. High temperature reduction easily reduces the NiO but the nickel particles formed may become mobile and fuse together. This 'sintering' will lower the available nickel surface area. Sintering becomes significant within a narrow range of temperature near the so called Tammann temperature [130]. This empirical relationship is defined as αT_m, where T_m is the melting point of the metal concerned. The constant, α, is usually between 0.4 and 0.6. For nickel, T_m is 1453°C, giving a Tammann temperature of somewhere between 580°C and 870°C.

A balance between the incomplete thermodynamic reduction of Ni/Al_2O_3 at too low a temperature and sintering at too high a temperature, needs to be struck. A series of experiments was performed to measure the metal surface area as a function of reduction temperature. Figure 3.20 below illustrates the nickel surface area produced after reduction at each of a series of temperatures between 300°C and 700°C. Each sample of 30mg as-prepared Ni/Al_2O_3 was reduced for 1 hour in 100% hydrogen flowing at $100cm^3/min$. Nickel surface area was measured with hydrogen pulsed chemisorption (see next section).

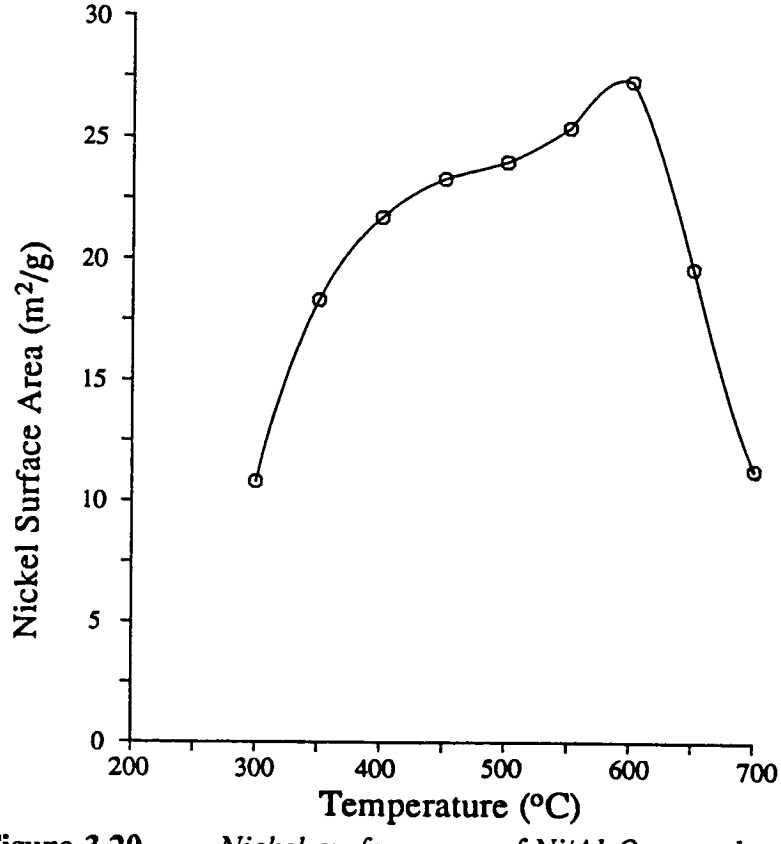

Figure 3.20 *Nickel surface area of Ni/Al_2O_3 samples as a function of reduction temperature.*

After each surface area measurement, A TPR was performed in order to establish the amount of the catalyst left to reduce. The results are illustrated in Figure 3.21 below.

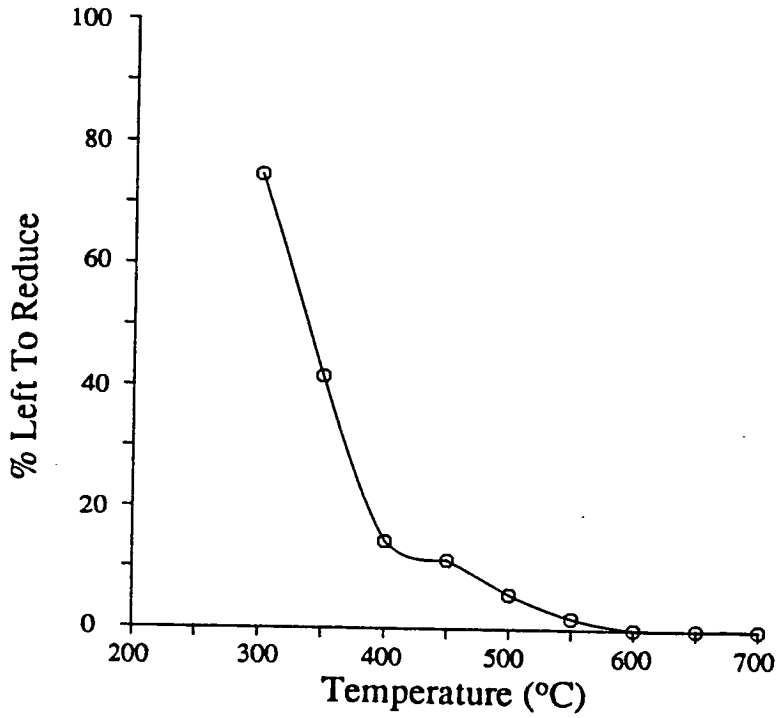

Figure 3.21 *% of catalyst left unreduced as a function of reduction temperature.*

Maximum surface area was obtained after reduction at 600°C. This is also the lowest temperature at which complete reduction occurs. With a reduction temperature greater than 600°C, sintering seems to rapidly reduce the nickel surface area. This implies that α in the Tammann equation is 0.45. These experiments illustrate the surface area as a function of reduction temperature, whilst all other variables have been kept constant. Other factors that may affect the overall nickel surface area are reduction time, catalyst mass, hydrogen flow rate and temperature ramping rate.

Interestingly, the maximum surface area occurs after reduction at temperatures higher than the maximum in the TPR of as-prepared Ni/Al_2O_3 (550°C - Figure 3.8A). This is probably due to the fact that reduction for an hour at 550°C was insufficient to fully reduce the sample, although reduction at this temperature for longer than 1 hour may well provide a higher nickel surface area than reduction at 600°C.

To fully explore all combinations of variables in order to determine optimum conditions would require an inordinate number of experiments. Statistical methods can be usefully employed in designing such experiments as efficiently as possible, and although not dealt with here, are considered in Chapter 6.

3.6 Metal Surface Area and Particle Size Determination.

Metal surface areas can be directly assessed with selective chemisorption techniques, or indirectly determined by particle size measurements with Transmission Electron Microscopy (TEM) or X-ray Diffraction (XRD). Chemisorption of hydrogen is most commonly used, although oxygen or carbon monoxide are also sometimes employed [131], [132]. Hydrogen adsorption appears to be the most well defined of the techniques, with a surface nickel to adsorbed hydrogen ratio, Ni_s:H, of 1:1 [131]. Carbon monoxide adsorption is more troublesome, with a stoichiometry varying as a function of particle size, and also the possibility of carbonyl formation at 25°C causing redispersion of the nickel. With oxygen adsorption, some bulk oxidation at 25°C leading to a variable Ni_s:O ratio, has been reported [131]. As we have seen, carbon monoxide adsorption does have a role in conjunction with infrared spectroscopy in helping to determine the nature of the reduced sample. All chemisorption techniques run into problems when a strong metal-support interaction (SMSI) affects the nickel. This is particularly so for Ni/TiO_2 [133] and Ni/Nb_2O_5 [134]. The SMSI state has been observed in Ni/Al_2O_3 only with Ni loadings less than 3% and nickel particle diameters of less than 2 → 3nm. [132].

3.6.1 Hydrogen Chemisorption.

A Ni_s:H ratio of 1:1 is apparently valid over a large temperature and pressure range [132], and gives surface areas in good agreement with other measurements [135]. Some criticism can be directed at this technique however. Many different researchers have used various experimental conditions, often badly defined. No universally acceptable set of conditions has been defined as a standard. There are also doubts about the interpretation of results [136].

It is generally accepted that hydrogen adsorption has both irreversible and reversible components [137]. Initial adsorption is rapid and irreversible. At higher coverage and higher hydrogen pressure, additional adsorption becomes reversible, in that evacuation of the adsorbate from the system removes this component from the surface. Complete irreversible adsorption occurs at less than a full monolayer and the

exact onset of reversible adsorption varies between catalyst samples. Most studies have found that even reversible adsorption does not proceed to saturation [136]. If this is the case, then the Langmuir or any other isotherm may not be applied. Richard and Cale [136] propose that this reversible phase is caused by diffusion into subsurface layers or to some usually inaccessible interface of the nickel. Consequently, they conclude that extrapolation to zero pressure in hydrogen chemisorption isotherms is the best method for estimating the accessible nickel surface area. This will underestimate the area by an amount which is a function of many factors including catalyst loading and particle size.

Another possible problem with hydrogen chemisorption is that the Ni/H ratio of 1:1 may not hold for very small particles. Ross *et al.* have proposed that some monodispersed Ni atoms may co-exist with more massive nickel particles, giving a 'bimodel' distribution of sizes after reduction of co-precipitated catalysts [138]. The monodispersed atoms are believed to be generated from the nickel aluminate phase mentioned previously, whereas the large nickel particles derive from the NiO phase. This distribution does not appear to occur in catalysts prepared by impregnation methods. As mentioned previously, SMSI effects may influence these monodispersed particles, reducing the hydrogen adsorption ability in a similar manner to SMSI effects in Ni/TiO_2 [139]. An average Ni/H ratio of less than 1:1 would result, tending to lead to an underestimation of the nickel surface area.

3.6.2 N_2O Reaction at Nickel Surfaces.

An attractive alternative to hydrogen chemisorption as a method for metal surface area determination is the reactive decomposition of nitrous oxide to form a surface oxide layer on the metal (M), evolving nitrogen as shown in Reaction 3.01.

$$M + xN_2O \rightarrow MO_x + xN_2 \qquad \text{Reaction 3.01}$$

This method has recently been applied to determine metal surface area in copper catalysts [140]. A reaction temperature of 60°C was used, and one monolayer of copper (I) oxide (Cu_2O) was formed. The quantity of nitrogen evolved was measured and this gave a direct measure of the copper surface area.

The interaction of nitrous oxide with nickel has been studied by Zielinski [141], indicating that the reaction proceeds as,

$$Ni_s + N_2O \rightarrow NiO + N_2 \qquad \text{Reaction 3.02}$$

This equation gives a Ni_s/O ratio of 1:1. Extensive bulk oxidation did not occur until a temperature in excess of 50°C. Similar decomposition was found on both powdered nickel and alumina supported nickel. Reaction proceeds in two stages;

i) fast chemisorption of O on the nickel surface until $Ni_s/O = 1:0.3 \rightarrow 0.4$
ii) slower nucleation and growth of NiO islands until a closed layer is obtained.

How fast this second process is and how fast its rate varies with temperature and pressure is not clear. Experiments described in this thesis are designed to assess the suitability of N_2O decomposition as a tool for nickel surface area measurements.

3.6.3 Nitrous Oxide Decomposition Experimental.

If nitrous oxide decomposition is to be used as a surface technique then the fastest rate of decomposition to a monolayer of oxide should be used, but without onset of bulk oxidation. In order to determine the correct temperature at which to perform the decomposition, a Temperature Programmed Surface Reaction (TPSR) of N_2O over nickel was performed.

Using the apparatus illustrated in Figure 3.26, and described later, 10% N_2O in He flowing at $50cm^3/min$ was passed through a reactor tube containing nickel catalyst. The catalyst had previously been reduced at 600°C for 1hour in 100% H_2 flowing at $100cm^3/min$, and outgassed for 30 minutes in $50cm^3/min$ He at the same temperature. The temperature was increased linearly from -80°C to 300°C in the N_2O/He flow with the eluent gas stream being monitored for evolved N_2 and unreacted N_2O, using the mass spectrometer.

3.6.4 Results

A plot of the N_2 and N_2O concentration as a function of temperature is shown in Figure 3.22 below.

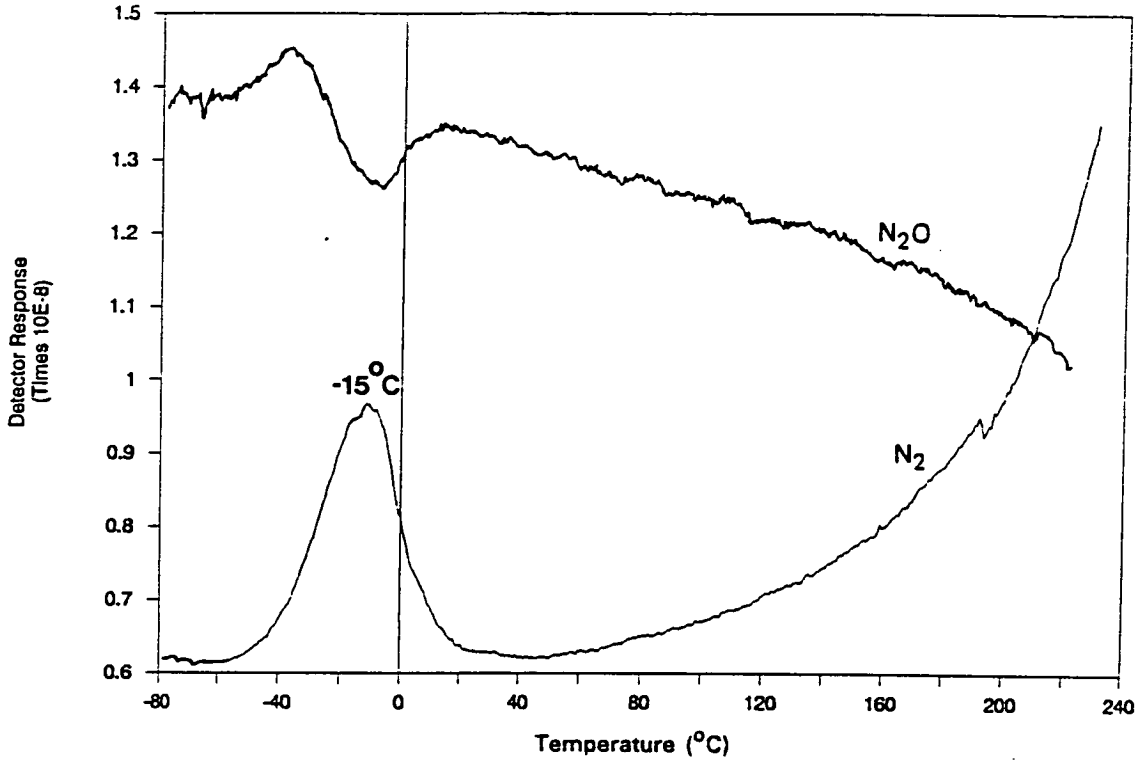

Figure 3.22 *A TPSR spectrum of evolved N_2 and unreacted N_2O after passing through 0.156g of Ni/Al_2O_3 with temperature increasing at 10°C/min.*

No reaction appears to occur until a peak in desorption rate is seen in the N_2 evolution trace at -15°C, falling back down to zero evolution rate again by 20°C. A gradual rise, becoming steeper, then begins at 55°C. Throughout the reaction, changes in N_2 evolution are mirrored in the unreacted N_2O trace above.

3.6.5 Discussion

In view of the work by Zielinski [141], it seems that the gradual rise in the amount of N_2 evolved at a temperature greater than 55°C can be assigned to the onset of bulk oxidation. The peak at -15°C may be assigned to monolayer surface oxidation. Integrating gives a value of 6.44 x 10^{19} N_2 molecules evolved for 0.156g of Ni/Al_2O_3 catalyst. If a 1:1 Ni_s:O ratio is assumed, this would give a nickel surface area of 22.9m^2/g (Reactive Frontal Chemisorption at 50°C on the same sample gave 30.9m^2/g).

The activation energy for surface oxidation (E_a) may be obtained by plotting a ln(rate) *versus* 1/T graph for the leading edge of the -15°C peak in the TPSR

(Figure 3.22). Figure 3.23 illustrates such a graph plotted for rates between -55°C and -35°C.

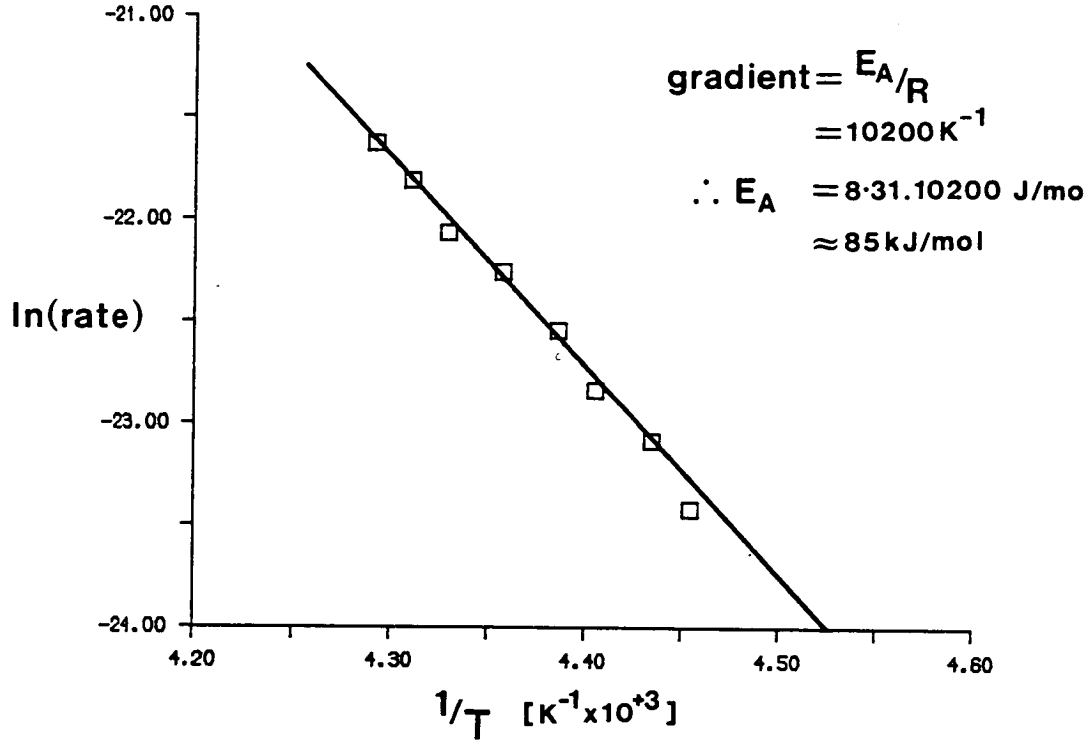

Figure 3.23 *ln(rate) versus 1/T for the -15°C peak in the TPSR spectrum of N_2O over Ni/Al_2O_3.*

A value for E_a of 85 kJ/mol is obtained. If N_2O decomposition is to be used as a measure of surface area, a temperature below the onset of bulk oxidation must be used. This is between -15°C and 55°C. It is also desirable to achieve the fastest rate of surface reaction, so the highest possible temperature must be employed for this. Consequently, 50°C was chosen as the standard reaction temperature. The bulk oxidation rate can be estimated from Figure 3.22. At 60°C this is 2×10^{14} atoms/s, rising to 4×10^{14} atoms/s at 80°C. This would be insignificant over the timescale of a typical Reactive Frontal Chromatography experiment of under 300 seconds.

3.7 Surface Chemisorption and Reaction Techniques.

Three main types of apparatus are commonly employed for surface area measurements by selective chemisorption.

- **Pulsed Flow** [142]

- **Continuous Flow** [143]
- **Static Volume** [144]

In this work both pulsed flow and continuous flow apparatus are investigated, each for hydrogen chemisorption and nitrous oxide decomposition. This gives four estimates of the metal surface area.

3.7.1 Pulsed Experiments for H_2 Chemisorption and N_2O Decomposition.

The pulsed flow apparatus has already been described and is illustrated in Figure 3.7. Gas pulses are injected *via* three way sampling valves (Carle) into the carrier gas stream, usually helium or argon. Hydrogen pulses are prepared by flowing hydrogen through the other side of a sampling valve (valve A in Figure 3.7) and by turning the valve, a $0.2cm^3$ volume at slightly greater than atmospheric pressure is injected into the stream. Turning the valve back releases the volume of carrier gas that will have been trapped, allowing it to be flushed away by the hydrogen flow. In this way, the sample valve is always replenished with hydrogen. Nitrous oxide pulses are prepared from a static volume vacuum line. The sample valve (valve B in Figure 3.7) is first evacuated and then N_2O at 400mbar is expanded into the vacuum. After closing the N_2O line a $0.16cm^3$ pulse of N_2O is injected into the carrier stream by turning valve B. When the sample valve is turned back, it must first be evacuated, to remove the trapped volume of carrier gas, before another pulse can be injected.

The uptake of a pulse of gas is measured either by change in thermal conductivity of gas flowing before and after the catalyst or by mass spectral observation of the eluent gas stream. For hydrogen chemisorption, an argon carrier gas and thermal conductivity measurements were used. For nitrous oxide decomposition, monitoring of the unreacted N_2O (mass 44) peak with a mass spectrometer was used. A typical thermal conductivity trace is shown in Figure 3.24 below.

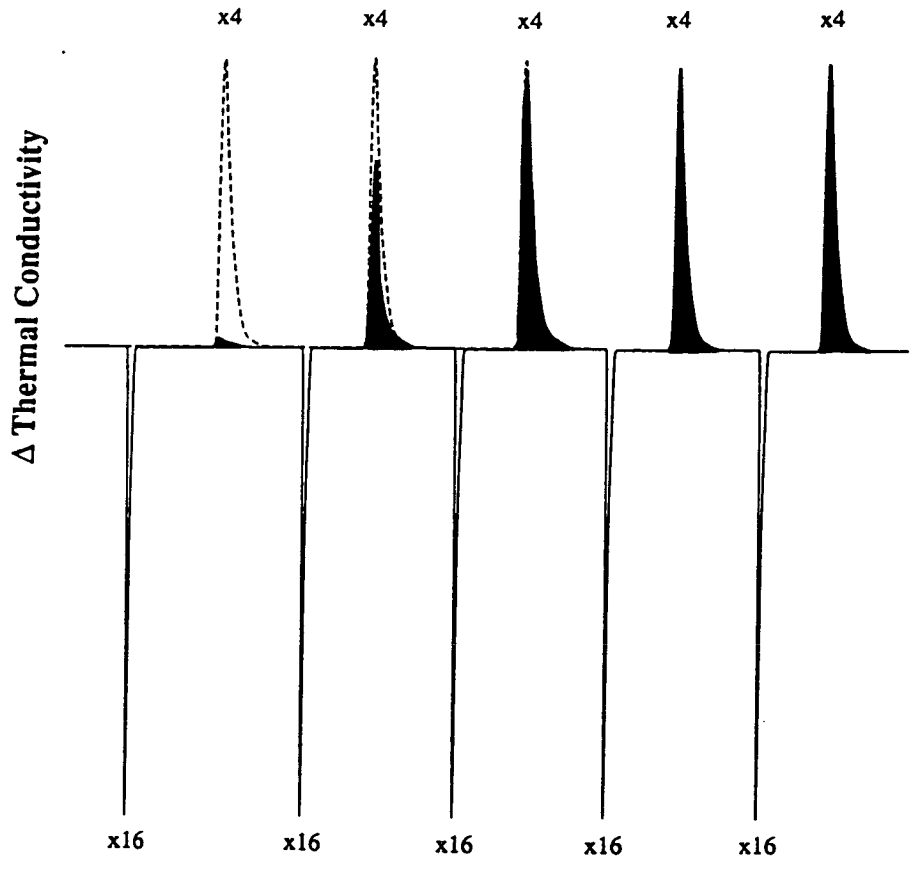

Figure 3.24 *Change in thermal conductivity as pulses of hydrogen are injected into an argon carrier gas and passed over the two sides of the thermal conductivity detector.*

After a pulse has been injected it first passes through one side of the TCD cell giving a negative peak in the diagram. It then passes over the catalyst and subsequently through the other side of the TCD, giving a positive peak. This is modified by the extent of adsorption by the catalyst. In Figure 3.24 the black shaded areas above the line indicate the unadsorbed gas, the dashed line is what the peak would have looked like without being affected by adsorption. Pulses are injected until no more adsorption is observable i.e. the surface is apparently saturated. By integrating the detected peaks the amount of gas adsorbed may be calculated.

For N_2O reaction, since there is a gaseous product in the reaction, namely N_2, monitoring thermal conductivity changes is difficult since N_2 and N_2O have similar thermal conductivity. Using the mass spectrometer to follow either N_2O (mass 44) or N_2 (mass 28) (more difficult because of a large background peak at 28), the extent of reaction of N_2 pulses may be followed in a similar way to δTC measurements. The

amount of N_2O reacting may be quantified by integrating the peaks. Since N_2O pulses are generated from a fixed volume of gas, the size of the pulses decreases slightly during an experiment as gas is drawn away for each pulse. This must be included in calculations of total gas reacting.

Reduced catalyst is generated in an identical manner for all experiments by reduction in 100% H_2 flowing at $20cm^2/min$ at 600°C for 1 hour. Subsequently, the sample was outgassed in flowing helium at $20cm^3/min$ at the same temperature for half an hour, before cooling to the reaction temperature (25°C for H_2 and 50°C for N_2O).

3.7.2 Results.

Table 3.7 below shows the number of molecules of H_2 and N_2O reacting for a given amount of reduced catalyst. Metal surface areas per gram, using an assumed Ni_s:reactant ratio of 1:1 are also shown. The surface density of Ni atoms is taken to be that of Ni(111), 1.8×10^{19} atoms/m^2.

Table 3.7 Summary of Pulsed Experiments.

Sample mass (mg)	Molecules adsorbed	Pulse size (Torr)	Ni area if 1:1 Ni_s:H m^2/g	Sample mass (mg)	Molecules adsorbed	Pulse size (Torr)	Ni area if 1:1 Ni_s:N_2O m^2/g
12.7	3.23×10^{18}	800	28.4	32.1	1.22×10^{19}	390	25.2
50.8	1.24×10^{19}	800	27.3	27.4	1.41×10^{19}	390	26.9
99.1	2.6×10^{19}	800	29.3	50.2	2.7×10^{19}	420	30.1
				27.5	8.3×10^{18}	240	16.9

Hydrogen chemisorption from pulses provides a fairly constant value of nickel surface area, between 27.3 and $29.3m^2/g$. These values seem to be independent of catalyst mass. Nitrous oxide decomposition from pulses provides a variable answer of between 16.9 and $30.1m^2/g$. Pulse size seems to be an important factor, with larger pulses producing more extensive reaction, providing larger values of nickel surface area. Catalyst sample mass seems less important. The effect of different pulse sizes of hydrogen was not investigated.

3.7.3 Continuous Flow Experiments.

H_2 adsorption and N_2O decomposition.

Methods in this category are commonly known as Frontal Chromatographic techniques [119]. For N_2O decomposition this gives Reactive Frontal Chromatography (RFC), and Frontal Chemisorption Chromatography (FCC) for H_2 chemisorption. By switching in a continuous flow of reactive gas and measuring the difference in expected time and actual time of arrival at the detector after passing through the reduced catalyst, a measure of the uptake or amount of gas reacting can be obtained. This process is illustrated in Figure 3.25 below for N_2O decomposition.

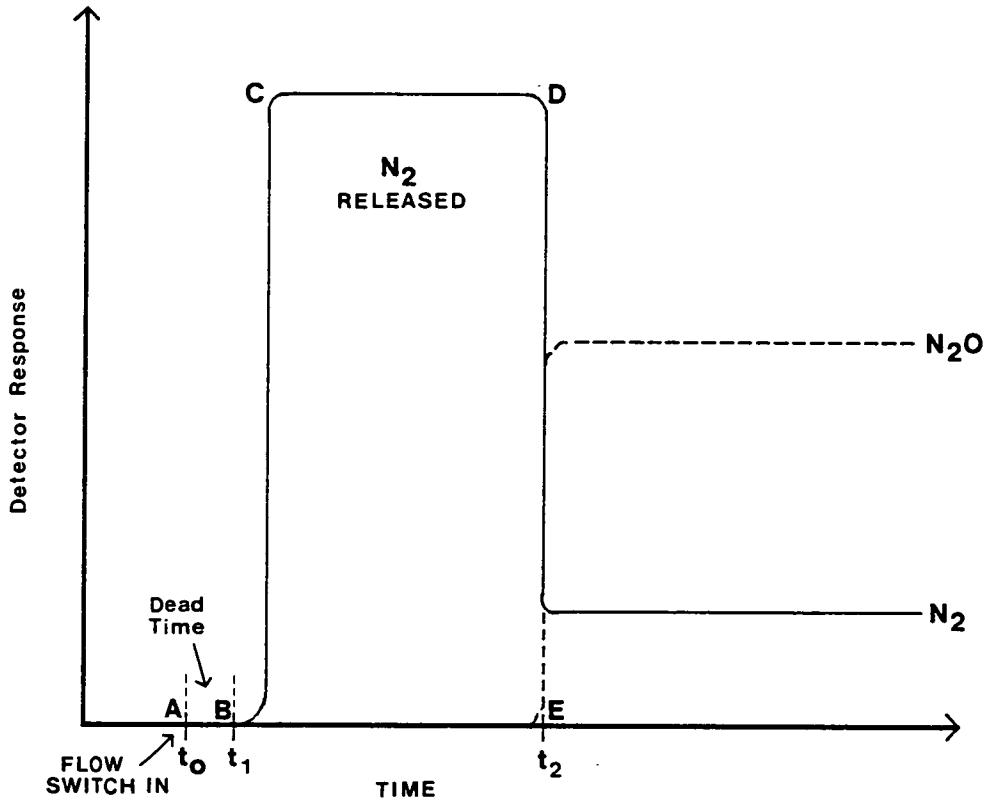

Figure 3.25 *Idealised Reactive Frontal Chromatography of N_2O over a metal surface.*

The reactive stream (10% N_2O in He) is switched in at t_o. The N_2O flows through the catalyst and decomposes over the reduced nickel surface, releasing nitrogen. The evolved nitrogen signal is detected at t_1. t_1-t_o is known as the dead time, the time between switching in gases and detecting them with the mass spectrometer. The nitrogen signal rises to a plateau as all of the N_2O flowing through the catalyst is decomposed to nitrogen. As the surface sites become oxidised, unreacted N_2O breaks through at t_2, indicating the end of surface oxidation. The nitrogen signal drops

simultaneously, stabilising at a level due only to the fragmentation pattern of N_2O. By integrating the area BCDE, the amount of nitrogen evolved can be determined, and consequently the amount of N_2O reacting can be deduced. Knowing the Ni_s:N_2O ratio allows determination of Ni_s, the number of surface nickel atoms.

3.7.4 Experimental.

The apparatus used for the continuous flow experiments is illustrated below in Figure 3.26.

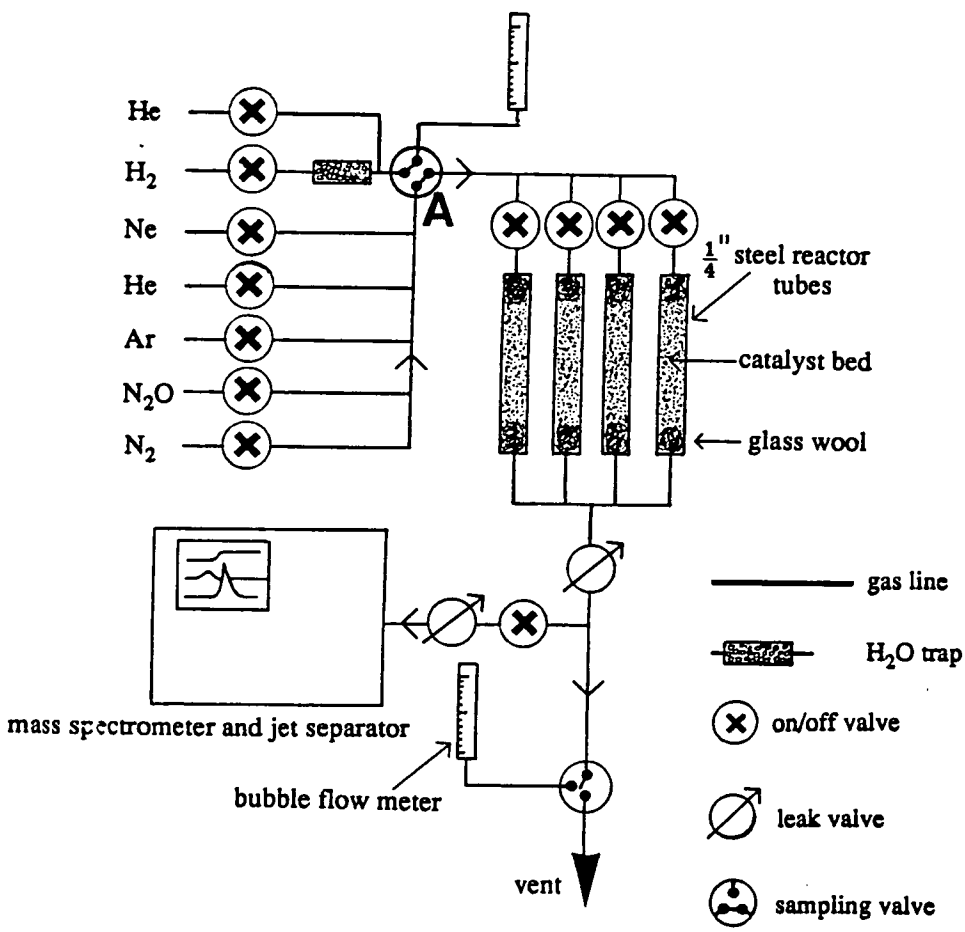

Figure 3.26 *Schematic diagram of flow apparatus (ICI Billingham).*

Gas flows from the left hand side of the diagram, through one of four reactor tubes and to vent. A portion of the output is taken by the mass spectrometer, which is capable of monitoring up to 8 masses simultaneously. Gas mixtures are made on the left hand side, e.g. 10% N_2O in He, be setting appropriate flow rates, before switching

from He to 10% N_2O/He by moving valve A.

3.7.5 Results.

Using the chosen temperature of 50°C, Reactive Frontal Chromatography of N_2O was performed on the Ni/Al_2O_3 catalyst. A typical RFC spectrum is shown in Figure 3.27 below.

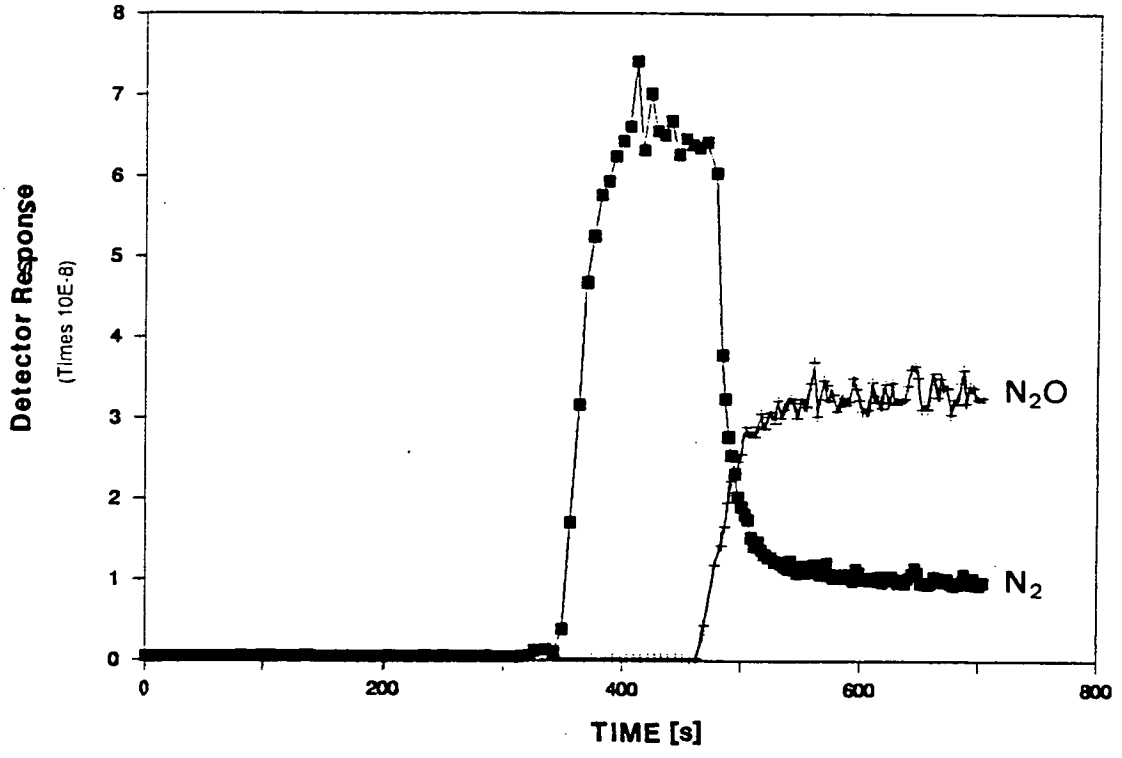

Figure 3.27 *Reactive Frontal Chromatography. N_2O decomposition over 0.324g of reduced Ni/Al_2O_3 at 50°C with 8.5% N_2O in He.*

By running at 50°C, sharp leading and trailing edges of the nitrogen signal are obtained, allowing easy integration. An RFC experiment at 35°C is shown in Figure 3.28 below, illustrating how slowing of the reaction rate at a lower temperature affects the 'plug' flow characteristics.

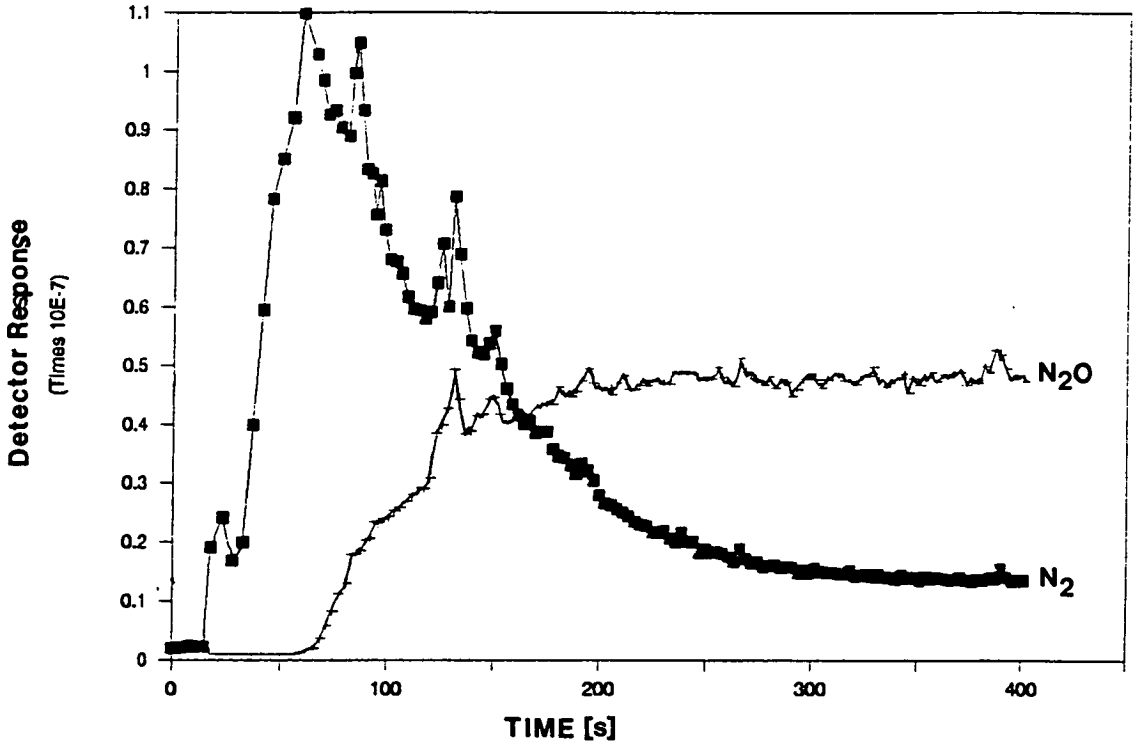

Figure 3.28 *N_2O Reactive Frontal Chromatography at 35°C over Ni/Al_2O_3.*

The trailing edge of the N_2 and breakthrough of the N_2O are not well defined and consequently integration of the N_2 evolved is more difficult. 50°C would seem to be the best temperature at which to perform RFC of N_2O over nickel.

The integrated mass spectrum signal for mass 28 (N_2) (BCDE) between t_1 and t_2 in Figure 3.25 is 1.87 x 10^{20} molecules N_2. Assuming a Ni_s:O ratio of 1:1, for 0.324g of Ni/Al_2O_3, this gives a nickel surface area of 31.9m^2/g.

Frontal Chemisorption Chromatography (FCC) is performed in a similar way to RFC, using a 10% H_2/15% Ne in He mixture switched in at t_o. The neon breaks through at t_1 without interacting with the catalyst. By measuring the difference in time between this and the hydrogen breakthrough at a time t_2, the extent of hydrogen chemisorption can be assessed. A series of FCC experiments with H_2 at 25°C were performed, as were a series of RFC experiments with N_2O at 50°C. The results are illustrated in Table 3.8 below.

Table 3.8 Summary of Frontal Chromatography results.

Frontal Chemisorption Chromatography Hydrogen (25°C)				Reactive Frontal Chromatography Nitrous Oxide (50°C)			
% H_2 in He	Catalyst Mass (g)	H_2 used (cm^3)	Ni Area if 1:1 Ni_s:H (m^2/g)	% N_2O in He	Catalyst Mass (g)	N_2O used (cm^3)	Ni Area if 1:1 Ni_s:N_2O (m^2/g)
9.5	0.318	5.11	45.6	8.5	0.324	7.97	31.9
9.5	0.209	3.06	41.7	8.5	0.171	4.21	31.8
21.1	0.250	3.73	42.5	5.1	0.250	4.45	23.1
				17.9	0.248	8.85	45.6

As before, the nickel surface area is calculated assuming a nickel surface atom : adsorbed atom ratio of 1:1 and using the surface density of 1.8×10^{19} atoms/cm^2 for Ni(111).

Hydrogen chemisorption chromatography produces results of between 41.7 and 45.6m^2/g. Catalyst mass may have a slight effect. The %H_2 in the helium stream, which is proportional to the partial pressure of H_2 applied to the sample, does not seem to have a significant effect on nickel surface area measurements.

Nitrous oxide decomposition *via* RFC provides variable answers to the nickel surface area, between 23.1 and 45.6m^2/g. The applied pressure of N_2O and the %N_2O in the helium stream, seems to affect results with higher partial pressures of N_2O, providing higher nickel surface area measurements. Variation of the catalyst mass does not affect the decomposition of N_2O and subsequent nickel surface areas obtained.

Heat generated during the exothermic reaction will cause the temperature of the sample to rise during the reaction if there is insufficient heat conduction away from the catalyst. The temperature of the catalyst bed was monitored during the 50°C RFC experiment shown in Figure 3.27 and is illustrated in Figure 3.29 below.

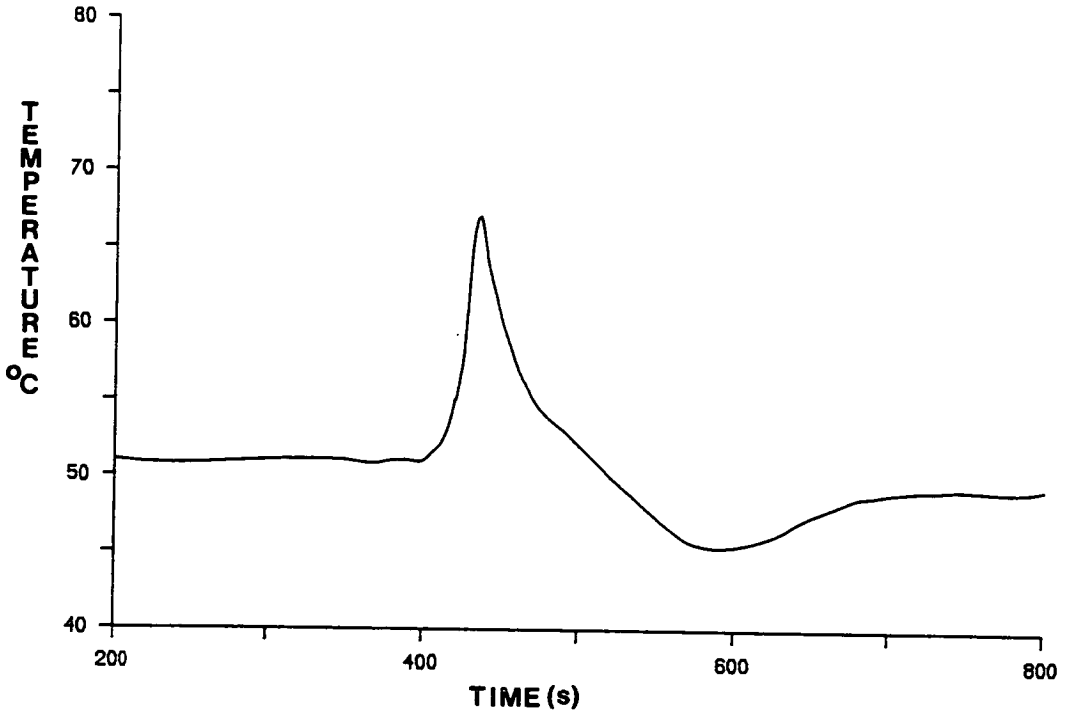

Figure 3.29 *Temperature during RFC experiment of N_2O decomposition over Ni/Al_2O_3 shown in Figure 3.27.*

Evidently there is insufficient heat conduction away from the sample in this experiment as the temperature rises to 67°C during the course of the reaction. This has unfortunate consequences for the calibration of RFC experiments. With reference to the TPSR of N_2O over Ni/Al_2O_3 (Figure 3.22), raising the temperature above 50°C will lead to some bulk oxidation of the nickel. Although this will be at a low level, 3-4 x 10^{14} atoms/s, the extent of it may be difficult to assess. If the temperature is above 50°C for 100s, this will mean 3-4 x 10^{16} bulk nickel atoms oxidised in this time. The measured number of N_2 molecules evolved during this RFC is 1.87 x 10^{20}. Therefore only 0.03% of this may be due to bulk oxidation caused by temperature rise during the reaction, and can be neglected.

3.8 Calibration of Ni_s:N_2O Ratio During RFC.

In the preceding text two assumptions have been made. Firstly the ratio of nickel surface atoms to reacting nitrous oxide molecules is 1:1. Secondly, it was stated that the reaction proceeds to a complete monolayer of oxide and then no further oxidation occurs. The validity of these assumptions can be assessed as follows:

3.8.1 Surface nickel:N_2O ratio.

Attempts to calibrate the Ni_s:N_2O ratio were performed by using a nickel sample of known surface area for reactive frontal chromatography. One of the most accurate methods for total surface area determination is the physical adsorption of nitrogen at -196°C applying the BET method (this is discussed later in this chapter). The total surface area is measured, not just the metal metal area.

Several experiments were performed on physical mixtures of NiO/α-Al_2O_3. The α-Al_2O_3 had a known surface area of 0.44m^2/g and was necessary to prevent tube blockage on reduction of the nickel NiO powder. After reduction, an RFC experiment at 50°C was performed to determine the nickel surface area, and the sample cooled rapidly to -196°C. Frontal Uptake of N_2 (see later) was then used to determine the total surface area of the Ni/α-Al_2O_3. Knowing the surface area of the α-Al_2O_3, the nickel surface area was determined. Therefore the Ni_s:N_2O ratio could be evaluated.

The results of several experiments are shown below in Table 3.9.

Table 3.9 N_2O calibration results.

Mass NiO (g)	Mass α-Al_2O_3 (g)	%N_2O in He	Flow rate N_2O (cm^3/min)	N_2O:Ni_s ratio
1.207	2.444	5.3	45	1.09
1.207	2.444	5.3	42	0.92
1.207	2.444	7.7	38	0.61
1.234	2.099	5.7	40.5	0.51
1.997	0	5.4	36.5	0.49

Accurate determination of such small surface areas is very difficult, so the large spread of Ni_s:N_2O ratios is not surprising. BET areas are subject to an error of at least $\pm 0.5m^2$.

3.8.2 How Deep is the Oxidation?

The extent of oxidation may be assessed by integrating the area under TPR profiles produced by reducing the samples oxidised by N_2O decomposition. If the nickel surface area is known, the depth of oxidation may be determined from the amount of NiO reduced in the TPR.

Several TPRs were performed, each one indicating that all of the N_2O decomposed had formed NiO, with T_m at 170°C. There was good agreement between the number of N_2O molecules consumed in RFC experiments and the amount of NiO re-reduced in the TPRs. However unless the true surface area is known, the depth of oxidation cannot be assessed.

3.8.3 Discussion.

Some caution needs to be used is discussing the significance of the calibration experiments. The BET areas are not very accurate, although some general conclusions can be drawn. Only one result provided an answer significantly greater than 1 N_2O molecule per Ni surface atom (1.09), possibly indicating the onset of bulk oxidation. The rest of the results were between 0.49 and 0.91 N_2O:Ni_s, indicating that less than one monolayer of NiO has been formed. It is likely that under the conditions of 30→40cm^3/min flow rate and 5→10% N_2O in He mixtures, that only a full monolayer or less will form. As the flow rate and % N_2O are increased, larger N_2O:Ni_s ratios occur, tending to indicate that bulk oxidation is dependent on the flow rate of N_2O. This may be explained by assuming that reaction is rapid up to a point, and then becomes more of a function of the N_2O space velocity. This ties in with the work of Zielinski [141] who found fast chemisorption up to Ni_s:O ratios of 1:0.3→0.4. Thereafter slower nucleation of NiO islands occurred. Increasing the % N_2O in the carrier gas, and the flow rate of the gas will both increase the collision rate of N_2O with the surface. Larger N_2O pulse sizes in the pulsed experiment have a similar effect.

Since the experimental conditions used in both pulsed and continuous flow techniques seem to produce less than a monolayer of NiO, then both will tend to produce an underestimate of the nickel surface area. The exact N_2O:Ni_s ratio seems variable, although between 0.5 and 1 for the conditions used here. The previous values of nickel surface area shown in Tables 3.7 and 3.8 are likely to be too small.

As far as hydrogen chemisorption is concerned, the two methods used, namely

pulsed chemisorption and frontal chemisorption chromatography, clearly produce different results. H_2 pulsed chemisorption is independent of catalyst mass, giving results of between 27.3 and 29.3 m^2/g. H_2 FCC is also independent of catalyst mass and flow rate but produces values of between 41.7 and 45.6m^2/g. The difference may be assigned to the difference in contact time of the hydrogen with the Ni/Al_2O_3 sample. Contact time is greater during FCC, of the order of minutes with a partial pressure of hydrogen over the sample, compared to pulse widths of the order of seconds with the pulsed chemisorption technique.

An explanation of this enhanced hydrogen adsorption may be that the 'reversibly' adsorbed hydrogen discussed previously by several authors e.g. [137], could be adsorbed during H_2 FCC but not during the pulsed chemisorption experiment. The exact nature of this reversible adsorption is not known, although Cale and Richardson [137] propose hydrogen diffusion onto inaccessible Ni/Al interfaces in order to explain enhanced adsorption. An alternative explanation, as discussed in the next section (Temperature Programmed Desorption), is that enhanced adsorption may be due to spillover of hydrogen molecules onto the alumina support *via* the nickel surface. Experimental conditions used for H_2 FCC , with a long hydrogen contact time, will tend to enhance spillover relative to the amount in pulsed chemisorption experiments, if spillover is a slow process. Enhanced adsorption occurs because the hydrogen that diffuses onto the support is replaced by more hydrogen from the gas phase. This explanation, when discussed in conjunction with TPD results (next section) seems most persuasive.

3.9 Hydrogen Desorption and Re-adsorption.

Hydrogen Temperature Programmed Desorption (TPD) from the Ni/Al_2O_3 was studied in two systems. Using TCD measurements (apparatus in Figure 3.7), TPD between 25°C and 450°C was examined after H_2 pulsed chemisorption. H_2 TPD was also followed by mass spectrometry (apparatus in Figure 3.26) from -190°C up to 600°C after Frontal Chemisorption Chromatography of H_2 and cooling to -190°C. Traces from the two experiments are shown below in Figures 3.30 and 3.31 respectively.

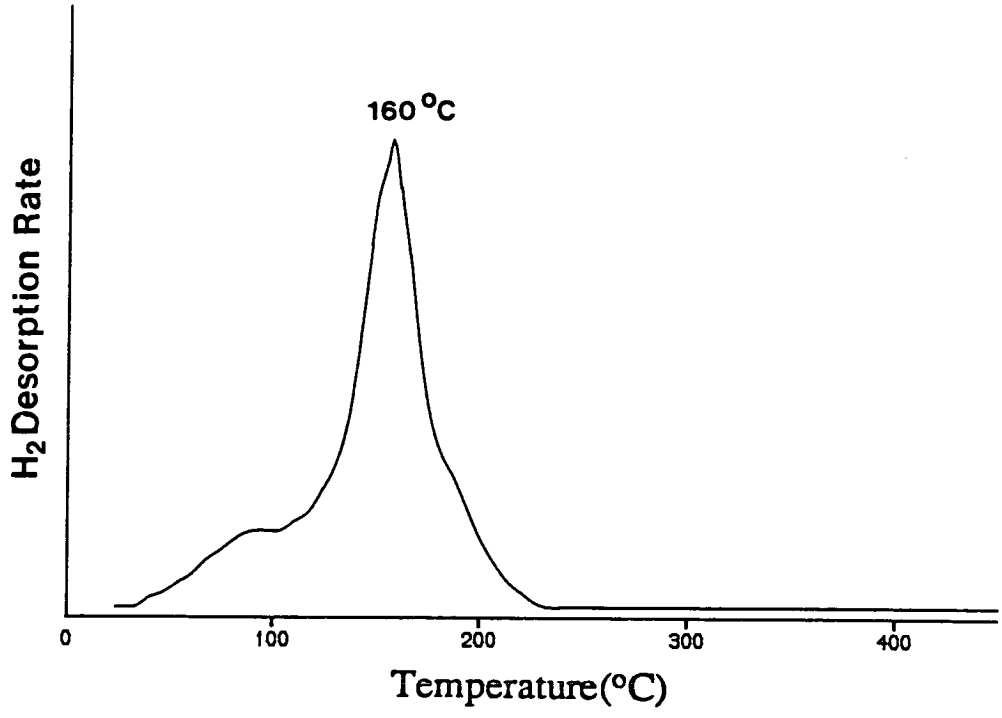

Figure 3.30 *TPD of H_2 into argon from Ni/Al_2O_3 after pulsed chemisorption with 32.8mg catalyst, 40°C/min heating rate and 20cm^3/min Ar flow rate.*

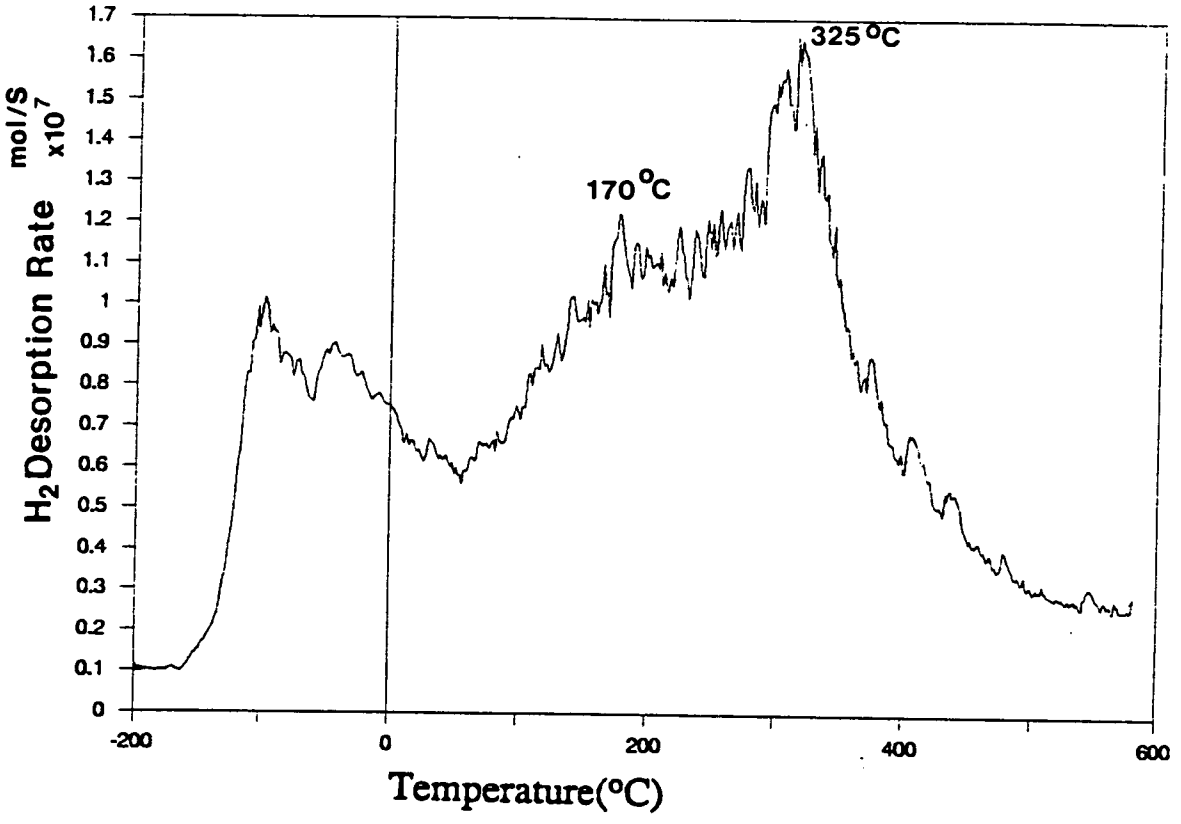

Figure 3.31 *TPD of H_2 into He from Ni/Al_2O_3 after frontal chemisorption chromatography with 0.258g catalyst, 20°C/min heating rate and 50cm^3/min He flow rate.*

It is immediately obvious that the two traces differ considerably. Figure 3.30 shows one desorption peak at 160°C whilst Figure 3.31 has several peaks, at -100, -50, 170 and 325°C. The difference in traces may be assigned to the pre-treatment.

The results shown in Figure 3.30 were obtained from hydrogen pulsed on in small amounts at 25°C, covering only the metal. In the TPD, this simple chemisorbed hydrogen desorbed at 160°C. Integrating the area underneath this peak indicates that 94% of the original amount adsorbed comes of during TPD. This is in excellent agreement with the work of Lee and Schwarz [145]. They found a single desorption maximum at 170°C for hydrogen coverage approaching saturation after pulsed chemisorption. Desorption was found to follow second order kinetics, involving the recombination of two surface hydrogen atoms.

The results in Figure 3.31 were obtained for hydrogen adsorbed by flowing through the catalyst during FCC and then subsequently cooling the sample to -190°C in hydrogen. Considerably more opportunity for hydrogen adsorption thus existed.

Integration of this TPD profile reveals that 164% of the hydrogen that would have been expected from pulsed chemisorption had desorbed. This 'extra' hydrogen may be associated with the support, as has been previously noted. It is clear that hydrogen exists in several more surface forms when the Ni/Al_2O_3 is cooled to -190°C compared to the surface species produced from pulsed chemisorption at room temperature. The -100°C peak shows evidence of a very weakly adsorbed hydrogen species.

3.9.1 Hydrogen Re-Adsorption.

When a reduced catalyst at 600°C is cooled in the reducing 5% H_2 in Ar, hydrogen adsorption onto the cooling sample can be monitored by changes in thermal conductivity. Figure 3.32 illustrates such a 're-adsorption' of hydrogen onto 27.6mg of Ni/Al_2O_3 after reduction in 5% H_2 in Ar at 600°C for 1 hour. The linear cooling rate is achieved with the Stanton Redcroft temperature programmer shown in Figure 3.7, provided external cooling air is blown over the furnace.

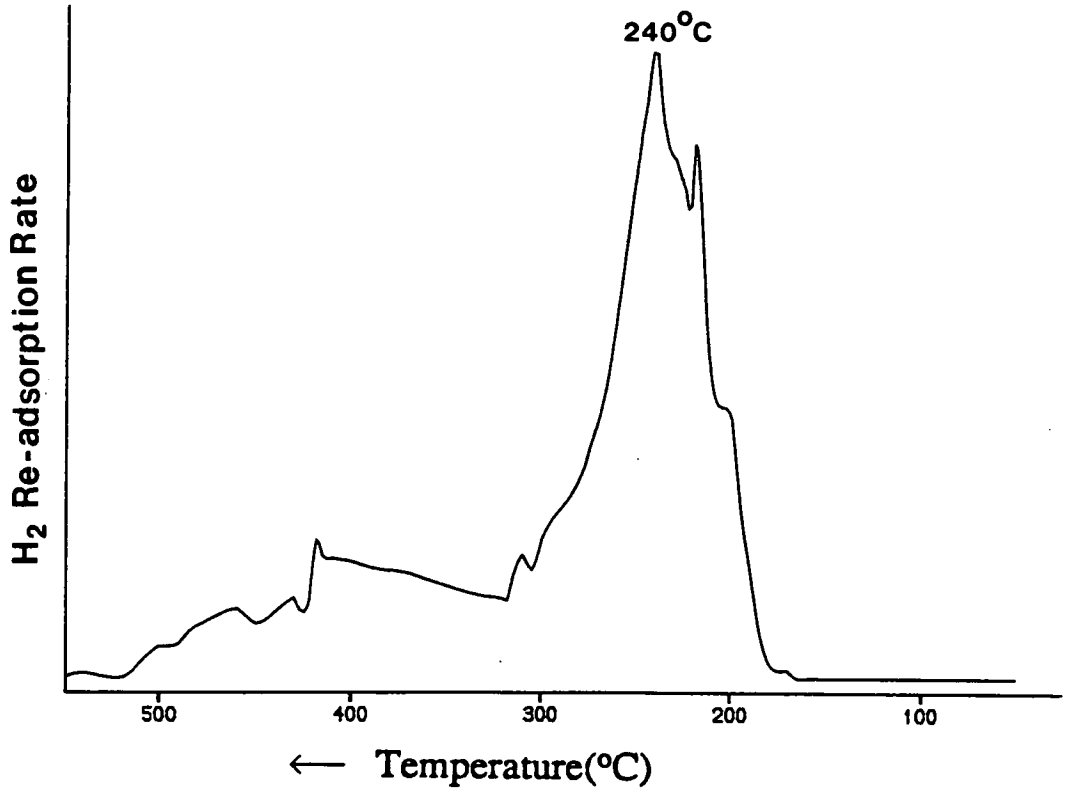

Figure 3.32 *Hydrogen re-adsorption onto Ni/Al_2O_3 whilst cooling at 30°C/min with 27.6mg of sample in a flow of 20 cm^3/min 5%H_2 in Ar.*

One peak at 240°C is apparent in the re-adsorption trace, with a lower feature at

220°C. A broad, weak feature can be seen at 400°C. Integration of this peak gives 152% of the quantity of adsorbed hydrogen of what would be expected from pulsed chemisorption.

3.9.2 Discussion.

Evidence of enhanced hydrogen adsorption under some circumstances comes from three sources. Firstly, larger than expected nickel surface area measurements. Secondly, additional peaks in desorption spectra after adsorption of hydrogen by cooling to -190°C, and subsequent integration of the peaks to reveal 164% adsorption. Finally, by cooling in hydrogen, the re-adsorption reveals 152% adsorption of what would have been expected from a nickel surface area determined by both pulsed hydrogen chemisorption and nitrous oxide decomposition.

Phenomena of this type are generally assigned to 'spillover'. Here hydrogen is considered to diffuse onto the support of the catalyst *via* the metal surface. An extensive review of the spillover process has been published recently [146]. It is tempting to postulate that when the catalyst is cooled in hydrogen or when frontal chemisorption chromatography is applied, the high partial pressure of hydrogen above the sample and relatively long contact time provide conditions suitable for hydrogen to be transferred onto the alumina support of the Ni/Al_2O_3. In subsequent TPD experiments, hydrogen may transfer back to the metal to desorb, and may explain the high temperature (325°C) peak in Figure 3.31. Whether this high temperature peak is present because desorption of spillover hydrogen is not activated until this temperature, or whether it is simply kinetically limited and would appear at a lower temperature if a slower heating rate was employed cannot be answered here.

If spillover is an activated process with an energy barrier, then cooling from high temperature would enhance the amount of hydrogen spilling over onto the support, compared to the amount of spillover at room temperature, where the rate would be relatively lower. This may explain the enhanced re-adsorption of hydrogen (Figure 3.31). Although the rate may be lower at room temperature, it may be enhanced with increased hydrogen partial pressure and hydrogen contact time, explaining the larger values obtained for surface area with H_2 FCC.

3.9.3 Conclusions.

In conclusion, it is likely that the true nickel surface area of the Ni/Al_2O_3 lies between the underestimation of the H_2 pulsed chemisorption and N_2O techniques, and the probable overestimation of the hydrogen frontal chemisorption chromatography technique. Numerically, this makes the nickel surface area between $28m^2/g$ and $45m^2/g$.

3.10 Metal Particle Size Analysis by Direct Methods.

3.10.1 X-Ray Diffraction.

As the size of a crystal decreases, lines in XRD patterns become broader. By measuring the extent of broadening of line widths, a direct measurement of the average crystallite size of the sample may be obtained. A quantitative measurement of the broadening is given by the Scherrer equation [147], Equation 3.02 below.

$$d = \frac{K\lambda}{B\cos\theta} \qquad \text{Equation 3.02}$$

where d is the average crystallite diameter (nm).
K is a constant, 57 for spherical particles.
λ is the X-ray wavelength (0.1542nm here).
θ is the diffraction angle of a line in the XRD pattern.
B is the width of this line at half maximum intensity.

As particles become very small, the line broadening becomes so great that it becomes impossible to characterise accurately. In practice this occurs for crystallites less than 2nm in diameter, and consequently, line broadening may not be used for particles in this regime. Another important point is that the size of crystals is determined, which is not necessarily the particle size. A metal particle may contain several different crystals in variable orientations.

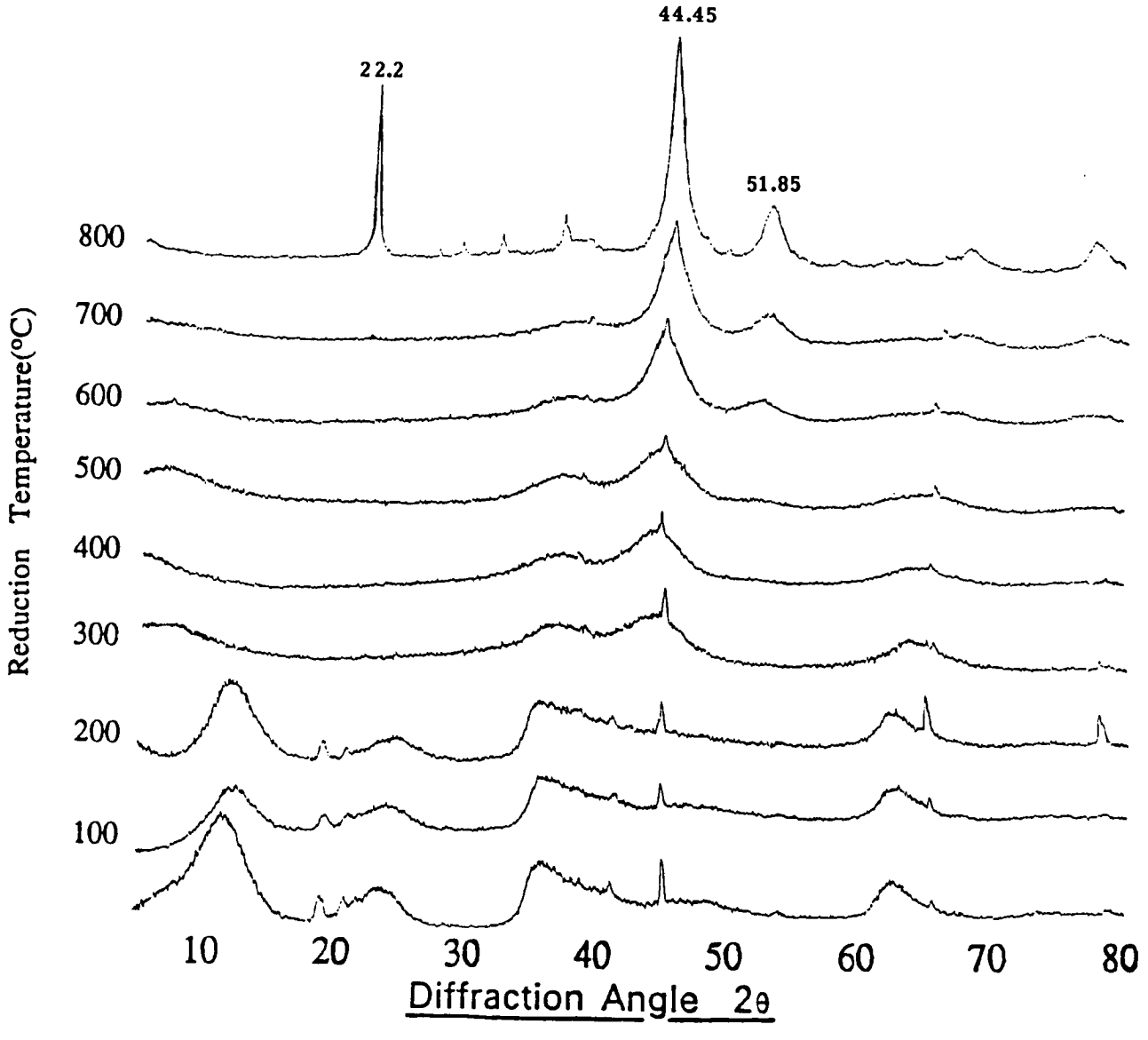

Figure 3.33 *XRD patterns from Ni/Al_2O_3 reduced at a series of temperatures between 25 and 800°C.*

3.10.2 Experimental.

A series of as-prepared catalysts were reduced at temperatures between 25°C and 800°C in 100% H_2 for 1 hour. An XRD pattern was obtained for each sample, and are illustrated in Figure 3.33 above.

The main nickel peaks appear at 2θ values of 44.45° and 51.85°. These nickel peaks appear only significantly at temperatures of 600°C and above, when the catalyst is totally reduced. Applying the Scherrer equation (Equation 3.02) gives the following values of average crystallite diameter,d_{XRD}, listed in Table 3.10 below.

Table 3.10 Nickel crystallite diameter.

	2θ = 44.45°			**2θ = 51.85°**		
	Reduction Temperature			Reduction Temperature		
	600°C	700°C	800°C	600°C	700°C	800°C
Average Nickel Crystallite Size (d_{XRD}) (nm)	4.2	4.5	8.4	4.1	4.4	6.8

The peak at 2θ=22.2° and the smaller peaks at higher values that appear after reduction at 800°C are due to a crystalline alumina phase, probably δ-Al_2O_3 formed from the amorphous γ-Al_2O_3 phase.

3.10.3 Transmission Electron Microscopy.

Transmission Electron Microscopy (TEM) allows a direct image of metal particle sizes, and from this a particle size distribution may be calculated. Only a very small amount of material is examined at any one time and therefore may not be truly representative of the bulk sample. For this reason, as with all techniques for particle size analysis, TEM should not be used in isolation, but as part of a broad approach to solving this problem.

3.10.4 Experimental.

Catalyst samples for TEM were mixed with methanol and 'sonicated' for 1 minute in order to generate a fine liquid suspension. Samples were supported in the microscope by 'Formvar' coated copper grids, stabilised with an additional carbon coating, with drops of the methanol/catalyst suspension being placed onto the prepared grids. A JEOL 100s Transmission Electron Microscope was used for imaging, usually with an accelerating voltage of 100kV and a beam current of 60μA. Images were photographed with a magnification of 100,000 X, with a resolution of better than 3nm. Only bright field images were used. A typical micrograph of a sample, reduced at 600°C in 100% H_2, is shown in Plate 3.1 below.

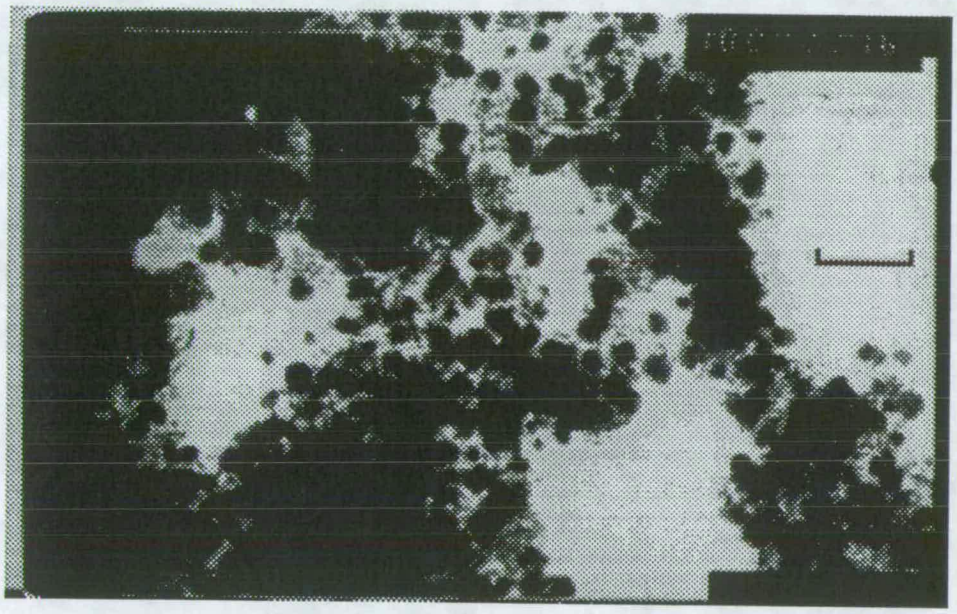

Plate 3.1 *Electron micrograph of reduced Ni/Al_2O_3 at 100,000 X magnification. The scale, as indicated by the 10mm scale bar, is 1mm to 10nm.*

The dark areas of the image correspond to the metallic nickel phase. The lighter, more diffuse areas are the alumina support. A nickel particle size distribution can be produced by simply measuring the micrographs, appropriately enlarged. A size distribution based on measurement of 100 particles is shown below in Figure 3.34.

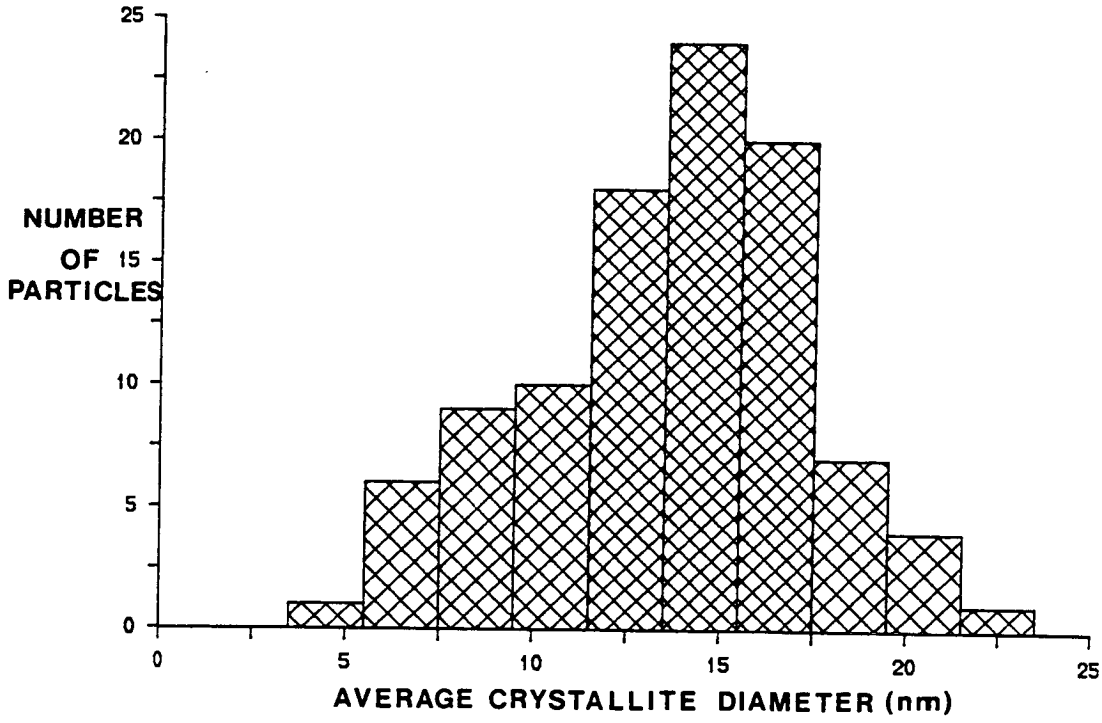

Figure 3.34 *Distribution of nickel particle size in 100 crystallites.*

Weighted averages can be obtained using Equation 3.03 below

$$d_{TEM} = \frac{N_i\, d_i^{n}}{N_i\, d_i^{n-1}} \qquad \text{Equation 3.03}$$

where N_i is the number of particles with diameter d_i.
if n=1 → arithmetic average.
n=3 → surface average.
n=4 → volume average.

This gives an arithmetic average of d_{TEM} = 13.6nm. Surface and volume averages are 15.4 and 16.1nm respectively.

3.10.5 Discussion.

For the catalyst reduced at 600°C, the XRD results give an average crystallite size (d_{XRD}) of 4.1-4.2nm diameter. TEM results show the arithmetic average of nickel particle diameter to be 13.6nm. Both techniques cannot be used in isolation as each

has qualifying restrictions. For XRD, small particles <2nm in diameter may not be detected. Also, the size of the metal crystals is measured and this may not be the particle size. There is evidence that nickel particles are paracrystalline i.e. consist of a series of randomly oriented crystals, with the lattice of nickel crystallites disrupted by defects consisting of Al^{3+} groups [115]. This would give an artificially low value of the average nickel particle diameter, and may explain the value of 4nm obtained with XRD.

Results from TEM micrographs are assessed on observation of only a few hundred particles out of the order of 10^{20}/g in the whole sample. It is impossible to say whether the few particles under observation are representative of the sample as a whole. Again, small particles, below the resolution of the microscope (better than 3nm), will not be observed. This may mean that average particle diameter is an overestimate.

With these restrictions in mind, several conclusions can be drawn. Knowing the reduced sample under observation has a nickel content of 50%, the average crystallite sizes, d_{TEM} and d_{XRD}, can be used to work out the average surface area per nickel particle, assuming spherical particles. The average mass of these particles may be assessed (ρNi = 8902 kg/m^3), and the average number of particles determined. From this, the nickel surface area may be obtained. The results are shown in Table 3.11 below.

Table 3.11 Nickel surface areas from XRD and TEM.

Size (nm)	Surface Area (m^3 x10^{18})	Volume (nm^3 x10^{26})	Mass (kg x10^{22})	Particles in 1kg (x10^{-19})	Nickel Area (m^2/g)
d_{XRD} = 4.2	55.4	3.88	3.45	144.8	80.2
d_{TEM} = 13.6	581.1	131.7	117.2	4.26	24.8

Hydrogen chemisorption results give a value of nickel surface area of 28m^2/g. The average particle size giving this surface area may be determined by solving Equations 3.04 and 3.05 below for 1g of Ni/Al_2O_3, obtaining a value of d_H.

Nickel Area ≡ no. of Ni particles x surface area of particle. Equation 3.04

$$28 = N.4.\pi.r^2$$

Mass of Ni ≡ no. of Ni particles x density x volume of particle. Equation 3.05

$$0.5 = N.\rho.4/3.\pi.r^3$$

Solving these gives r≈6nm, and therefore d_H≈12nm. Evidently the d_{TEM} and d_H provide similar answers. d_{TEM} may be slightly larger as the small particles may not have been included in the arithmetic average for size distribution. d_{XRD} values are much smaller than this at 4nm and provide evidence for the paracrystallinity of nickel particles. As discussed previously, a small quantity of Al^{3+} ions is present in the Ni(0) phase, disrupting the crystalline structure.

Dispersion (%D) is often used as an alternative indication of particle size and metal surface area. It is defined as the number of surface atoms of a particle/the total number of atoms in the particle. The assumption is made that all of the nickel is reduced and that the particles are spherical. The results for TEM and hydrogen chemisorption are D_{TEM}=10.9% and D_H=12.4% respectively.

3.11 Total Surface Area Measurement.

Physical adsorption of nitrogen at -196°C *via* the BET (Brunauer, Emmett and Teller) technique [148] has been adopted as the IUPAC standard procedure for determining the total surface area of finely divided solids [149]. A single layer of adsorbed nitrogen covers the entire surface, both external and internal pore surface under these conditions. The volume of this adsorbed layer can be determined with a series of applied pressure of N_2 *versus* volume measurements, which are then linearised with the BET equation, Equation 3.06 below.

$$\frac{P}{V(P_0-P)} = \frac{1}{V_m C} + \left(\frac{C-1}{V_m C}\right)\frac{P}{P_0} \qquad \text{Equation 3.06}$$

where P is the applied pressure of N_2.
P_o is the saturated vapour pressure of N_2 at -196°C.
V is the volume above the sample.
V_m is the volume of an adsorbed monolayer.
C is a constant.

From V_m, the total surface area of the solid may be determined assuming that each N_2 molecule occupies the same cross-sectional area as it does in liquid nitrogen ($1.62 \times 10^{-19} m^2$). The apparatus used for the BET measurements is illustrated in Figure 3.35 below.

After evacuation at 200°C to remove any interstitial gas, a fixed volume of nitrogen is let into the line. The volume of the line is altered in several steps by forcing mercury into the calibrated volumes. A series of applied pressure *versus* volume readings are obtained, and are linearised by plotting with the BET equation. Figure 3.36 below illustrates two linearised plots produced from two samples before reduction A) as-prepared and C) calcined Ni/Al_2O_3. Surface areas are designated BET_{sv} (static volume).

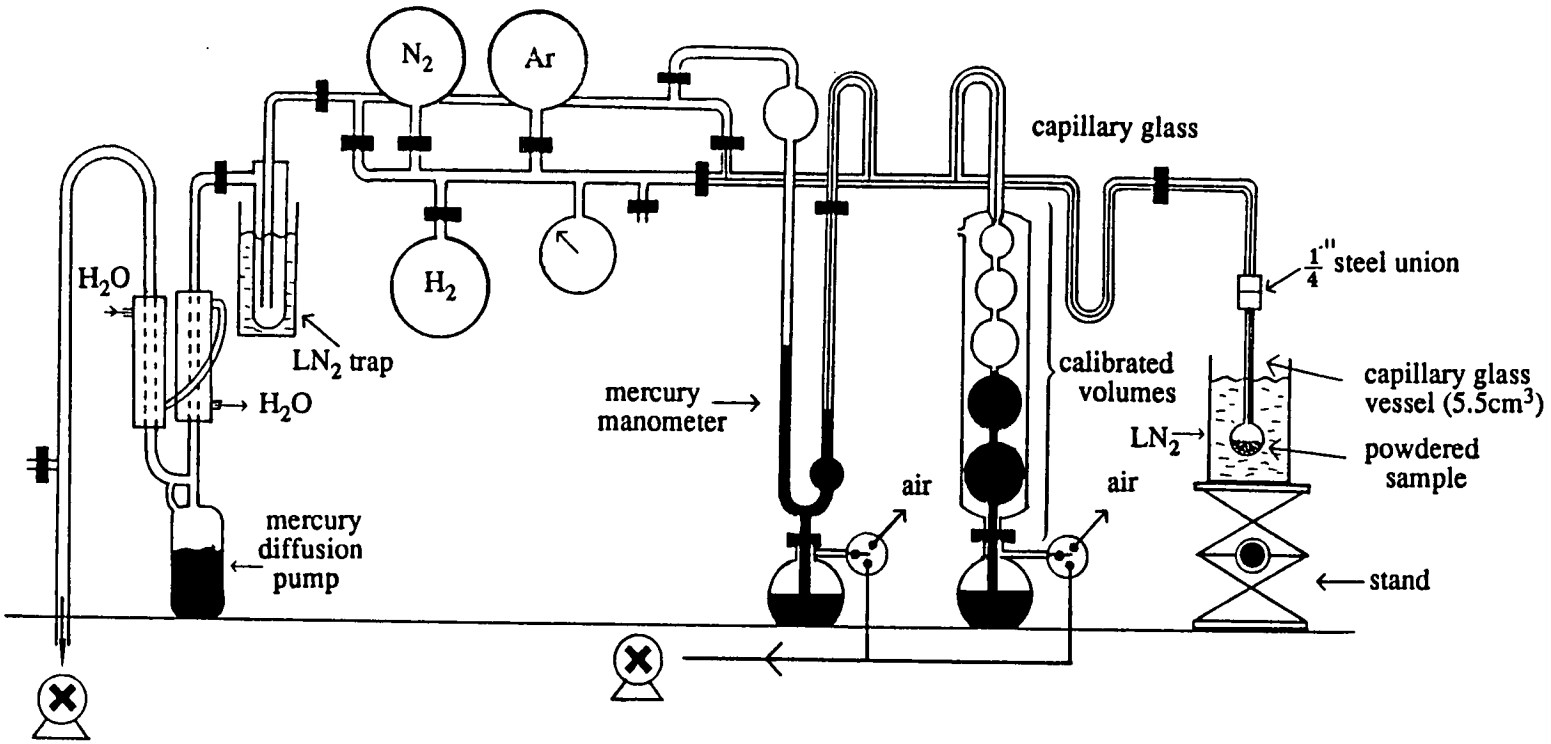

Figure 3.35 *Schematic diagram of apparatus used for evaluation of surface areas using the BET static volume method. The powdered sample is placed in the capillary glass vessel on the right hand side of the diagram.*

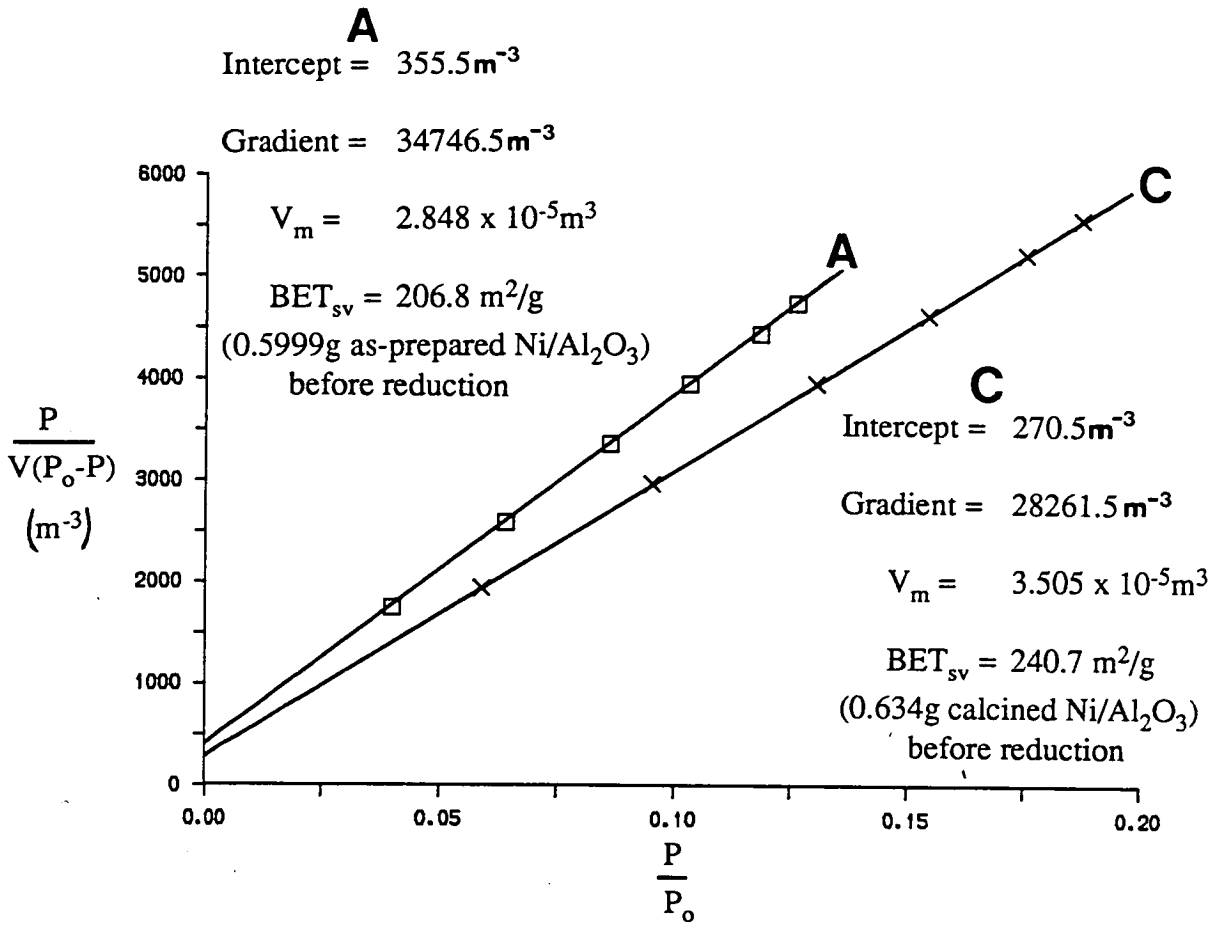

Figure 3.36 *BET plots of data for A) as-prepared and* C) *calcined* Ni/Al_2O_3.

An alternative method for total surface area determination is *via* the Frontal Chromatography Technique [119], [150] in a similar way to the reactive chromatography already discussed. Figure 3.37 below illustrates the process.

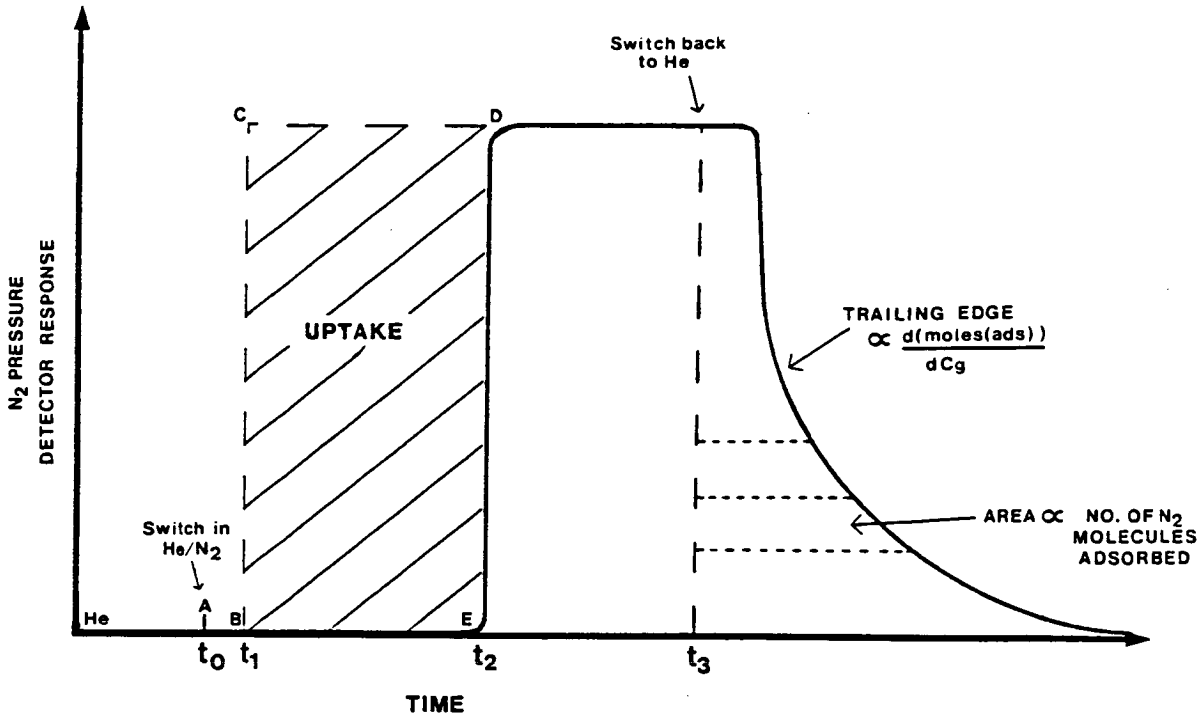

Figure 3.37 *Determination of the total surface area by frontal chromatography of nitrogen at -196°C.*

The sample is cooled to -196°C in a He carrier gas. At time t_o a 10% N_2/10% Ne in He stream is switched in. Ne breaks through at time t_1, leaving the nitrogen to be adsorbed. When a complete monolayer has been formed, nitrogen breaks through at time t_2. By integrating area BCDE, (t_2-t_1) x height, the total nitrogen 'frontal' uptake can be determined and therefore the surface area of the solid can be deduced. A trace of such an experiment, following only the nitrogen trace in shown in Figure 3.38 below.

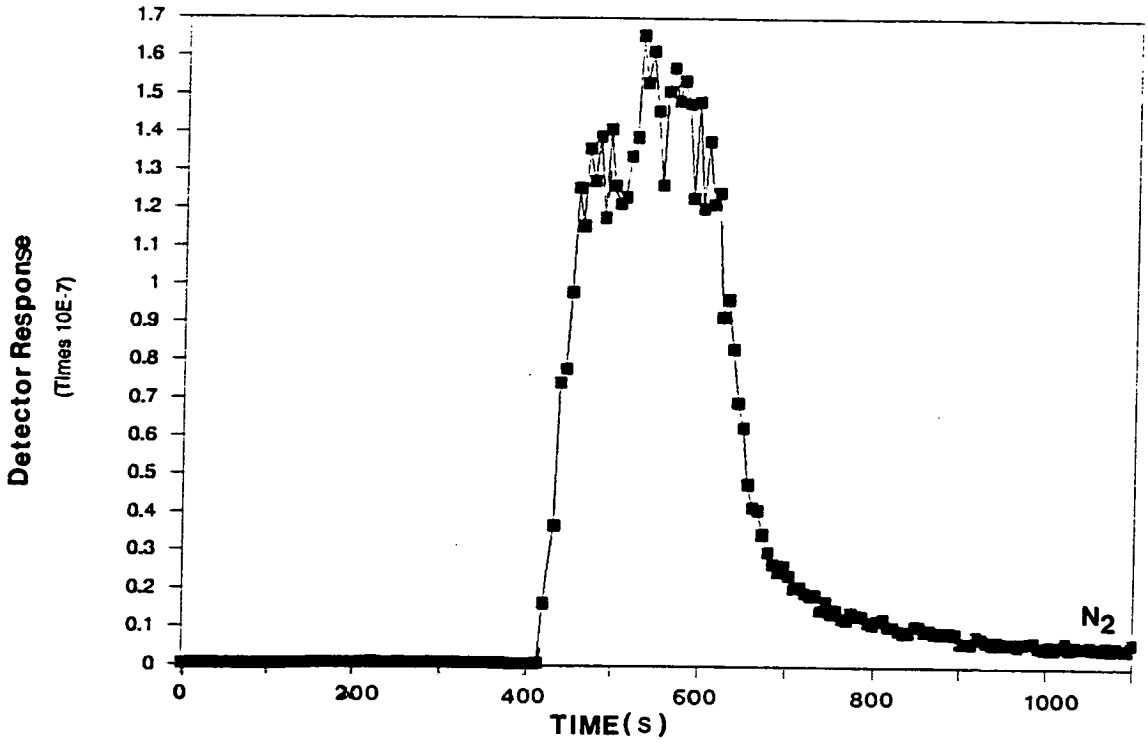

Figure 3.38 *Frontal uptake of N_2 and signal decay.*

At time t_3 the 10% N_2/10% Ne in He is switched back to He. After the dead volume has been swept out, the nitrogen signal decays down to zero. Each point along the trailing edge of this curve is proportional to the differential adsorption isotherm. By integrating horizontally in strips a conventional isotherm may be obtained. Figure 3.39 below illustrates an isotherm derived from analysis of the trailing edge in the frontal chromatography experiment illustrated in Figure 3.38.

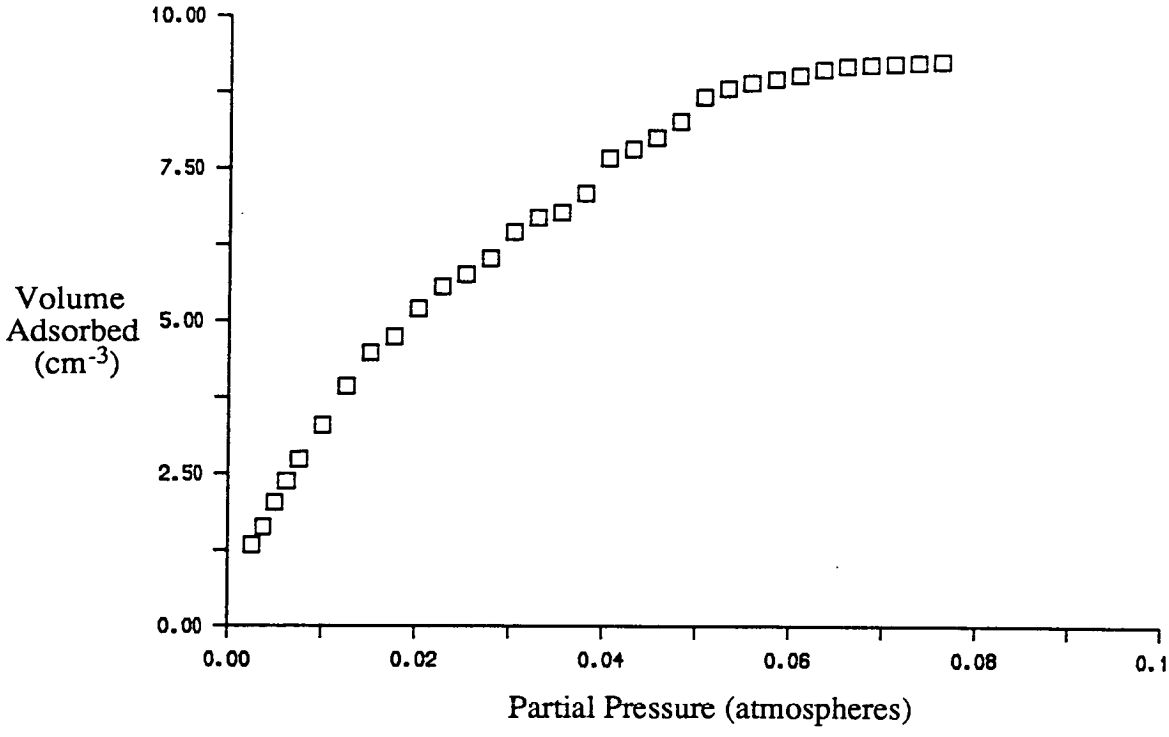

Figure 3.39 *Adsorption isotherm of nitrogen on Ni/Al_2O_3 at -196°C produced by stripwise integration of the trailing edge in Figure 3.38.*

By linearisation of the isotherm in Figure 3.39 with the BET equation (Equation 3.06 above), another value of V_m, the volume of an adsorbed monolayer of nitrogen can be determined and thus another measure of total surface area, BET_U is obtained. This is indicated in Figure 3.40 below.

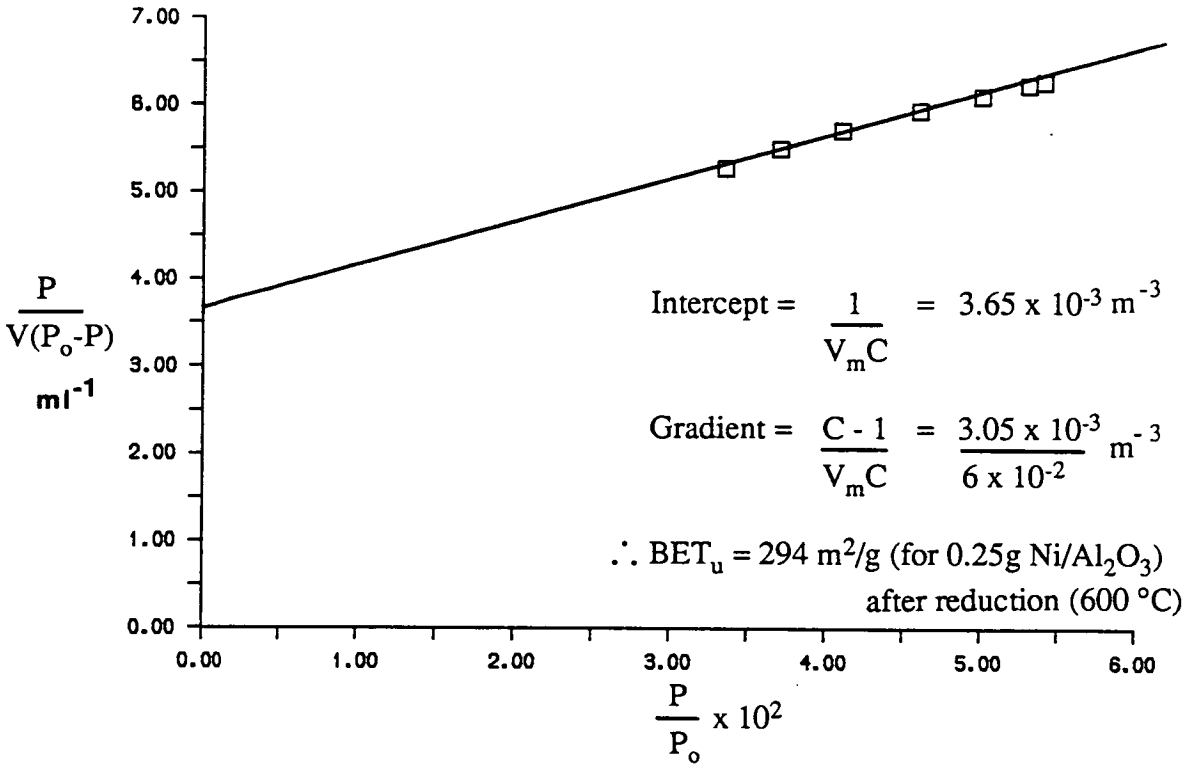

Figure 3.40 *Linearisation of the adsorption isotherm in Figure 3.39.*

3.11.1 Results.

Table 3.12 below shows total surface area measurements of as-prepared, calcined and reduced samples of Ni/Al_2O_3. Values from static volume (BET_{SV}), Frontal Chromatography (FC) and from the trailing edge analysis of frontal chromatography traces (BET_U) are shown.

Table 3.12 Total surface area measurements.

Catalyst Sample	Total Surface Area (m^2/g)		
	BET_{SV}	FC	BET_U
As-prepared	206	204	-
Calcined	240	230	-
As-prepared (reduced 600°C)	275	300	294
(reduced 750°C)	145	-	-
Calcined (reduced 600°C)	280	318	-
(reduced 750°C)	130	-	-
As-prepared, reduced 600°C and pressed into discs for transmission IR spectroscopy	176	-	-

Results from all these techniques show similar values. The catalyst as-prepared has a surface area of just over $200m^2/g$. This increases to $230 \rightarrow 240m^2/g$ on calcination at 400°C. Reduction at 600°C further enhances the surface area, with both samples having a surface area of $300m^2/g$. Reduction at 750°C produces a sharp decline in total surface area. This is probably due to the onset of the $\gamma\text{-}Al_2O_3 \rightarrow \delta\text{-}Al_2O_3$ phase transition which has its maximum rate at 730°C [151]. $\delta\text{-}Al_2O_3$ has a low surface area, usually less than $50m^2/g$.

Pressing discs for use in transmission infrared spectroscopy reduces the total surface area by 35%. This is probably due to blocking of pores in the γ-alumina support, not a phase change to another alumina phase. The method used for disc preparation has been described in Chapter 2.

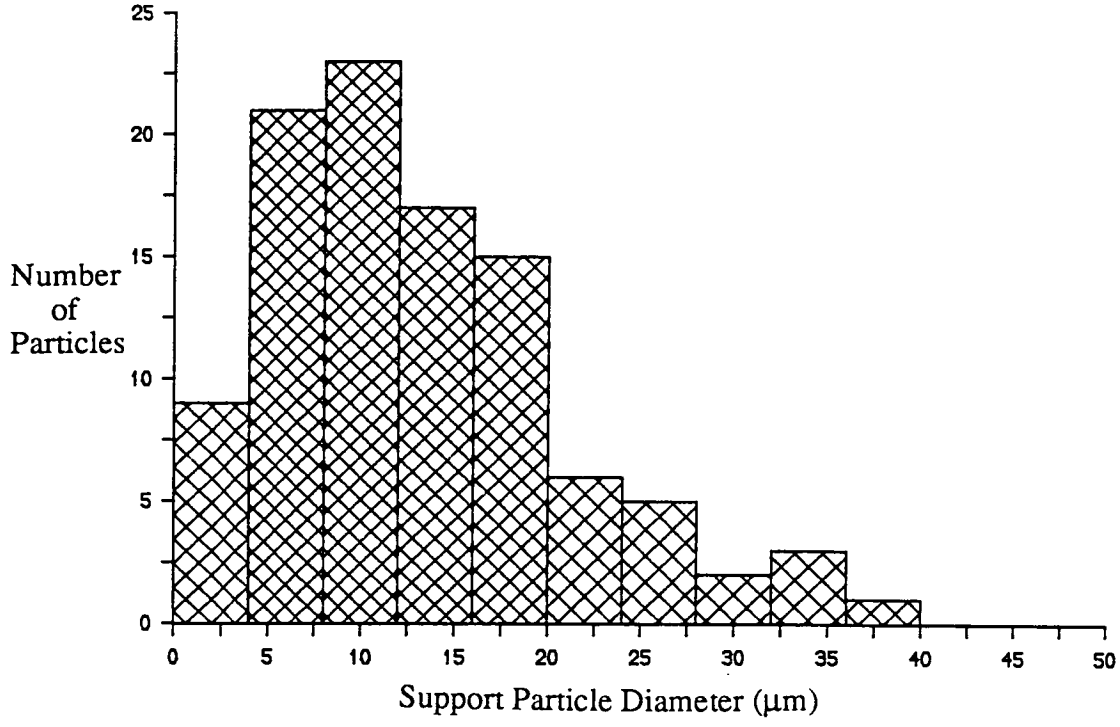

Figure 3.41 *Support particle size distribution for as-prepared* Ni/Al_2O_3.

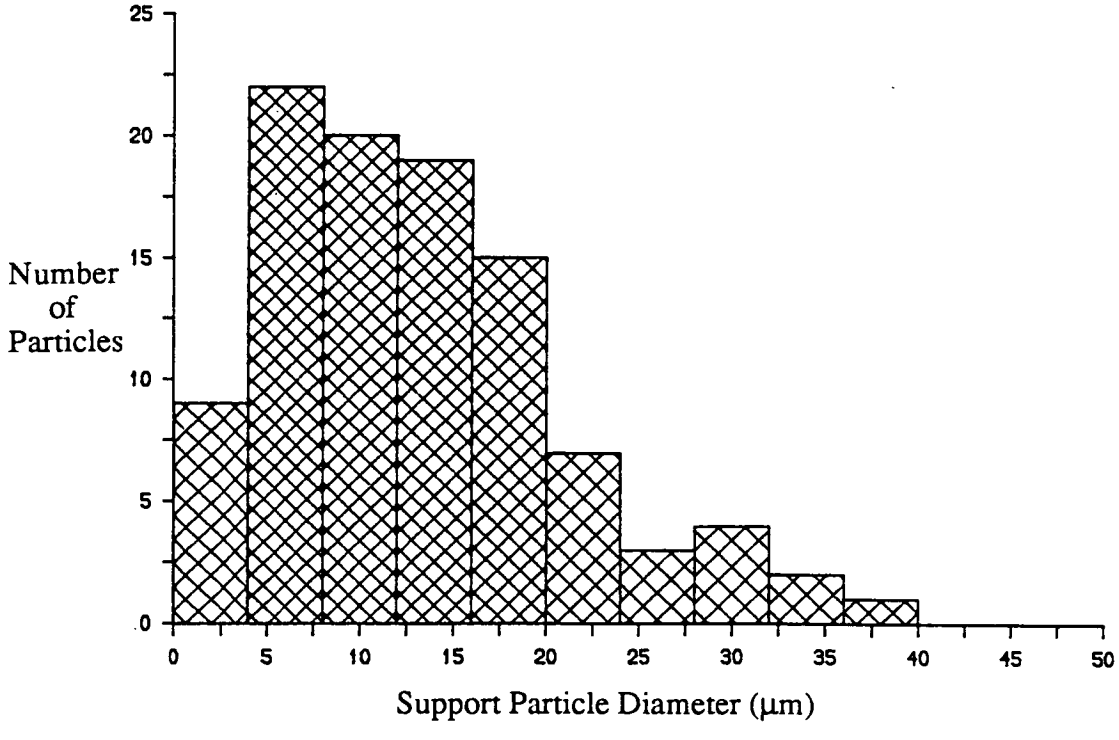

Figure 3.42 *Support particle size distribution for calcined* Ni/Al_2O_3.

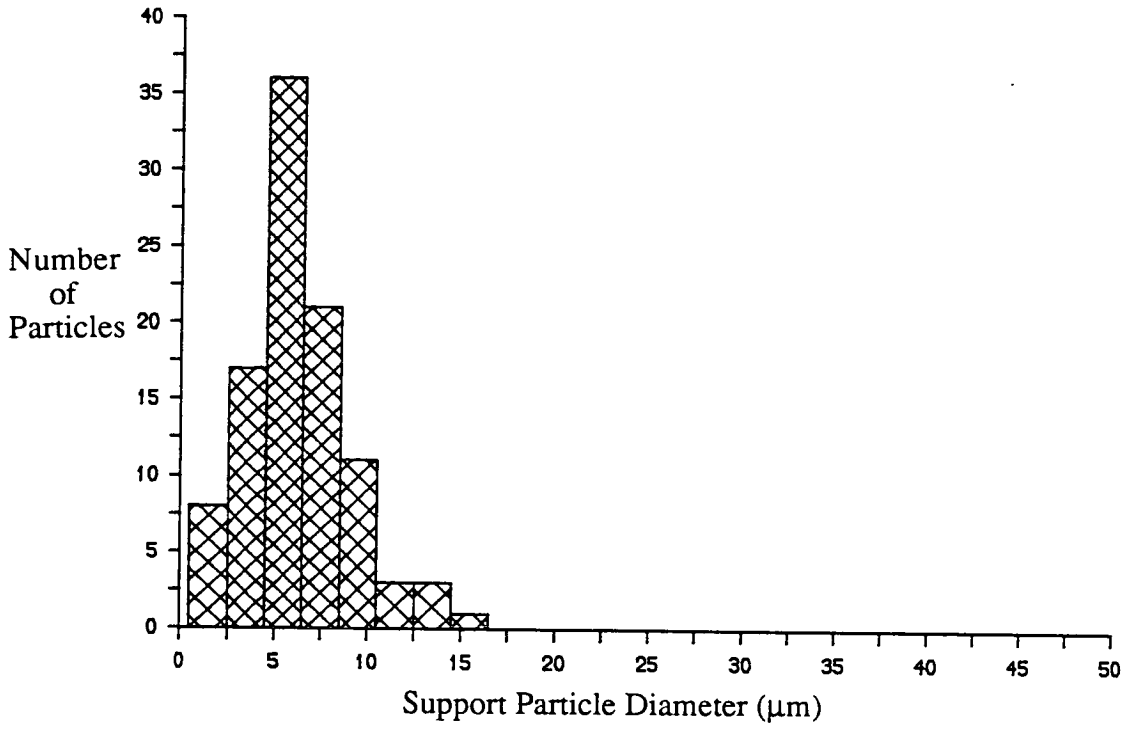

Figure 3.43 *Support particle size distribution for reduced Ni/Al_2O_3 (600°C for 1 hour in 100% hydrogen).*

3.12 Support Particle Size Distribution.

The size of alumina support particles is an important property of the Ni/Al_2O_3 and affects the extent of specular reflectance obtained in infrared studies, as described in Chapter 2. Consequently, analysis of particle sizes as a function of calcination and reduction is useful.

A Vickers Photoplan optical microscope, with a resolution of 1μm, was used to photograph samples as as-prepared, calcined and reduced Ni/Al_2O_3. Particle size distributions based on measurement of 100 particles of each sample from suitably enlarged photographs, are shown in Figures 3.41, 3.42 and 3.43 above.

Calculating the average arithmetic particle diameter, using Equation 3.05, for the as-prepared, calcined and reduced samples gives diameters of d_{ASP}=13.4μm, d_{CAL}=13.4μm and d_{RED}=6.2μm respectively. Calcining the sample appears to have no effect on the average particle diameter of the alumina, whereas reducing the sample more then halves the average particle size. These values of particle diameter are

probably overestimates because very small particles, <1-2μm, are not observable in the microscope. This will particularly affect the distribution of reduced particles.

3.13 Conclusions.

Although there have been reports that calcination reduces the attainable metal surface area [124], this has not been found to be true for the catalyst used here. Both as-prepared and calcined catalyst, once reduced, have been shown to have broadly similar properties. Consequently, both as-prepared and calcined samples are used here. After reduction at 600°C for 1 hour in 100% H_2, the catalyst is fully reduced (within detection limits). The support aluminium phase forms $Al(OH)_3$ (boehmite) on calcination, decaying to an amorphous γ-Al_2O_3 on reduction.

The essential properties of the reduced catalyst, as used in the DRIFTS and transmission accessories are summarised in Table 3.13 below.

Table 3.13 Properties of the reduced Ni/Al_2O_3 catalyst.

% loading	48 % Ni on Al_2O_3 by weight.
Maximum nickel surface area (reduction at 600°C)	$50m^2/g$ ($28m^2/g$ relative to the as-prepared mass)
Nickel area on passivation (and re-reduction)	$38m^2/g$ ($20m^2/g$ relative to the as-prepared mass)
Average nickel particle diameter	12→13nm.
Total surface area (reduction at 600°C)	$275m^2/g$.

CHAPTER 4

Ethene Adsorption on Ni/Al_2O_3.

4.1 Historical Aspects.

As mentioned in the introduction, the adsorption and subsequent reaction of ethene over nickel to produce ethane was one of the first examples of catalytic hydrogenation. Since then a large amount of work has been published devoted to the study of various aspects of ethene adsorption and reaction, making it the 'classical' organic-metal system.

Some of the earliest infrared studies of C_2 species on nickel involved the use of evaporated nickel films. Beeck [152] examined C_2H_4 adsorption at 23°C, finding dissociation to adsorbed C_2H_2 and 2H species. Similar findings were published by Jenkins and Rideal [153]. No evidence for chemisorbed ethene at room temperature was reported.

Supported nickel catalysts were first studied in the pioneering work of Pliskin and Eischens with Ni/SiO_2 [154]. They reported that upon adsorption of C_2H_4, at room temperature, a $-CH_2CH_2-$ type species was formed. Hydrogenation produced a $-CH_2CH_3$ 'half hydrogenated' state. An easily re-hydrogenated carbidic species was also reported.

The first low temperature study of the system was by Morrow and Sheppard [155], [156]. Examining only the CH stretching region they proposed species of the form MCH_2CH_2M at -78°C. Hydrogenation produced n-butyl like surface species, with gas phase products consisting mainly of ethane. Hydrogenation at 20°C produced predominantly butane in the gas phase.

An extensive study of C_2H_4 adsorption on Ni/Al_2O_3 and Ni/SiO_2, below room temperature, has been published recently by Lapinski and Ekerdt [157], [158]. Initial adsorption at temperatures below -93°C appears to form two types of π-bonded species, designated type A and type B. On warming, a '$\sigma\pi$' species begins to form and the type A π species decays. On further warming, an ethylidyne (CCH_3) species appears to dominate at temperatures of -43°C and over, and this study was the first to unambiguously demonstrate ethylidyne formation on nickel. This led Lapinski and

Ekerdt to restrospectively re-assign the original work by Morrow and Sheppard [155], which proved entirely consistent with the observation of the ethylidyne species. At room temperature, several other species, probably C1s and C4s as well as CCH_3 are thought to exist side by side.

The chemistry of C_2H_4 adsorption on many other supported Group 8, 9 and 10 metals is dominated by the ethylidyne species e.g.. Rh/Al_2O_3, Pd/Al_2O_3, Pt/Al_2O_3 [159], Ir/Al_2O_3 [160] etc. The accepted chemistry of C_2 species on supported nickel is illustrated schematically in Figure 4.1 below.

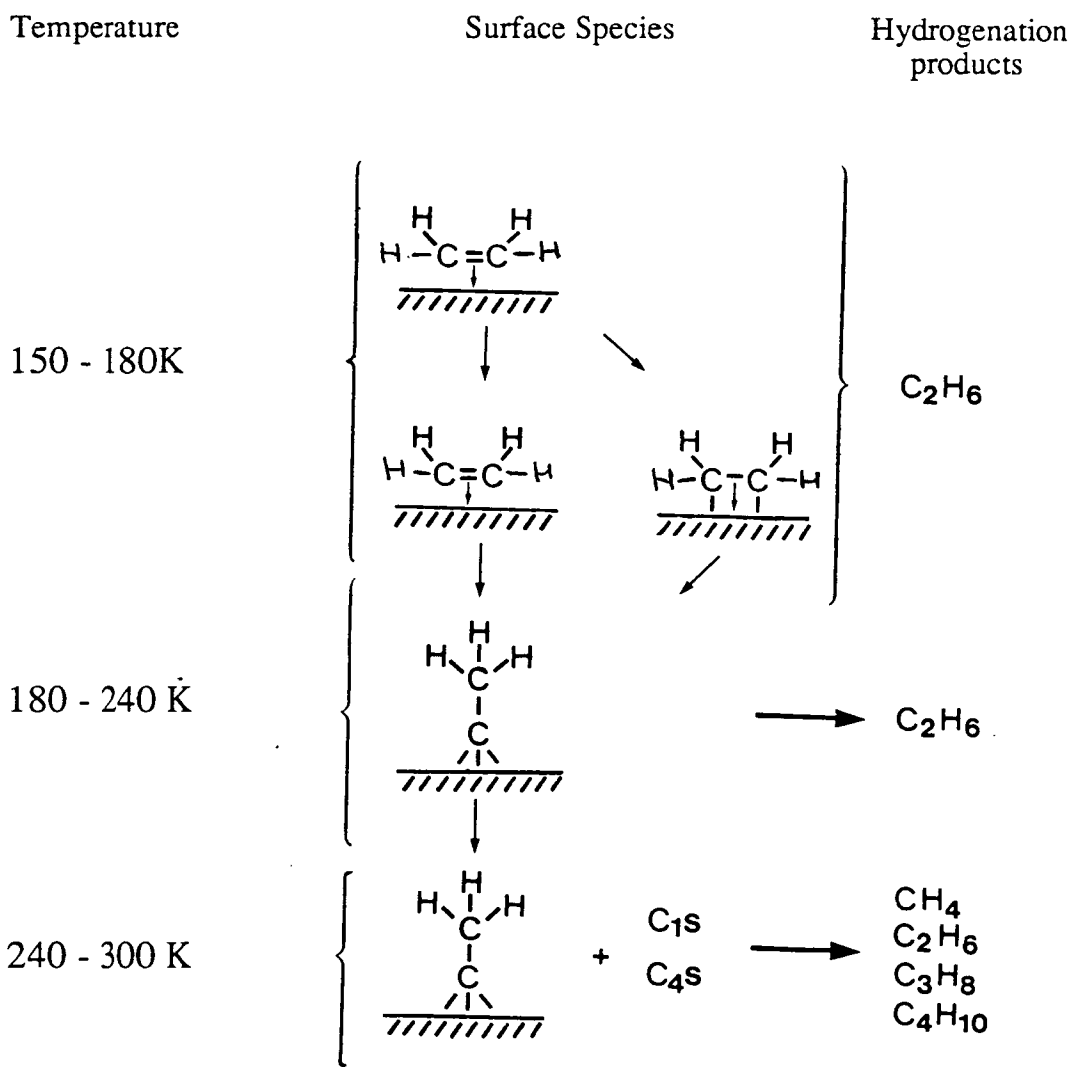

Figure 4.1 *Schematic diagram of C_2H_4 chemistry on supported nickel up to 300K (adapted from* [157].)

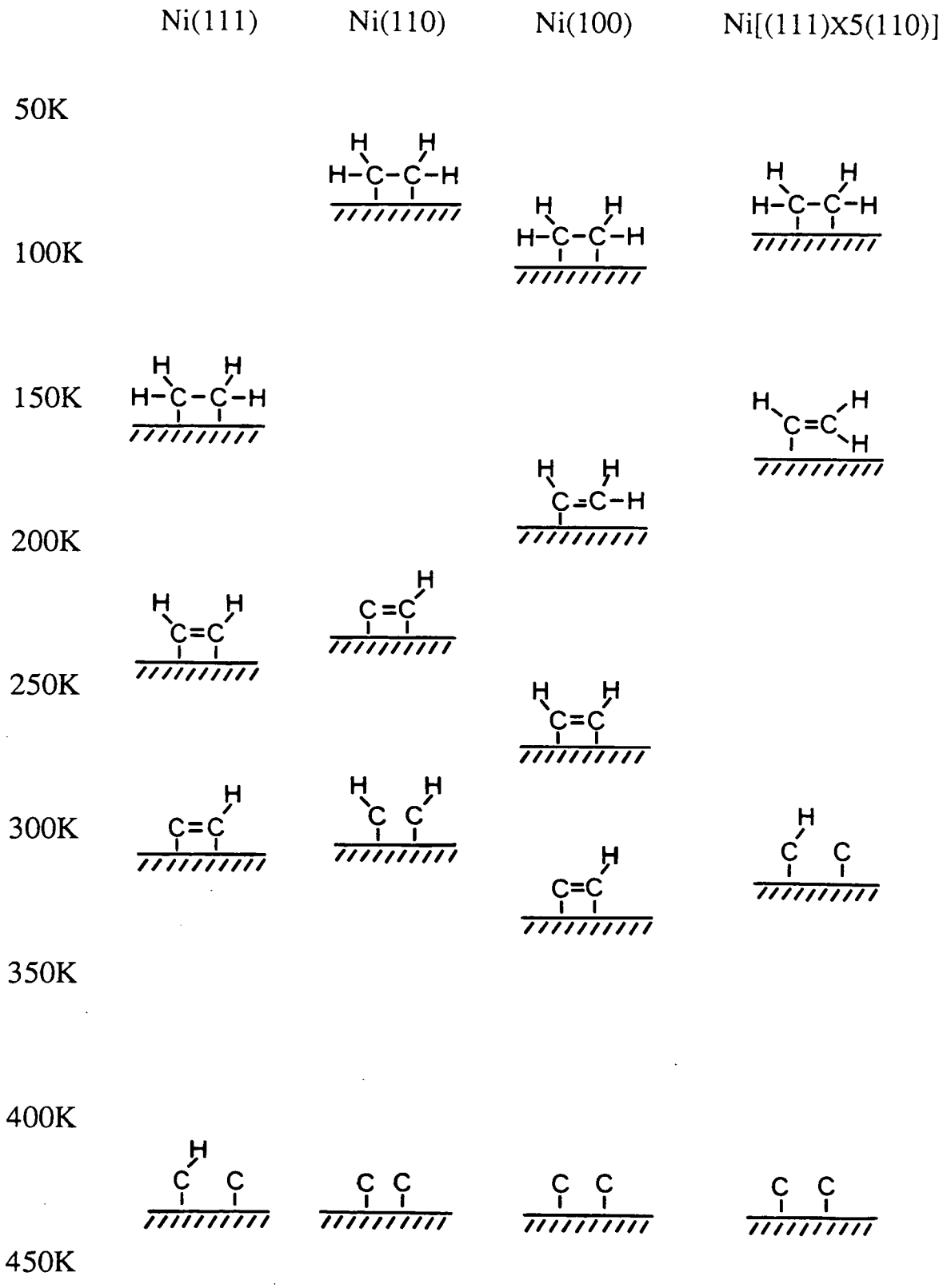

Figure 4.2 *Surface species as a function of temperature formed from C_2H_4 adsorption onto various nickel single crystals.*

4.1.1 Single Crystals.

As mentioned above, ethylidyne has been detected on supported nickel catalysts and also dominates the chemistry of C_2 hydrocarbons on most Group 8, 9 and 10 single crystals [23]. Ethylidyne has not been observed on any nickel single crystals with vibrational spectroscopy to date. A recent static secondary ion mass spectroscopy (SSIMS) study by Zhu and White [161] has demonstrated that ethylidyne does form on Ni(111) from adsorption of both ethene and ethyne, although only at ethene coverage greater than 80%. They proposed that adsorbate-adsorbate repulsion causes the surface species to 'stand up' with C-C bonds perpendicular to the surface.

The accepted chemistry of ethene on nickel single crystals can be summarised as illustrated in Figure 4.2 above. On Ni(111) [162], [163] a di-σ species is formed on adsorption of C_2H_4 at 150K. On warming to 230K and above an acetylene type species was formed. For Ni(100) at 90K, sp^2-hybridised π-bonded C_2H_4 was formed [164], although this is disputed by Sheppard [23]. This transformed into a vinyl ($-CH=CH_2$) species at 175K before finally forming acetylene by 275K.

Ni(110) is different again, C_2H_4 adsorption at 80K generates di-σ bonded ethene and this evolves to acetylide (CCH) by 220K [165]. The stepped surface Ni[5(111)x5(110)] produced the vinyl species by 150K upon adsorption of C_2H_4 [162]. The ethylidyne species is conspicuously absent in the single crystal chemistry as determined with spectroscopic methods, exclusively Electron Energy Loss Spectroscopy (EELS) in this case.

4.1.2 Vibrational Data.

The vibrational data for the chemistry described above is summarised in Table 4.1 below. Fundamental to the identification of surface hydrocarbon structure has been the use of hydrocarbon ligands in organometallic compounds to model these surface species. Vibrational assignments of several compounds are also indicated in Table 4.1. Data acquired by EELS will generally have been collected with an instrument resolution of poorer than $50cm^{-1}$, compared to infrared data of usually better than $10cm^{-1}$.

Table 4.1 Vibrational Frequencies of some Hydrocarbon Species.

Species	Frequencies (cm^{-1})	Origin	Reference
CH	2980, 790	Ni(111) EELS	[166]
methyne or	2980, 780	Ni(111) EELS	[162]
methylidyne	3041, 850	$Co_3(CO)_9(\mu\text{-}CH)$ IR	[167]
CH_2	1330	Ni(111) EELS	[168], [162]
methylene	2990, 2949,1426, 974, 850, 796	$Os_3(CO)_{10}(\mu\text{-}CO)(\mu\text{-}CH_2)$ IR	[169]
	2984, 2935, 1428, 961, 881, 869, 660	$(\mu_2H)_2Os_3(CO)_{10}(\mu_2\text{-}CH_2)$ IR	[169]
CCH	2990, 1290, 890	Ni(110) EELS	[165]
acetylidyne	2910, 1360, 820, 730	Ni(100) EELS	[164]
or acetylide	3157, 1534, 861, 854, 762, 759	$Os_3(CO)_9(\mu\text{-}H)(\mu_3\text{-}\eta^2\text{-}CCH)$ IR	[171]
CCH_2	3052, 2990, 1467, 1328, 1048	$H_2Os_3(CO)_9(C{=}CH_2)$ IR	[170]
vinylidene	3094, 3032, 1586, 988, 973	$Ru_2(CO)_3(C_5H_5)(C{=}CH_2)$ IR	[171]
$CHCH_2$	3090, 2920, 1555, 1405, 1280,1160,915	Ni(100) EELS	[173]
vinyl	3100, 2940, 1410, 1335, 975	Ni(100) EELS	[164]
	3100, 3000, 1510, 1120	Ni[(111)x5(110)] EELS	[162]
	3052, 2998, 2920, 1476, 1310, 1226 1005, 990, 987, 782	$HOs_3(CO)_{10}(CH{=}CH_2)$ IR	[170]
CCH_3	2930, 2888, 1420, 1356, 1163, 1004	$Co_3(CO)_9(CH_3C)$ IR	[21]
ethylidyne	2870, 1340, 1125	Ni/Al_2O_3 IR	[157]
$CHCH_3$	2947,2903,2868,2835,1445,1264,968	$Ru_2(CO)_3(C_5H_5)_2(CHCH_3)$ IR	[171]
ethylidene			
CH_3	2940, 1360, 1220, 370	Ni(111) EELS	[172]
methyl			
C_2H_4	3000, 1580, 1385	Ni(100) EELS	[173]
di-σ ethene	2970, 1440, 1100, 800	Ni(111) EELS	[162]
	2970, 1435, 1145	Ni(110) EELS	[165]
C_2H_4	1515, 1243	$K[(C_2H_4)PtCl_3].H_2O$ IR	[174]
π ethene	1547, 1227	Ni/Al_2O_3 IR	[157]
	1525, 1255	Ni/Al_2O_3 IR	[157]
C_2H_2	2944, 1218	Ni(111) EELS	[163]
acetylene	2925, 1220	Ni(111) EELS	[162]
	2930, 1370, 1220, 1080, 860	Ni(111) EELS	[175]
	2920, 1200	Ni[(111)x5(110)] EELS	[162]
	2928, 2915, 1260	Ni/Al_2O_3 IR	[157]
C_2H_4	1470, 1182	Ni/Al_2O_3 IR	[157]
$\sigma\pi$ ethene			

4.2 Apparatus and Experimental Procedure.

Described in this chapter are experiments involving the adsorption of C_2H_4 and C_2D_4 on Ni/Al_2O_3. Both infrared spectroscopy and mass spectrometry were employed to help identify both surface species and gas phase products. Temperature programming was used to follow surface reaction and to analyse desorption products. Mixed H/D systems were investigated to study the incorporation of D_2 into C_2H_4 derived products and *vice versa*. The carbonaceous deposits produced on C_2H_4 adsorption were analysed by Temperature Programmed Hydrogenation and Temperature Programmed Oxidation, producing a 'carbon audit'. Reaction of C_2H_4 was also investigated at a series of temperatures between 25 and 300°C, with analysis of both surface and gas phase products.

The infrared experiments described in this thesis were performed using both transmission infrared and DRIFTS. As established in Chapter 2, transmission infrared spectroscopy is more sensitive than DRIFTS in the CH deformation region of the spectrum (1500-1100cm^{-1}), as well as having a potentially useful 50cm^{-1} lower cut-off frequency. For higher wavenumber observations (3000-2500cm^{-1}) DRIFTS becomes more sensitive, and observation of surface bands with the transmission cell becomes impossible, discussed below.

Typical sequential spectra of 30 or 50 scans were recorded and ratioed against background spectra of 250 scans to produce absorbance plots. Background spectra were recorded after reduction and before adsorption of reactant gases. A standard procedure of *in situ* sample processing before adsorption was developed. The pre-reduced and passivated catalyst samples were reduced in 100% hydrogen flowing at 100cm^3/min for 1 hour at 300°C. Although the transmission cell could be operated at higher temperatures than this, 300°C was used so that direct comparison with DRIFTS could be made. After reduction, the samples were outgassed in the carrier gas flowing at 10-20cm^3/min for 30 minutes at the same reduction temperature of 300°C, before being cooled to the reaction temperature. Neither infrared cell was capable of operating below room temperature, hence all experiments discussed here were performed at temperatures between 25 and 300°C. A resolution of 4cm^{-1} was used as standard throughout.

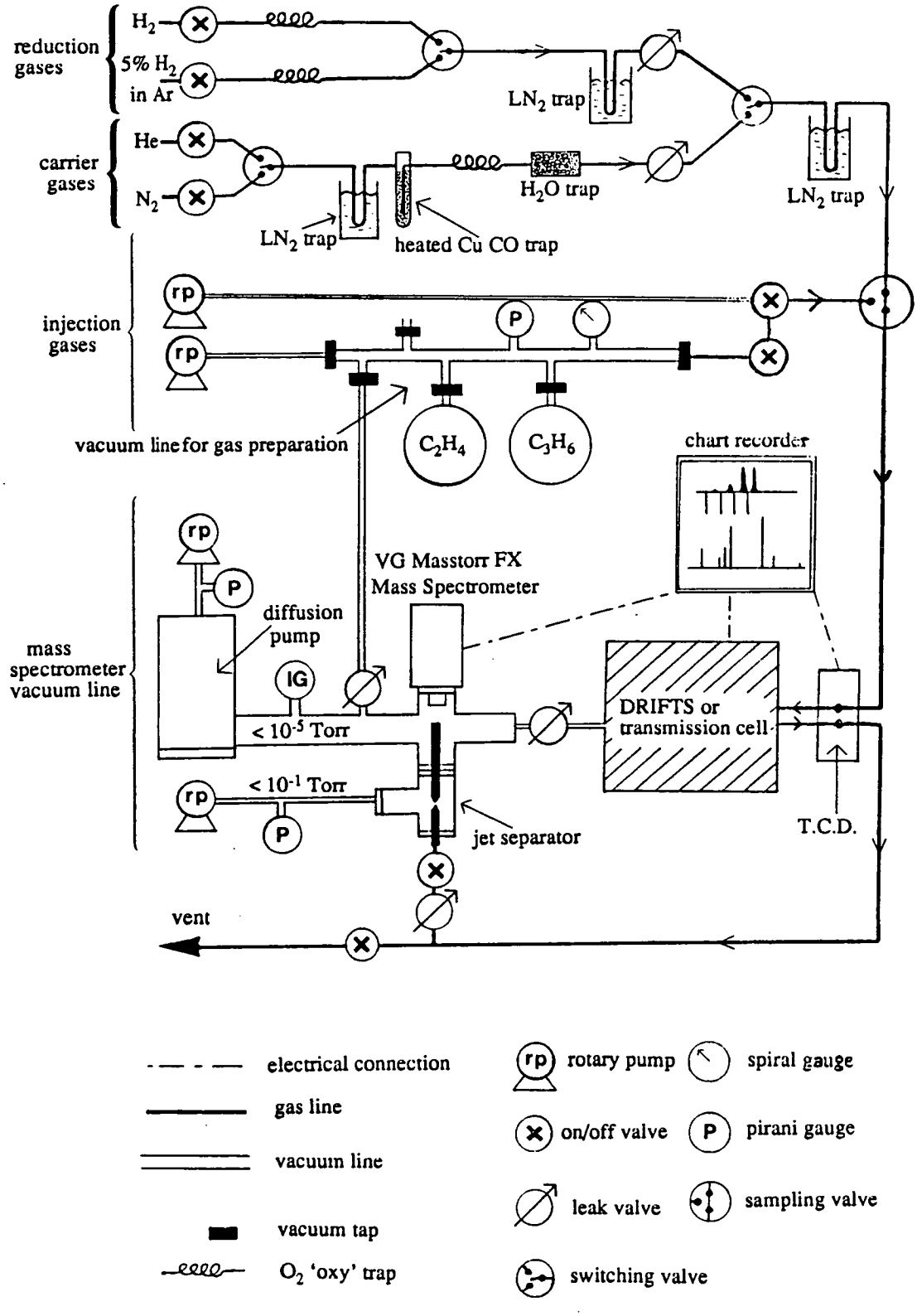

Figure 4.3 *Flow/vacuum system used in conjunction with both the DRIFTS cell and transmission infrared cell.*

The Digilab FTS-40 spectrometer, discussed in Chapter 2, could produce a single scan $4cm^{-1}$ spectrum in ≈0.5 of a second. Consequently, 30 and 50 scan spectra took 15 and 25 seconds respectively. File handling time between spectra was 30 seconds, meaning that sequential series of spectra could be produced with a separation of 45 or 55 seconds for 30 scan and 50 scan spectra respectively.

The carrier gas flow system used for all the infrared experiments is illustrated in Figure 4.3 above. Carrier gas purity proved to be an important problem in the work described here. Both water and carbon oxides were significant impurities and both produce strong absorbance features in the infrared spectrum, which can obscure the weaker hydrocarbon features. Additionally, the coadsorption of water/carbon oxides with hydrocarbon molecules may well alter the observed chemistry of the system. Consequently the carrier gas, typically helium, passed through a series of impurity traps before reaching the catalyst sample. Firstly a heated copper trap containing copper turnings at 300°C removed CO, producing CO_2. A 'oxy' trap then removed traces of oxygen. Subsequently a silica gel trap removed the largest fraction of water, before the final liquid nitrogen trap, which froze out the remaining water and CO_2. The hydrogen stream was cleaned with two liquid nitrogen traps. A thermal conductivity detector (TCD) was used to monitor uptake of gas by measuring the thermal conductivity of the gas stream before and after the infrared cell. Gases for adsorption were prepared in the glass line illustrated. A portion of the output from the infrared cell could be sampled by the jet separator. This consists of two pin-hole nozzles facing each other across a rotary pumped volume, with a pressure of 10^{-2}mbar. Gas at atmospheric pressure from the carrier gas stream is sucked down one nozzle and while most is pumped away, a small proportion is captured by the other nozzle. This leads into the mass spectrometer system, with a vacuum of 10^{-6}mbar or better. The jet separator introduces a degree of mass selection, since it concentrates higher masses at the expense of the lower mass molecules.

Hydrocarbon gases for adsorption were purified in the gas preparation line with a series of freeze-pump-thaw steps. A standard pressure of 500mbar of C_2H_4, C_2D_4 etc. was adopted for pulses throughout the infrared experiments. This gave pulses of 4μmol when injected into the carrier gas stream *via* sampling valve A. All details of gas purity and suppliers are listed in Appendix 1.

Analysis of gas phase products with high sensitivity was often hampered by the small sample mass (40mg) that was used in both infrared cells. Consequently parallel adsorption/reaction experiments were carried out using the microreactor system

illustrated in Figure 3.26. With sample masses in the range 1-2g, this enabled copious quantities of gas phase products to be analysed. Examination of the below room temperature chemistry of C_2H_4 was also possible on this system, down to -190°C.

Results.

4.3 Infrared Study of C_2H_4 Adsorption at 25°C.

All infrared spectra from adsorption and reaction experiments are grouped together at the end of this chapter for the sake of simplicity.

4.3.1 Experimental.

Figure 4.4A and B show sequential 50 scan DRIFTS spectra produced on adsorption of one 4μmol pulse of C_2H_4 onto Ni/Al_2O_3 at 25°C after the standard preparation procedure described above. Figure 4.4A shows the CH stretching region (νCH) (3100-2700cm^{-1}) of the infrared spectrum and Figure 4.4B the CH deformation (δCH) region (1550-1080cm^{-1}). Initially bands at 2872cm^{-1}, 2795cm^{-1}(weak) 1339cm^{-1} and 1122cm^{-1} appear, along with broad gas phase features centred on 2954cm^{-1} (ν_5CH of gas phase ethane). The 1339cm^{-1} band shifts to 1334cm^{-1} as it increases in intensity, as does the 1122cm^{-1} band to 1115cm^{-1}. Bands at 2894cm^{-1} and 1360cm^{-1} begin to grow into the spectra as a function of time, shifting to 2891cm^{-1} and 1356cm^{-1} as intensity increases. Bands in the νCH region of the spectrum vary only slightly as a function of intensity.

The growth of the 2892/1356cm^{-1} bands is at the expense of the 2872/1334/1115cm^{-1} bands which begin to decay together, shifting back to 2872, 1337 and 1122cm^{-1} as their intensity decreases. The 2872:1337:1122 band ratio was 1:1.53:0.76 on initial formation. As the gas phase envelope decreases, with the gas being swept out of the system, several other bands at 2955cm^{-1} and 2925cm^{-1} are revealed. These are associated with the 1455cm^{-1} and 1415cm^{-1} features in Figure 4.4B. By plotting band intensity with time, several bands can be shown to behave in concert, revealing at least four different surface species, designated A, B, C and D. Figure 4.5 shows the band intensities plotted as a function of time. Table 4.2 below lists the four species with band assignments.

Table 4.2 Band assignment of species A, B, C and D.

Species	Absorption bands	Strength	Assignment	Identification
A	1115-1122cm^{-1}	medium	νCC	
	1334-1339cm^{-1}	strong	δCH_3s	Ethylidyne
	2795-2800cm^{-1}	weak	$2x\delta CH_3as$	CCH_3
	2870-2875cm^{-1}	medium	νCH_3s	
B	1355-1360cm^{-1}	strong	δCH_3s	
	2890-2894cm^{-1}	medium	νCH_3s	
C	1425-1430cm^{-1}	medium	$\delta CH_2s/\nu CC$	
	2925cm^{-1}	medium	νCH_2s	
D	1455-1460cm^{-1}	strong	$\delta CH_2s/\nu CC$	
	2955cm^{-1}	medium	νCH_2s	

+ gas phase ethane band centred at 2954cm^{-1} (ν_5)

4.3.2 Band Assignment.

Species A may be immediately associated with with ethylidyne structure, CCH_3, with the band assignment as indicated above. Asymmetric modes are not observed, as they were on the smaller crystallites of Pt/Al_2O_3 [159], indicating that the metal surface selection rule fully attenuates all non symmetric modes for Ni/Al_2O_3. The gas phase envelope, centred at 2954cm^{-1}, can be identified as the ν_5CH vibration of ethane [44]. Species B, characterised by bands at 1360cm^{-1} and 2894cm^{-1} appears to be a product of the decay of the ethylidyne species.

The single crystal chemistry, as illustrated in Figure 4.2, shows that acetylenic or C_2H type species are the expected products of C_2H_4 decay. Species B, C and D all differ totally in their spectral characteristics from these acetylenic species, or any other characterised surface bands on nickel single crystals.

Comparison of the frequencies of species B with the data in Table 4.1 suggests that species B contains a methyl (CH_3) group, with the 2894 and 1360cm^{-1} bands identified as the symmetric CH_3 stretching and deformation vibrations respectively. This does however give a number of possibilities for B such as surface ethyl,

ethylidene or methyl species. A methyl containing C_4 species is also possible, as suggested in the early transmission studies by Morrow and Sheppard [155], [156]. If B remains as a C_2 species, the loss of the CC stretch at 1122cm^{-1} during decay from A to B may be due to either bending of the CCH_3 structure so that the CC bond has a much lower perpendicular component, or a shift of the CC stretch frequency for some reason to below the infrared cut-off of the Al_2O_3 support at ≈1100cm^{-1}.

The frequencies associated with the species C and D are similar to those of symmetric CH_2 and coupled CC stretch/CH_2 deformation vibrations of a methylene (CH_2) group. This gives the possibility of vinyl, vinylidene, methylene or once again C_4 fragments as the identity of C and D. Vinylidene has been mentioned in both the formation and decomposition of ethylidyne in several studies [23].

4.3.3 Blank Experiment.

C_2H_4 was adsorbed at 25°C on both γ-Al_2O_3 and on the passivated Ni/Al_2O_3 catalyst before reduction. The γ-Al_2O_3 was subjected to the same treatment as the Ni/Al_2O_3 samples were with 1hr. in 100% H_2 at 300°C followed by outgassing in He for 30 minutes. Neither this, or the unreduced Ni/Al_2O_3 showed any evidence for the adsorption or reaction of C_2H_4.

4.3.4 The Effect of Surface Hydrogen.

The spectra shown in Figure 4.4 were produced by adsorption of C_2H_4 onto the catalyst after the standard preparation procedure. Ethene adsorption was repeated over three differently prepared surfaces. Band intensities of the four species A, B, C and D produced by adsorption of C_2H_4 on a H_2 saturated, H_2/C covered surface and a considerably outgassed, 'H_2 free' surface are shown in Figure 4.6. The 'H_2 free', considerably outgassed samples were prepared by first outgassing in the helium carrier gas at 300°C for 1hour, cooling to 25°C, rapidly heating back to 300°C, holding for 30 minutes, before cooling back down to 25°C for adsorption of C_2H_4. All bands show the same correlation as previously with the 'H_2 free' surface, although only the bands in the CH deformation region of the spectrum are shown in Figure 4.6 for simplicity. The hydrogen saturated surface was produced by adsorption of 3μmol pulses of H_2 until no more adsorption occurred. The H_2/C covered surface, as described later, was produced by re-hydrogenation of coke deposits produced after thermal processing of the species produced at room temperature. Absorption bands at 2960 and 1460cm^{-1} were regenerated during this hydrogenation.

Immediately obvious in Figure 4.6 is that the initial intensity of ethylidyne bands is sensitive to the nature of the adsorption surface. The 1337cm^{-1} band is approximately 2 times as intense for the H_2 saturated surface, relative to the 'H_2 free' and H_2/C covered surfaces. The band intensities for the 'H_2 free' surface were very sensitive to outgassing time, with the longer the outgassing time producing the more rapid 1337cm^{-1} decay. All three traces can be divided into two sections. For the first 200 seconds, the ethylidyne species decays with the corresponding build up of the 1360cm^{-1} feature accompanying this. After approximately 200 seconds, the band intensities stabilise with only gradual changes as a function of time. Particularly noticeable is the 1425cm^{-1} band which grows in very slowly on the H_2 saturated and H_2/C covered surfaces. The level at which the 1337cm^{-1} and 1360cm^{-1} stabilise during this second phase is very sensitive to the surface pre-treatment. The 1337:1360 peak intensity ratio varies from 2 for the H_2 saturated surface, to 0.4 for the 'H_2 free' surface, with the 1337 and 1360cm^{-1} absorbance values approximately the same for the H_2/C covered surface. The absolute value of the 1337cm^{-1} band varies from an absorbance of 0.008 for the H_2 saturated surface, to 0.005 for the H_2/C covered surface and 0.002 for the 'H_2 free' surface.

The ratio of the 2872:1337:1122cm^{-1} bands is 1:1.48:0.72 on the hydrogen saturated surface. This is similar to that found for CCH_3 on the 'H_2 free' surface, indicating that no new species is adding to the observed intensity of the CCH_3 bands. Evidently the formation of ethylidyne is strongly influenced by co-adsorption of other species. Pre-adsorbed hydrogen and causes more CCH_3 to form initially than on the other two surfaces, which seem to allow similar amounts of CCH_3 to form. The decay of CCH_3 is also a function of co-adsorbed material. Starting from similar amounts of CCH_3, the CCH_3 signal decays to a much greater extent on the 'H_2 free' surface compared to the H_2/C covered surface. It may be that the pre-adsorbed H_2/C is blocking the decomposition of the ethylidyne, preventing build up of the 1360cm^{-1} band to the same extent as on the 'H_2 free' surface. A similar proportion of the absorbance intensity (≈50%) was lost for the decay of CCH_3 on both H_2 saturated and H_2/C covered surfaces. 75% of the 1337cm^{-1} intensity is lost on the 'H_2 free' surface.

Examination of the 1337 and 1360cm^{-1} bands over a longer timescale than shown in Figure 4.5 reveals that the decay of the 1337cm^{-1} band continued over many hours, with the 1360cm^{-1} bands remaining approximately the same intensity throughout and the 1337cm^{-1} band decaying. The absorbance values of these bands after 5 hours, on all three surfaces are listed in Table 4.3 below.

Table 4.3 Band intensities after 5 hours.

	Catalyst Surface		
Band (cm^{-1})	H_2 saturated	'H_2 free'	H_2/C covered
1337	0.005	0.001	0.003
1360	0.004	0.005	0.004

Species C at 1425/2925cm^{-1} appears to grow in slowly throughout this time, achieving a comparable absorbance value to the 1337cm^{-1} band.

Figure 4.7A and B show sequential spectra produced with transmission infrared spectroscopy, and are directly comparable to the DRIFTS spectra of the same reaction shown in Figure 4.4. The greater signal to noise achievable in transmission compared to DRIFTS is apparent in Figure 4.7B. Interestingly, Figure 4.7A, the νCH region of the spectrum, shows only gas phase spectra, and no bands due to surface species can be detected. This is particularly perplexing as examination of the single beam spectrum in transmission (Figure 2.14) around the 3100-2800cm^{-1} region indicates that while the signal level is decreasing rapidly to higher wavenumbers at this point, there is apparently sufficient throughput to make observation of surface bands possible. Carter *et al.* [176] have reported a similar lack of infrared absorption bands in this region when studying the adsorption of ethene on near-faujasite zeolite. They were unable to explain this phenomenon. As mentioned previously, the transmission cell does produce excellent gas phase spectra, as illustrated in Figure 4.7A. Evidently all transmission infrared spectra can only be analysed in the δCH region for surface bands.

The effect of successive adsorption of C_2H_4 is illustrated in Figure 4.7B, showing broadly similar chemistry to the DRIFTS study. Injection of a second or additional pulse of C_2H_4 into the carrier gas initially causes only the CCH_3 bands to increase in intensity. In other words, adsorption is always *via* CCH_3. Once formed, the CCH_3 decays as usual to the 2894 and 1360cm^{-1} species B and species D at 2955 and 1455cm^{-1}.

4.3.5 Hydrogenation of Surface Species.

Figure 4.8A shows the effect of hydrogenation of surface bands by injecting a 2μmol pulse of H_2 into the carrier gas. Only the 1360cm^{-1} band is significantly attenuated and a new band at 1377cm^{-1} forms, together with a broad, weak feature at 1210cm^{-1}. Detail of the single spectrum at which hydrogenation causes surface bands to alter is shown in Figure 4.8B and C. Similar DRIFTS spectra show the 1377cm^{-1} band to be associated with a band at 2847cm^{-1}. Figure 4.8C reveals the spectrum of gas phase products. Although several species are produced on hydrogenation (see section 4.6), the main feature at 2966cm^{-1} is likely to be a νCH_3 stretch of an alkane greater than C_2 in size [44]. Mass spectral evidence shows this to be predominantly butane, which is confirmed in mass spectral studies discussed later. An additional pulse of H_2 totally removes the 1360cm^{-1} band, integration reveals that 3.72 μmol of H_2 are consumed.

On hydrogenation the band at 1455cm^{-1} (species D) shifts to 1460cm^{-1} and increases in intensity. This may be due to removal of species D and generation of a new species at 1460cm^{-1}, or merely shifting and strengthening of the band due to changes in the adsorption environment of D. The ethylidyne bands are not significantly affected, although they shift slightly in frequency (1337→1340cm^{-1}, 1122→1114cm^{-1}).

4.3.6 Temperature Programmed Desorption.

Figure 4.9 shows successive transmission spectra taken during temperature programming of a catalyst sample from 25°C to 225°C, after adsorption of C_2H_4. The ethylidyne band at 1337cm^{-1} decays by 125°C, with a shift in intensity from 1337cm^{-1} to species B at 1360cm^{-1} between 75 and 100°C. The 1455cm^{-1} band of species D increases in intensity to reach a maximum between 150 and 175°C, before decaying to near zero by 225°C.

4.4 Infrared Study of C_2D_4 Adsorption at 25°C.

Catalyst samples for C_2D_4 adsorption were prepared as for C_2H_4 adsorption i.e. *via* reduction with hydrogen. No reduction using deuterium was undertaken. Hence all surfaces are truly D_2 free before adsorption of D_2.

Figure 4.10 and 4.11 show sequential transmission infrared spectra produced on

adsorption of two 4μmol pulses of C_2D_4 onto 'H_2 free' Ni/Al_2O_3 at room temperature. Figure 4.10 shows the 1600-1050cm^{-1} region and Figure 4.11 the 2400-1950cm^{-1} region. DRIFTS spectra of the 2400-1950cm^{-1} region for the same reaction are shown in Figure 4.12. Initial adsorption produces strong surface bands at 2222, 2034, 1138 and 1077cm^{-1} with gas phase bands at 2236 and 2087cm^{-1}. There is also a weak feature at 1238cm^{-1} with a broad band appearing briefly at 1360cm^{-1}.

4.4.1 Band Assignment.

The vibrational frequency of these C-D bands may be directly related to their C-H cousins using $\sqrt{2}$ reduced mass. The gas phase bands at 2236 and 2087cm^{-1} are easily identified as the ν_7CD and $\nu_8+\nu_{11}$CD vibrations of C_2D_6 respectively [44]. The fact that a significant amount of C_2D_6 is observed reveals that some form of self-hydrogenation of C_2D_4 is the principal mechanism for production of ethane over a 'H_2' surface, since it must also be D_2 free before adsorption of C_2D_4. Very weak features between 3000 and 2800cm^{-1} reveal that a small amount of mixed ethane is formed i.e. $C_2D_4H_2$. Evidently the surface is not totally 'H_2 free', even after extensive outgassing. The mixed ethane must have been formed by reaction of C_2D_4 with residual H_2 from reduction.

The νCD 2034cm^{-1} band can immediately be assigned to the νCD stretch in CCD_3 and is very close to the value of 2033cm^{-1} observed by Lapinski and Ekerdt [157] on Ni/Al_2O_3. This band shows a shift of 1/1.41 which is very close to the theoretical $1/\sqrt{2}$ value. The 1138cm^{-1} band, which behaves in a parallel manner, is assigned to the νCC stretch in CCD_3, once again in relatively close agreement with Lapinski and Ekerdts' value of 1147cm^{-1}. This band has shifted up by 16cm^{-1} from the 1122cm^{-1} value for νCC in CCH_3. A similar shift has been reported by Lapinski and Ekerdt [158]. The fact that the νCC band has shifted from CCH_3 to CCD_3 at all indicates a certain degree of mode mixing. Whether this is greater between the νCC and a symmetric CH mode in CCH_3 or between νCC and a symmetric CD mode in CCD_3 is difficult to assess.

The 1077cm^{-1} band may be the δCD_{3s} vibration of CCD_3, shifted from 1337cm^{-1} in CCH_3. The is a shift of 1/1.24. It could also be the δCD_{3s} vibration of species B (methyl), shifted from 1360cm^{-1}. This is a shift of 1/1.26.

The Teller-Redlich Product rule [44] states that the product of the observed shifts for all vibrational modes of the same symmetry type is approximately equal to the

product of all the 'predicted shifts'. The band positions and assignment for CCD_3 on various single crystals and $CD_3Co_3(CO)_9$ are shown below in Table 4.4.

Table 4.4 Band position(cm^{-1}) and assignment for CCD_3.

Ni/Al_2O_3 this work	$CD_3CCo_3(CO)_9$ [21]	Rh(111) [177]	Pt(111) [178]	Assignment
2034	-	2080	2080	νCD_{3s}
1138	1182	1150	1145	νCC
1077	1002	990	1050	δCD_{3s}

The band positions of CCD_3 on Ni/Al_2O_3 reported here are broadly in agreement with those from the other work in Table 4.4. The alumina support in Ni/Al_2O_3 prevents observation of modes below that at $1077cm^{-1}$, and without knowledge of all totally symmetric modes the extent of mode mixing cannot be determined with the Teller-Redlich Product rule.

The $1238cm^{-1}$ band is likely to be a vibration of a mixed ethylidyne species, $CCHD_2$. The $\chi(CH_2)+\delta(CH)$ vibration has been observed on Rh(111) at $1246\text{-}1242cm^{-1}$ [179], $1236cm^{-1}$ on Pd/Al_2O_3 [180] and between 1240 and $1237cm^{-1}$ on Ni/Al_2O_3 [157]. This provides evidence of incorporation of stray H atoms into ethylidyne that remain on the catalyst surface after reduction and outgassing. As Figures 4.14 and 4.15 indicate, successive adsorption of C_2D_4 always occurs *via* CCD_3 (2034 and $1138cm^{-1}$). There is also an increase in the $1077cm^{-1}$ band. The $1238cm^{-1}$ mixed ethylidyne band seems to remain constant throughout.

The $2222cm^{-1}$ band may be associated with a νCD_{2s} vibration, similar to that of species C or D previously ($2955/2925cm^{-1}$). This is a shift of 1/1.33 upon deuteration for the $2222cm^{-1}$ band. The weak bands at 2131 and $2068cm^{-1}$ may be either a νCH_{2s} (species C) or νCH_{3s} (species B).

4.4.2 D_2 Covered Surface.

D_2 saturated surfaces were prepared by adsorption of successive 2μmol pulses of D_2 until no more adsorption could be detected. Transmission infrared spectra taken during the adsorption reveal a broad band occurring at $1440cm^{-1}$, as illustrated in

Figure 4.13. Similar bands do not occur for H_2 adsorption at any point in spectra shown here. This may be because, as has already been demonstrated, the catalyst will never be truly 'H_2 free' after reduction and outgassing and so significant bands due to H_2 will already exist in the background spectra recorded before adsorption. Bands due to D_2 will obviously not exist in background spectra, since the catalyst sample has not seen any D_2 prior to D_2 adsorption. Bands assigned to νPtH have been observed on Pt/SiO_2 at 2120cm^{-1} [181] and at 2130cm^{-1} [182], and on Pt(111) at 2160cm^{-1} [183]. This makes it likely that the 1440cm^{-1} band is a νNiD vibration. A $1/\sqrt{2}$ shift of the νNiD band from 1440cm^{-1} would give a νNiH vibration a potential value of 2036cm^{-1}.

Successive transmission infrared spectra produced after adsorption of C_2D_4 onto a D_2 covered surface are shown in Figure 4.14 (1630-1050cm^{-1}) and Figure 4.15 (2400-1950cm^{-1}). The CCD_3 bands at 2034 and 1138cm^{-1} are less intense on this D_2 covered surface relative to the same bands on the D_2 free surface. This is apparently the reverse of the situation of CCH_3 intensities on 'H_2 free' and H_2 saturated surfaces. Significantly more C_2D_6 is produced, as would be expected. Successive adsorption of C_2D_4, as with successive pulses of C_2H_4, increases the ethylidyne CCD_3 (2034, 1138 and 1077cm^{-1} bands). No effect on the νNiD band at 1440cm^{-1} could be detected.

4.4.3 Deuteration of surface species.

The effect of a 2μmol pulse of D_2 injected into the carrier gas on surface bands is shown in Figure 4.16 with successive DRIFTS spectra. The 2222cm^{-1} feature is approximately doubled in intensity, with a slight loss in intensity for the 2034cm^{-1} band. Very little effect is seen on the bands in the 1600-1050cm^{-1} region (not shown). This is consistent with the behaviour of C_2H_4 derived species upon hydrogenation. The 2222cm^{-1} band is strengthened by deuteration of carbonaceous deposits to form new species, previously identified as ethyl or C_4s. The 2131cm^{-1} band disappeared on deuteration, indicating that this must be associated with the easily hydrogenated species B and not the 2068cm^{-1} band. The fact that the 1077cm^{-1} band is not attenuated confirms that this is the δCD_{3s} vibration of CCD_3, and not therefore associated with species B.

4.4.4 Temperature Programmed Desorption.

Transmission infrared spectra recorded as a function of temperature between 25°C and 190°C are illustrated in Figure 4.17 (2400-1950cm^{-1}) and Figure 4.18 (1630-1050cm^{-1}). CCD_3 appears to be lost at 100→115°C. The mixed ethylidyne decays between 115 and 130°C. The 2222cm^{-1} band disappears between 130 and 145°C. The 1440cm^{-1} band also begins to decay at this temperature, but only disappears at 190°C.

The loss of D_2 by 190°C is in agreement with the maximum in desorption rate of H_2 from Ni/Al_2O_3 at 170°C (Figure 3.30), assuming that D_2 and H_2 desorb at the same rate.

The chemistry of C_2H_4 and C_2D_4 is broadly in agreement. CCD_3 was formed upon initial adsorption of C_2D_4. A deuterated equivalent of species B (methyl) was formed from the decay of CCD_3 at 2131cm^{-1} (the 1360cm^{-1} band had shifted to below the alumina cut-off). The 2222cm^{-1} bands is likely to be the same as the previously designated species D. A strengthening of this band upon deuteration is consistent with the deuteration of carbonaceous species as before. The complete identification of the deuterated equivalents of species B, C, and D is hampered by lack of CD deformation data in the infrared spectra, although the overall C_2D_4 chemistry appears consistent with that of C_2H_4.

4.5 H/D Mixed Systems.

4.5.1 Deuteration of C_2H_4 derived adsorbates.

Figure 4.19 shows successive transmission infrared spectra produced on adsorption of C_2H_4 on a 'H_2 free' surface. A 2μmol pulse of D_2 is introduced at the third spectrum. The 1337 and 1122cm^{-1} ethylidyne bands are reduced in intensity by about two thirds. The usually attenuated 1360cm^{-1} band is again mostly removed, and a new band at 1238cm^{-1} forms.

This 1238cm^{-1} band is again attributed to the $CCHD_2$ 'mixed' ethylidyne species. Since the CCH_3 bands are reduced, the $CCHD_2$ seems to form by replacement of hydrogen in the existing CCH_3 with a D_2 molecule. However, Figure 4.8 reveals that hydrogenation does not affect the CCH_3 band intensities, although the bands do shift slightly. Deuteration gives direct evidence that there is significant movement of

hydrogen within the CCH_3 structure, with continual exchange between this and surface hydrogen. A peak at 2034cm^{-1} was not observed, indicating that there was not significant formation of the completely deuterated CCD_3.

No new species at 1377cm^{-1} was formed on deuteration, unlike for hydrogenation of C_2H_4 derived surface species, although the 1360cm^{-1} band is removed in both cases. Evidently this 1377cm^{-1} is produced by incorporation of hydrogen into the structure, and so when deuterium is added, the band is shifted to below the infrared cut-off of the Al_2O_3 support. This would indicate a shift of greater than 1/1.3.

4.5.2 C_2H_4 Adsorption onto a D_2 Covered Surface.

Figure 4.20 illustrates successive transmission infrared spectra produced on adsorption of a 4μmol pulse of C_2H_4 onto a previously D_2 saturated surface. As usual the CCH_3 bands appear at 1337 and 1122cm^{-1} as well as the mixed $CCHD_2$ band at 1238cm^{-1}. As the 1337 and 1122cm^{-1} bands decay, the usual 1355→1360cm^{-1} is not formed as the decay product. No other band can be observed to increase as the ethylidyne decays. Adsorption of another pulse of C_2H_4 again only regenerates these ethylidyne bands. Decay of these regenerated bands appears to be slower and there is evidence of the 1360cm^{-1} band (species B) making its first appearance as the 1337cm^{-1} band decreases. This may be because initial CCH_3 decay involves incorporation of the remaining D_2, but forms a species that is not observable. Once used up, the ethylidyne decays as before with incorporation of hydrogen to form the 1360/2894cm^{-1} species.

4.6 Mass Spectral Analysis.

4.6.1 C_2H_4 adsorption.

Figure 4.21 shows analysis of gas phase products released on interaction of 3 pulses of C_2H_4 over Ni/Al_2O_3 at 25°C, using the equipment described in Figure 3.26. The initial pulse produces a large burst of ethane, which leads the breakthrough of unreacted ethene. The 2nd and 3rd pulses each produce small amounts of ethane. Approximately 5% CH_4 is also produced at each pulse, as is 0.5% C_4H_{10}.

Figure 4.22 illustrates a frontal chemisorption chromatography experiment (FCC) of C_2H_4 over Ni/Al_2O_3. A flow of 15% C_2H_4 in He, flowing at 58cm^3/min, is switched in and the eluent gas stream monitored for C_2H_4 and C_2H_6. Once again a

pulse of C_2H_6 is observed, before unreacted C_2H_4 breaks through. Integration of the ethane traces for both experiments, and the ethene adsorbed/reacted is shown in Table 4.5 below.

Table 4.5 Quantity of ethene adsorbed/reacted and ethane produced at 25°C.

	Pulsed Chemisorption (0.195g Ni/Al_2O_3)	Reactive Frontal Chromatography (0.184g Ni/Al_2O_3)
Total C_2H_4 adsorbed or reacted (molecules)	5.02×10^{19}	4.4×10^{19}
C_2H_6 produced (molecules)	1.48×10^{19}	1.39×10^{19}
∴ C_2H_4 adsorbed (molecules)	3.54×10^{19}	3.01×10^{19}
No. of nickel surface atoms if $28m^2/g$ (Ni_s)	9.83×10^{19}	9.29×10^{19}
Ni_s : total C_2H_4 ratio	1 : 0.51	1 : 0.47
Ni_s : C_2H_6 ratio	1 : 0.15	1 : 0.15
∴ Ni_s : adsorbed C_2H_4	1 : 0.36	1 : 0.32

Knowing that the nickel surface area is $28m^2/g$, reveals that the ratio of the number of nickel surface atoms:C_2H_6 molecules produced is 1:0.15 i.e. 1 ethane molecule produced for every six nickel surface atoms. Experiments reveal that that the nickel surface atom:C_2H_4 adsorbed/reacted ratio is 1:0.47→0.51 i.e. approximately one C_2H_4 molecule either reacts or is adsorbed by 2 nickel atoms. Removing the known amount of ethene used up as $C_2H_4 \rightarrow C_2H_6$, reveals that approximately 1 ethene molecule is left adsorbed per 3 nickel surface atoms after production of ethane. If it is assumed that the majority of hydrogenation of C_2H_4 to C_2H_6 is self-hydrogenation then each carbon atom in the C_2H_4 requires one nickel atom for bonding and reaction.

4.6.2 Temperature Programmed Desorption.

Figure 4.23 shows the gas phase products desorbed during a temperature programmed desorption experiment from 25°C up to 550°C, after adsorption of C_2H_4 at 25°C *via* Reactive Frontal Chromatography. Only CH_4 is produced in significant quantities during desorption, with three distinct desorption maxima at 220, 270 and 335°C. Integration of the CH_4 profile reveals that the number of CH_4 molecules desorbed is 2.16×10^{19}, produced from a known amount of C_2H_4 adsorbed of 3.01×10^{19} molecules. In other words, approximately one third of the carbon atoms laid down by the C_2H_4 adsorption are removed in desorption.

The H:C ratio of coke deposits before and after desorption may be calculated by taking into account the number of carbon and hydrogen atoms required for self-hydrogenation and the number required for desorption of CH_4. This 'C/H audit' is listed in Table 4.6 below.

Table 4.6 C/H audit for C_2H_4 adsorption, reaction and desorption.

	No. C atoms	No. H atoms	H:C ratio
Total C_2H_4 consumed	1.004×10^{20}	2.008×10^{20}	2
C_2H_6 formed	2.96×10^{19}	8.88×10^{19}	3
Remaining surface deposit after C_2H_6 evolution	7.08×10^{19}	1.12×10^{20}	1.58
CH_4 desorbed	2.16×10^{19}	8.64×10^{19}	4
Remaining surface deposit after TPD of CH_4	4.92×10^{19}	2.56×10^{19}	0.52

The number of nickel surface atoms is approximately 9.3×10^{19}, calculated assuming a surface density to be the same as that of Ni(111) i.e. 1.8×10^{19}atoms/m^2. The above C/H audit is calculated on the basis that the surface was both hydrogen and carbon free before C_2H_4 adsorption. As has already been demonstrated, a small quantity of hydrogen always seems to be present on the surface, even after extensive outgassing and desorption. The H:C ratio of 1.58 of the species present on the surface after C_2H_4 adsorption is approximate for C_2H_3 (1.5). This would appear consistent with the initial formation of CCH_3 as the dominant product. Thus, self hydrogenation

of C_2H_4 to C_2H_6 appears to proceed until the C/H deposit has the approximate formula C_2H_3. One hydrogen atom has been lost by each ethene molecule left on the surface.

Figure 4.24 illustrates a TPD experiment performed after C_2H_4 reactive frontal chromatography at -133°C. The RFC revealed that at this temperature only C_2H_4 was adsorbed, without any hydrogenation to C_2H_6. Calculation showed that for 0.264g of Ni/Al_2O_3 (9.5 x 10^{19} surface nickel atoms) that 6.4 x 10^{20} molecules of C_2H_4 were adsorbed (approximately 6.8 for each nickel atom). As the boiling point of ethene is -103°C, it is evidently condensing onto both metal and support at this temperature.

The TPD experiment illustrated in Figure 4.24 does not show the C_2H_4 trace, because a huge desorption (detector response 1 x 10^{-7}) occurs at -100°C as the C_2H_4 'boils off' from the catalyst. Integrating the area underneath this desorption peak reveals that 5.85 x 10^{20} molecules are desorbed, leaving 5.5 x 10^{19} C_2H_4 molecules on the surface. No further desorption of C_2H_4 occurred. The peaks at -100°C in the CH_4 and C_2H_6 (broad) traces, may be due to impurities in the original C_2H_4.

The next significant event occurs at -40°C with a peak in the C_2H_6 trace. The boiling point of ethane is -89°C and so distilling off of liquid ethane contributes to the broad peak at -100°C. The peak at -40°C is due to self hydrogenation of C_2H_4 to C_2H_6. Integration of this peak reveals that 1.33 x 10^{18} molecules of C_2H_6 are desorbed. CH_4 desorbs over a large temperature range from 100°C up to 500°C, with peaks at 200 and 410°C. This desorption is broadly similar to that in Figure 4.23 from the adsorption of C_2H_4 at 25°C. Integration shows that 1.08 x 10^{19} CH_4 molecules are desorbed.

4.7 Analysis of Coke Deposits.

Both Temperature Programmed Oxidation (TPO) [184] and Temperature Programmed Hydrogenation (TPH) [185], [186] have been used for characterisation of surface carbonaceous species. Both are used here to study coke deposits left after temperature programming of C_2H_4 covered surfaces up to 300°C, and cooling back to room temperature.

4.7.1 Temperature Programmed Oxidation.

Coke deposits are analysed by temperature programming a coked catalyst in a 10% O_2 in He stream. The eluent gas stream was monitored for both carbon monoxide and carbon dioxide as well as for water and for oxygen. Figure 4.25 shows the trace of such an experiment from 25°C up to 600°C at 10°C/min. The upper trace of O_2 shows that there was a peak in O_2 consumption centred at 300°C. Figure 4.26 shows the scale expanded CO_2, CO and H_2O traces. A broad production in CO_2 begins at 130°C. The CO trace decays throughout the TPO because CO is produced initially on switching in the oxygen stream (see below). Production of H_2O begins at 370°C. Integration of the CO_2 trace reveals that 1.84×10^{19} molecules of CO_2 are produced, from a known remaining coke deposit of 4.92×10^{19} carbon atoms (Table 4.6). Integration of the O_2 trace reveals that 5.04×10^{20} molecules are consumed. Significant oxidation of the nickel is evidently occurring at this temperature.

In order to analyse the contribution of the oxidation of coke deposits to CO rather than CO_2, a TPO reaction was performed from -130°C up to 550°C at 10°C/min. Figure 4.27 illustrates the results from this experiment, showing traces from the CO and CO_2 production and O_2 consumption. A peak in production of CO occurs at -70°C before the production of CO_2 commences at 130°C. This is shown in more detail in Figure 4.28. Examination of the oxygen consumption trace indicates that most of the oxygen is consumed at 300°C, evidently because the nickel is oxidised at this temperature. Integration of the CO peak reveals that 4.14×10^{19} CO molecules were released, against 1.28×10^{19} molecules produced for a known deposit of 5.07×10^{19} carbon atoms. This reveals that all of the available carbon is oxidised, and in the ratio of $CO:CO_2$ produced of $2 \rightarrow 3:1$. This study shows that monitoring only CO_2 production will underestimate the coke deposit by greater than 50%.

4.7.2 Temperature Programmed Hydrogenation.

Coke deposits were characterised here by temperature programming the coked catalyst samples in a 10% H_2 in He stream. The eluent stream was monitored for CH_4 production and H_2 consumption. Figure 4.29 shows the TPH trace of a coked catalyst, heated from 25°C up to 330°C. Figure 4.30 is a larger scale view of the CH_4 production trace. A single peak in CH_4 production and H_2 consumption occurs at 175°C.

Integration of this CH_4 peak shows 3.4×10^{19} molecules evolved (for a known number of 4.39×10^{19} carbon atoms in the coke deposit). This means that 77% of the surface carbon is hydrogenated to CH_4. No significant production of other hydrocarbons was detected.

A single peak in CH_4 production between 130 and 230°C has been identified by McCarty *et al.* [186] as hydrogenation of very reactive chemisorbed carbon atoms, designated α-carbon. The fact that only 77% of the surface carbon is hydrogenated may mean that this proportion of the carbon exists in this α form. Several other forms of carbon have been identified, such as bulk nickel carbide, amorphous carbon (β) and filamentous carbon (δ). They are less reactive than α-carbon and are characterised by hydrogenation at much higher temperatures, beyond the range of experiments here. It may be that the 'lost' 23% of the carbon exists in some unreactive form and is therefore not affected by hydrogenation under the experimental conditions used here. This has an important lesson in that complete removal of carbon in order to regenerate the catalyst for further reaction appears impossible if the catalyst is simply re-reduced at 300°C as before during the standard reduction procedure. Treatment with oxygen is necessary in order to remove all of the carbon. However, as demonstrated in Chapter 3, re-oxidising the catalyst inevitably incurs a loss of metal surface area of up to 35% upon re-reduction.

4.8 C_2H_4 Adsorption at Higher Temperatures.

A series of experiments investigating the effect of temperatures between 25 and 200°C on C_2H_4 adsorption and reaction were performed with both infrared and mass spectral analysis.

Table 4.7 shows the gas phase products as a percentage of total gas evolved on adsorption of two 4μmol pulses of C_2H_4 at a series of temperatures between 25 and 200°C. The C_2H_4 value is the amount of C_2H_4 apparently not reacting. Table 4.8 shows gas phase products released on hydrogenation of the surface species, again as a percentage of the total gas evolved.

Table 4.7 Gas Phase Products on C_2H_4 adsorption.

Temperature (°C)	Pulse No.	% Composition of Hydrocarbon Detected				
		CH_4	C_2H_4	C_2H_6	C_4H_{10}	C_3,C_5+
25	1	5.2	44.2	50.1	0.5	-
	2	5.3	53.2	41.0	0.5	-
50	1	6.2	35.9	57.4	0.5	-
	2	23.0	40.0	37.0	-	-
75	1	8.7	43.4	47.1	0.8	-
	2	8.3	48.3	43.3	-	-
100	1	7.9	44.9	46.2	1.0	-
	2	7.8	4.9	43.2	-	-
125	1	9.6	41.9	47.8	0.7	-
	2	9.6	55.8	34.6	-	-
150	1	9.7	53.3	37.0	-	-
	2	25.8	45.2	29.0	-	-
175	1	43.2	22.2	34.5	-	-
	2	62.8	19.1	18.1	-	-
200	1	85.7	7.5	6.9	-	-
	2	88.8	5.9	5.3	-	-

Table 4.8 Gas Phase Products on Hydrogenation of Surface Species.

Temperature (°C)	% Composition of Hydrocarbon Detected				
	CH_4	C_2H_4	C_2H_6	C_4H_{10}	C_3,C_5+
25	16.2	-	54.1	27.0	2.7
50	51.0	-	-	46.1	2.9
75	78.3	-	-	20.2	1.5
100	90.9	-	-	9.1	-
125	97.1	-	-	2.9	-
150	97.2	-	-	2.8	-
175	99.1	-	-	0.9	-
200	99.6	-	-	0.4	-

Figure 4.31 shows the corresponding DRIFTS surface and gas phase absorption bands of the experiments listed in Tables 4.7 and 4.8. Only the bands in the 1600-1080cm^{-1} region are plotted for simplicity. The eight graphs show the surface bands generated on adsorption of two pulses of ethene and subsequent hydrogenation, at a series of temperatures between 25 and 200°C.

The 25°C plot shows the C_2H_4 adsorption behaviour that has been discussed already. Initially CCH_3 formed, decaying into the species designated B (at 1360cm^{-1}), C (at 1425cm^{-1}) and D (at 1455cm^{-1}). Between 50 and 125°C, C_2H_4 adsorption generated progressively smaller quantities of CCH_3 and the decay to species B became much more rapid. The quantity of B formed also became gradually smaller from 50 to 125°C. At 125°C the CCH_3 decayed totally between pulses, as did the 1455cm^{-1} band of species D. This left the 1360cm^{-1} band of species B as the only infrared surface band between pulses. At 150°C, the only surface band generated was that of species B, and this was only on the second pulse of C_2H_4. The first pulse of C_2H_4 did not generate either surface or gaseous absorption bands. The second pulse generated methane (1306cm^{-1}). At 175°C, only gas phase methane was generated on the second C_2H_4 pulse, without surface bands. Finally, at 200°C, methane was again generated, but this time on adsorption of both pulses of C_2H_4.

Adsorption of C_2H_4 produces mainly C_2H_6 and CH_4 in the gas phase, along with unreacted C_2H_4, as illustrated in Table 4.7. A small amount of C_4H_{10} (<1%) is also

detected. The amount of CH_4 detected increases as a function of temperature, from 5% of the gas stream at 25°C up to over 85% of the stream at 200°C. Until 150°C, the percentage of C_2H_6 in the stream remains at 50% with 45% of the C_2H_4 not reacting and the balance methane. At 150°C, the amount of ethane produced decreased to 37%, falling to 7.2% by 200°C. This is mirrored by a correspondingly greater production of methane, at 9.7% for 150°C adsorption rising to 85.7% for 200°C adsorption of C_2H_4. At these higher temperatures the percentage of ethene reacting increases, with only 7.2% not reacted at 200°C.

On hydrogenation at 25°C in Figure 4.31, new bands at 1377 and 1460cm^{-1} were generated, with loss of the 1360 and 1455cm^{-1} bands. Ethane was only produced upon hydrogenation at 25°C. Above this temperature the gas phase products on hydrogenation were dominated by CH_4 and C_4H_{10}. The CCH_3 bands remained largely unaffected. No gas phase infrared absorption bands could be detected. At 50°C, the behaviour was similar, with methane an additional gas phase product on hydrogenation. At 75°C, the CCH_3 was itself hydrogenated with all intensity at 1337cm^{-1} lost. More methane was produced. By 100°C, the production of methane on hydrogenation dominates the spectrum, although 1460 and 1377cm^{-1} bands were still generated. At 125°C the behaviour is similar, although the 1360cm^{-1} band remains before hydrogenation. At 150°C and above, no surface bands were produced and only methane was observed in the gas phase.

Methane is produced by hydrogenating any C_1 containing fragment i.e. CH_3, CH_2, CH or C. Carbonaceous deposits with a low H:C ratio are unlikely to be observed in the infrared as the C-C bonds will probably be parallel to the nickel surface. Consequently, the metal surface selection rule will not enable the vibrations of these bonds to be observed. The νNiC vibrations are not visible either as they are likely to be at approximately 400cm^{-1}. Lehwald *et al.* have observed a CC frequency of 2220cm^{-1} with EELS on the stepped nickel surface Ni[5(111)x(110)], indicative of a CC triple bond [187].

By hydrogenating these carbonaceous deposits, methane may be produced without apparent attenuation of any surface infrared band. This is the case at 150°C and above, where methane is evolved without the existence of any surface bands before hydrogenation. At 125°C methane was produced from both species B and by hydrogenation of carbonaceous deposits. Above this temperature, carbonaceous deposits were the only source of methane on hydrogenation. The fact that species B is a source of methane indicates that it has only one carbon atom. Additionally, single

chemisorbed carbon atoms must exist, which are easily hydrogenated.

Butane is observed on hydrogenation at a maximum at 50°C. The source of this butane must be the hydrogenation of a C_4 species, that has formed on C_2H_4 adsorption. The obvious candidate for the butane pre-cursor is species D. The 1455cm^{-1} band of species D was at a maximum at 50°C prior to hydrogenation. This correlates with the maximum in butane production in Table 4.7. At 125°C and above, species D has decayed and consequently very little butane was observed in the gas phase on hydrogenation. Consequently species D must contain four carbon atoms.

The bands generated by hydrogenation are at 1377, 1460, 2847 and 2960cm^{-1} (Figure 4.8). The 1425 and 2925cm^{-1} peaks (species C) remain throughout. The hydrogenated bands form only at temperature up to 125°C, and can be designated species E. This group of frequencies is remarkably similar to those of CH_2 and CH_3 groups in adsorbed alkanes [188]. Table 4.9 below illustrates the group frequencies of the alkanes (adapted from [188]).

Table 4.9 Group Frequencies of Adsorbed Alkanes.

Group	Frequency	Assignment
CH_3	2955 ±5	νCH_{as}
	2870 ±5	νCH_s
	1462 ±5	δCH_{as}
	1380	δCH_s
CH_2	2927 ±5	νCH_{as}
	2855 ±5	νCH_s
	1467 ±5	δCH_s

The formation of bands at 2960, 1460 and 1377cm^{-1} on hydrogenation seem to indicate CH_3 groups in a chemisorbed alkane species. The 2870cm^{-1} band is already present as the CH_3 stretch in CCH_3. Bands at 2925 and 2847cm^{-1} (both weak), indicate the presence of CH_2 groups in the adsorbed alkane. The asymmetric bands can only be seen because the CH_2 and CH_3 group are free to rotate. The exact chain length of these alkane species is difficult to determine. Campione and Ekerdt [188] describe a strongly adsorbed metallabutane species bonded in the 1,1,3 or 1,1,2 configuration, which is very resistant to hydrogenation. Species E may be a similar

species to this, although the number of carbon atoms in the structure is difficult to determined. The relative intensities of the 2960cm^{-1} (νCH_{3as}) and 2925cm^{-1} (νCH_{2as}) peaks have been used to determine the number of these groups in a molecule and, assuming no chain branching, can give a value for carbon chain length [45]. For hydrogenation at 25°C, the 2925/2960cm^{-1} ratio of species E was measured to be ≈0.5. This is close to that reported by Eischens and Pliskin [41] of 0.6, which they assigned to a CH_2/CH_3 ratio of 1:1, i.e. $-CH_2CH_3$ (ethyl), $CH_3CH_2CH_2CH_3$ (metallabutane) etc. However, this technique is possibly suspect, as one must first be sure that all intensity at 2960 and 2925cm^{-1} belongs to one species.

A possible identity of species E is that of the ethyl group, $-CH_2CH_3$. De la Cruz and Sheppard [182] have identified peaks on Pt/SiO_2 at 2960 (νCH_{3as}), 2930 (νCH_{2s}), 2875 (νCH_{3s}), 1470 (δCH_{3as}) and 1380cm^{-1} (δCH_{3s}) as those of an ethyl type structure, generated by hydrogenation of C_2H_4 derived surface species. These bands are generally consistent with the bands remaining after hydrogenation of C_2H_4 derived surface species on Ni/Al_2O_3.

4.8.1 Species Identification.

Species A, characterised by infrared absorption bands at 2870-2875, 1334-1339 and 1115-1122cm^{-1} has been unambiguously assigned to the ethylidyne (CCH_3) species. Since CCH_3 has C_{3v} symmetry it may only be bound to a 3-fold or on top nickel sate. As mentioned in the Introduction, the (111) face is predominant in nickel particles greater than 5nm in diameter, which is the case for the Ni/Al_2O_3 used here. It is likely that the ethylidyne is bound to the 3-fold sites on the (111) surfaces. In fact CCH_3 formation has been used as a measure of the extent of Pd(111) in a Pd/Al_2O_3 catalyst [189].

From infrared evidence, species B is known to contain a CH_3 group. Hydrogenation of B has been shown to be accompanied by production of methane, revealing that it contains a single carbon atom. It is likely that B is a methyl ($-CH_3$) species. Species D contains CH_2 groups from infrared evidence, and is associated with the production of butane in the gas phase on hydrogenation. A C_4, CH_2 containing species, that does not contain CH_3 groups, is likely to be an n-butyl type species ($-CH_2CH_2CH_2CH_2-$). Species C is not always present, and its exact behaviour is difficult to predict. It does appear to be associated with species D, and infrared spectra show it contains CH_2 groups. It was generally too weak to be correlated with production of species in the gas phase on hydrogenation. It may simply be that C is

different CH_2 vibrations of the same species D discussed above. On hydrogenation, a new species E forms, which may be an adsorbed ethyl or metallabutane type species.

4.9 Conclusions.

Several surface reactions for the 'H_2 free' system are summarised in Scheme 1, 2, and 3 below. As Table 4.5 illustrates, for three reacting C_2H_4 molecules, approximately one C_2H_6 molecule is produced. This leaves two partially dehydrogenated species of the formula C_2H_3 left on the surface. Infrared studies show that the first species to form on adsorption of C_2H_4 is always ethylidyne, CCH_3. The initial formation of ethylidyne apparently agrees with the C_2H_4 consumption in Table 4.6, revealing that most of the C_2H_4 not forming C_2H_6, forms CCH_3. Since ethylidyne is believed to occupy three fold sites, each CCH_3 species requires three nickel surface atoms. Table 4.5 shows that each C_2 species adsorb with a Ni_s:C_2 ratio of 1:0.32→0.36 i.e. approximately one C_2 species per three nickel surface atoms. Initially then it appears that most of the consumption of C_2H_4 and surface coverage can be accounted for with the formation of ethylidyne. Saturation of the nickel surface with hydrogen both allows more CCH_3 to form and also prevents its decay to the same extent as on 'H_2 free' surfaces. Much greater production of C_2H_6 is detected.

It is known that ethylidyne decays to both -CH_3 and a CH_2 containing C_4 species. The CCH_3 decays to the greatest extent on the 'H_2 free' surface, possibly because on the H-saturated and H_2/C covered surfaces, more of the nickel surface area is taken up with species other than CCH_3. Thus the decay of CCH_3 may be blocked by lack of surface sites for the decay products. The formation of species C/D involves the polymerisation of four carbon atoms as the CCH_3 decays. The formation of B leaves a single dehydrogenated carbon atom. In these conditions growth of carbon chains is expected. The overall C:H ratio of the carbon deposits formed from CCH_3 decay, excluding the known -CH_3 methyl species, is only approximately 2:3 at most, and likely to be considerably less. In these conditions, it is perhaps not surprising that CH_3 groups cannot be detected.

A proposed reaction scheme for the formation, decay and hydrogenation of ethylidyne on Ni/Al_2O_3 is shown in Figure 4.32 below.

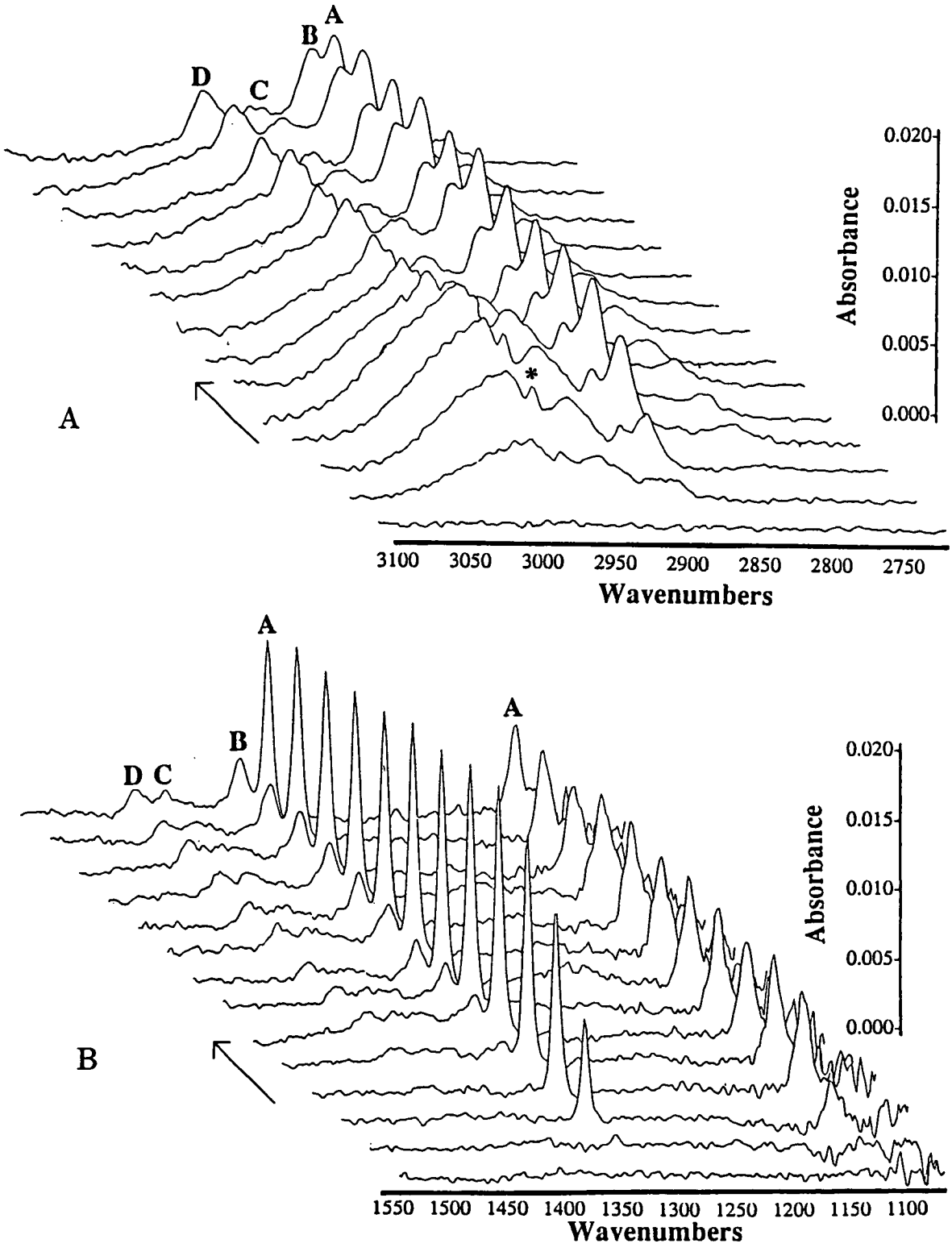

Figure 4.4 *DRIFTS spectra of C_2H_4 adsorption on Ni/Al_2O_3 A) 3100-2700cm^{-1} and B) 1550-1080cm^{-1}.*

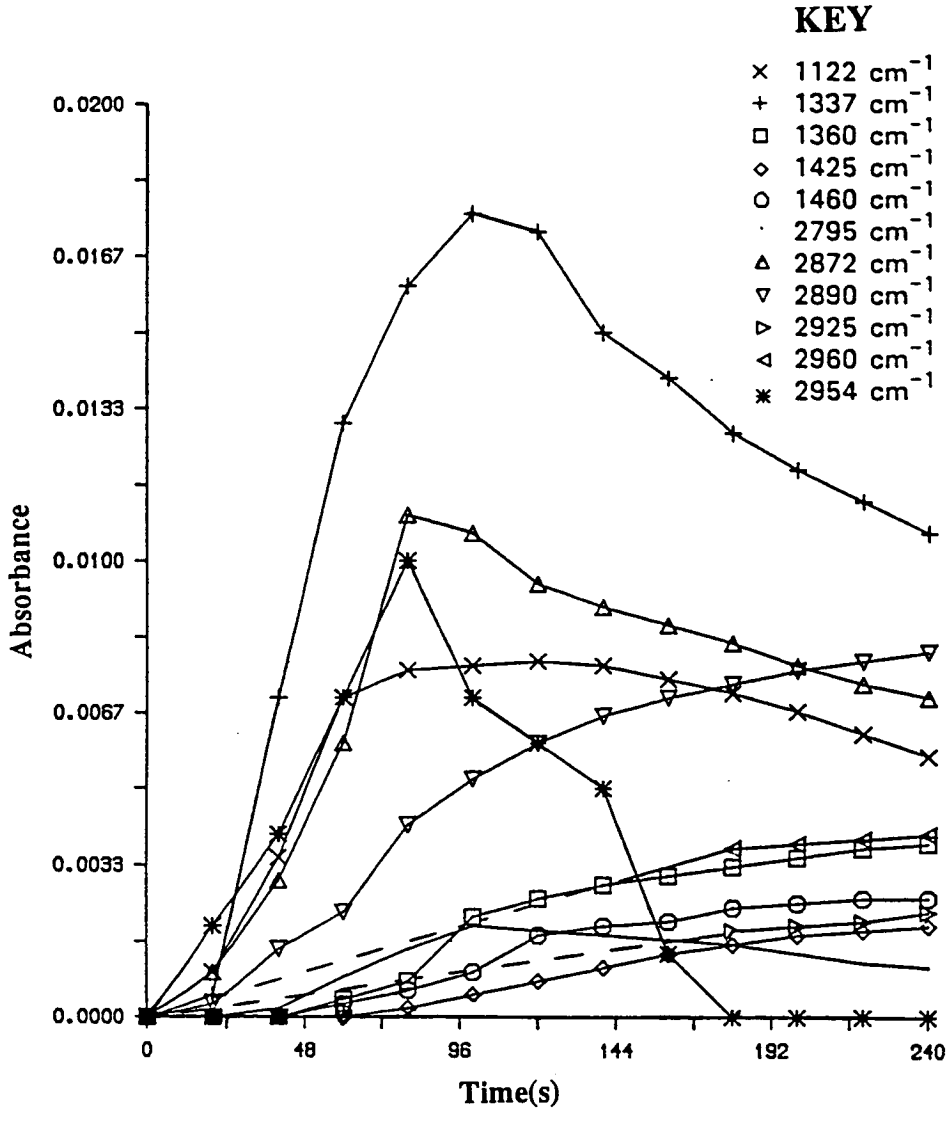

Figure 4.5 *Strength of absorption bands as a function of time produced on adsorption of C_2H_4 on Ni/Al_2O_3.*

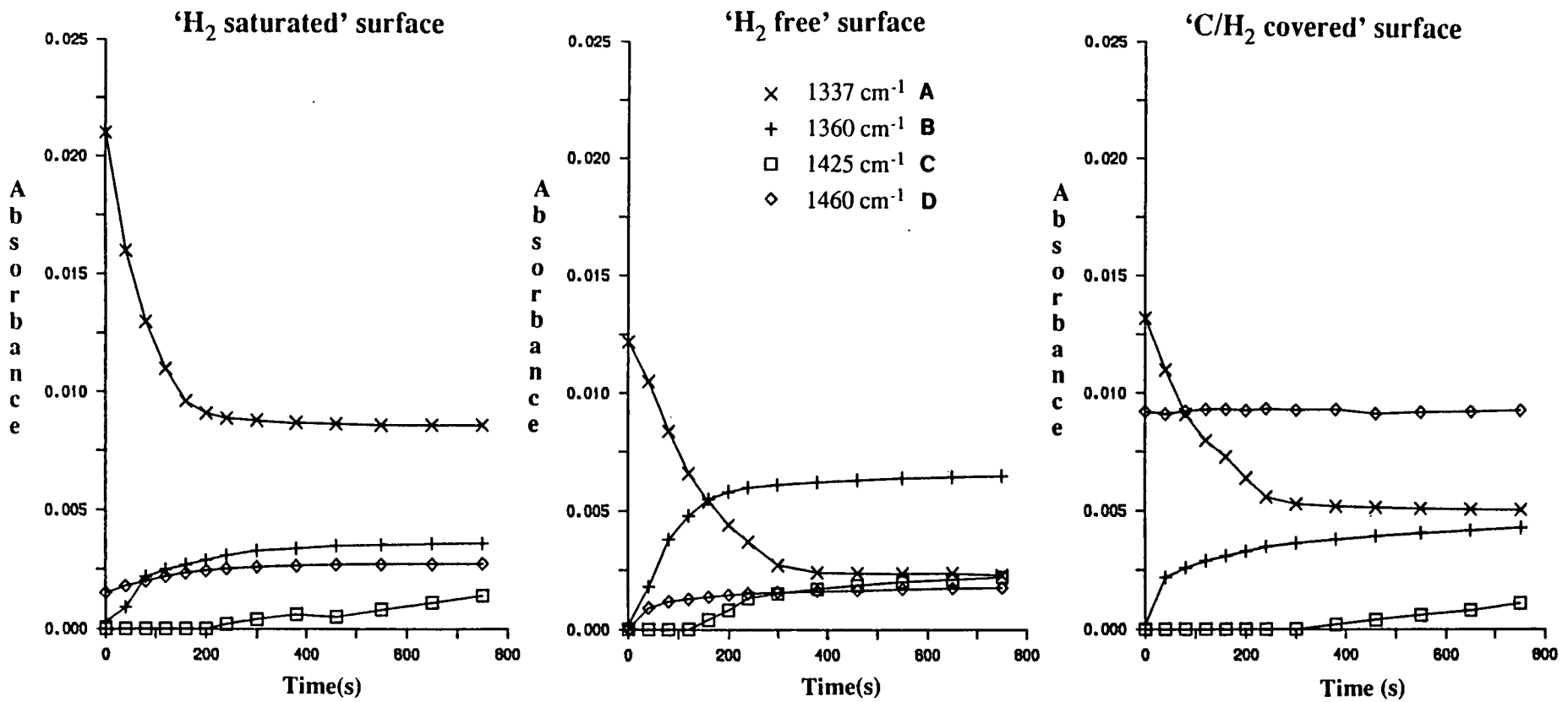

Figure 4.6 *Absorbance bands, in the δCH region, as a function of surface pre-treatment i) H_2saturated, ii) 'H_2 free' and iii) H_2/C covered.*

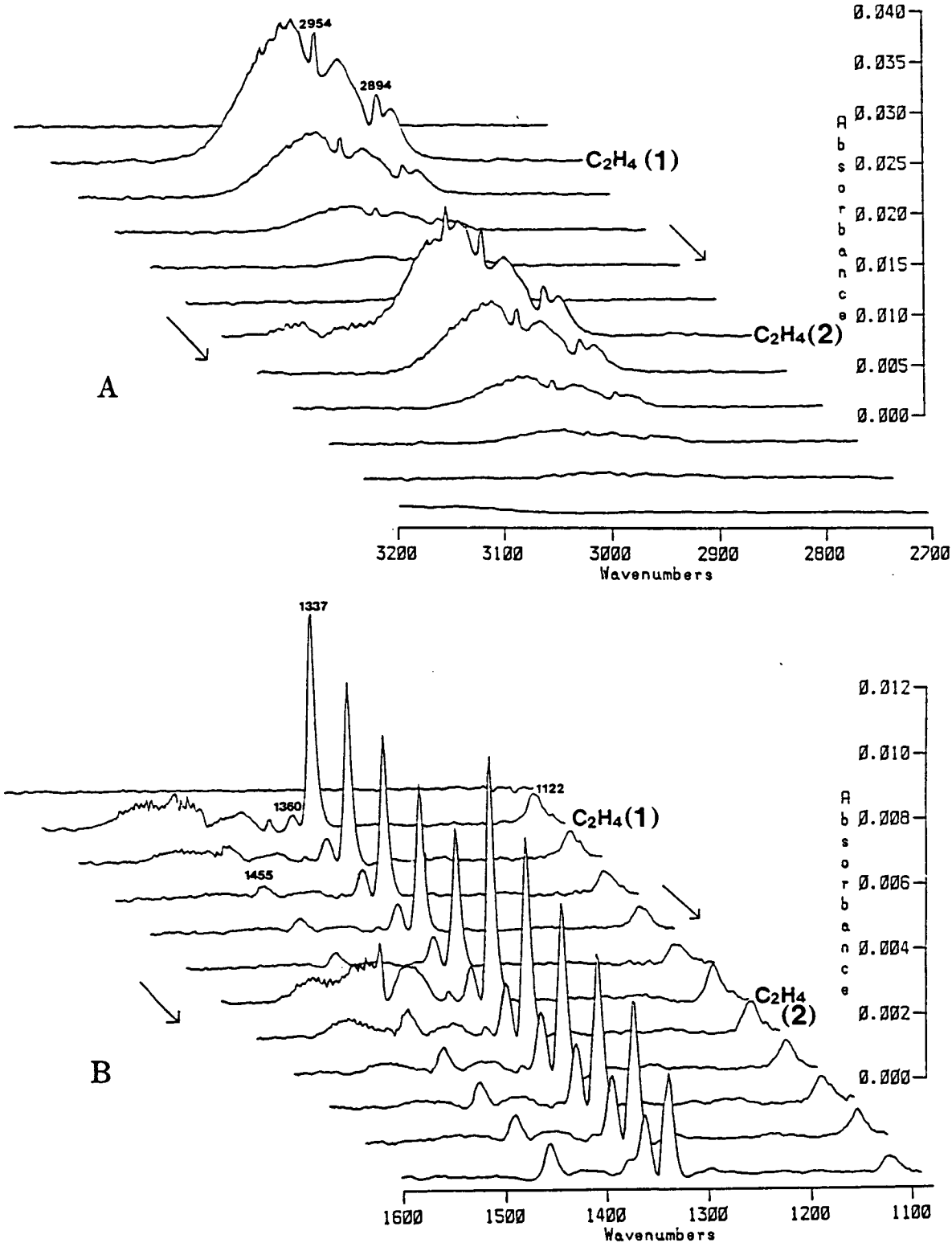

Figure 4.7 *Transmission infrared spectra produced on adsorption of C_2H_4 A) 3200-2700cm^{-1} and B) 1600-1080cm^{-1}.*

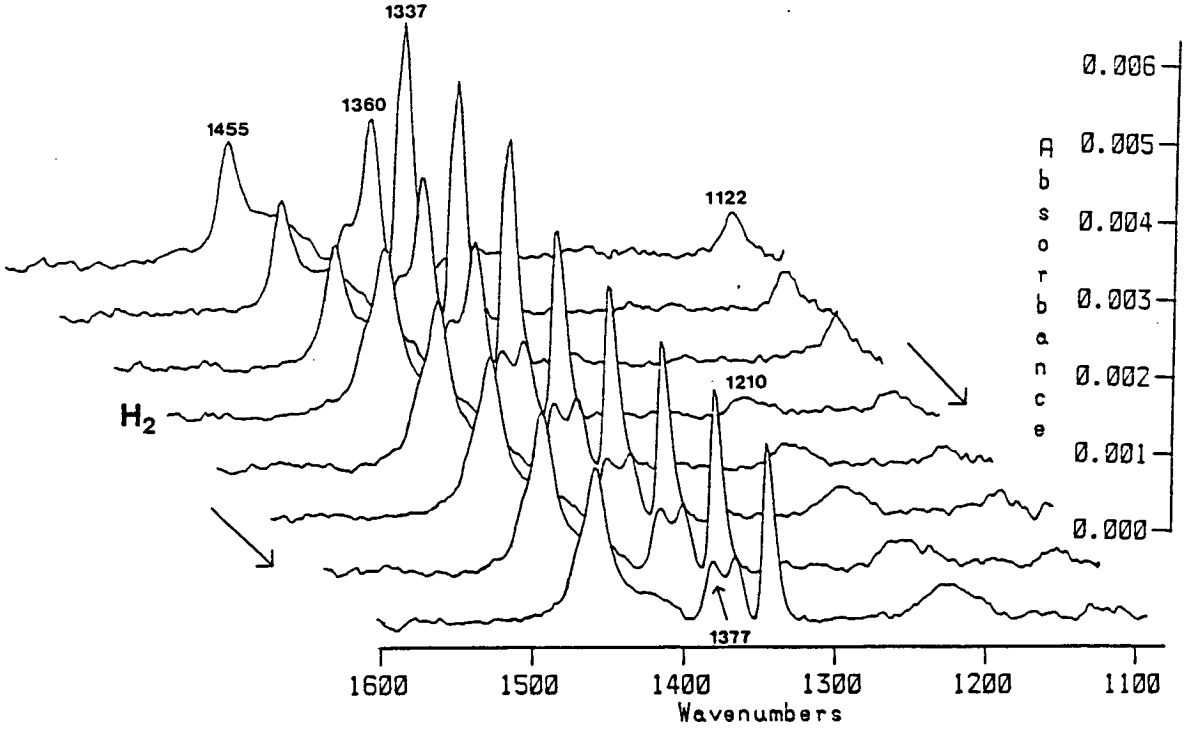

Figure 4.8 A *The effect of hydrogenation on surface bands (transmission spectra, 1600-1080cm^{-1}).*

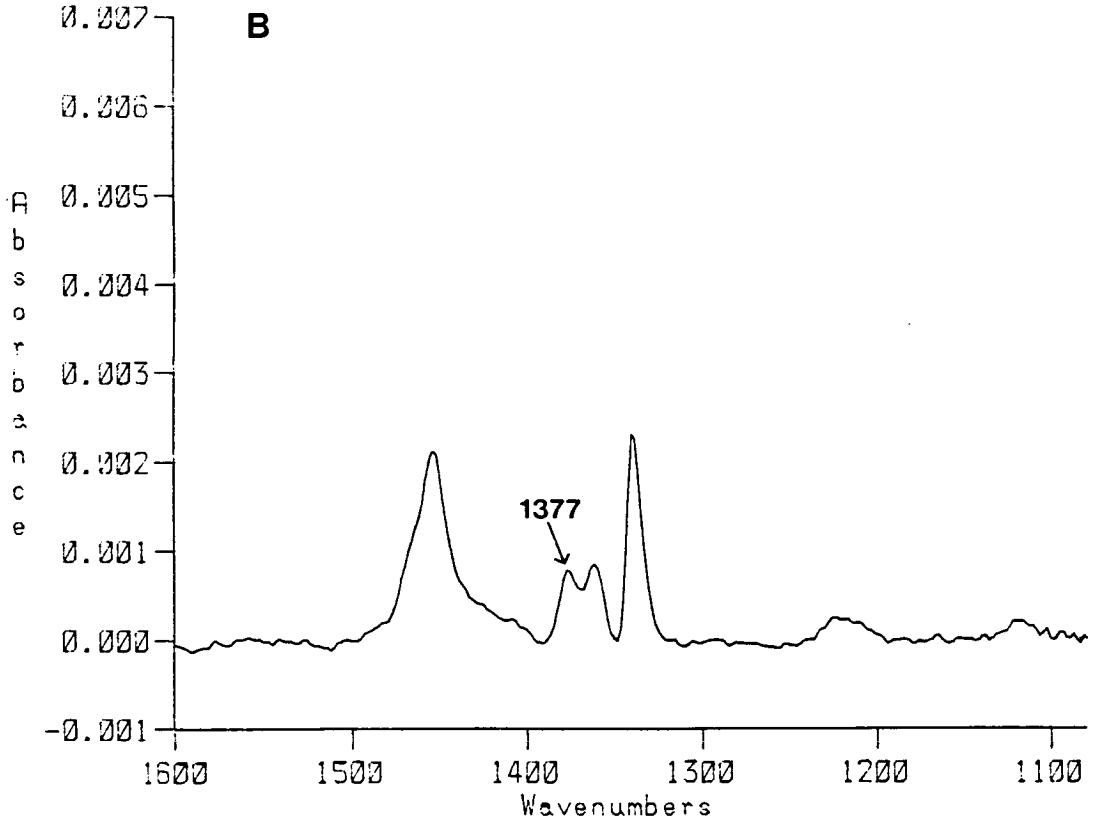

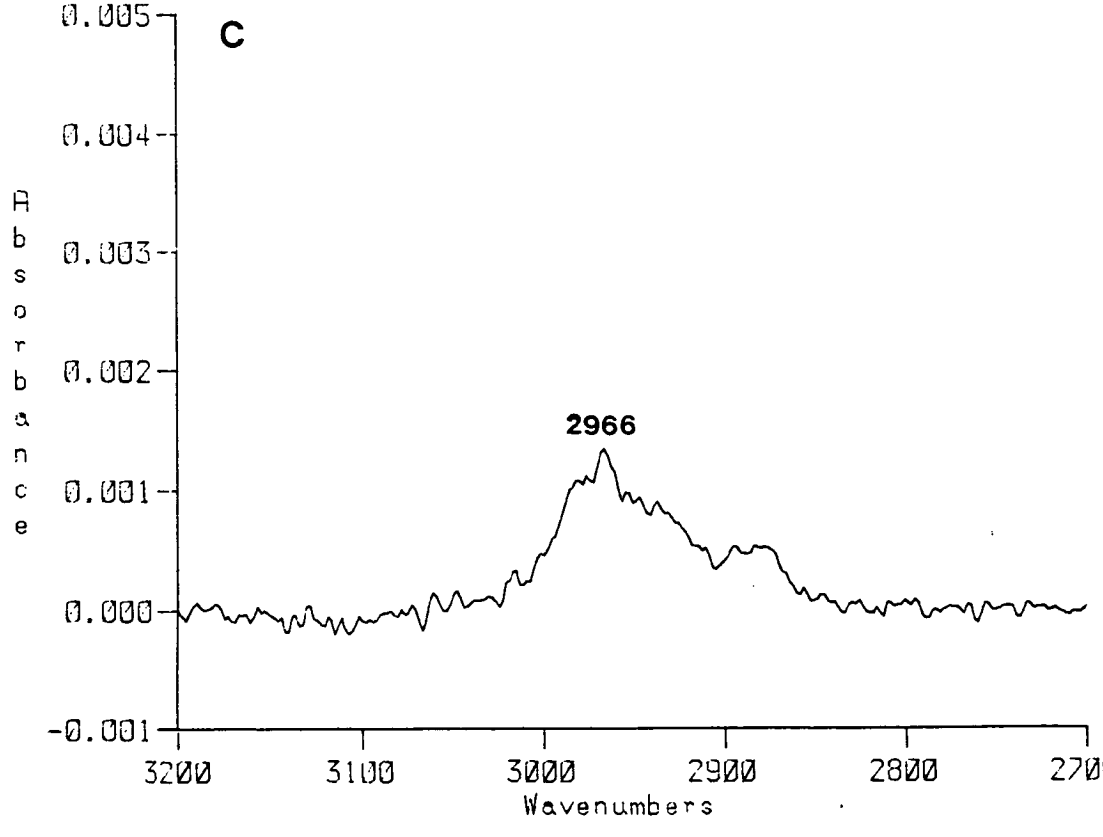

Figure 4.8 B and C *Detail of the single spectrum in Figure 4.8 A at which hydrogenation occurs B) 3200-2700cm^{-1} and C) 1600-1080cm^{-1}.*

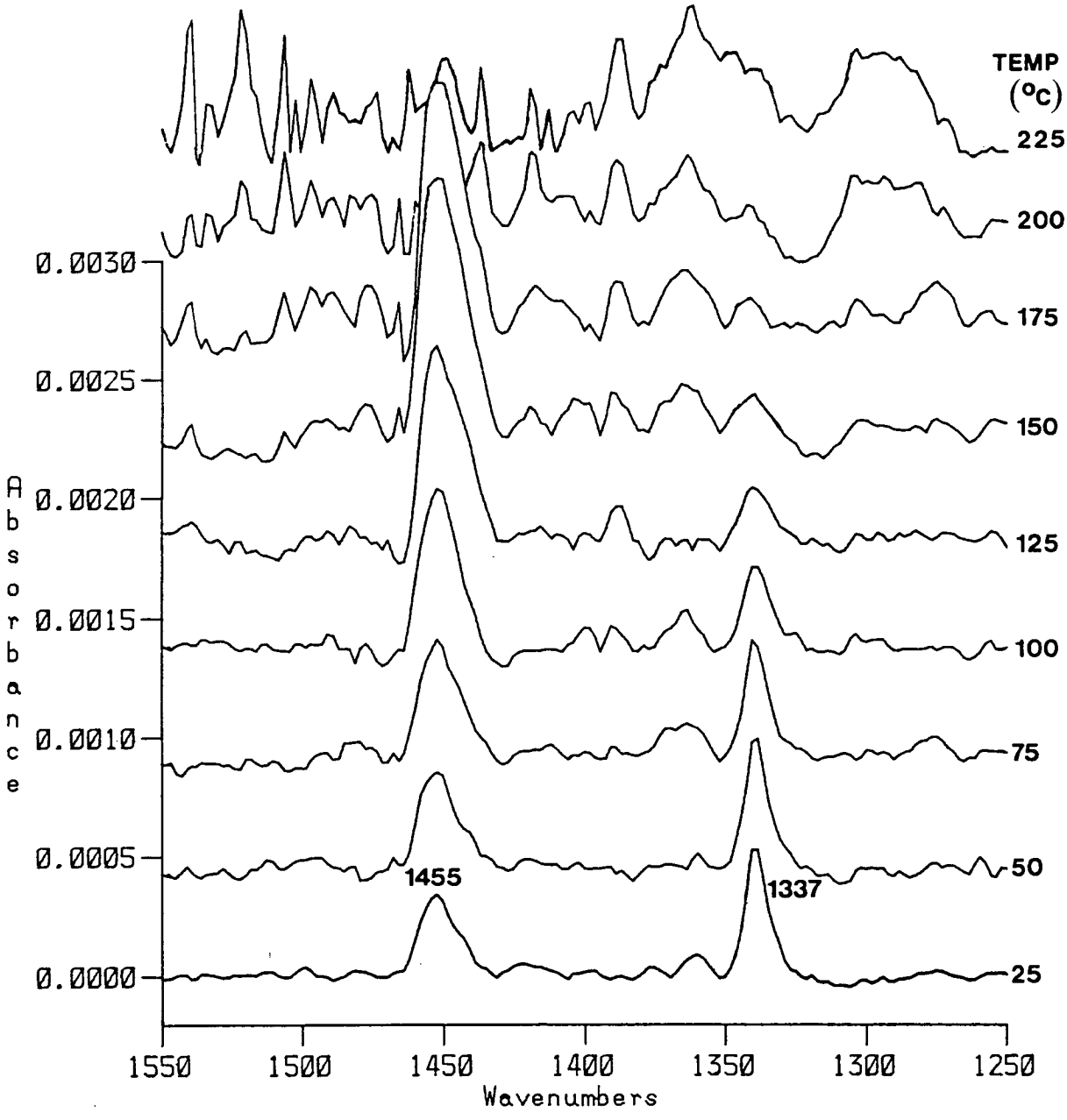

Figure 4.9 *Temperature programmed infrared experiment from 25→225°C (transmission spectra, 1550-1250cm^{-1}).*

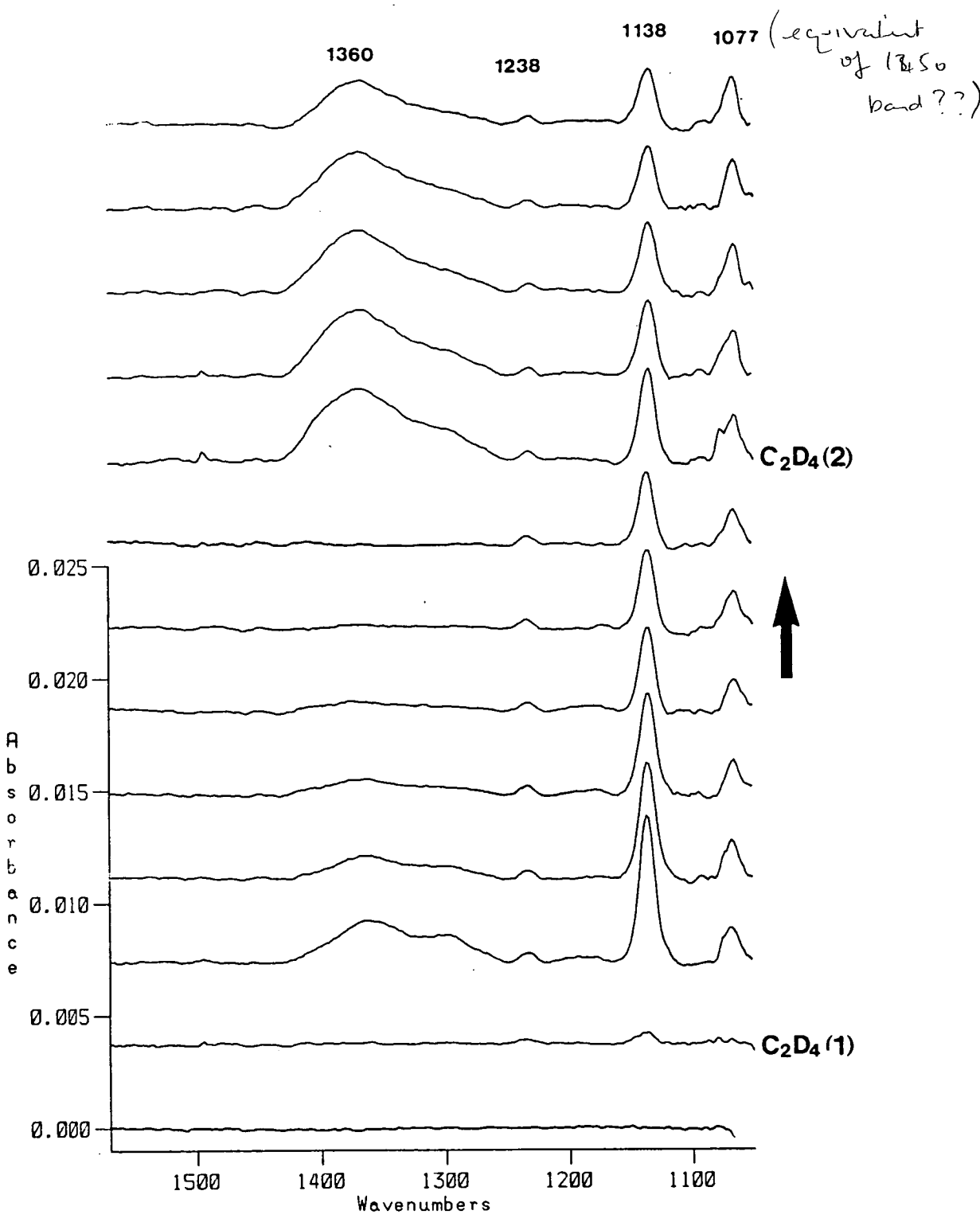

Figure 4.10 *Transmission infrared spectra of C_2D_4 adsorption (2 pulses) onto a 'H_2 free' surface (1600-1050cm^{-1}).*

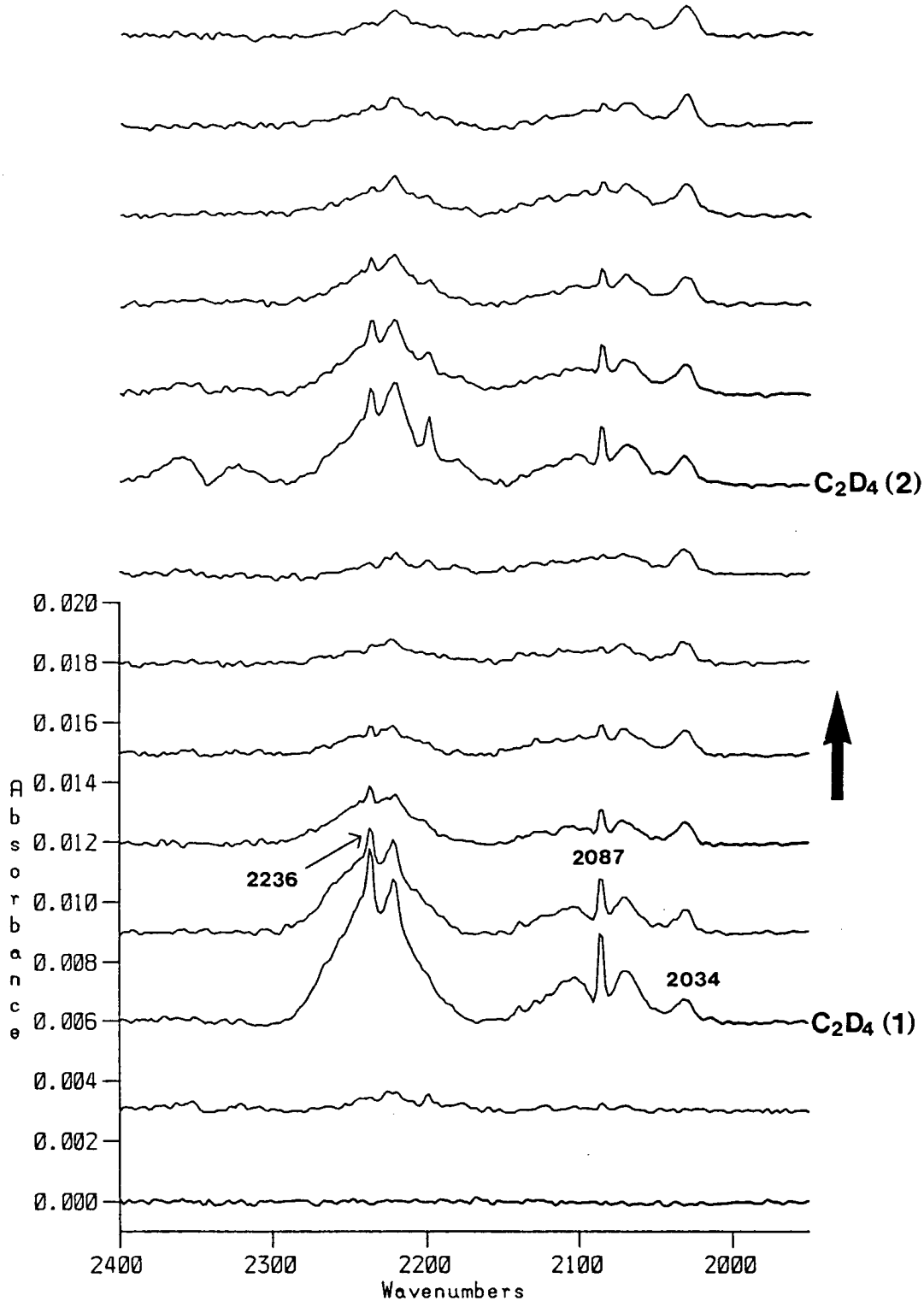

Figure 4.11 *Transmission infrared spectra of C_2D_4 adsorption (2 pulses) onto a 'H_2 free' surface (2400-1950cm^{-1}).*

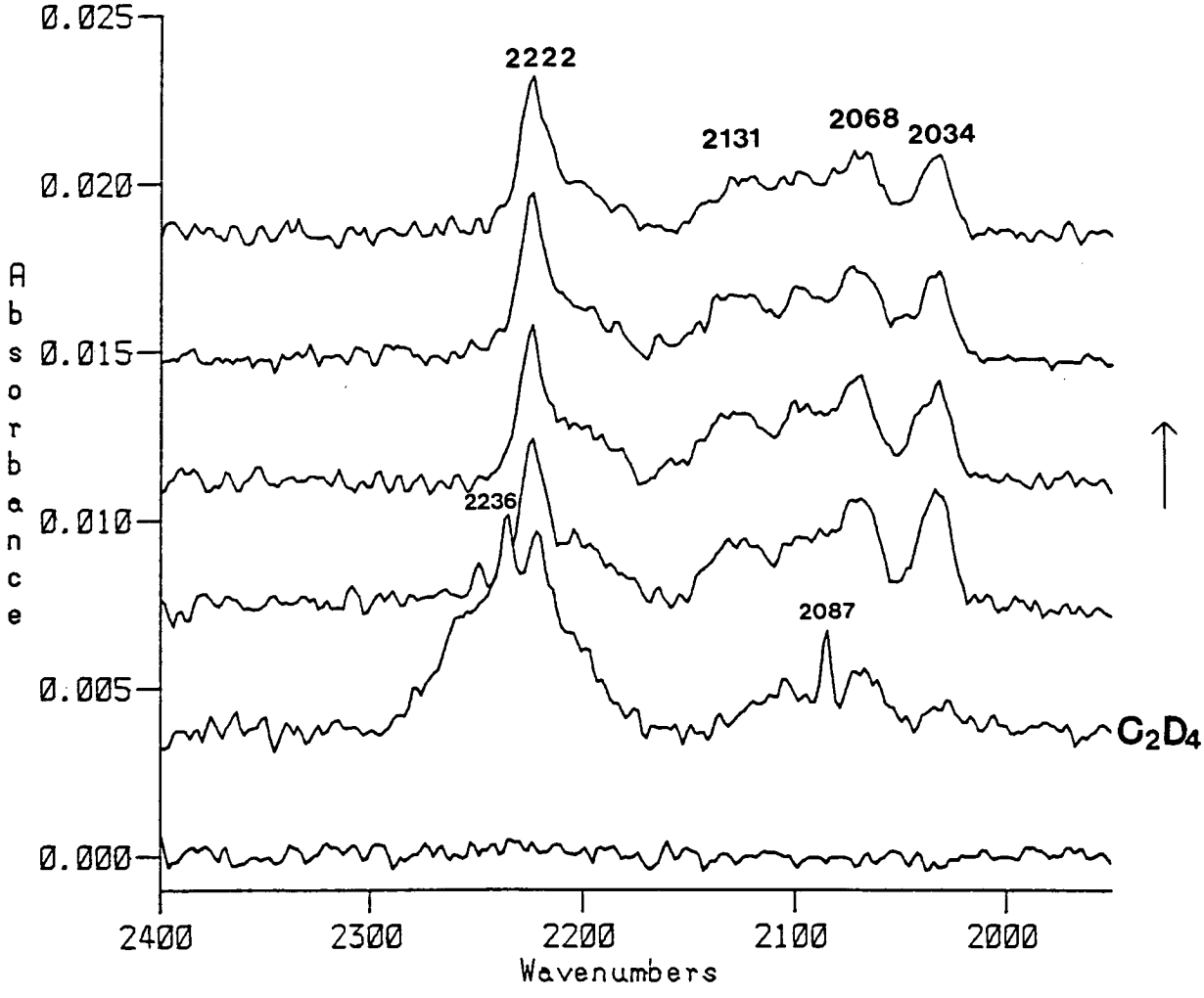

Figure 4.12 *DRIFTS spectra of C_2D_4 adsorption onto a H_2 'free' surface (2400-1950cm^{-1}).*

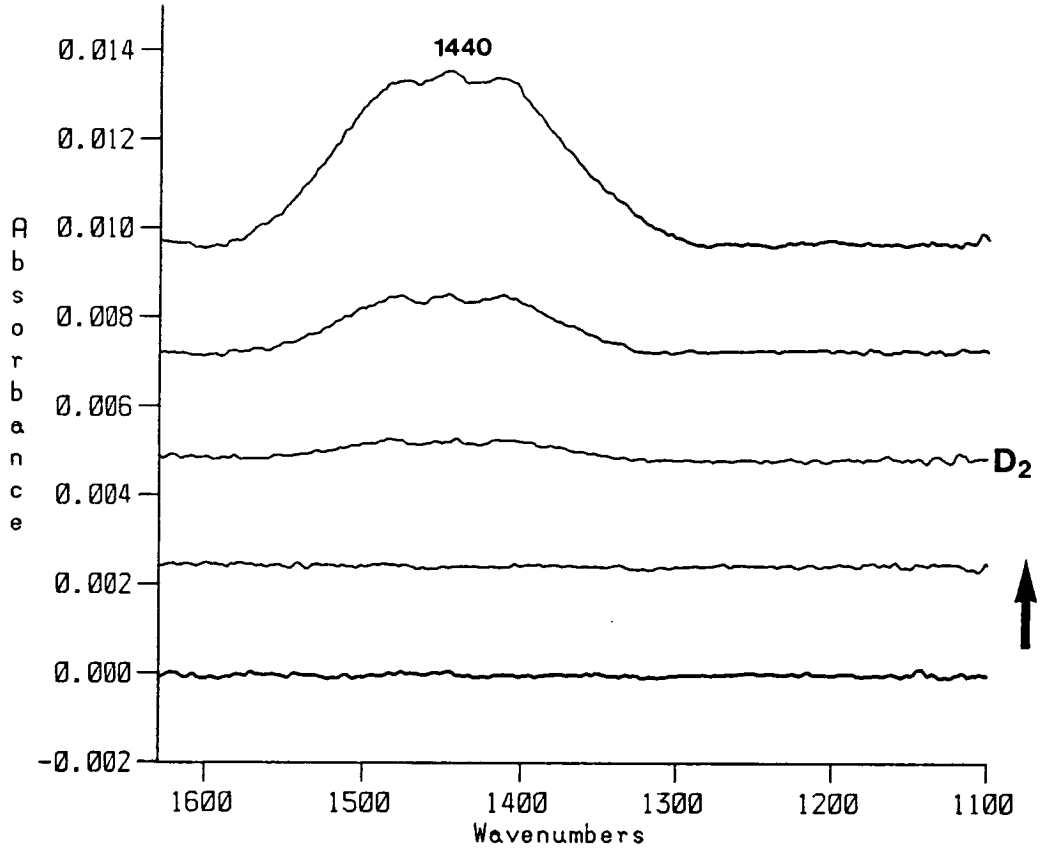

Figure 4.13 *Transmission infrared spectra of D_2 adsorption onto a 'H_2 free' surface (1630-1100cm^{-1}).*

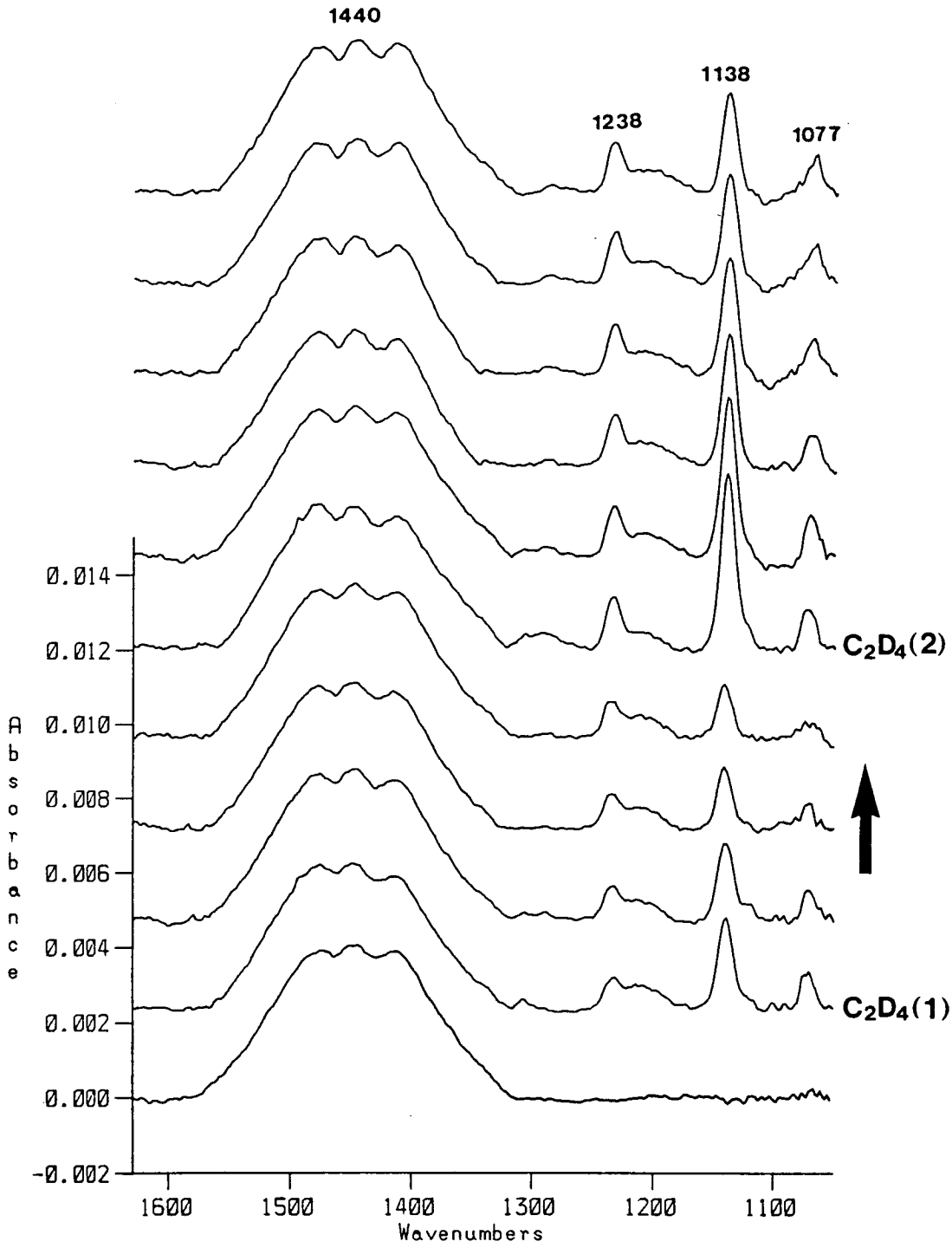

Figure 4.14 *Transmission infrared spectra of C_2D_4 adsorption (2 pulses) onto a D_2 covered surface (1630-1050cm^{-1}).*

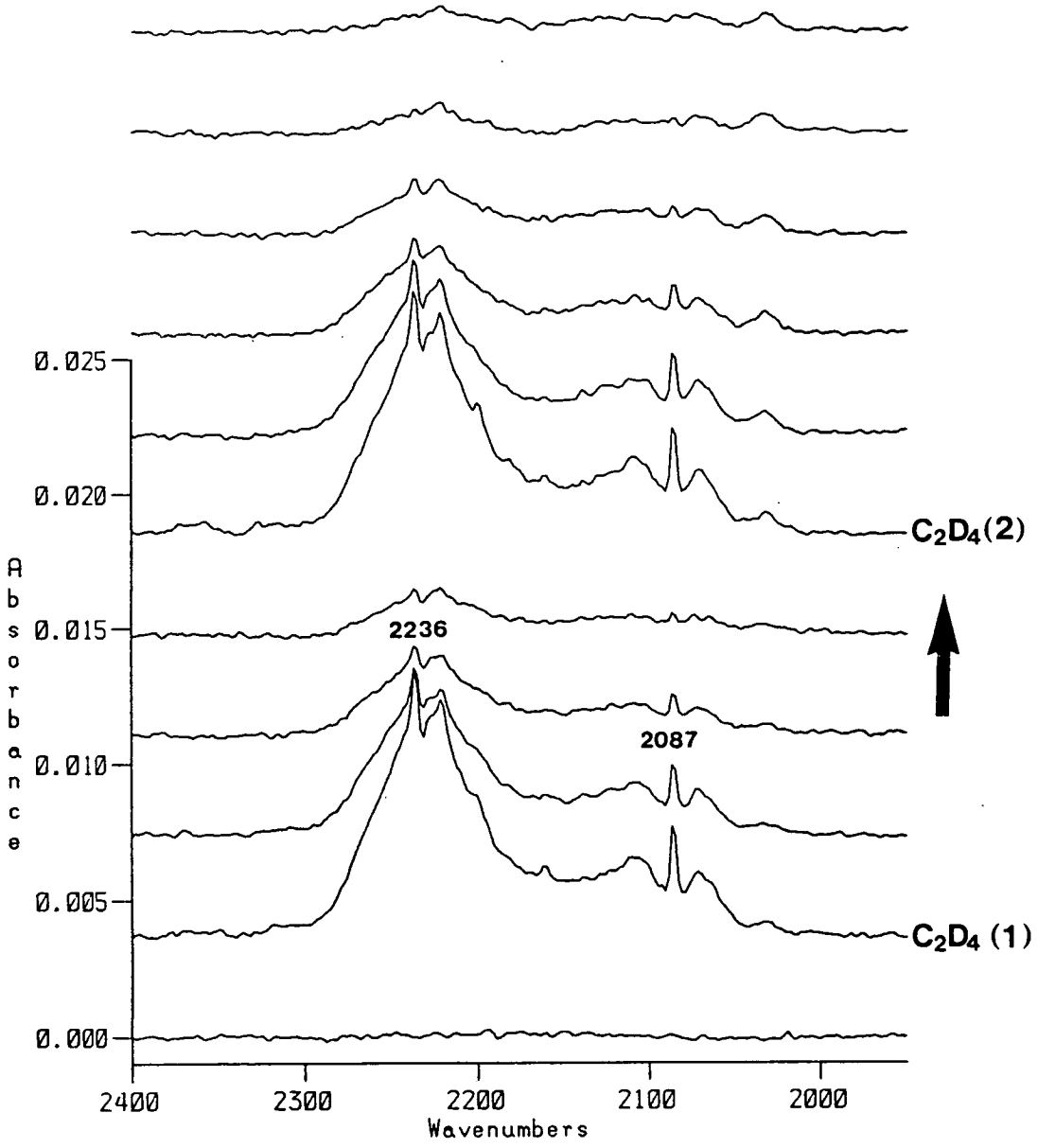

Figure 4.15 *Transmission infrared spectra of C_2D_4 adsorption (2 pulses) onto a D_2 covered surface (2400-1950cm^{-1}).*

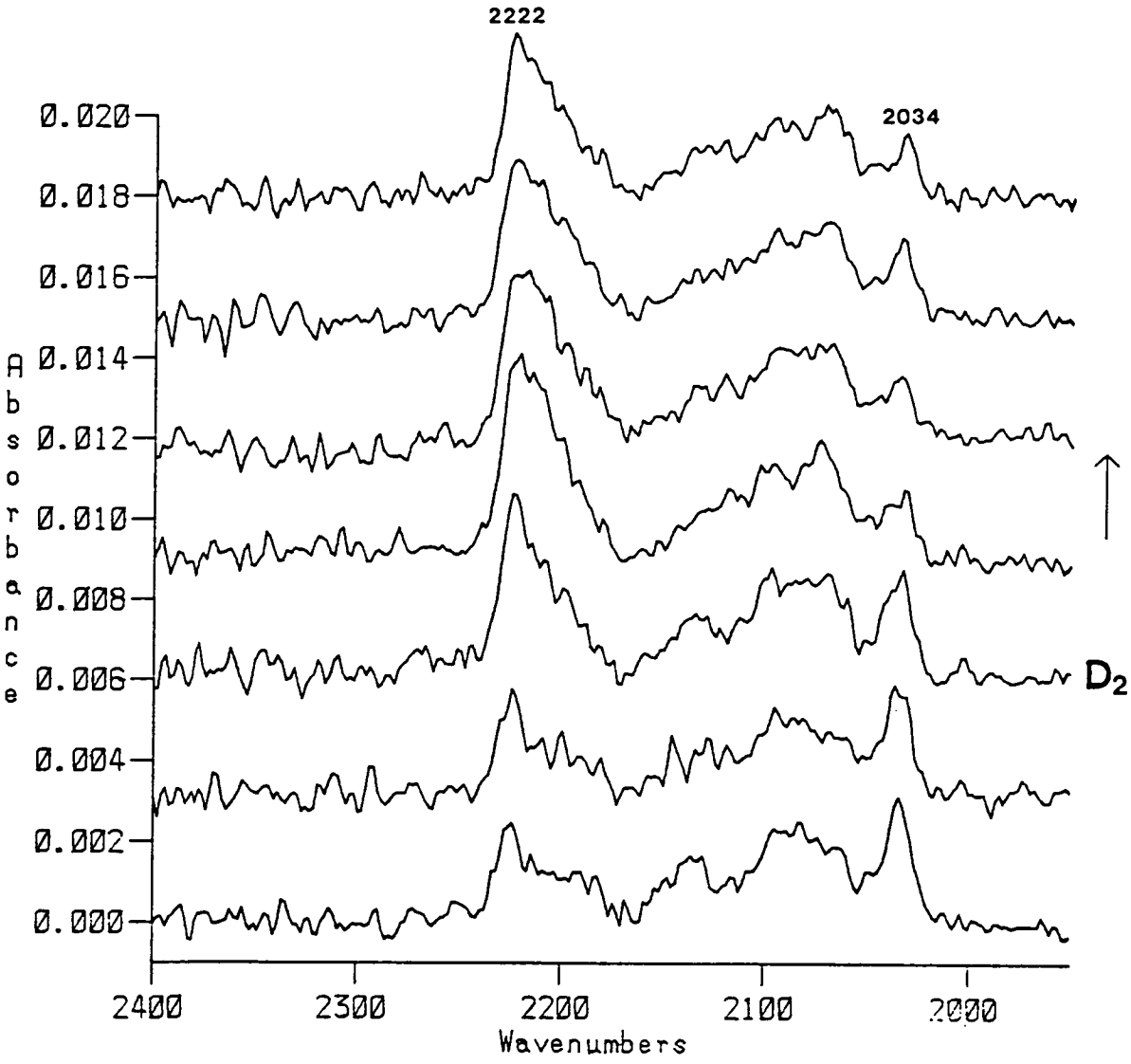

Figure 4.16 *Deuteration of C_2D_4 derived surface species (DRIFTS spectra, 2400-1950cm^{-1}).*

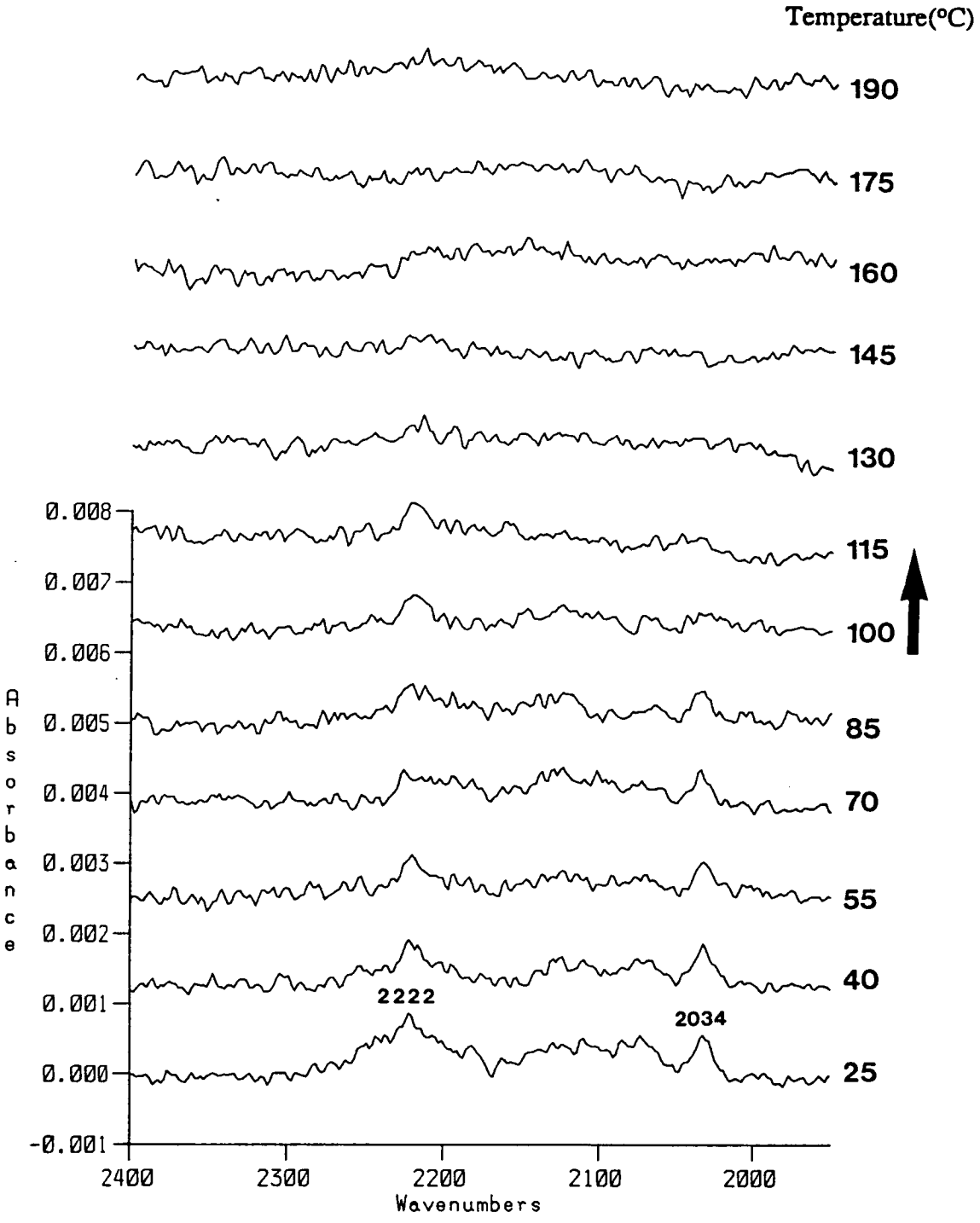

Figure 4.17 *Temperature programmed transmission infrared spectra of C_2D_4 derived surface species (2400-1950cm^{-1}).*

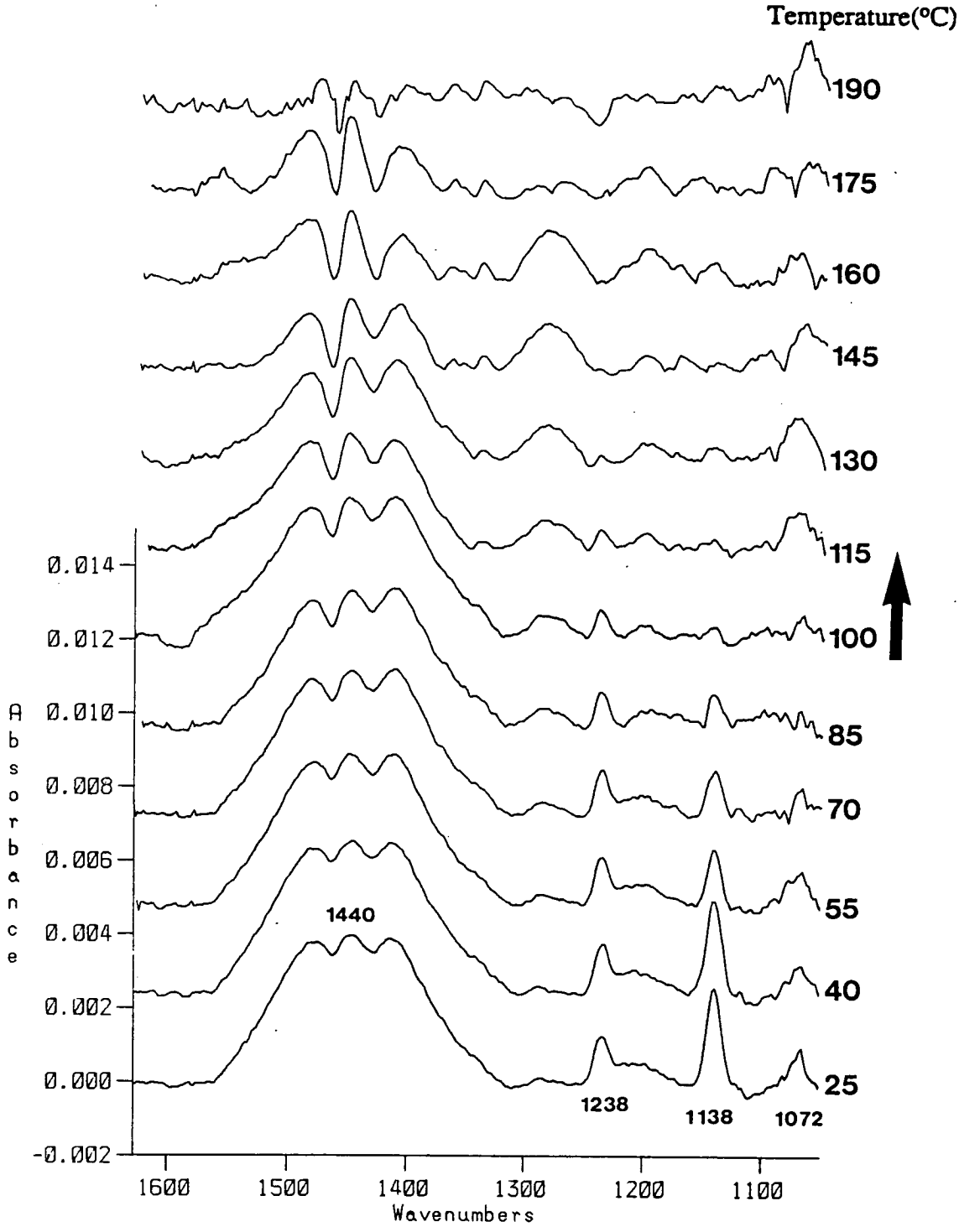

Figure 4.18 *Temperature programmed transmission infrared spectra of C_2D_4 derived surface species (1630-1050cm^{-1}).*

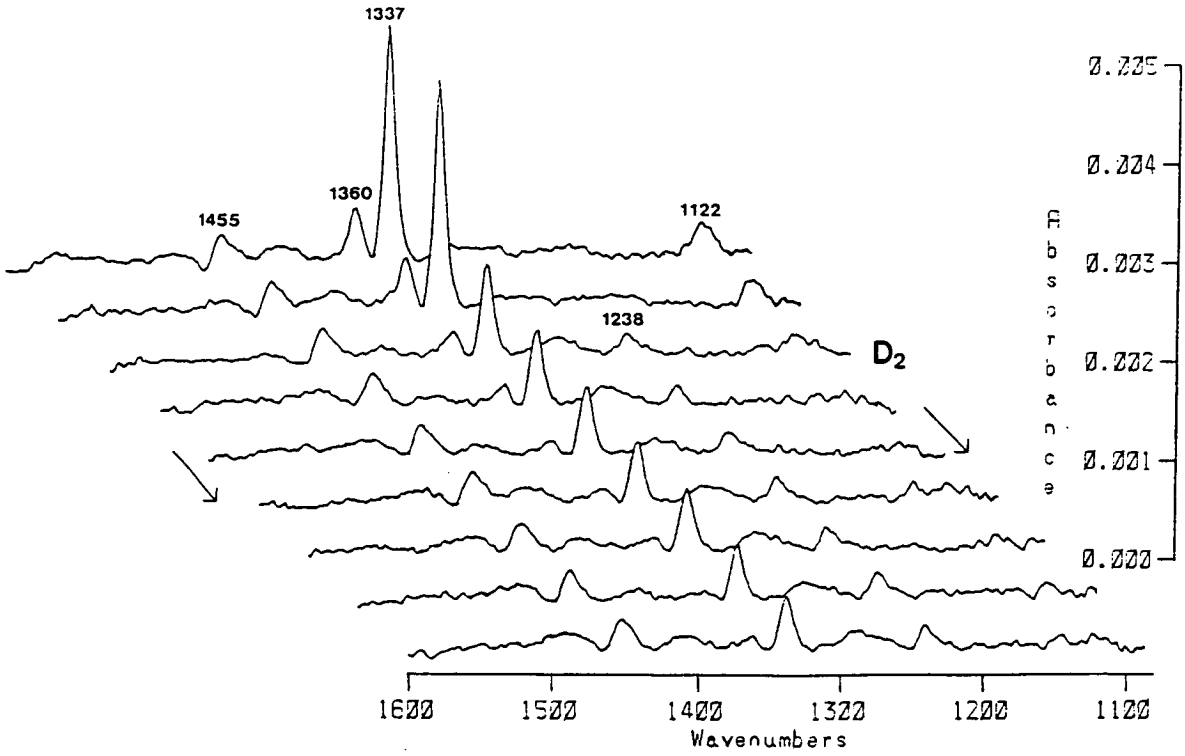

Figure 4.19 *Transmission infrared spectra of deuteration of C_2H_4 derived surface species (1600-1080cm^{-1}).*

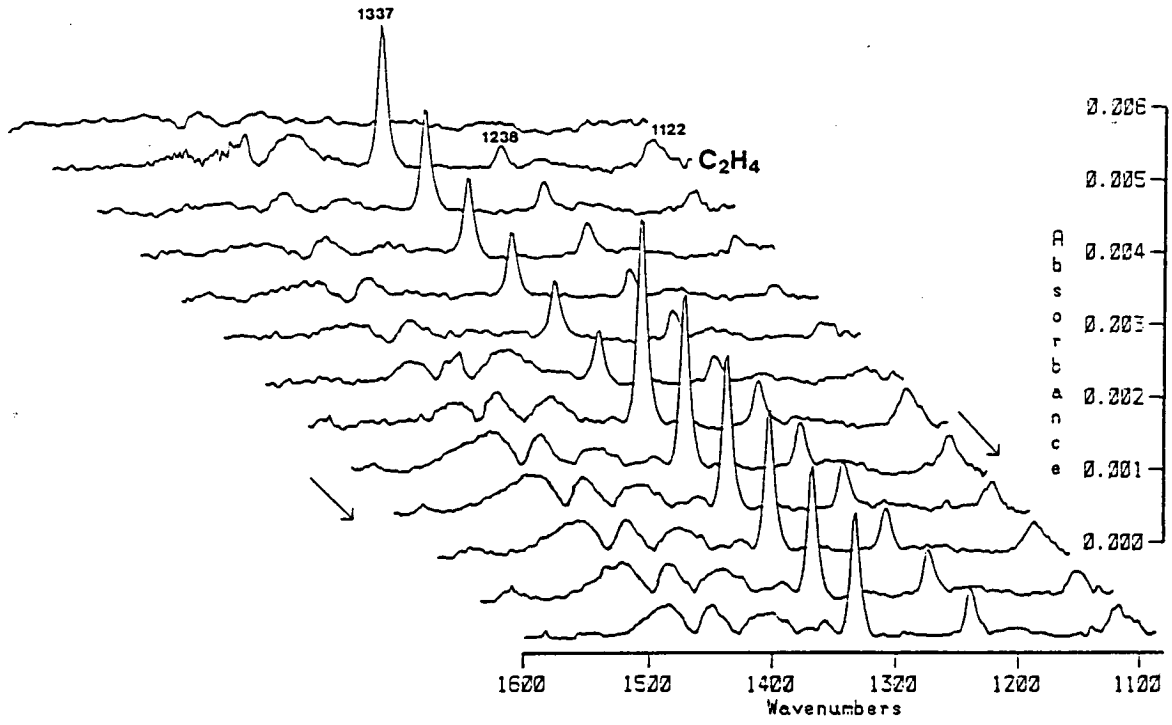

Figure 4.20 *Transmission infrared spectra of C_2H_4 adsorption onto a D_2 saturated surface (1600-1080cm^{-1}).*

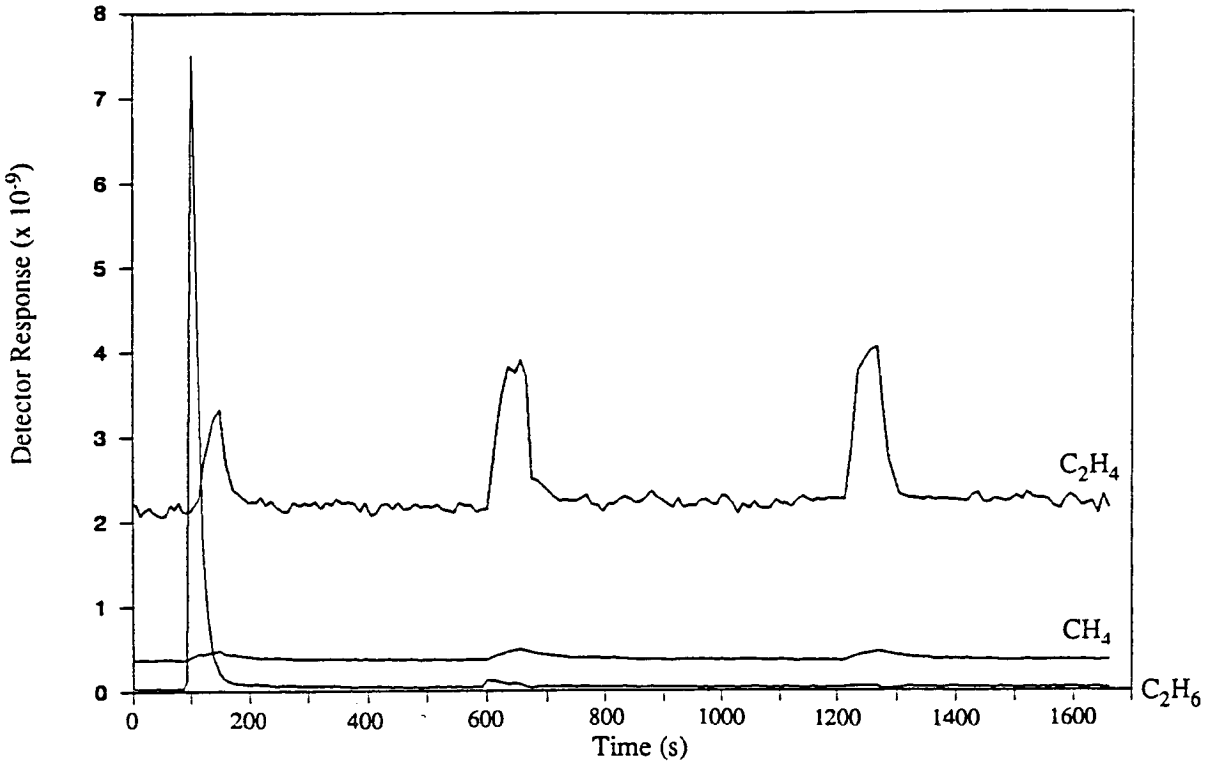

Figure 4.21 *Gas phase products produced on adsorption of three pulses C_2H_4.*

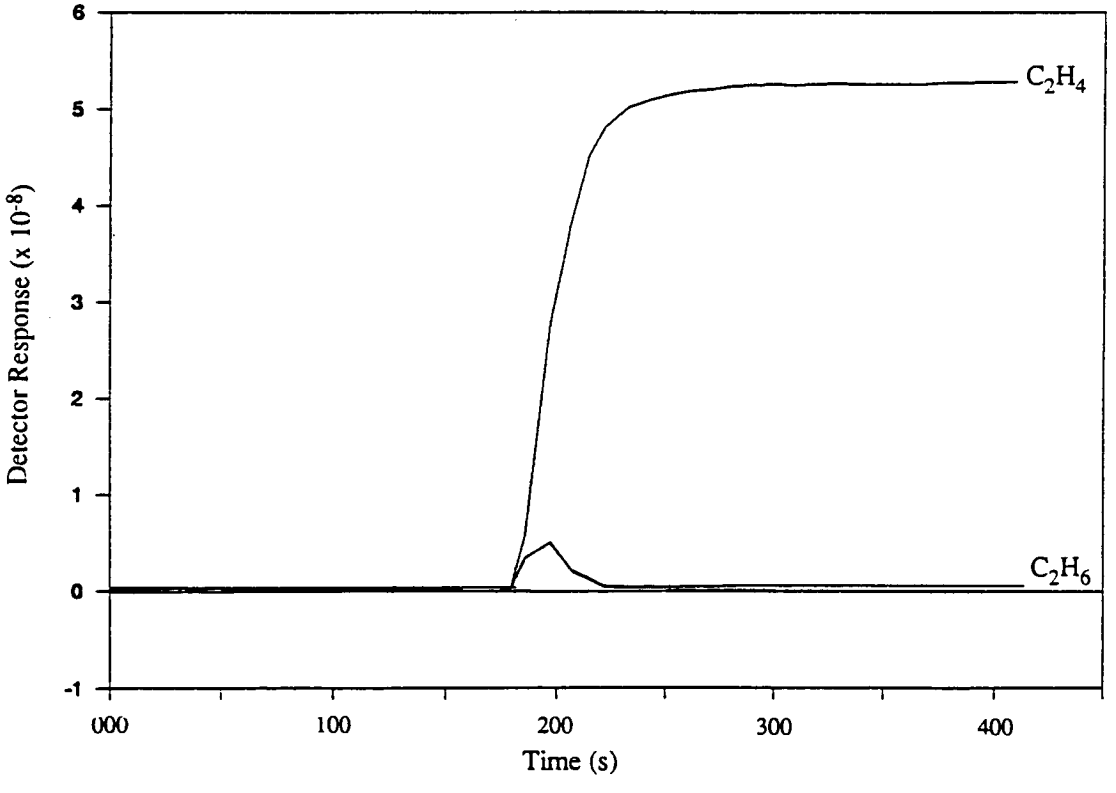

Figure 4.22 *Gas phase analysis during Reactive Frontal Chromatography of C_2H_4.*

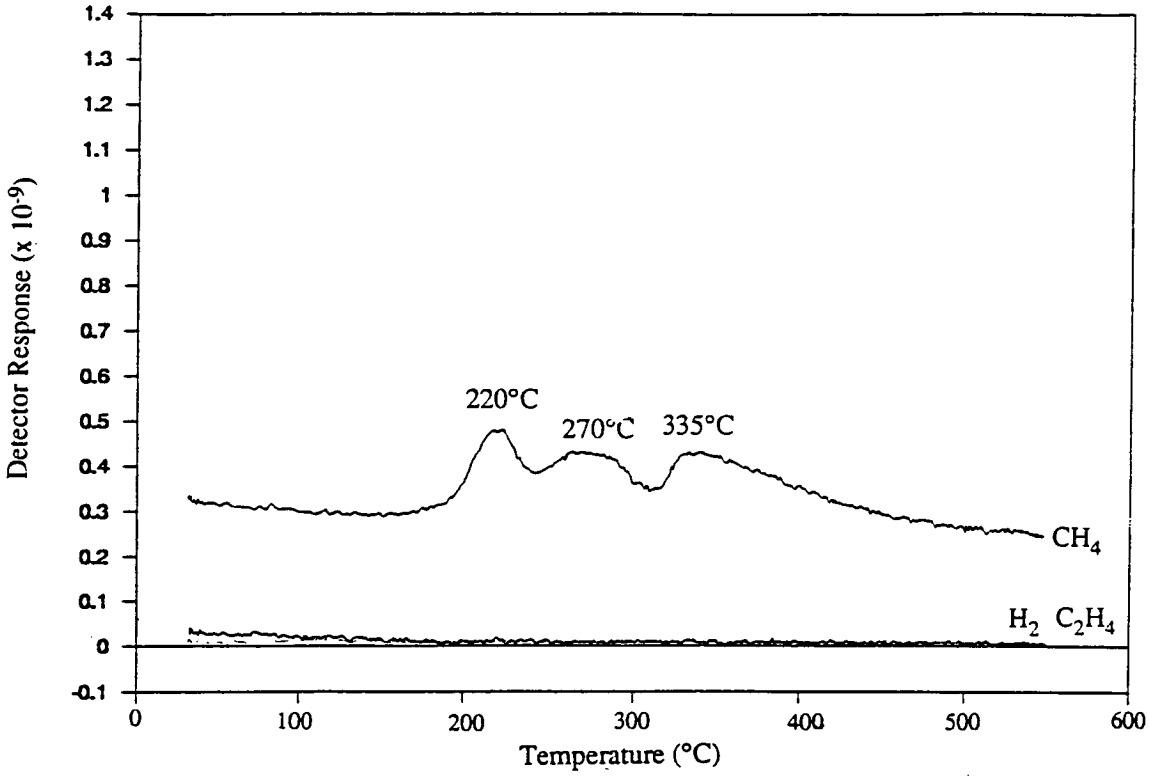

Figure 4.23 *Gas phase analysis during temperature programmed desorption of C_2H_4 derived species (25→550°C).*

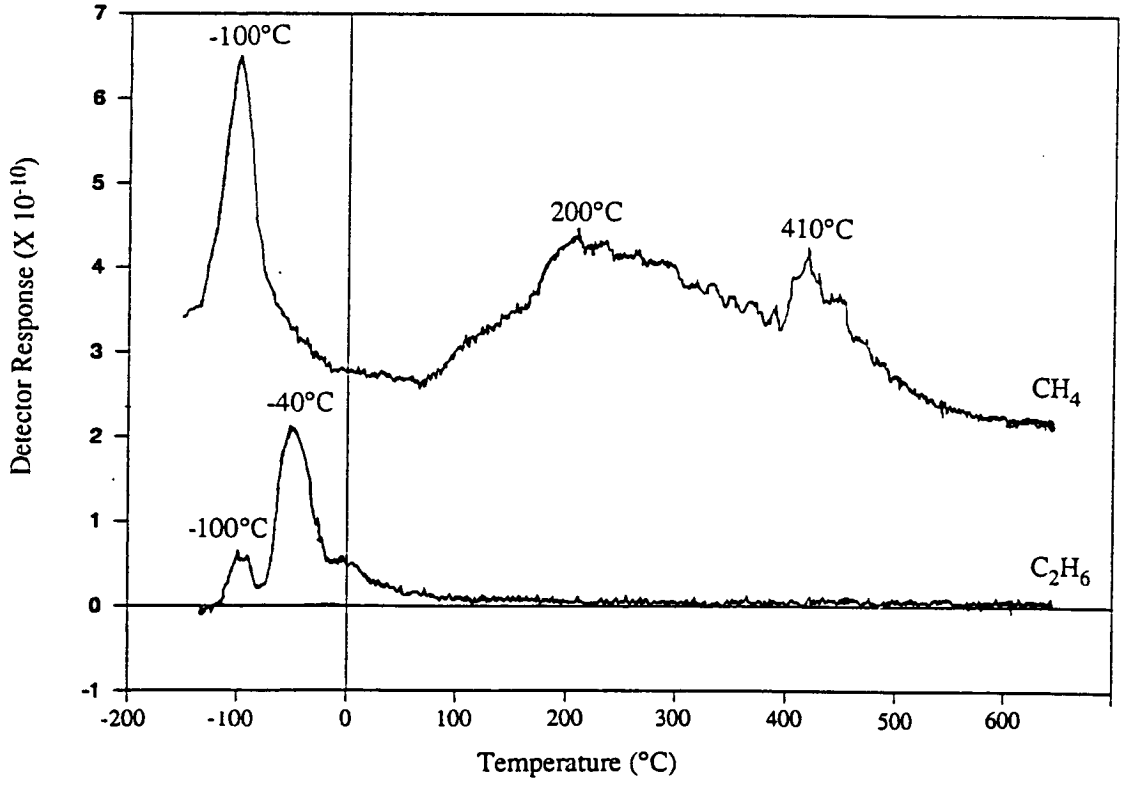

Figure 4.24 *Gas phase analysis during temperature programmed desorption of C_2H_4 derived species (-130→550°C).*

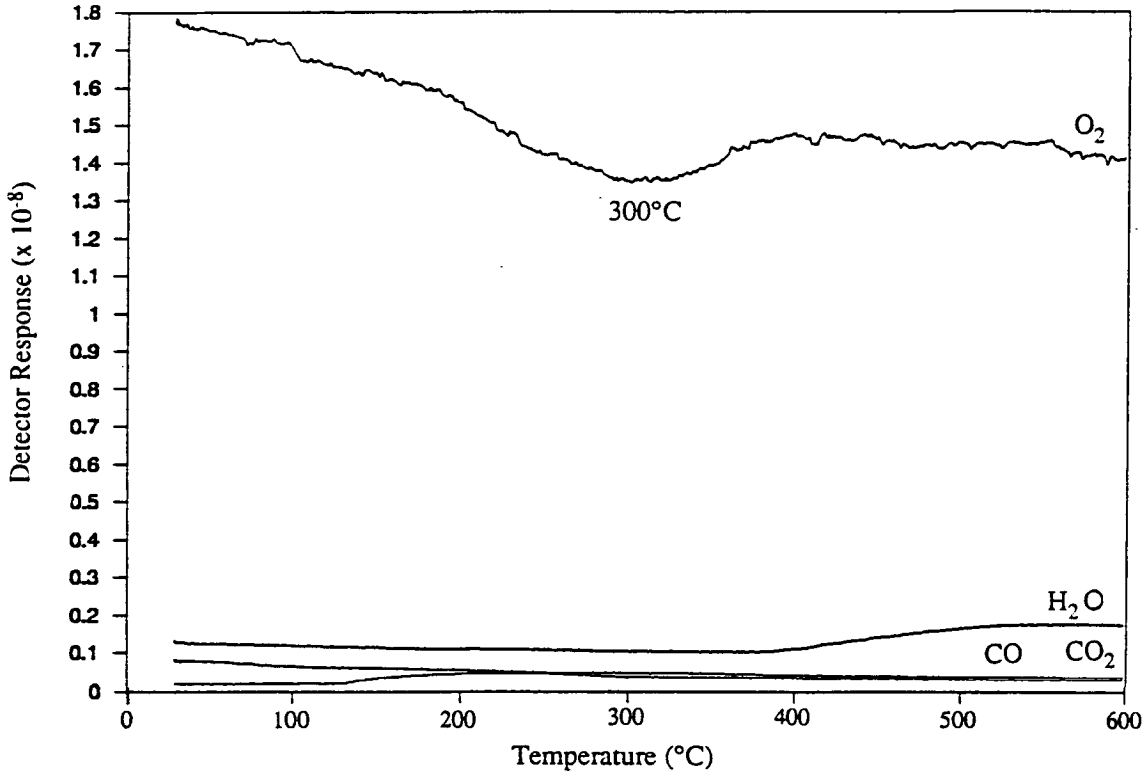

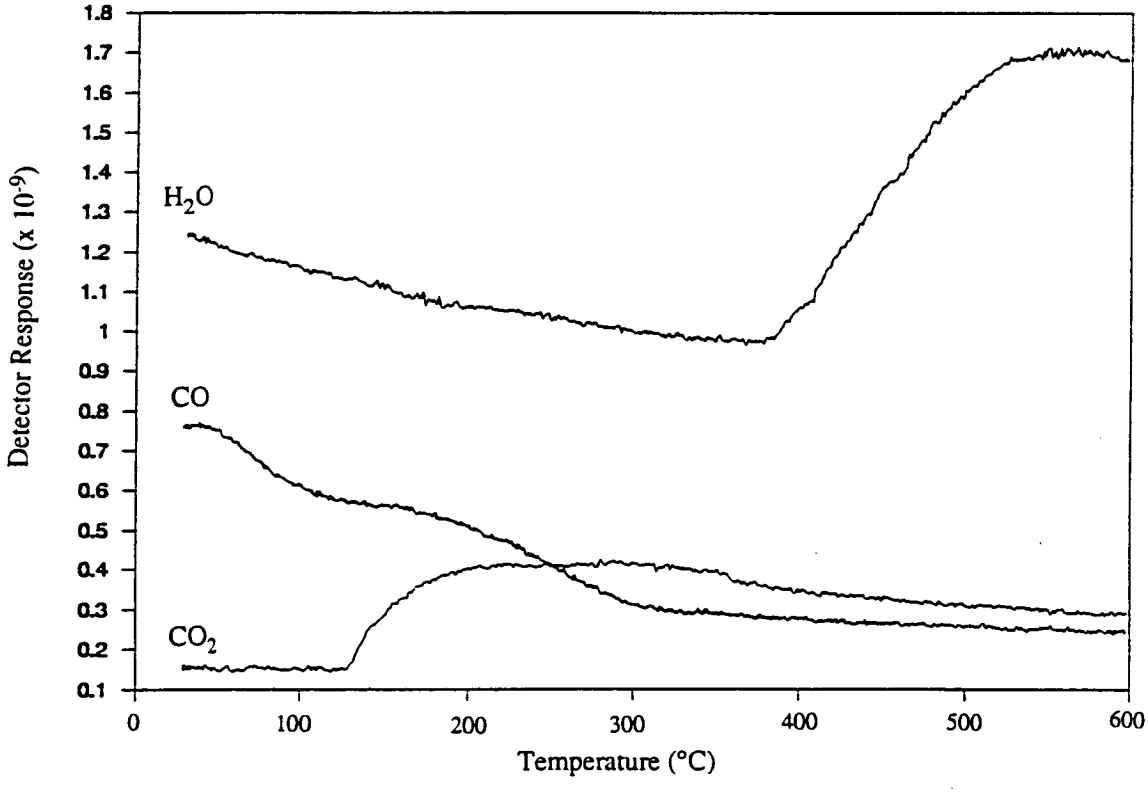

Figure 4.25 and 4.26 *Temperature programmed oxidation of a C_2H_4 derived carbonaceous deposit (25→600°C).*

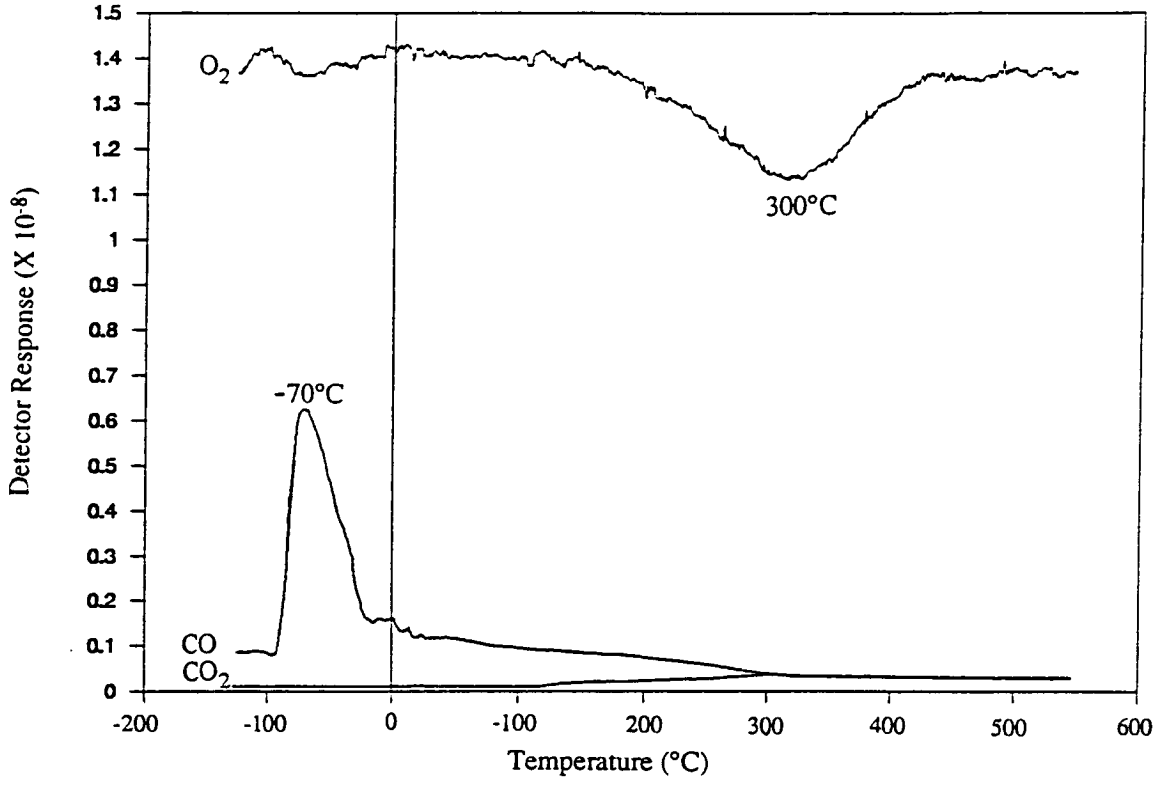

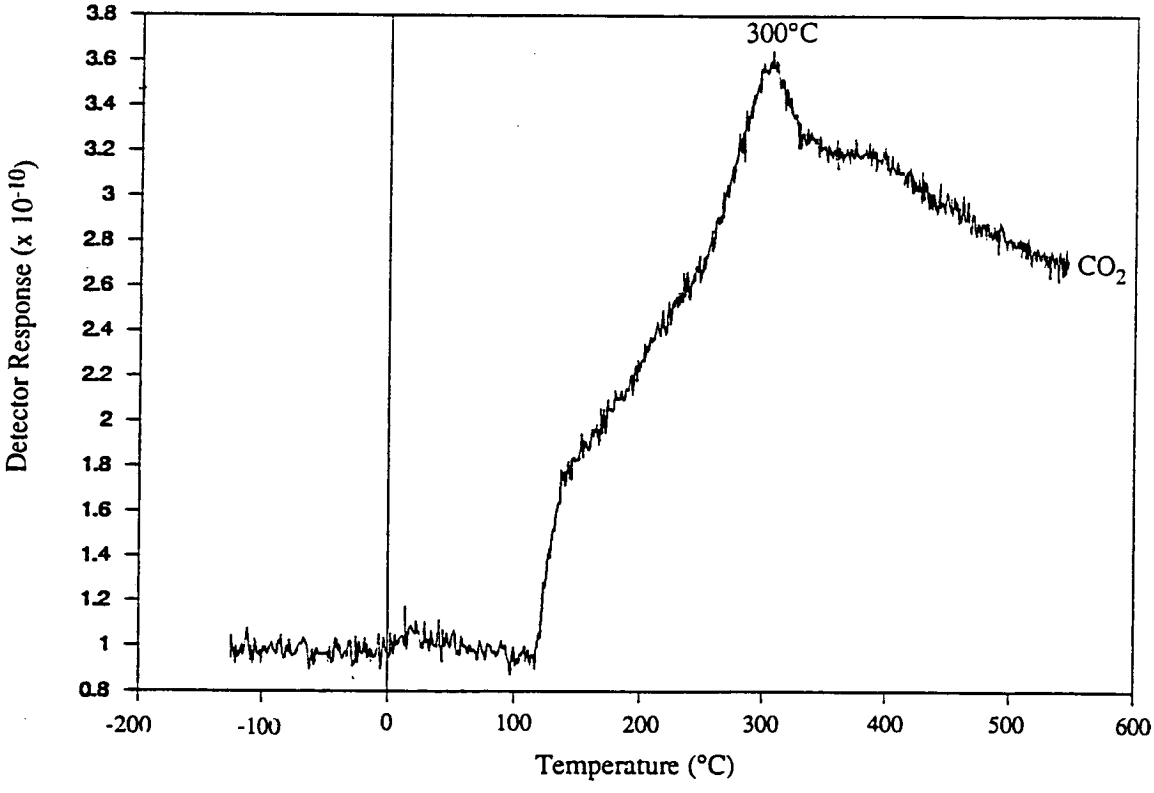

Figure 4.27 and 4.28 *Temperature programmed oxidation of a C_2H_4 derived carbonaceous deposit (-130→550°C).*

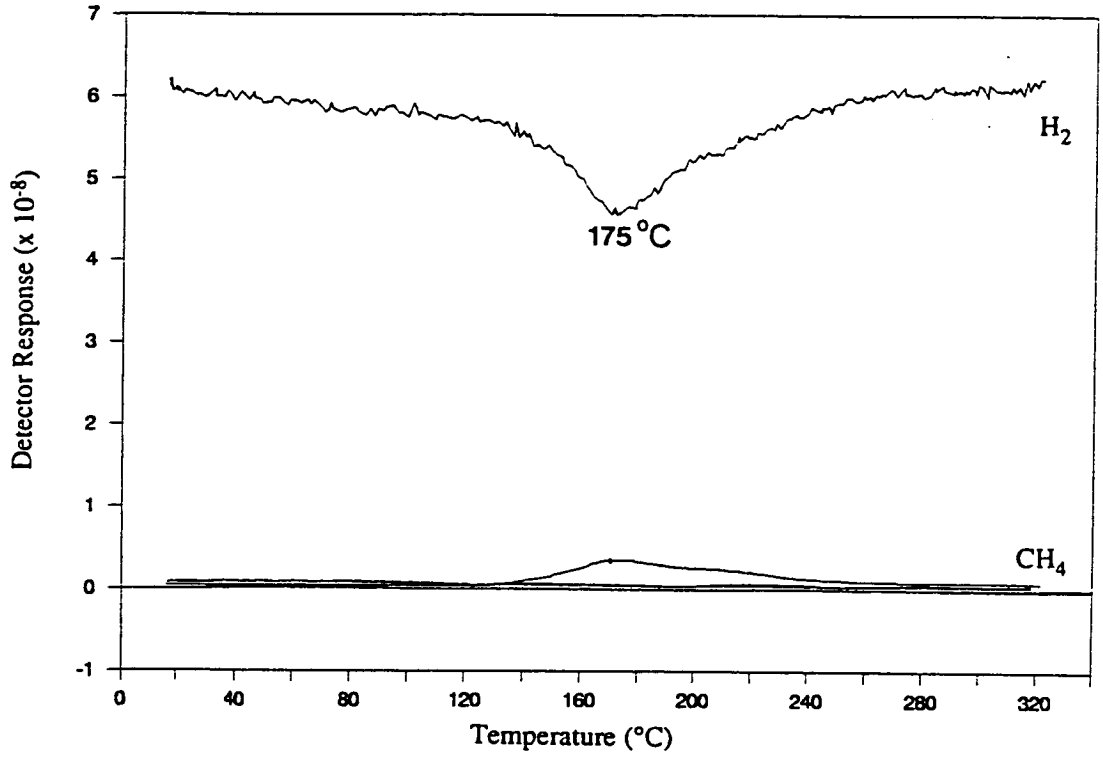

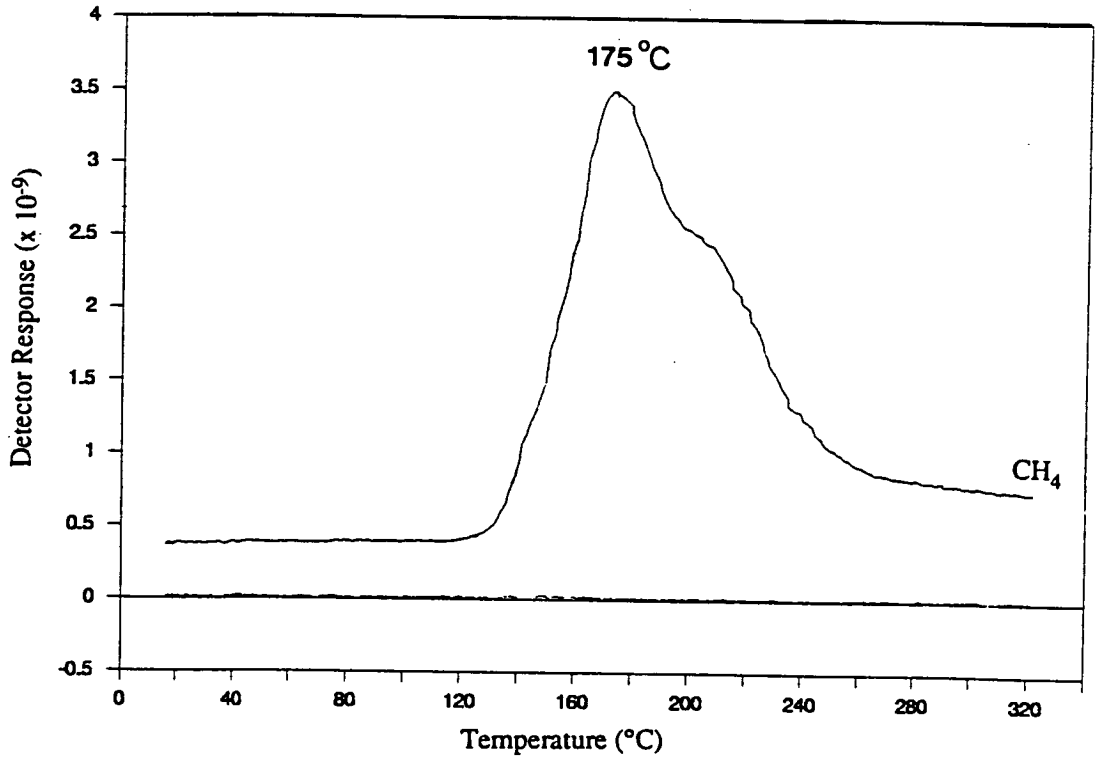

Figure 4.29 and 4.30 *Temperature programmed hydrogenation of a C_2H_4 derived carbonaceous deposit (25→330°C).*

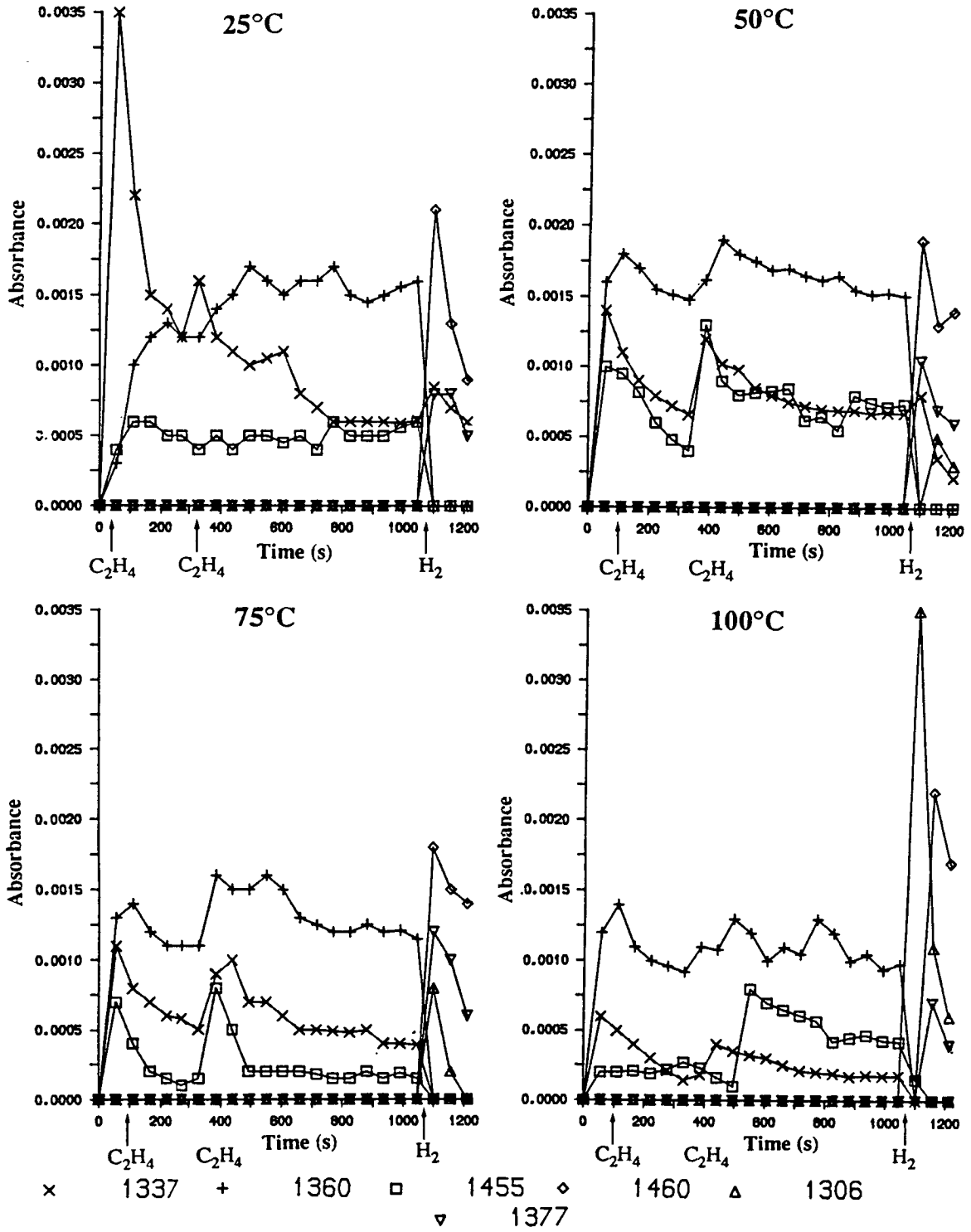

Figure 4.31 *Surface and gas phase bands produced on adsorption of C_2H_4 at 25, 50, 75 and 100°C.*

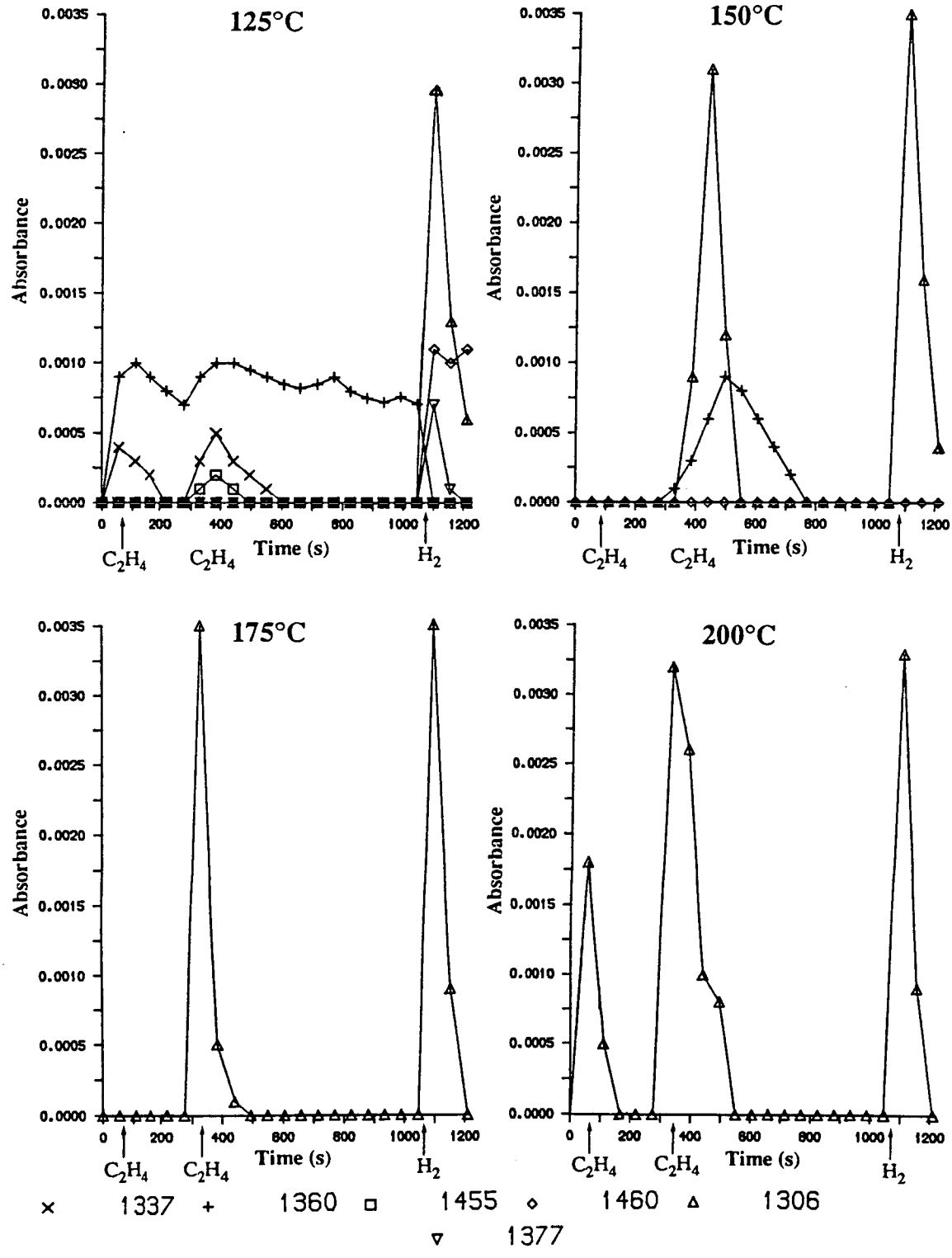

Figure 4.31 *Surface and gas phase bands produced on adsorption of C_2H_4 at 125, 150, 175 and 200°C.*

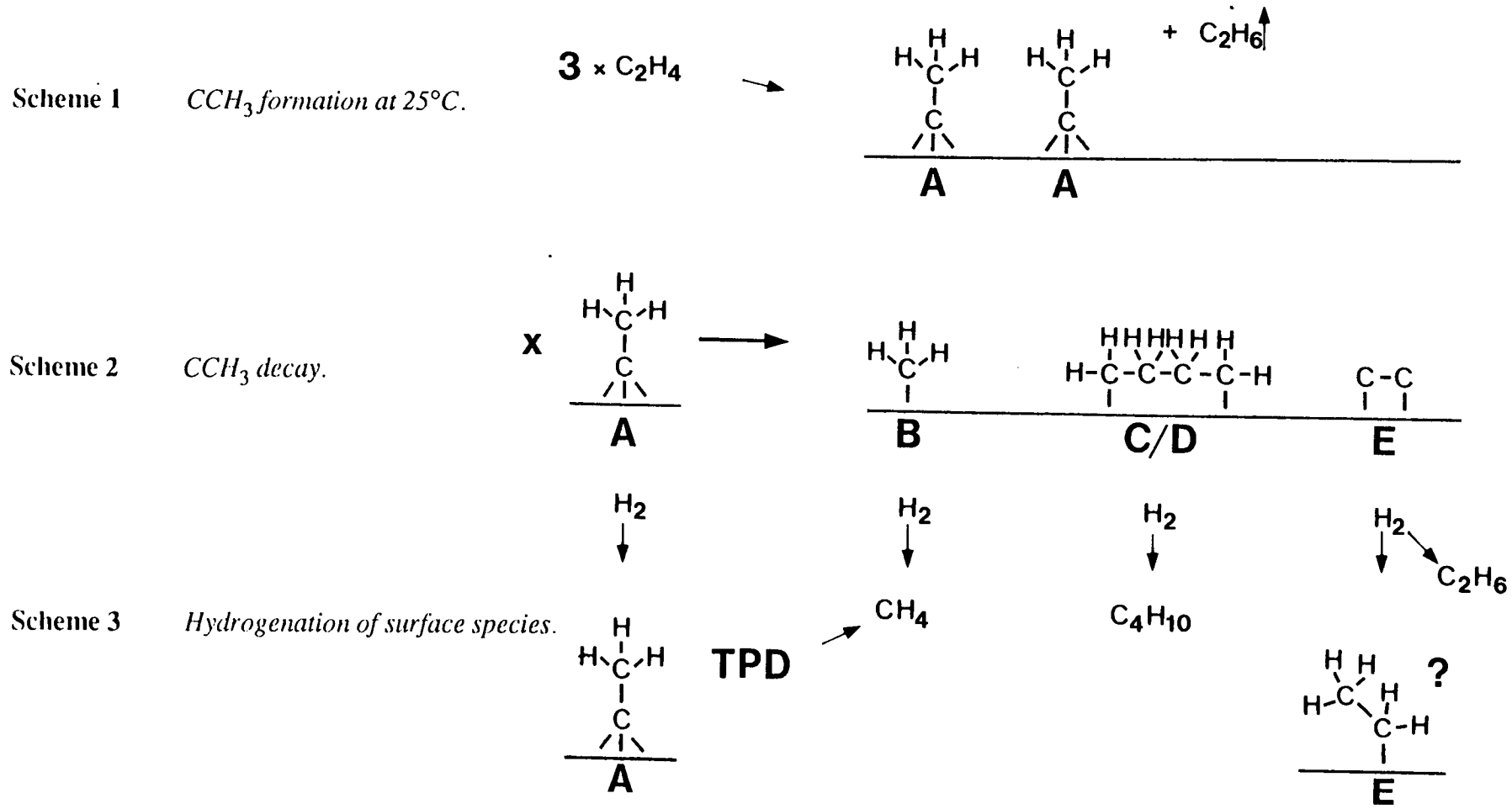

Figure 4.32 *Proposed reaction schemes for ethylidyne formation, decay and hydrogenation on Ni/Al_2O_3.*

CHAPTER 5

Propene Adsorption on Ni/Al_2O_3.

5.1 Historical Aspects.

The chemistry of C_3H_6 adsorption and reaction has received far less attention than the C_2 chemistry discussed in the preceding chapter. Chesters *et al.* have published a joint study of C_3H_6 adsorption on Pt/SiO_2, using transmission infrared spectroscopy, and on Pt(111) using RAIRS [190]. C_3H_6 adsorption onto Pt(111) at 65°C produced the propylidyne species (CCH_2CH_3), in a similar manner to C_2H_4 adsorption producing ethylidyne. This is in agreement with earlier work on Pt(111) using EELS by Avery and Sheppard [191]. Propylidyne has also been observed on Rh(111) between -73°C and 0°C using EELS [192]. Above 0°C on this surface the CCH_2CH_3 decays to ethylidyne (CCH_3), and to C_xH fragments at higher temperatures. On Pt/SiO_2 [190], again propylidyne was observed to form on adsorption of propene at 25°C. Additional features in the spectrum were assigned to a di-σ propene species which co-existed with the propylidyne species.

Table 5.1 Band Positions (cm^{-1}) and Assignments for the Propylidyne Species.

Pt/SiO_2 IR	Pt(111) EELS	Pt(111) RAIRS	Rh(111) EELS	$Cl_3CCH_2CH_3$ IR	Vibration
2960	2980	2961		2989	νCH_3as
2920	2920	2921		2944	νCH_2sym
2860		2865		2933	νCH_3sym
1450	1465	1450	1445	1455	δCH_3as
1410		1407		1430	δCH_2scissors
1365			1385	1382	δCH_3sym
	1295	1303	1290	1323	CH_2wag
	1115	1103	1120	1107	νCC
	1055	1055	1055	1066	CH_3rock
		1039			CH_3rock
	940	929	950	929	νCC

Table 5.1 above illustrates the band positions and assignments for the propylidyne species discussed above. The vibrations of 1,1,1 trichloropropane ($Cl_3CCH_2CH_3$) are included for comparison [193].

5.2 Results.

Both transmission infrared spectroscopy and DRIFTS were used to examine C_3H_6 adsorption on Ni/Al_2O_3. The apparatus employed was as illustrated in Figure 4.3. 500mbar pulses of C_3H_6 were used as standard.

5.2.1 C_3H_6 Adsorption onto an 'H_2 Free' Surface - Infrared Results.

Figure 5.1A and B illustrate successive DRIFTS spectra recorded following adsorption of one pulse of C_3H_6 onto an 'H_2 free' surface. Figure 5.2A and B are the corresponding transmission spectra in the CH deformation and stretching regions respectively. Once again, no surface bands could be observed in the CH stretching region of the transmission infrared spectra (Figure 5.2B).

Surface bands are observed at 1452, 1402, 1354, 1334, 1230 and 1105cm^{-1} as shown in Figure 5.1A, and at 2960, 2920, 2895 and 2870 in Figure 5.1B. Similar features are seen in the corresponding transmission spectra in Figure 5.2A, with an additional band resolved at 1278cm^{-1} . Figure 5.2B reveals the production of a gas phase band centred on 2966cm^{-1} which forms on adsorption of C_3H_6. Adsorption of a second pulse of C_3H_6 enhances the 1452, 1354 and 1105cm^{-1} bands. Particularly apparent in Figure 5.2A is a gradual enhancement of the 1354cm^{-1} band at the expense of the 1452cm^{-1} band.

5.2.2 Band Assignment.

Comparison of the above bands with those listed in Table 5.1 above reveal the unambiguous formation of propylidyne on Ni/Al_2O_3, shown by the bands at 2960, 2920, 2870, 1452, 1402, 1354, 1278 and 1105cm^{-1}. However the 1354cm^{-1} band is at a somewhat lower frequency than would be expected and is also more intense than found by other authors [190], [191]. Examination of Figures 5.1A and 5.2A reveals a weak shoulder to higher wavenumber than 1354cm^{-1}, at between 1365 and 1370cm^{-1}. It may be that this is the expected δCH_3 vibration of propylidyne and that the main 1354cm^{-1} feature belongs to another species.

The 2966cm^{-1} gas phase band in Figure 5.2B can be immediately identified as the ν_{15},ν_{23}CH vibration of propane, C_3H_8 [44]. Propane has another strong feature at 1470cm^{-1} ($\nu_{24}CH_3$ vibration), which can be identified in Figures 5.1A and 5.2A. Evidently propene is hydrogenated to propane over nickel in a way analogous to the hydrogenation of ethene to ethane. Having identified the formation of propylidyne and propane, this leaves the following features as yet unassigned ; 2895, 1354, 1334 and 1230cm^{-1}.

The 2895 and 1354cm^{-1} bands are remarkably similar to those of species B identified as a methyl species (-CH_3) that was formed as a decay product of ethylidyne, discussed in Chapter 4. The much weaker 1334cm^{-1} feature is also likely to belong to a CH_3 containing species and is close to the δCH_3 frequency expected for ethylidyne (1334-1339cm^{-1}). If the 1334cm^{-1} band belongs to ethylidyne, then features near 2870cm^{-1} (νCH_3) and 1120cm^{-1} (νCC) would be expected. Propylidyne itself has a strong feature at 2870cm^{-1} and this would obscure any underlying νCH_3 vibration of CCH_3, which would be much weaker. The 1120cm^{-1} band of CCH_3 should be at least three times less intense than the 1334cm^{-1} feature and as such will probably be lost in the noise or incorporated into the broad 1105cm^{-1} band of propylidyne. Ethylidyne has been observed as a decay product of propylidyne on Rh(111) [192].

5.2.3 C_3H_6 Adsorption onto on H_2 Saturated Surface - Infrared Results.

Figure 5.3A and B illustrate successive DRIFTS spectra following adsorption of one pulse of C_3H_6 onto an H_2 saturated surface. Figure 5.4A and B illustrate the corresponding transmission spectra for a similar experiment. The formation of propylidyne was again apparent, with bands at identical positions to those produced on the 'H_2 free' surface. A far greater quantity of propane was produced, as is evident by the 1471 and 2966cm^{-1} bands in Figure 5.4A and B respectively. The features at 2895, 1354, 1334 and 1230cm^{-1} were again present, with a slight shift of the 1334cm^{-1} band to 1336cm^{-1}.

The intensity of the 1452 and 1354cm^{-1} bands produced on adsorption of two pulses of C_3H_6, on both the 'H_2 free' and H_2 saturated surface are illustrated in Figure 5.5. The graph shows that the initial intensity of the propylidyne band (1452cm^{-1}) was greater on the 'H_2 free' surface. Once formed, the propylidyne decayed to a species characterised by a vibrational band at 1354cm^{-1}, until stable levels were reached at 800 seconds after the first pulse. The 1452cm^{-1} band decayed

to a greater extent on the 'H_2 free' surface relative to the H_2 saturated surface. Thus hydrogen appears to stabilise propylidyne, as it does ethylidyne.

Interestingly, hydrogen covered surfaces allow a greater formation of ethylidyne (from C_2H_4) but a smaller amount of propylidyne (from C_3H_6) relative to the amounts formed on 'H_2 free' surfaces for both species.

5.2.4 Blank Experiments.

Adsorption of C_3H_6 onto both γ-Al_2O_3 and unreduced Ni/Al_2O_3 catalyst showed no formation of surface bands. There was no interaction with the catalyst other than physical broadening of the gas pulse on passing through the catalyst bed, as measured by the TCD.

5.2.5 Temperature Programmed Desorption.

Figure 5.6A shows spectra recorded in transmission (1600-1080cm^{-1}) during temperature programming of C_3H_6 derived surface species from 25°C up to 200°C in the helium carrier gas. Figure 5.6B illustrates the corresponding DRIFTS results of a similar experiment (3100-2750cm^{-1}) whilst temperature programming from 25°C up to 300°C.

The propylidyne bands began to decay between 100 and 120°C and only disappeared totally at temperatures above 200°C. The 1336cm^{-1} band disappeared at 120°C, which is consistent with the temperature of thermal decay for ethylidyne. The 1353cm^{-1} band shifted to 1364cm^{-1} by 100°C and then decayed by 180°C. Gas phase methane was detected at temperatures of 180°C and above. No other gas phase products were detected.

5.2.6 Hydrogenation.

Figure 5.7A and B show transmission spectra taken during hydrogenation of C_3H_6 derived surface species at 25°C. Figure 5.7A shows the 1600-1080cm^{-1} region, with Figure 5.7B the corresponding 3200-2700cm^{-1} region. Hydrogenation occurred as the third spectrum was being recorded.

The propylidyne bands at 1454, 1402, 1278 and 1105cm^{-1} were not affected dramatically, with only a slight shift of the 1402cm^{-1} band to 1407cm^{-1}. The 1354cm^{-1} band was removed with new bands being formed at 1378 and 1368cm^{-1}.

The 1336cm^{-1} band shifted to 1338cm^{-1}, and the 1454cm^{-1} band developed a shoulder at 1465cm^{-1}. Figure 5.7B shows significant production of a hydrocarbon species of C_3 or above on hydrogenation, characterised by an absorption band of a gas phase species at 2966cm^{-1}. The production of the 1378cm^{-1} band and attenuation of the 1354cm^{-1} band is identical to the hydrogenation behaviour for the C_2H_4 derived species (Chapter 4). Both CCH_2CH_3 and CCH_3 were not hydrogenated at 25°C.

5.2.7 Temperature Programmed Hydrogenation.

Figure 5.8A and B show successive transmission spectra taken during a temperature programmed hydrogenation experiment of C_3H_6 derived species, from 25°C up to 140°C. Figure 5.8A illustrates the 1600-1080cm^{-1} region, with Figure 5.8B the 3200-2700cm^{-1} region. The 1454cm^{-1} band was not hydrogenated until temperatures greater than 140°C. The other propylidyne bands at 1407 and 1278cm^{-1} were removed by 120°C. Both the 1338 and 1368/1378cm^{-1} bands were hydrogenated at 120°C. Significant production of methane (1304 and 3016cm^{-1}) was observed at 120°C and above. A small amount of hydrocarbon of C_3 or greater at 2966cm^{-1} was produced at 100°C.

Table 5.2 Gas phase products on adsorption of C_3H_6 at 25°C.

Surface	Pulse	CH_4	C_2	C_3H_6	C_3H_8	C_4,C_5	C_6
'H_2 free'	1	5.9%	-	6.3%	79.9%	3.9%	4.0%
	2	-	-	49.6%	50.4%	-	-
H_2 saturated	1	-	-	0.6%	99.4%	-	-
	2	-	-	1.3%	98.7%	-	-

Hydrogenation products

CH_4	C_2	C_3H_6	C_3H_8	C_4,C_5	C_6
26.5%	2.1%	-	66.5%	0.8%	4.1%

5.2.8 Mass Spectral Analysis.

Table 5.2 above shows the gas phase products following adsorption of two pulses of C_3H_6 onto both 'H_2 free' and H_2 saturated surfaces, as well as the gas phase products formed on hydrogenation. The m/e values used for species identification

were 16(CH_4), 30(C_2H_6), 42(C_3H_6), 44(C_3H_8), 43(C_4,C_5) and 57/86(C_6H_{14}) with appropriate corrections.

For the initial pulses of C_3H_6 on a hydrogen free surface, propane was the predominant product with small amounts of methane and $C_4 \rightarrow C_6$s. The second pulse produced only hydrogenation to propane and unreacted propene. The hydrogen saturated surface produces only propane, and a small amount of unreacted propene on adsorption of both pulses of C_3H_6.

Hydrogenation of C_3H_6 derived surface species at 25°C produced mainly C_3H_8 and CH_4, with small amounts of C_2H_6 and $C_4 \rightarrow C_6$s. Figure 5.9 shows the production of gas phase species during temperature programmed hydrogenation. Only CH_4 and C_6H_{14} were detected. Methane was the predominant gas phase product with a maximum rate of production at 150°C. A small amount of hexane is also produced at a maximum rate at 110°C.

5.2.9 Discussion

Propene adsorption onto both the 'H_2 free' and H_2 saturated surfaces is followed by production of propane and generation of the propylidyne species. By analogy with the adsorption and hydrogenation of C_2H_4 to C_2H_6, a combination of self hydrogenation and hydrogenation by chemisorbed hydrogen is expected for the hydrogenation of C_3H_6 to C_3H_8. Once formed the propylidyne decays to an ethylidyne species (CCH_3) and methyl (CH_3). This process is hindered by pre-adsorbed hydrogen, in a similar way to the hindering of ethylidyne decay, generated from ethene.

Hydrogenation removed species B at 2895/1354cm^{-1}, forming new species at 1465, 1378 and 1368cm^{-1}. Both methane and propane can be detected in the gas phase. In Chapter 4, species B was associated with the C_1 containing methyl group, and was easily hydrogenated to methane. If species B is the same when produced from C_3H_6 adsorption, then hydrogenation of this will account for the observed methane. However, 66.5% of the gas phase products was C_3H_8 and no other surface band was observed to decrease on hydrogenation. It may be that this propane was produced by hydrogenation of a highly dehydrogenated C_3 containing species invisible in the infrared. The only known C_3 containing species, propylidyne, is not hydrogenated at room temperature.

The new bands produced at 1465, 1378 and 1368cm^{-1} together with a

strengthening of the 1454cm^{-1} band can be associated with δCH_2 and δCH_3 vibrations of chemisorbed alkane species similar to those identified by Campione and Ekerdt [188] and listed in Table 4.9. From this it is clear that this additional species is adding to the intensity of the 1454cm^{-1} band in Figure 5.7. The exact chain length is not clear, although the temperature programmed hydrogenation spectrum in Figure 5.9 reveals the production of a small quantity of C_6H_{14} as the only other product other than methane.

The dimerisation of C_2H_4 derived surface fragments to C_4 containing species, which were hydrogenated to butane, was observed in Chapter 4 at a maximum rate at 50°C. In a similar manner, it appears that C_3H_6 derived fragments dimerise to C_6 containing species and are hydrogenated to hexane at a maximum rate at 110°C. A summary of the above reaction scheme is shown in Figure 5.10.

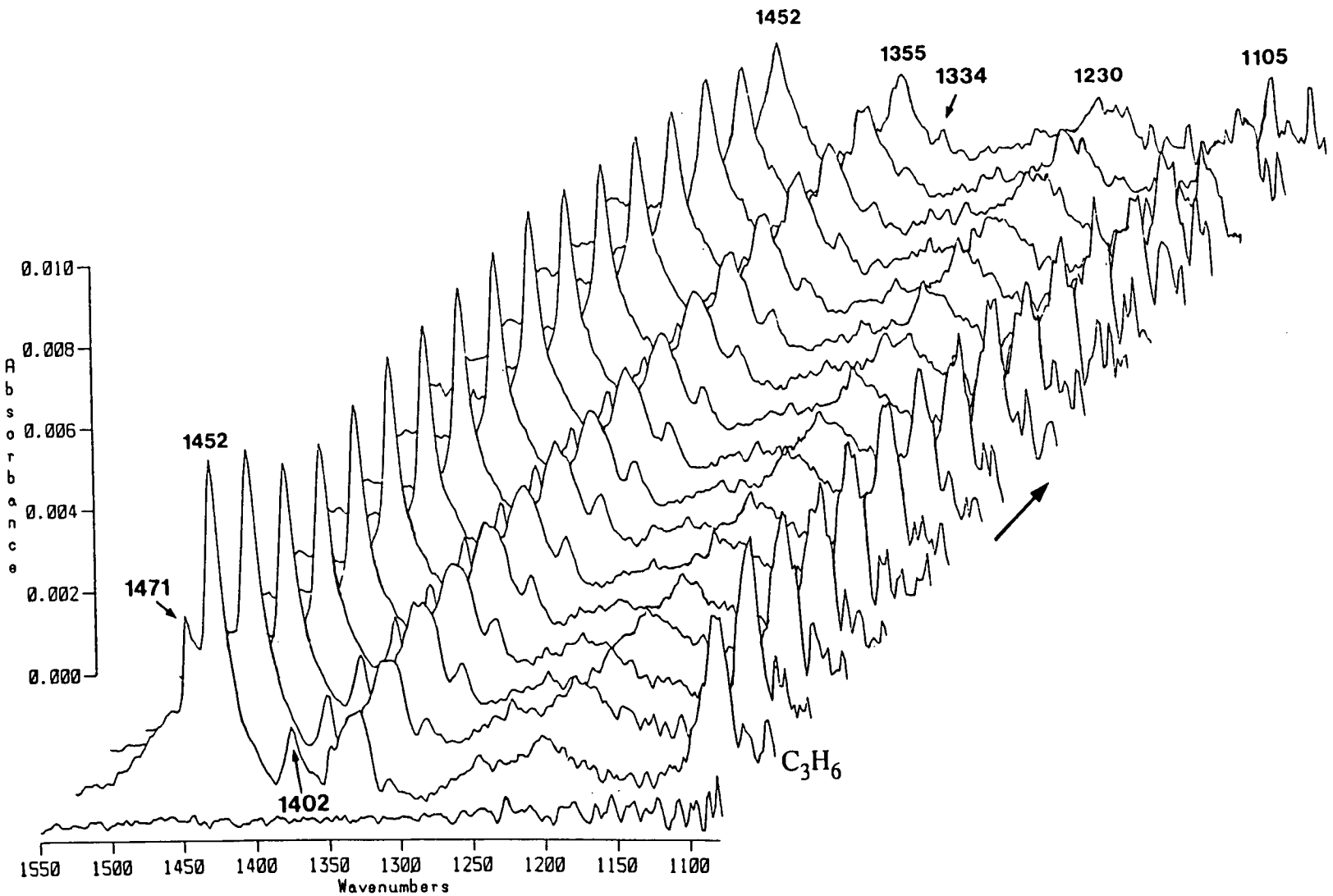

Figure 5.1 A *DRIFTS spectra of C_3H_6 adsorption onto an 'H-free' surface at 25°C (1550 - 1080cm^{-1}.)*

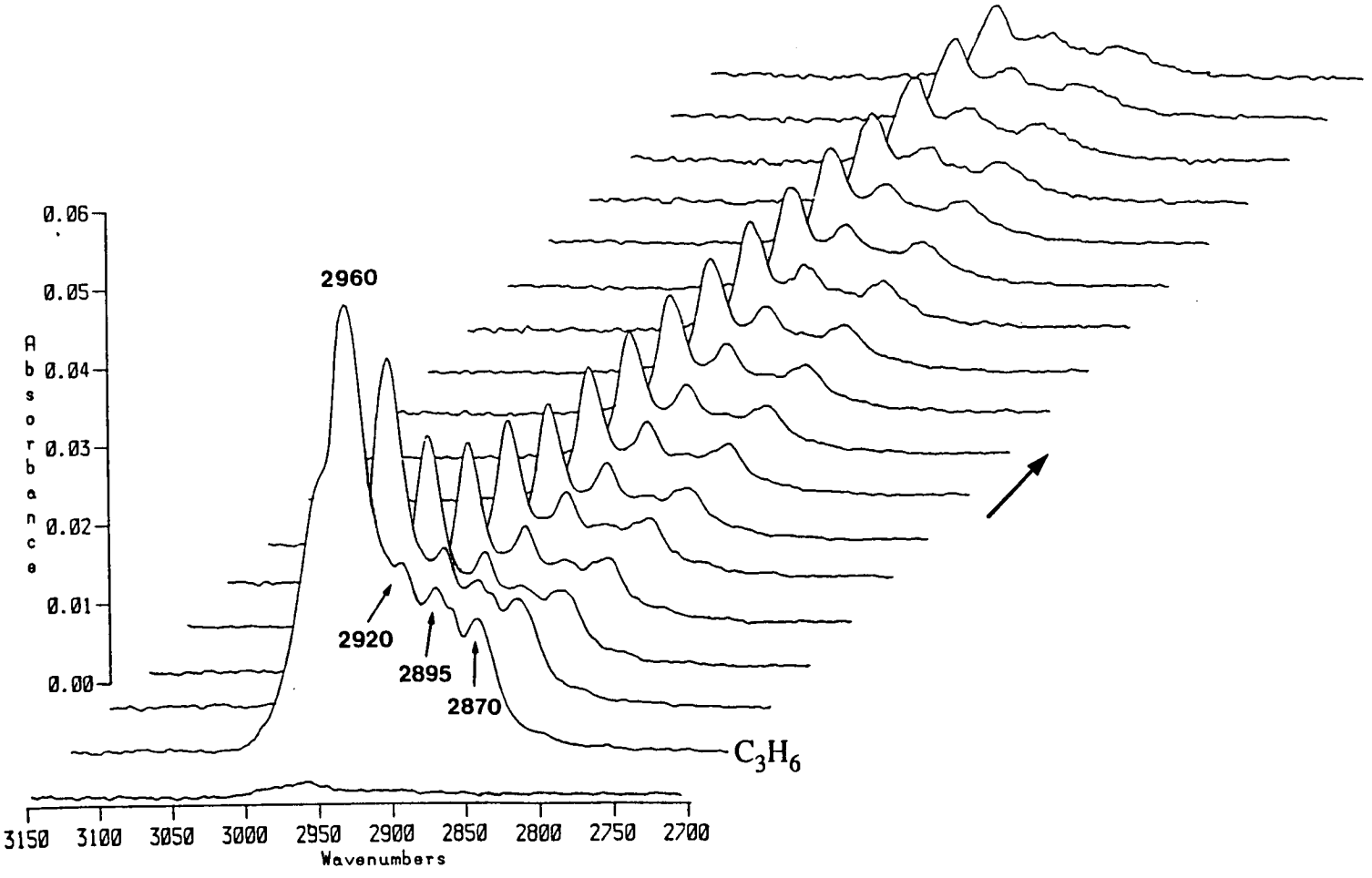

Figure 5.1 B *DRIFTS spectra of C_3H_6 adsorption onto an 'H-free' surface at 25°C (3150 - 2700cm^{-1}.)*

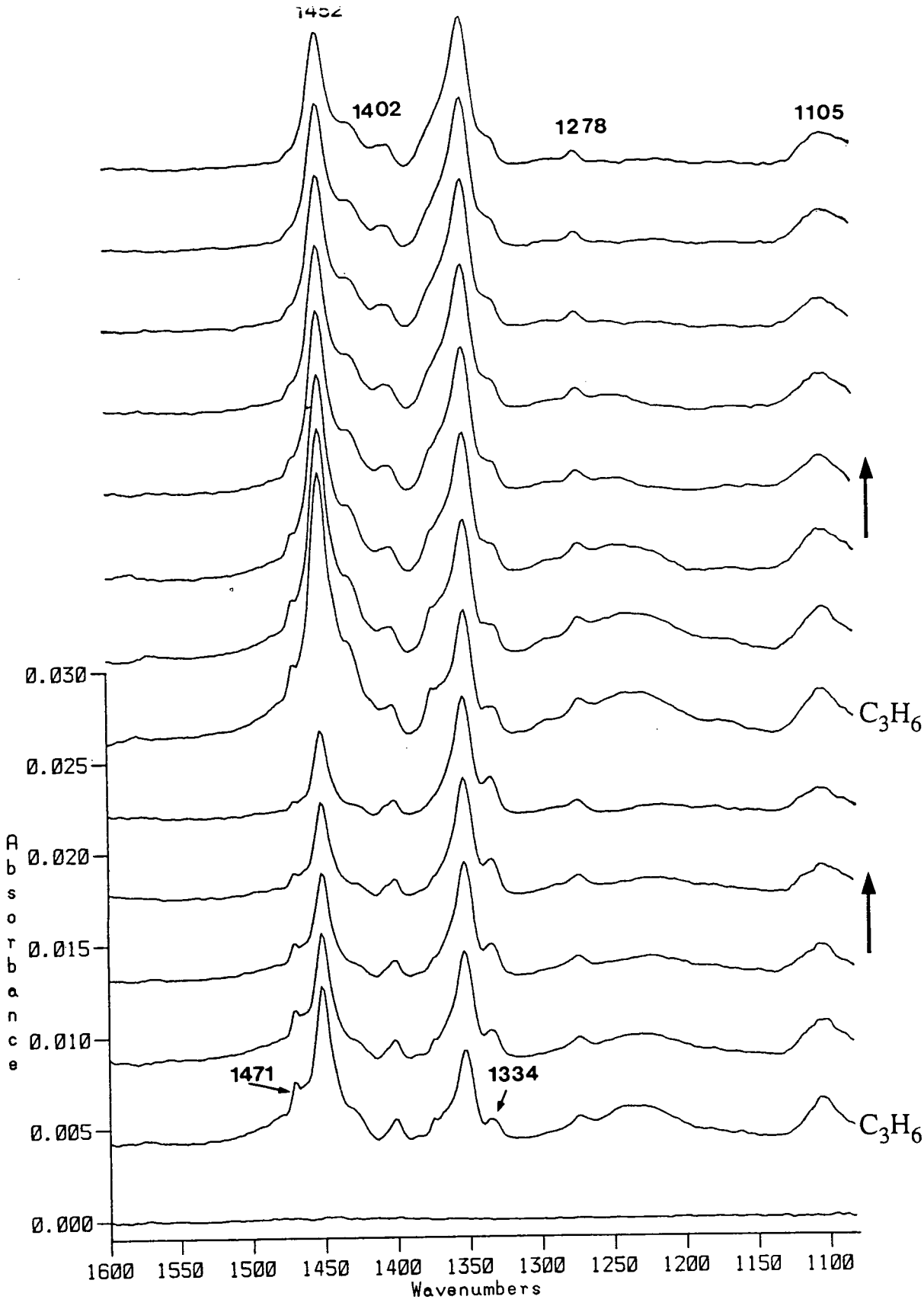

Figure 5.2 A *Transmission spectra of C_3H_6 adsorption onto an 'H_2 free' surface at 25°C (1600-1080cm^{-1}).*

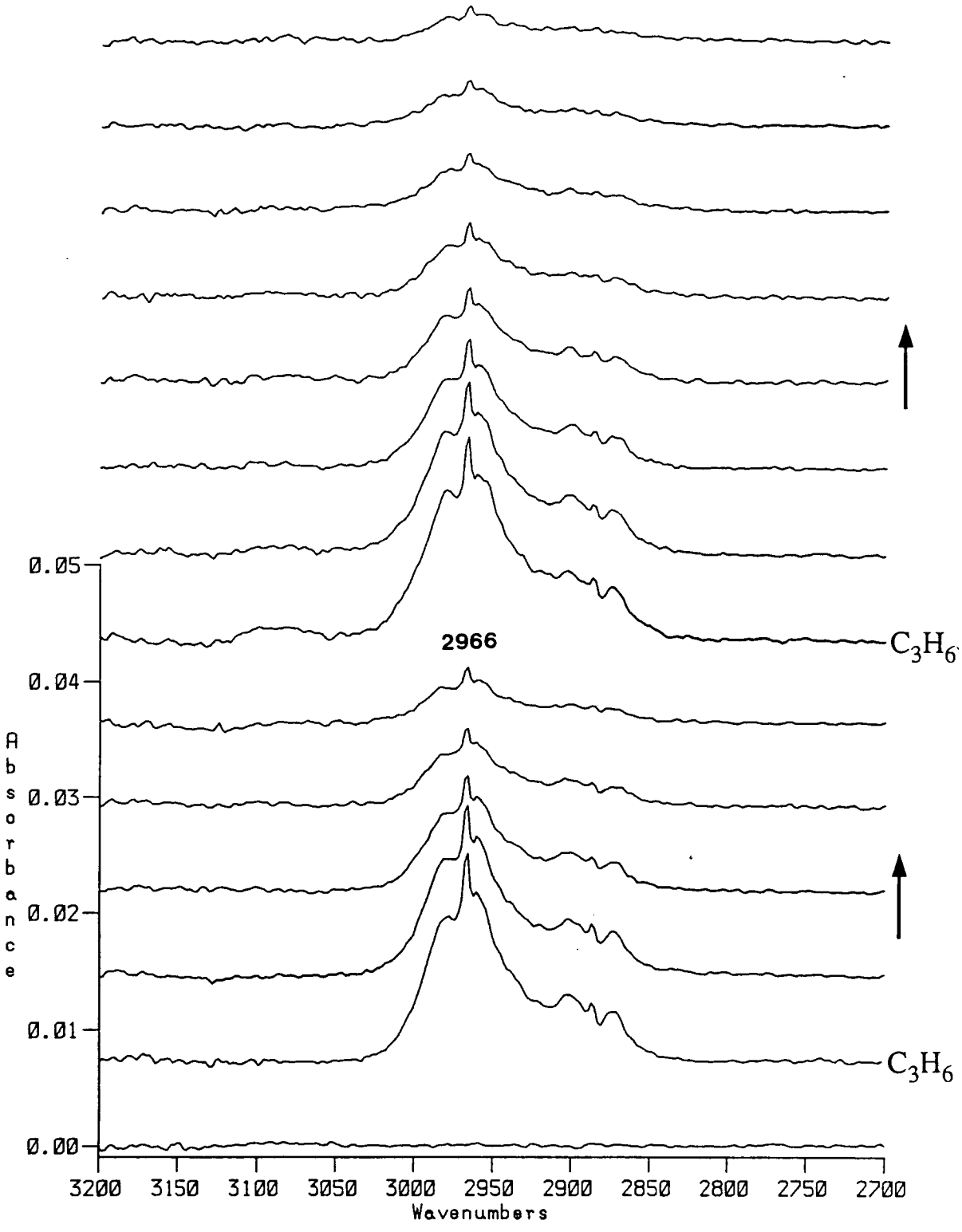

Figure 5.2 B *Transmission spectra of C_3H_6 adsorption onto an 'H_2 free' surface at 25°C (3200-2700cm^{-1}).*

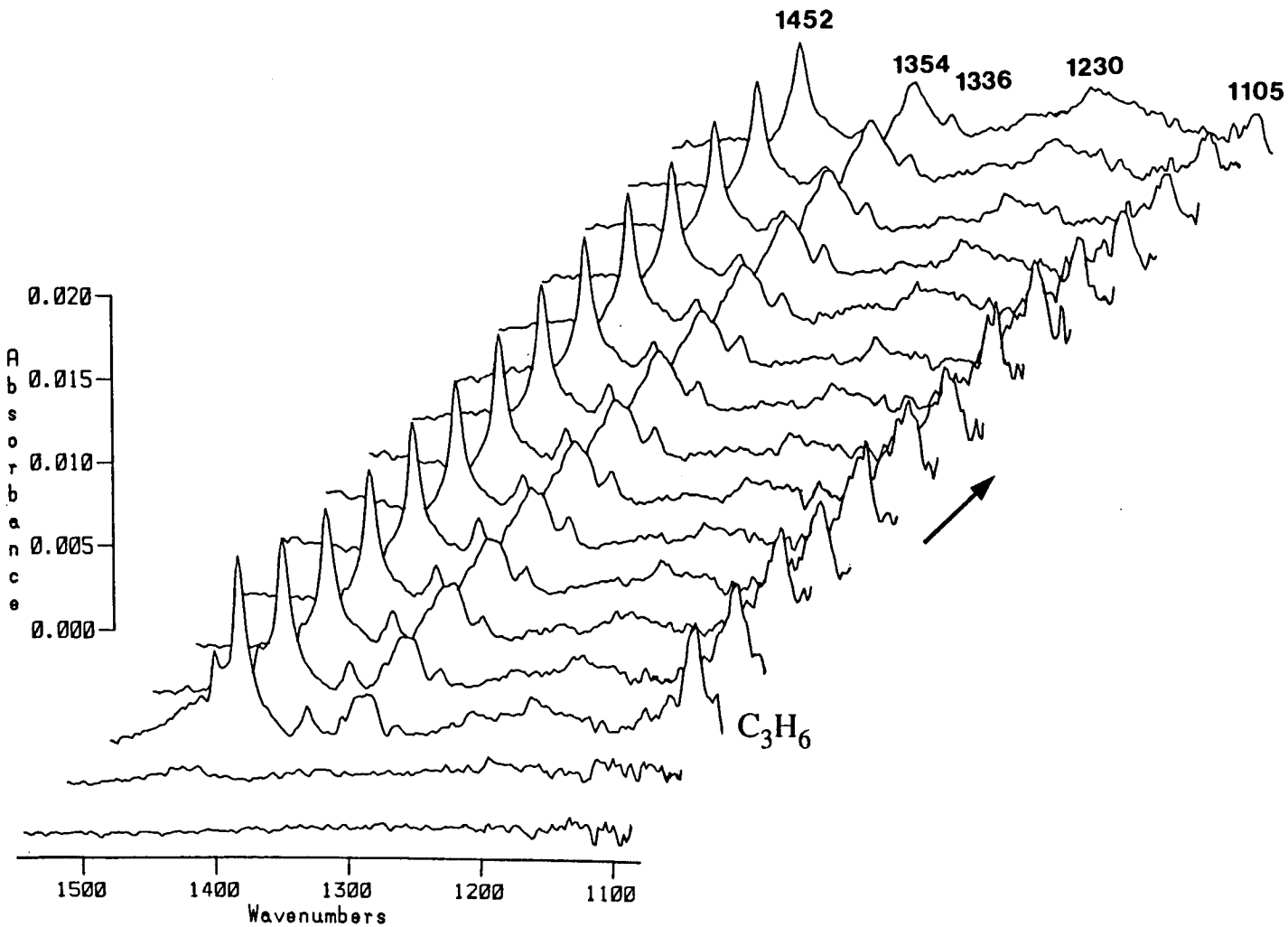

Figure 5.3 A *DRIFTS spectra of C_3H_6 adsorption onto an H_2-saturated surface at 25°C (1550 - 1080cm^{-1}.)*

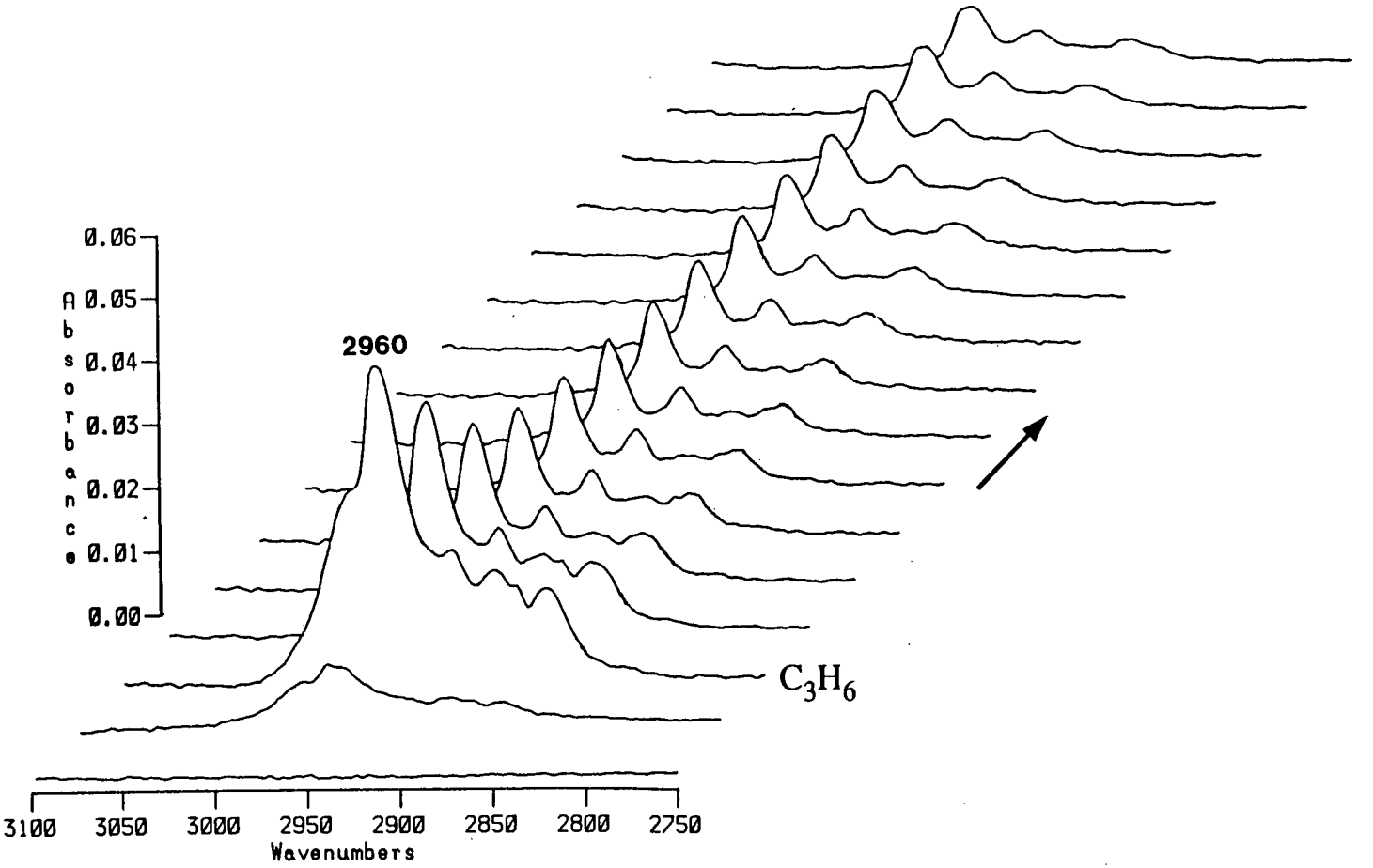

Figure 5.3 B *DRIFTS spectra of C_3H_6 adsorption onto an H_2-saturated surface at 25°C (3100 - 2750cm^{-1}.)*

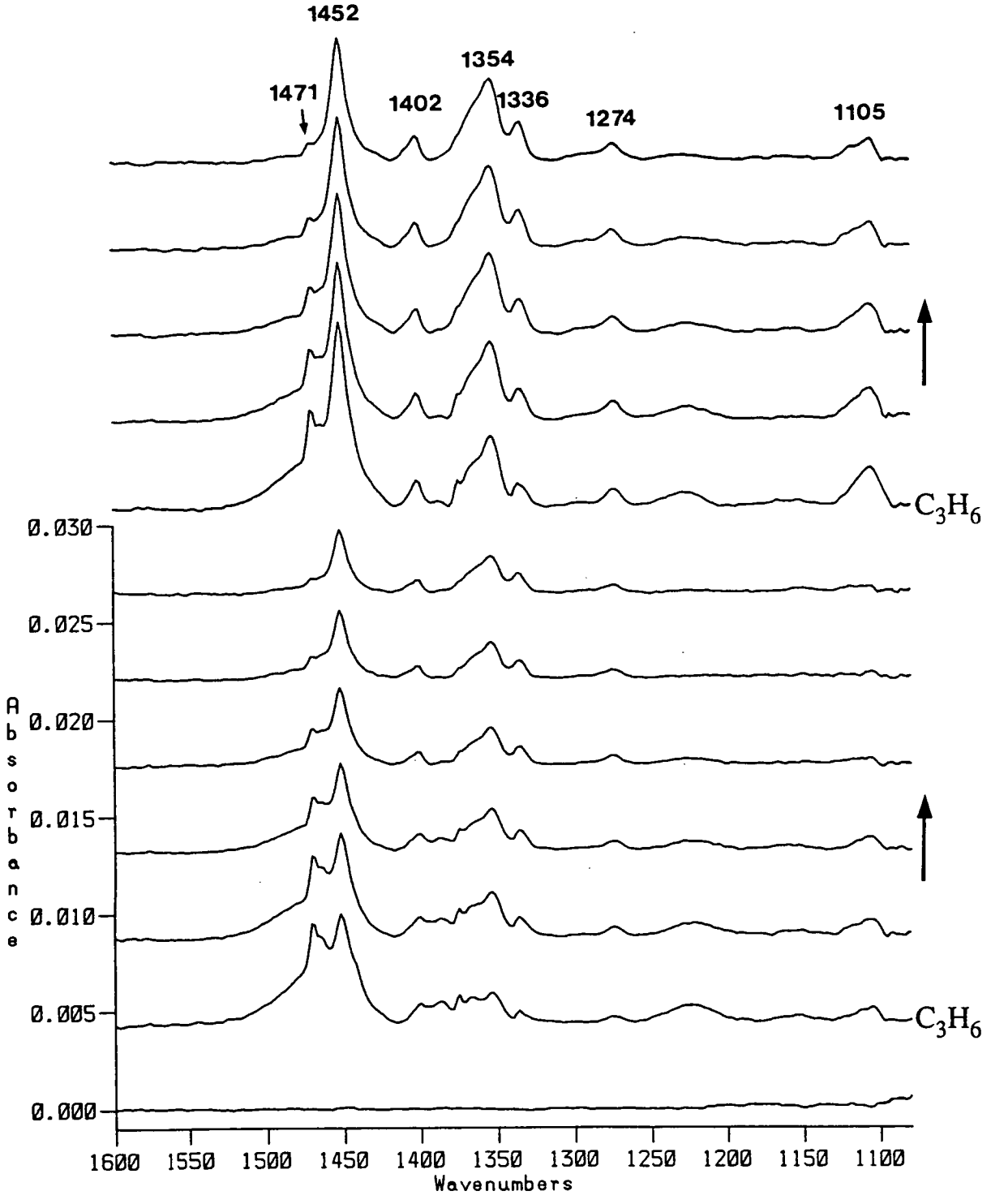

Figure 5.4 A *Transmission spectra of C_3H_6 adsorption onto an H_2 saturated surface at 25°C (1550-1080cm^{-1}).*

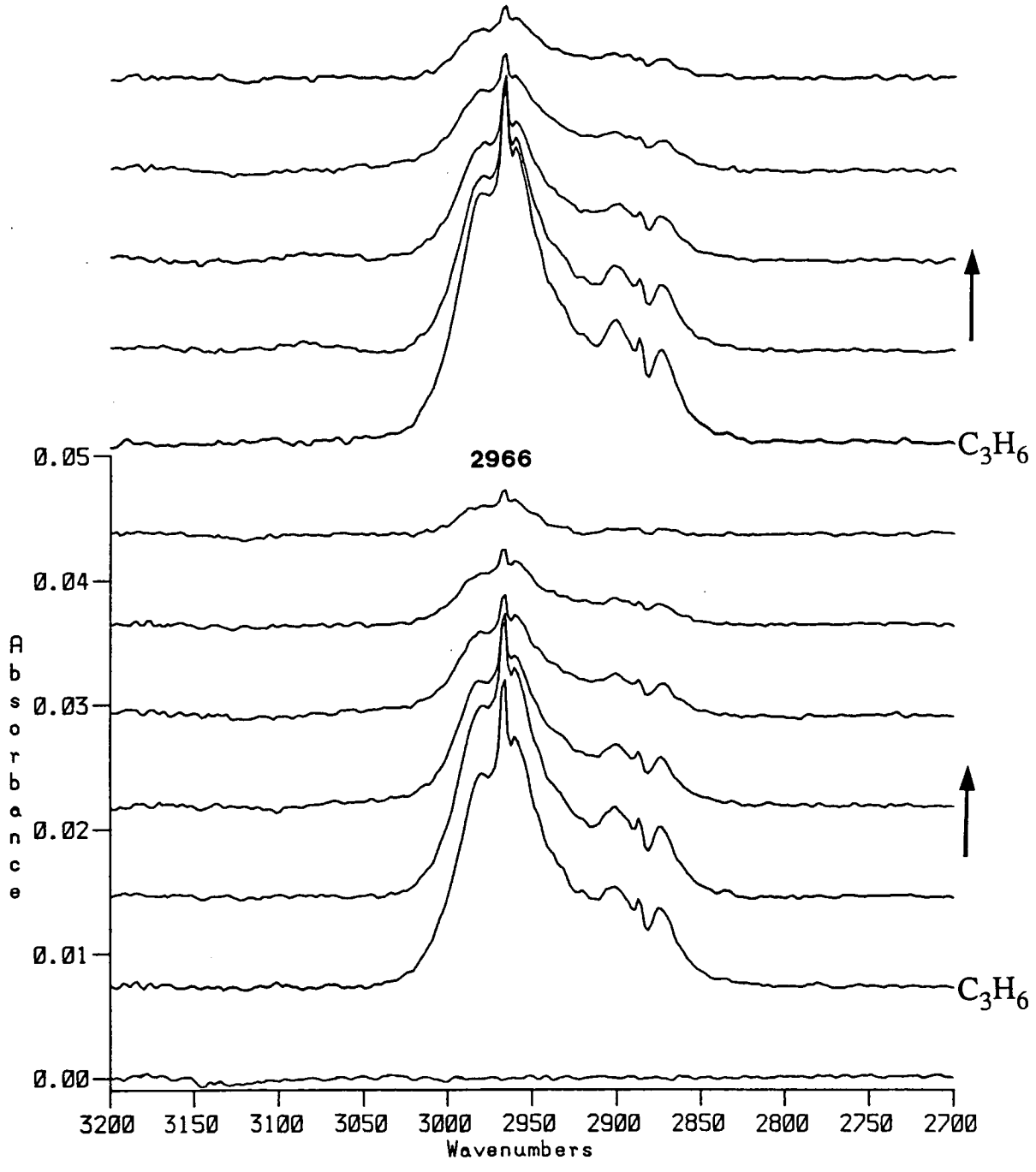

Figure 5.4 B *Transmission spectra of C_3H_6 adsorption onto an H_2 saturated surface at 25°C (3100-2750cm^{-1}).*

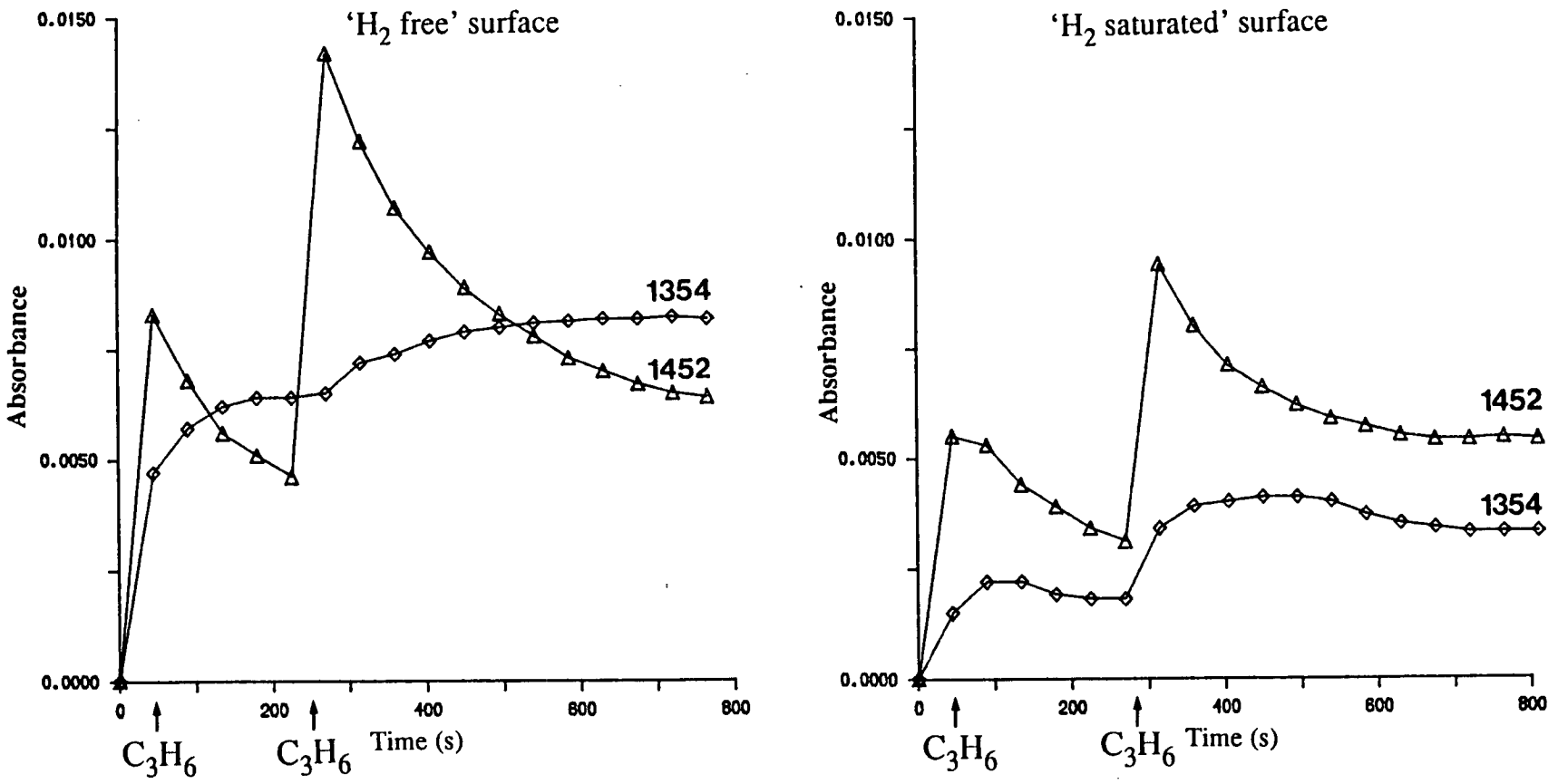

Figure 5.5 *Relative intensity of the 1452 and 1354cm^{-1} bands on H_2 free and H_2 saturated surfaces after C_3H_6 adsorption.*

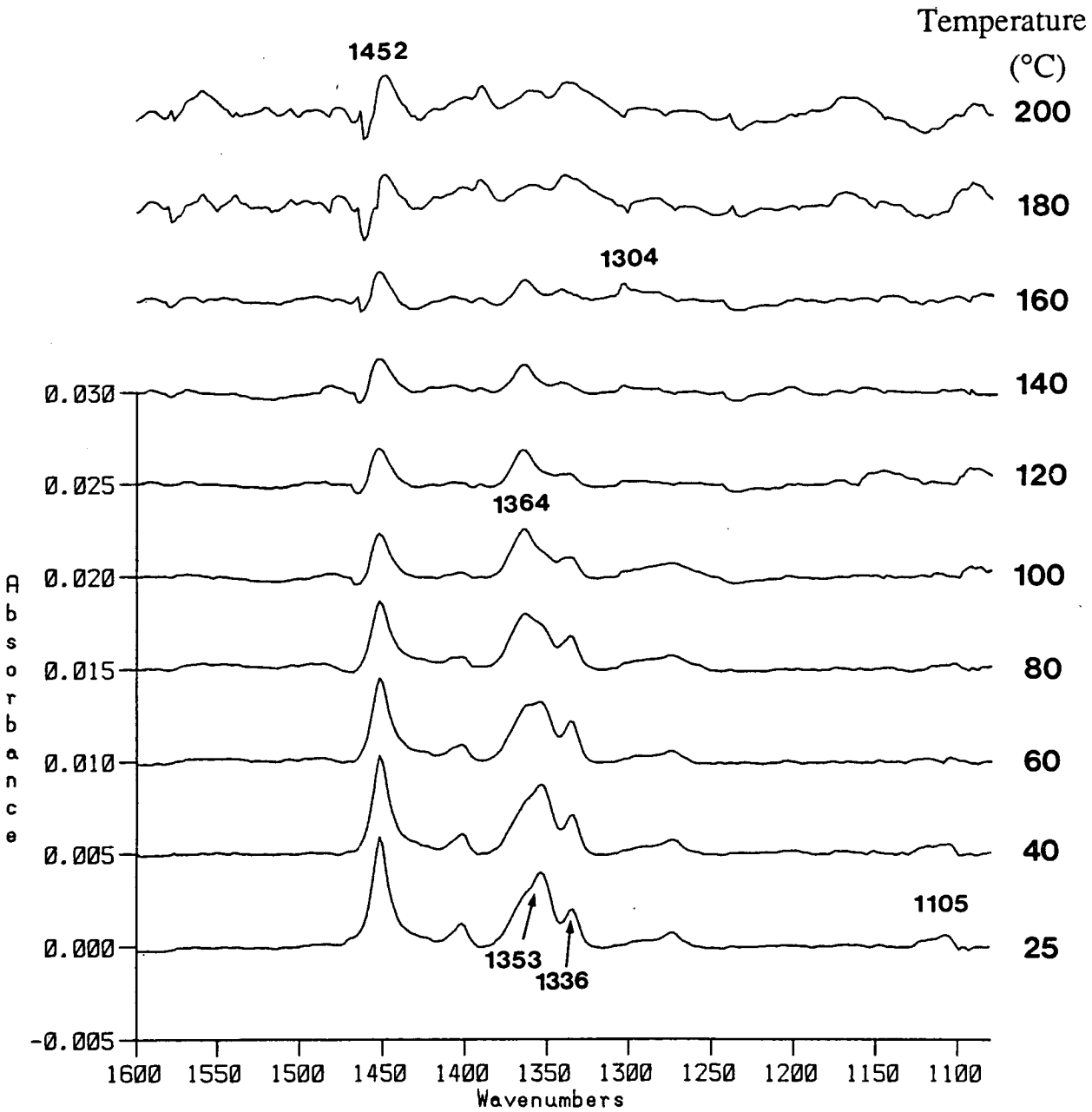

Figure 5.6 A *Transmission spectra during temperature programming between 25 and 200°C (1600-1080cm^{-1}).*

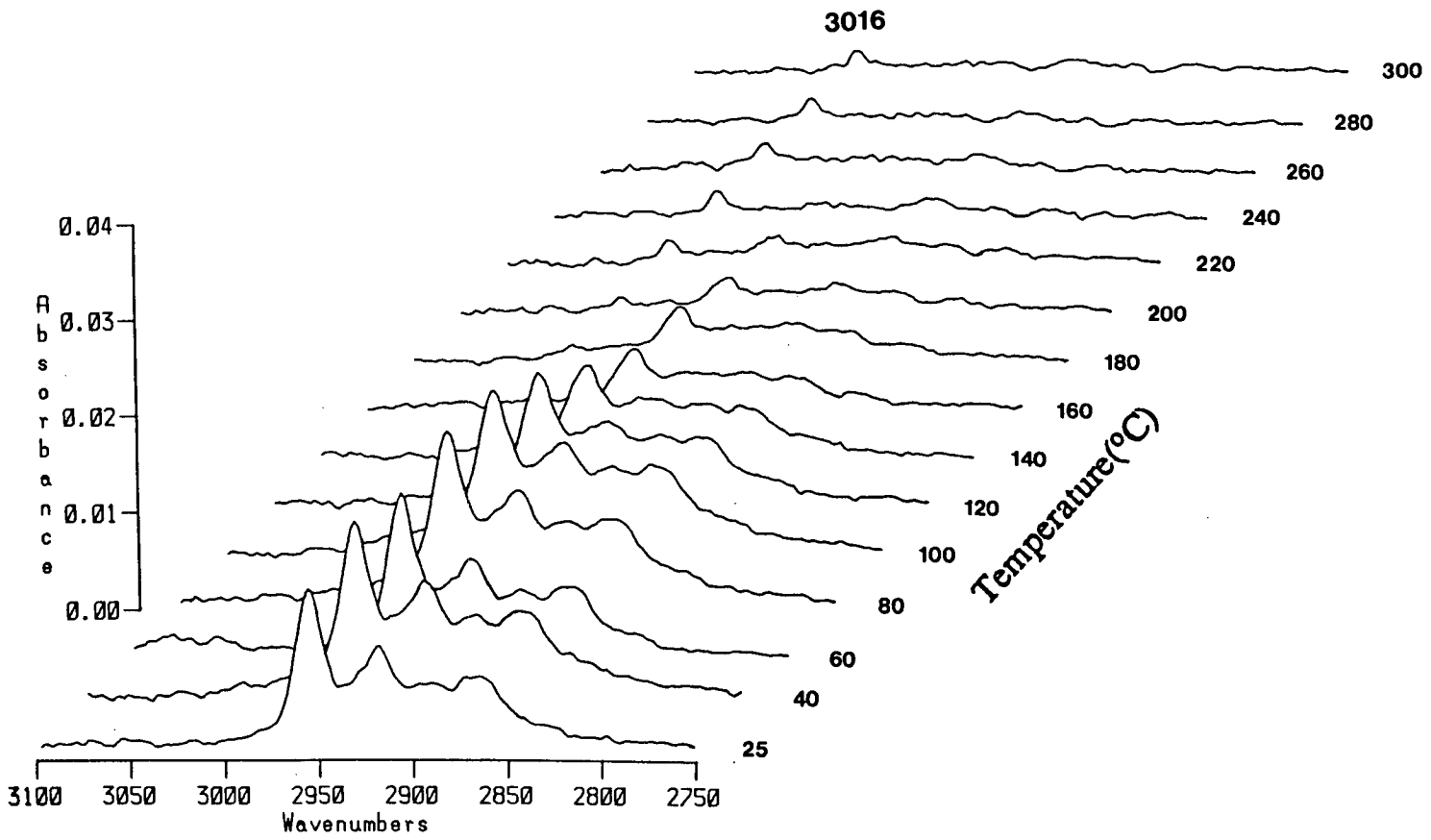

Figure 5.6 B *DRIFTS spectra during temperature programming between 25 and 300°C (3100 - 2750cm^{-1}).*

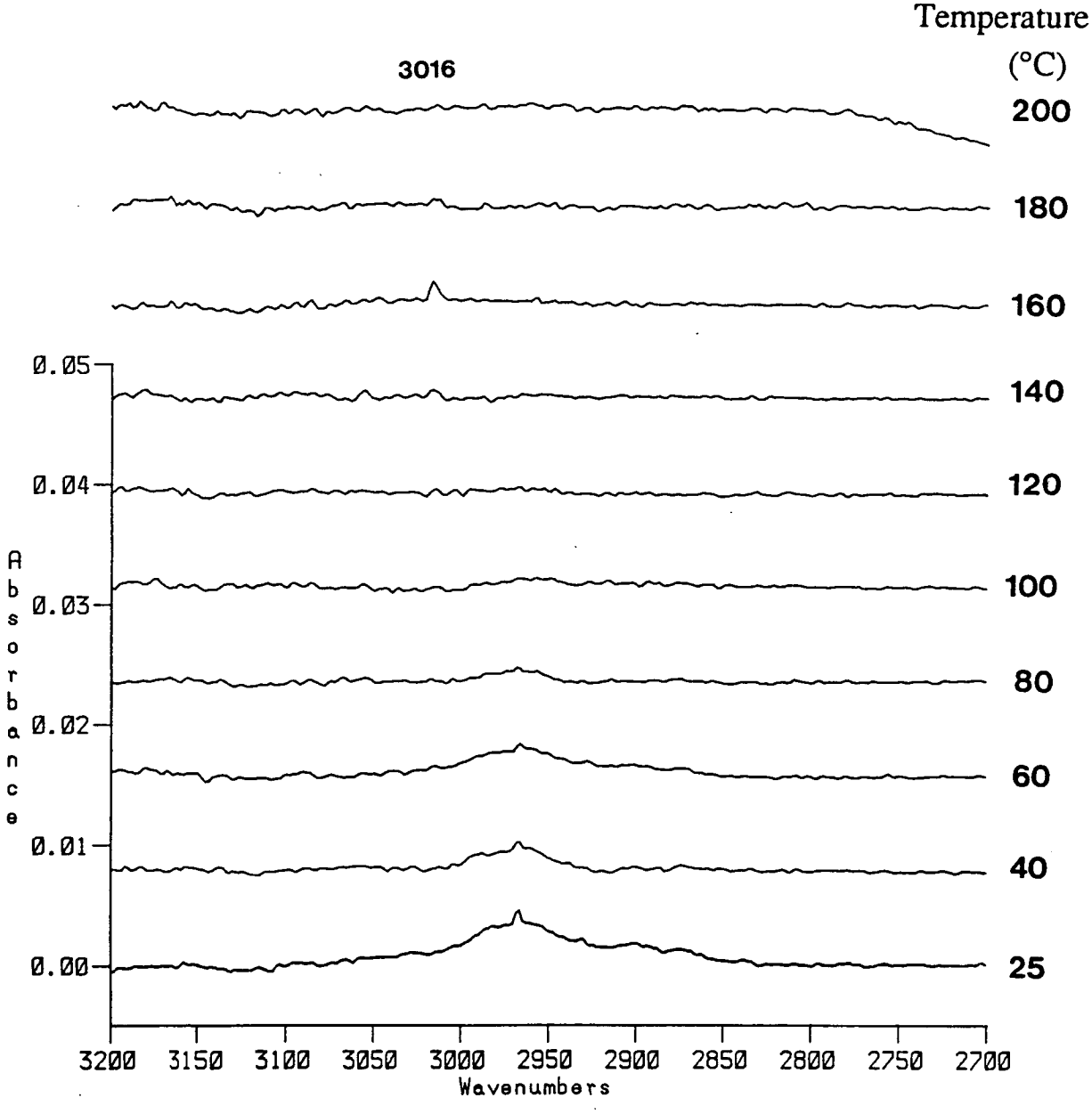

Figure 5.6 C *Transmission spectra during temperature programming between 25 and 200°C (3200-2700cm^{-1}).*

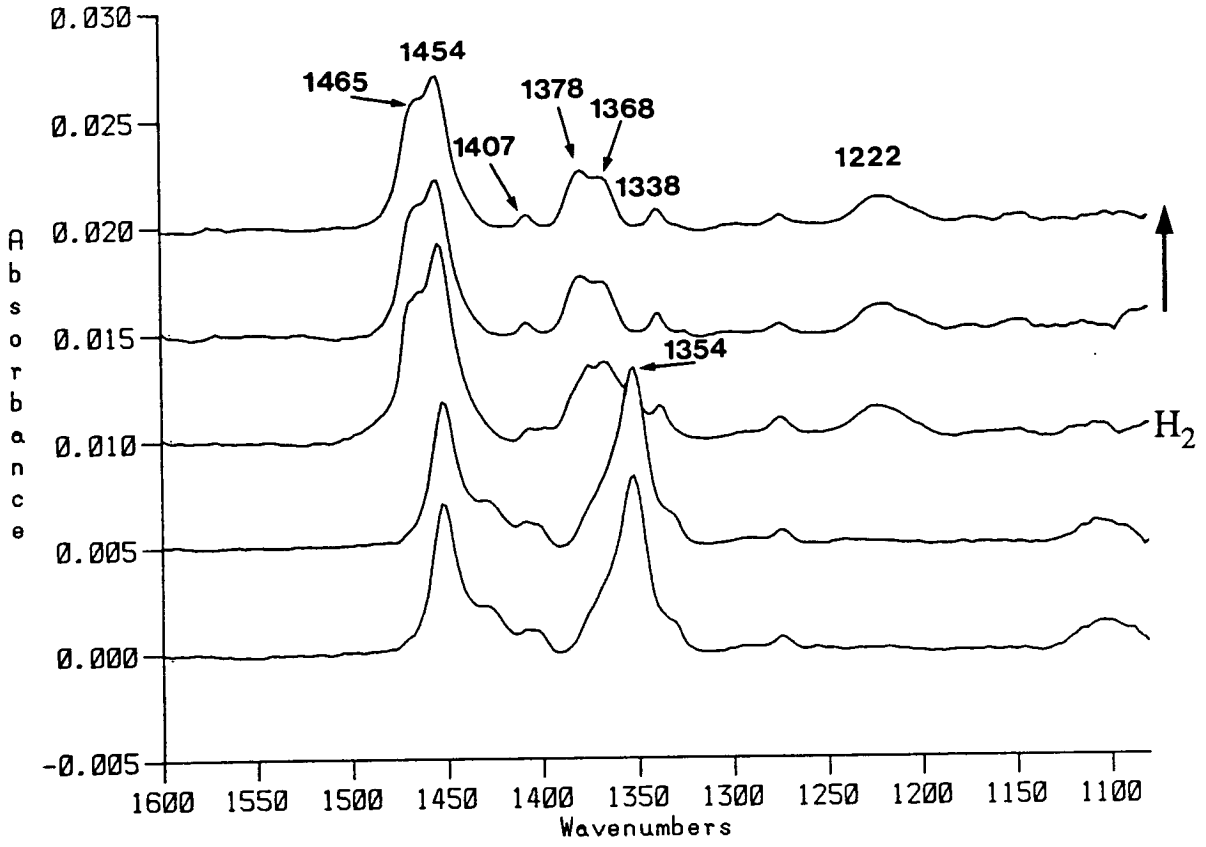

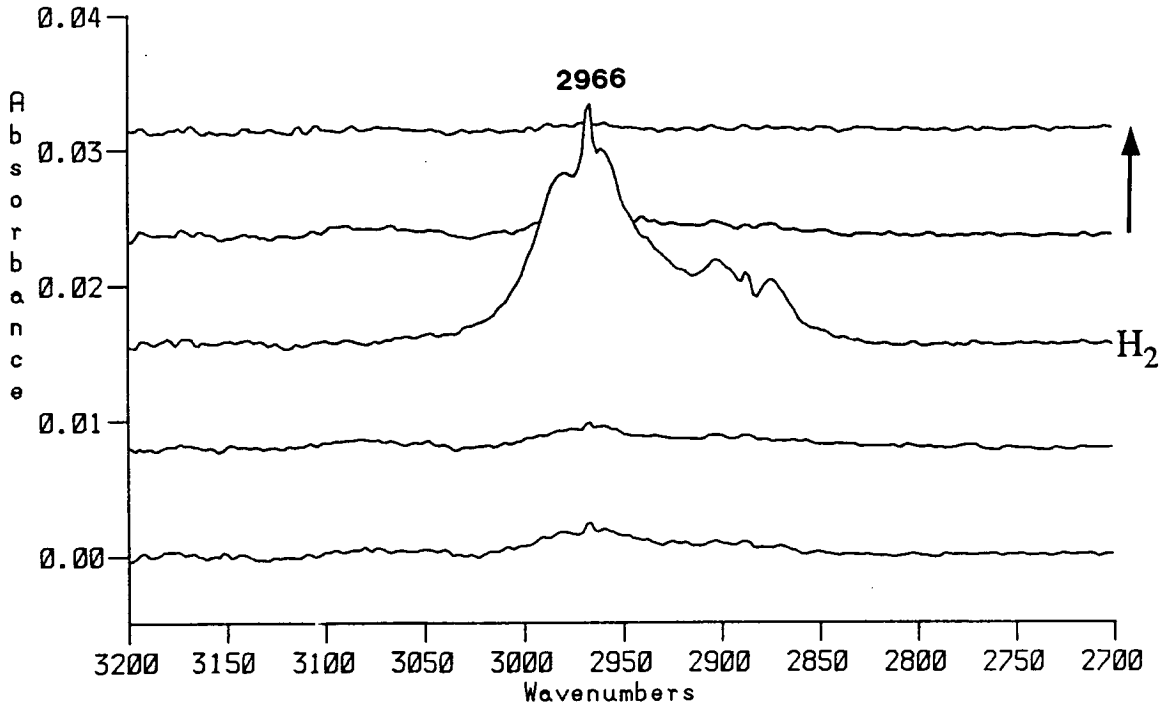

Figure 5.7 A and B. *Transmission spectra during hydrogenation of surface species at 25°C.*

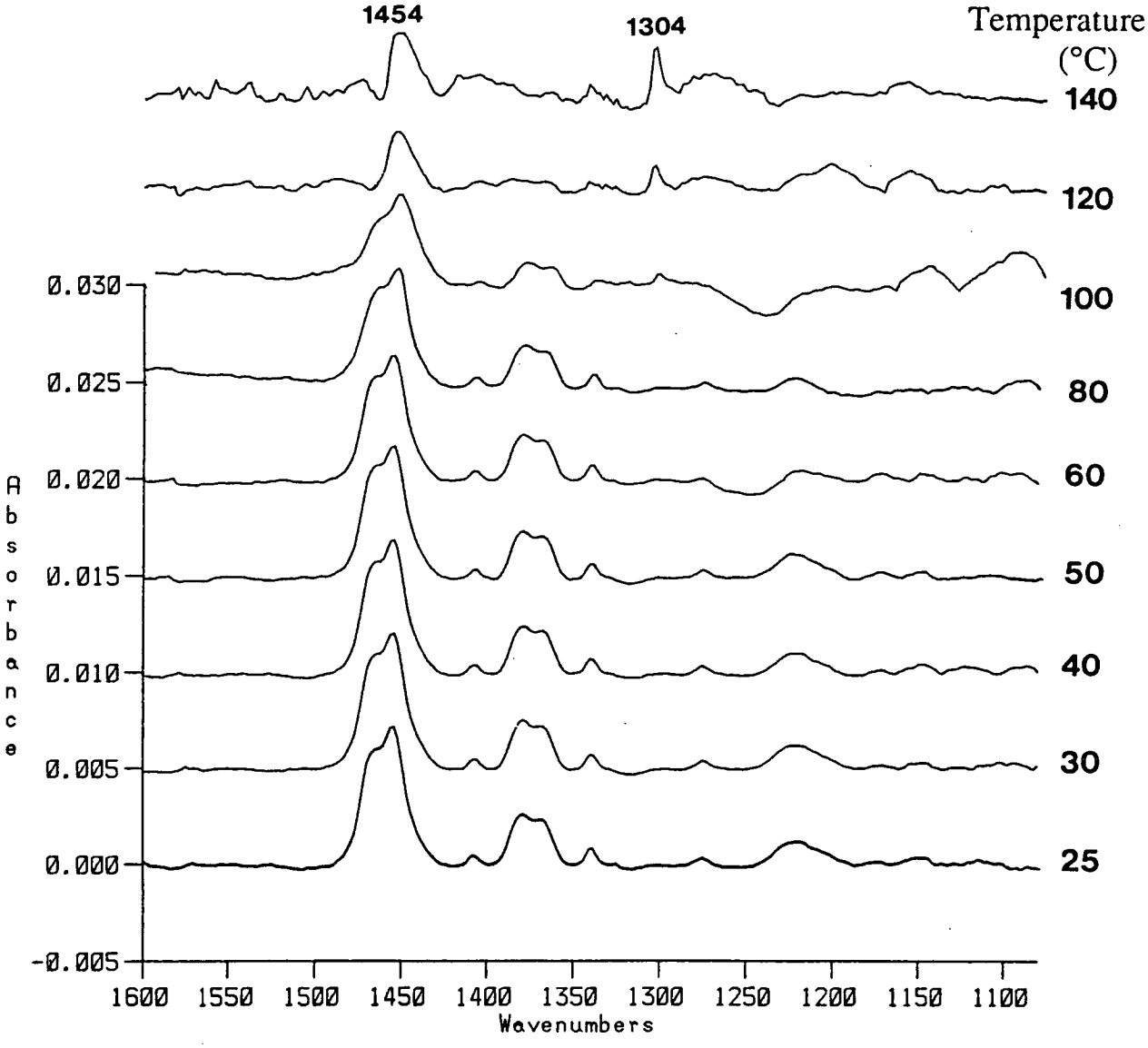

Figure 5.8 A *Transmission spectra during temperature programmed hydrogenation of C_3H_6 derived surface species from 25→140°C (1600-1080cm^{-1}).*

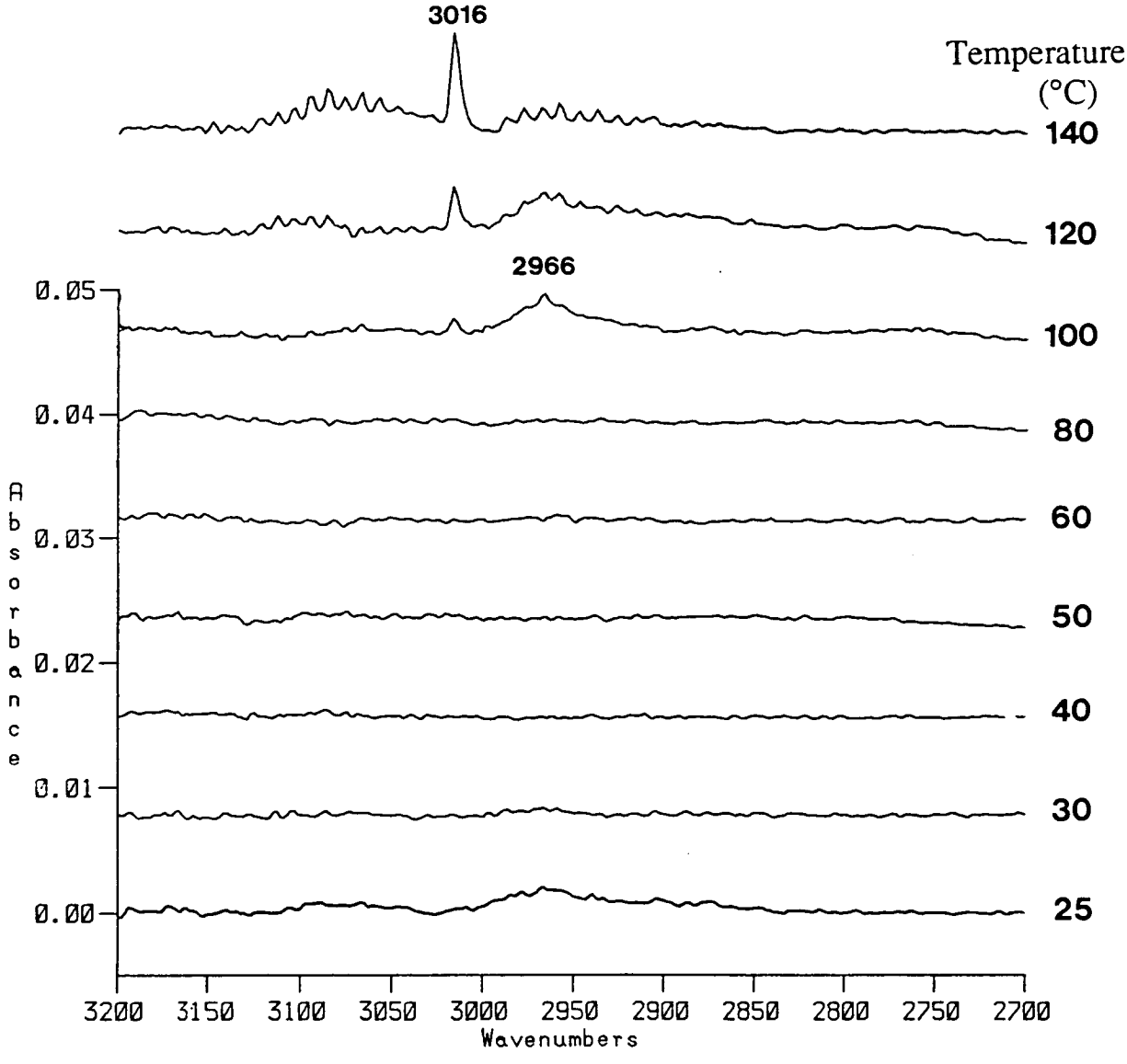

Figure 5.8 B *Transmission spectra during temperature programmed hydrogenation of C_3H_6 derived surface species from 25→140°C (3200-2700cm^{-1}).*

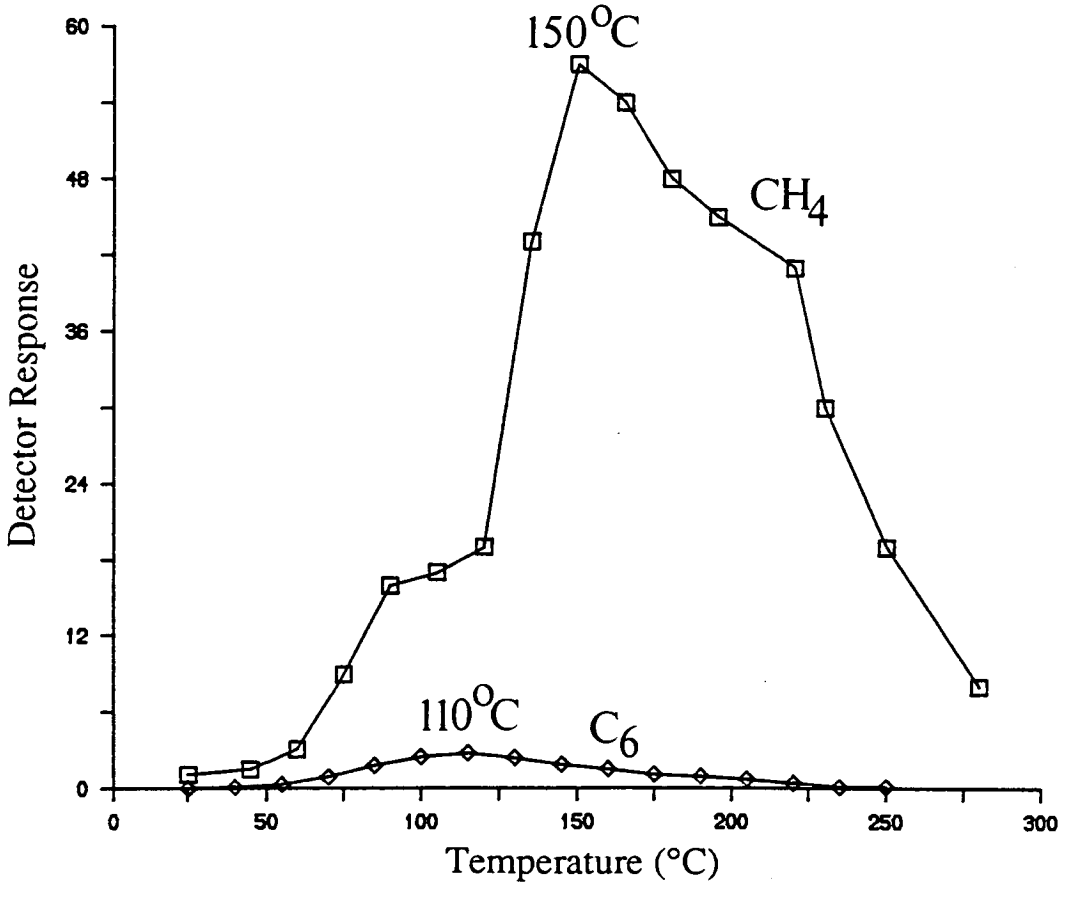

Figure 5.9 *Gas phase species released during temperature programmed hydrogenation of C_3H_6 derived surface species.*

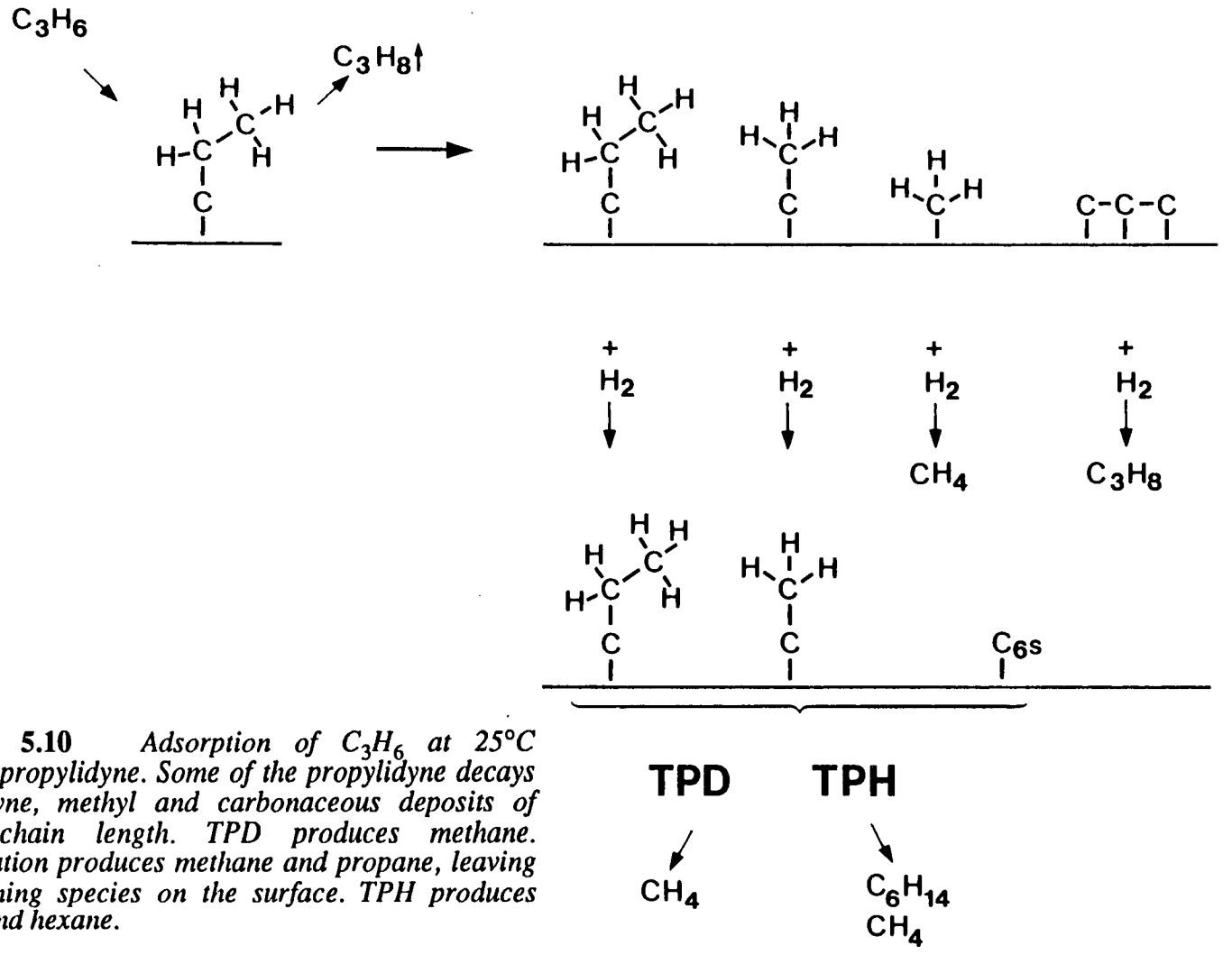

Figure 5.10 *Adsorption of C_3H_6 at 25°C producing propylidyne. Some of the propylidyne decays to ethylidyne, methyl and carbonaceous deposits of variable chain length. TPD produces methane. Hydrogenation produces methane and propane, leaving C_6 containing species on the surface. TPH produces methane and hexane.*

CHAPTER 6

Conclusions and Further Work.

1 Hydrocarbon Chemistry.

The observed chemistry of ethene on Ni/Al_2O_3 is clearly different from that reported to take place on nickel single crystals. Whilst alkylidyne species play a dominant role on supported nickel catalysts, as observed with DRIFTS/transmission infrared spectroscopy of both ethene and propene, the formation of acetylenic type fragments is the principal product of hydrocarbon adsorption on nickel single crystals, studied with EELS.

The reason for this difference must lie in the very different experimental conditions employed for each technique. Some of these are summarised in Table 6.1.

Table 6.1 Experimental conditions for DRIFTS/transmission and EELS.

Parameter	**DRIFTS/transmission**	**EELS**
Pressure	>1 atm	$<10^{-6}$ mbar
Hydrocarbon dose	500 mbar/s	$<10^{-6}$ mbar/s
Presence of hydrogen	never H_2 free	H_2 free
Spectrum acquisition time	<1 minute	>15 minutes

Firstly, the pressure at which experiments are performed is vastly different. DRIFTS/transmission infrared studies reported here employed a carrier gas at atmospheric pressure. Typical EELS studies on single crystals are restricted to a maximum pressure of 10^{-6}mbar. Similarly, the size of hydrocarbon doses used varies enormously. For supported catalyst studies, typical doses of 500mbar pressure were used *in situ*. Single crystal studies with EELS are once again restricted to 10^{-6}mbar dosing pressure *in situ*, although studies can be made of systems in high pressure cells and then evacuated for post reaction analysis.

Great effort is put into obtaining clean, well ordered metal single crystals for

adsorption studies, and they can be considered truly hydrogen free. As has been demonstrated for Ni/Al_2O_3, even after extensive outgassing, C_2D_4 adsorption formed 'mixed' ethylidyne ($CCHD_2$) on Ni/Al_2O_3. This indicated that some hydrogen is retained on the catalyst surface. It is also likely that there is a degree of contamination with carbon and sodium on the Ni/Al_2O_3 catalyst as remnants of the preparation procedure. Both hydrogen and carbonaceous deposits were discovered to have an important stabilising effect on ethylidyne on Ni/Al_2O_3 (Chapter 4). It may be that the totally hydrogen and carbon free environment that exists on single crystals leads to the rapid decay of ethylidyne and is therefore not observable with EELS.

A final factor that may be significant is the timescale of the experiments. DRIFTS/transmission spectra of high signal to noise ratio are easily obtained in less than one minute. EELS spectra from single crystals may take upwards of 15 minutes for acquisition of a spectrum of sufficient signal to noise ratio. Therefore, if ethylidyne forms at all on nickel single crystals, it may decay before it can be observed with EELS.

One answer to these questions may be to employ RAIRS on nickel single crystals. One of the advantages of RAIRS over EELS is that it is not restricted to low pressures. Thus high dose, high pressure and hydrogen rich environments could be studied, and such studies may reveal where the answer lies to this difference in hydrocarbon chemistry on nickel.

The use of isotopically labelled compounds in infrared spectroscopy can be an additional tool in helping to characterise the nature of carbon structures. ^{13}C-^{13}C bonds have a frequency of vibration that differs from ^{12}C-^{12}C bonds by about 10-15cm^{-1}. Detecting this difference is well within the resolution of the infrared experiments described in this thesis. ^{13}C labelled ethene could be used to produce surface species and the way that frequencies were different from the ^{12}C derived species may lead to more ideas about the structure and bonding of these species.

2 Nickel Surface Area Determination.

The surface area of a supported metal catalyst is a fundamental factor in the activity and efficiency of the catalyst. To maximise the number of active sites, the metal surface area must be optimised. This is especially true for studying adsorption of molecules by infrared spectroscopy where the mass of catalyst that can be studied *in situ* is limited. The more molecules that can be adsorbed on the surface in the

infrared beam, the better the signal to noise ratio in subsequent spectra will be. This makes possible the study of species, such as hydrocarbons, that are only weakly absorbing in the infrared region.

Hence maximising the nickel surface area in the Ni/Al_2O_3 system studied would be useful. As we have seen, to produce the reduced metal surface, the catalyst can be reduced in a flow of hydrogen. The temperature is ramped up at a particular rate and held there for a certain length of time. Once reduced, the metal surface area was measured using a variety of techniques (Chapter 3).

N_2O decomposition over Ni/Al_2O_3 at 50°C was shown to be a reliable source of nickel surface area measurements. The assumption was made that there was a ratio of 1:1 for N_2O molecule decomposed:Ni surface atom. Attempts to verify this were inconclusive and further work should be employed to more fully characterise this system. As already discussed, N_2O decomposition was found to be a function of both reaction temperature and pulse size. If these factors can be fully quantified, N_2O decomposition has the potential to be a powerful, metal specific surface area determination method.

3 Experimental Design.

The following factors may influence the eventual metal surface area produced;

1. temperature of reduction
2. temperature ramping rate
3. hydrogen flow rate
4. mass of catalyst being reduced
5. length of time of reduction
6. reduction vessel design

As described in Chapter 3, the reduction process for a nickel catalyst is essentially about choosing the correct temperature by achieving a balance between the incomplete thermodynamic reduction of the catalyst at temperatures that are too low and sintering of the metal produced when higher temperatures are used. Hence the temperature is certainly the most critical of the variables. But, what is better, a short reduction at high temperature or a long one at a lower temperature? The temperature *versus* time relationship is the fundamental problem to solve for this nickel system. The hydrogen flow rate and catalyst mass will obviously be factors in the problem, although in a sense they could be brought together as a 'hydrogen space velocity' term. The temperature ramping rate may affect sintering rates and the vessel design

will affect the exact nature of the flow of hydrogen, over or through the catalyst bed. This last term of vessel design is perhaps less easy to quantify than the previous terms. Evidently this is a multi-dimensional problem and approaching a solution which maximises the nickel surface area is not easily attained without embarking upon an inordinate number of experiments. Since each surface area measurement takes several hours in addition to the reduction time, a large number of experiments will be very time consuming. As the length of time for reduction is itself a variable, to fully explore all the possibilities of this variable will alone take many hours. Two traditional empirical methods are considered below [194].

Approaching a solution with a "one variable at a time" method means fixing all of the variables except one and then measuring the metal surface area produced at several levels of this variable. e.g. vary only the reduction temperature and measure the surface area produced, keeping time, hydrogen flow rate, temperature ramping rate, vessel design and catalyst mass constant.

For each variable, the best surface area is found, and the process is repeated for the other variables, until all have been considered. Whilst this method may work, it is very inefficient, taking many experiments to arrive at an answer. Also, if there are interactions among variables, this method may miss the best solution by not fully exploring the space of possible solutions.

A second traditional approach to the problem is to produce a matrix of all the interesting combinations of variables being considered. All of the combinations of variables in the matrix are then investigated. Whilst fully exploring experimental space, this method requires an unnecessarily large number of experiments. If, for example, ten values of each of the six variables were used, to fully explore the answer would produce a six dimensional matrix of 10^6 elements, requiring this number of experiments.

Evidently a statistical solution needs to be thought about carefully in order to solve the problem using a much smaller number of experiments [195]. Each experiment should carefully explore the experimental space, and a clear statistical strategy is used to ensure efficient progress towards a solution. Such experimental design procedures are widely used in engineering and biotechnology, but much less frequently in chemistry. Figure 6.1 below is a pictorial representation of the above points.

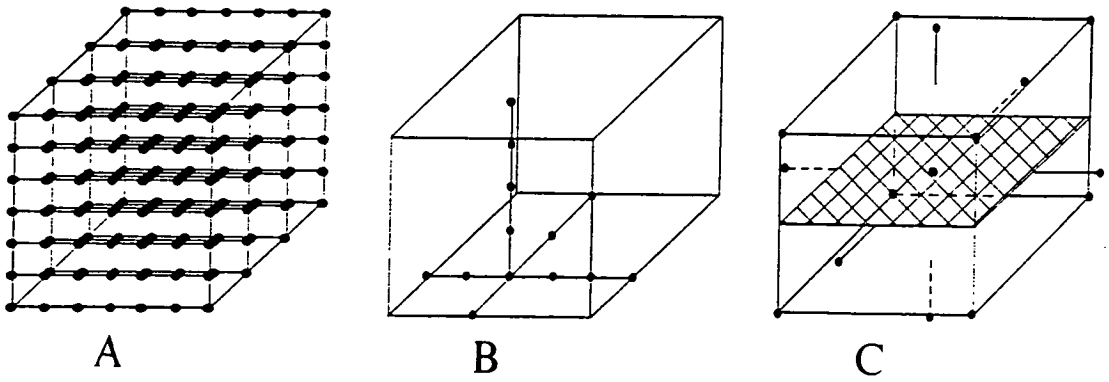

Figure 6.1 *Pictorial representation of three approaches to experimentation A) matrix, B) one at a time, C) statistical design (adapted from* [195]).

A statistical design approach to experimentation is also known as 'strategic experimentation' [194]. It combines statistical theory with an iterative problem solving strategy. In other words, results of previous experiments are analysed and by learning from these, the next experiments are refined and planned. This method always takes advantage of what has be learned so far and helps to 'home in' on the best solution.

Having come up with a list of experimental variables, they should be ranked in suspected order of importance. In this case, possibly;

1. temperature of reduction
2. length of time of reduction
3. hydrogen flow rate
4. reduction vessel design
5. mass of catalyst being reduced
6. temperature ramping rate

It is also useful to put them into categories; critical, probably important and possibly important variables. In this case, 1 and 2 are critical, 3,4 and 5 are probably important, with 6 possibly important. This ranking order may be useful if a balance has to be struck between the number of variables and the sample size and resolution that we want to use. An independent variable in the experiment, such as time, is usually referred to as an 'experimental factor' or just 'factor'. The measured result at the end of the experiment, in this case the nickel surface area, is generally referred to

as the 'response factor'.

Several approaches may be taken to reach an optimum solution. One such possibility is the use of principal components analysis [199], [200], [201]. Here a series of up to 20 randomly generated experiments are performed, the level of each variable must be randomly chosen, between two fixed limits. The principal components analysis will then generate a number, or 'loading' for each variable, between -100 and +100, giving an indication of the importance, or weight of each factor to the new synthetic variable, the principal component. A large positive number indicates a strong correlation between the variable (or factor) in question and the principal component. A large negative number indicates that the specific experimental factor is strongly anticorrelated with the principal component. A number near zero indicates that the specific experimental factor is not correlated, and largely irrelevant to the overall result. Knowing the unimportant factors, which can then be discarded, immediately simplifies the problem and reduces the number of experiments.

A large number of experimental designs exist (e.g. [196], [197], [198]), and there are many different designs to choose from for any particular experimental set-up. A design in this context is taken to mean a collection of settings of the experimental factors, generated in a logical way, at which the experiment will be run and the response variable measured. The difference in average experimental response between the highest and the lowest settings of a factor is known as the 'main effect'. When two effects cannot be estimated independently, they are said to be confounded. In the confounded pattern $A^*B + C^*D$, this means that the two factor interaction A^*B is confounded with the two factor interaction C^*D i.e. A^*B and C^*D cannot be distinguished from each other in this design, only the sum can be estimated. Two factors are said to interact when their joint effect cannot be explained by the sum of their effects.

Standard statistical designs consider only two values of each factor at a time, a high and a low setting, designated as -1 as +1. For the temperature this may be 550° and 600° for example. Haaland [194] presents a series of designs that can be run at different resolutions, depending on the situation;

Resolution V: All main effects and all two-factor interactions can be estimated. No two-factor interactions are confounded with other two-factor interactions or other main effects, and no main effects are confounded with each other. Every variable is totally independent.

Resolution IV: No main effects are confounded with two-factor interactions or other main effects. Some two-factor interactions may be confounded with others.

Resolution III: No main effects are confounded with other effects, main effects may be confounded with two-factor interactions.

The problem of surface area measurements will probably fall into the resolution V category. This should allow the independent estimation of all main effects and all two-factor interactions. This situation is known as a 'clear signal' design. A series of designs, designated FF0308, FF0416, FF0516 and FF0632 has been presented by Haaland [194]. The FF indicates that these are full factorial designs. The first two figures are the number of factors (experimental variables) that can be accommodated in the design and the second two are the sample size (number of experiments needed) generated by the design. In the nickel surface area problem, there are either 5 or 6 factors, depending on whether the sample vessel is included as a factor, which will therefore generate a sample size of either 16 or 32. If the experiment was run with resolution IV, only 16 experiments will be needed for a 6 factor problem. This would be reduced still further to only 8 for a 6 factor problem run with a design based on the resolution III criterion.

The FF0516 design for a 5 factor problem is shown in Table 6.2 below.

Table 6.2 FF0516 design for a 5 factor problem.

Run No.	Time	Temp.	Heat Rate	H_2 Rate	Cat Mass
1	-1	-1	-1	-1	+1
2	-1	-1	-1	+1	-1
3	-1	-1	+1	-1	-1
4	-1	-1	+1	+1	+1
5	-1	+1	-1	-1	-1
6	-1	+1	-1	+1	+1
7	-1	+1	+1	-1	+1
8	-1	+1	+1	+1	-1
9	+1	-1	-1	-1	-1
10	+1	-1	-1	+1	+1
11	+1	-1	+1	-1	+1
12	+1	-1	+1	+1	-1
13	+1	+1	-1	-1	+1
14	+1	+1	-1	+1	-1
15	+1	+1	+1	-1	-1
16	+1	+1	+1	+1	+1

This trial of 16 experiments fully explores the experimental space. The response variable, the measured surface area, will give a clear indication as to which factors are important and whether they have been set at their optimum values. The range of settings for factors can be refined and the process repeated. This logical, " stop, look and listen ", approach will home in on the optimum solution much more quickly than a blind empirical method.

References.

[1] Donnan, F.G. *Ostwald Memorial Lecture - J.Chem.Soc.* 316 (1933).

[2] Berzelius, J.J. *Annls.Chim.Phys.* **61** 146 (1836).

[3] Priestley, J. *Experiments and observations on different kinds of air* pp.425 Thomas Pearson (Printer), Birmingham 1790.

[4] Robertson, A.J.B. *Catalysis of Gas Reactions by Metals* Logos Press, London 1970.

[5] Thomson, S.J. and Webb, G. *Heterogeneous Catalysis* pp.5 Oliver and Boyd, Edinburgh 1968.

[6] De Bokx, P.K.; Kock, A.J.H.; Baellard, E.; Klop, W. and Geus, J.W. *J.Catal.* **96** 454 (1985).

[7] Lennard-Jones, J.E. *Trans.Faraday.Soc.* **28** 333 (1932).

[8] Gundry, P.M. and Tompkins, F.C. *Trans.Faraday.Soc.* **52** 1609 (1956).

[9] Sabatier, P. *La Catalyse en Chimie Organique* 2nd Ed. Beranger, Paris 1920.

[10] Sabatier,P. *Bull.Soc.Chim.Fr.* **9** 1261 (1939).

[11] ICI Catalysts *Manual for Steam Reforming 25-3, 46-9* pp.7 ICI Chemicals and Polymers, Billingham 1988.

[12] Ciocco, M.V. and Blackmond, D.G. *Appl.Catal.* **44** 105 (1988).

[13] Rootsaert, W.J.M. and Sachtler, W.M.H. *Z.Phys.Chem.* **26** 16 (1960).

[14] Bond, G.C. and Burch, R. in *Catalysis (Specialist Periodical Reports)* ed. Bond, G.C. and Webb, G. **6** pp.27 The Royal Society of Chemistry, London 1983.

[15] Woodruff, D.P. and Delchar, T.A. *Modern Techniques of Surface Science* Cambridge University Press 1988.

[16] Boudart, M. *Chemtech* 688 (1986).

[17] Thomson, S.J. and Webb, G.J. *J.Chem.Soc.,Chem.Commun.* 526 (1976).

[18] Ibach, H. and Lehwald, S. *J.Vac.Sci.Technol.* **15** 407 (1978).

[19] Kesmodel, L.L.; Dubois, L.H. and Somorjai, G.A. *J.Chem.Phys.* **70** 2130 (1979).

[20] Demuth, J.E. *Surf.Sci.* **80** 867 (1979).

[21] Skinner, P.; Howard, M.W.; Oxton, I.A.; Kettle, S.F.A.; Powell, D.B. and Sheppard, N. *J.Chem.Soc.Faraday Trans. II* **77** 1203 (1981).

[22] Burwell, R.L. *Catal.Letts.* **5** 237 (1990).

[23] Sheppard, N. *Ann.Rev.Phys.Chem.* **39** 589 (1988).

[24] Van Hardeveld, R. and Hartog, F. *Surf.Sci.* **15** 189 (1969).

[25] Halpern, J. in *Relationship between Homogeneous and Heterogeneous Catalysis* ed. Imelik, B. *et al.* CNRS (Paris) 1978.

[26] Goodman, D.W.; Kelley, R.D. and Madey, J.E. *J.Catal.* **63** 226 (1980).

[27] Judd, R.W.; Allen, H.J.; Hollins, P. and Pritchard, J. *Spectrochim.Acta* **43A** 1607 (1987).

[28] Vannice, M.A. in *Catalysis : Science and Technology* ed. Anderson, J. and Boudart, R. **Vol. 3** Springer-Verlag, Heidelberg 1982.

[29] Strongin, D.R.; Carrazza, J.; Bare, S.R. and Somorjai, G.A. *J.Catal.* **103** 213 (1987).

[30] Boudart, M. and Löffler, D.G. *J.Phys.Chem.* **88** 5763 (1984).

[31] Joyner, R.W. *J.Chem.Soc.Faraday.Trans.* **86** 2675 (1990).

[32] Somorjai, G.A. and Van Hove, M.A. *Progress in Surface Science* **30** 201 (1989).

[33] Boudart, M.; Collins, D.M.; Hanson, F.V. and Spicer, W.E. *J.Vac.Sci.Technol.* **14** 441 (1977).

[34] Dalmai-Imelik, G. and Massardier, J. in *Proceedings 6th International Congress on Catalysis, London 1976 pp.90* ed. Bond, G.C.; Wells, P.B. and Tompkins, F.C. The Chemical Society, London 1977.

[35] Propst, F.M. and Piper, T.C. *J.Vac.Sci.Technol.* **4** 53 (1967).

[36] Anderson, R.B. and Dawson P.T. (Eds.) *Characterisation of Surface Adsorbed Species,* **Vol. III** *Experimental Methods in Catalytic Research* Academic Press, London 1976.

[37] Somorjai, G.A. *Chemistry in Two Dimensions* Cornell University Press, Ithaca, New York 1981.

[38] Haller, G.T. *Catal.Rev.-Sci.Eng.* **23** 477 (1981).

[39] Falconer, J.L. and Schwarz, J.A. *Catal.Rev.-Sci.Eng.* **25** 141 (1983).

[40] Coblentz, W.W. *J.Franklin.Inst.* **172** 309 (1911).

[41] Eischens, R.P. and Pliskin, W.A. *Adv.Catal.* **10** 1 (1958).

[42] Ebsworth, E.A.V.; Rankin, D.W.H. and Cradock, S. *Structural Methods in Inorganic Chemistry* Blackwell Scientific Publications, London 1987.

[43] Cracknell, A.P. *Thin Solid Films* **21** 107 (1974).

[44] Herzberg, G. *Molecular Spectra and Molecular Structure* Van Nostrand, New York 1945.

[45] Little, L.H. *Infrared Spectra of Adsorbed Species* Academic Press, London 1966.

[46] Bandy, B.J.; Chesters, M.A.; James, D.I.; McDougall, G.S.; Pemble, M.E. and Sheppard, N. *Phil.Trans.Roy.Soc.A* **318** 141 (1986).

[47] Greenler, R.G.; Snider, D.R.; Witt, D. and Sorbello, R.S. *Surf.Sci.* **118** 415 (1982).

[48] Van de Hulst, H.C. *Light Scattering by Small Particles* Wiley, New York 1957.

[49] Longhurst, R.S. *Geometrical and Physical Optics* pp.492 Longman 1973.

[50] Mie, G. *Ann.Phys.* **25** 377 (1908).

[51] Theissing, H.H. *J.Op.Soc.Am.* **40** 232 (1950).

[52] Yates, J.T.Jr. and Madey, T.E. *Vibrational Spectroscopy of Molecules on Surfaces* Plenum, New York 1987.

[53] Agyare Yeboah, S.; Wang, S.-H. and Griffiths, P.R. *Appl.Spectrosc.* **38** 259 (1984).

[54] Eischens, R.P. and Pliskin, W.A. *J.Phys.Chem.* **60** 194 (1956).

[55] Basu, P.; Ballinger, T.H. and Yates, J.T.Jr. *Rev.Sci.Instrum.* **59** 1321 (1988).

[56] Yates, J.T.Jr.; Duncan, T.M.; Worley, S.D. and Vaughan, R.W. *J.Chem.Phys.* **70** 1219 (1979).

[57] Miura, H. and Gonzalez, R.D. *J.Phys.E:Sci.Instrum.* **15** 373 (1982).

[58] Karge, H.G.; Trevizan de Suarez, S. and Dalla Lana, I.G. *J.Phys.Chem.* **88** 1782 (1984).

[59] Gallei, E. and Schadow, E. *Rev.Sci.Instrum.* **45** 1504 (1974).

[60] Dalla Betta, R.A. and Shelef, M. *J.Catal.* **48** 111 (1977).

[61] Kaul, D.J and Wolf, E.E. *J.Catal.* **89** 348 (1984).

[62] Vannice, M.A.; Moon, S.H.; Twu, C.C. and Wang, S-Y. *J.Phys.E:Sci.Instrum.* **12** 849 (1979).

[63] O'Connor, C.T.; Fletcher, J.C.Q. and Rautenbach, M.W. *J.Phys.E:Sci.Instrum.* **19** 367 (1986).

[64] Larkins, F.P. and Nordin, M.R. *Appl.Spectros.* **42** 906 (1988).

[65] Prokopowicz, R.A.; Silveston, P.L.; Baudais, F.L.; Irish, D.E. and Hudgins, R.R. *Appl.Spectros.* **42** 385 (1988).

[66] Tan, H.S. and James, W.E. *Can.J.Spectros.* **34** 35 (1989).

[67] Hayes, K.E. *Can.J.Spectros.* **20** 57 (1975).

[68] Szilágyi, T.; Koranyi, T.I.; Paal, Z. and Zilgner, J. *Catal.Letts.* **2** 287 (1989).

[69] Penninger, J.M.L. *J.Catal.* **56** 287 (1979).

[70] Nagai, M.; Lucietto, L.L.; Yao-En, L. and Gonzalez, R.D. *J.Catal.* **101** 522 (1986).

[71] Hicks, R.F.; Kellner, C.S.; Savatsky, B.J.; Hecker, W.C. and Bell, A.T. *J.Catal.* **71** 216 (1981).

[72] Griffin, G.L. and Yates, J.T.Jr *J.Catal.* **73** 396 (1982).

[73] Ryason, P.R. *Rev.Sci.Instrum.* **44** 772 (1973).

[74] Ralajczykowa, I. and Stanasiuk, Z. *J.Phys.E:Sci.Instrum.* **21** 906 (1988).

[75] Friedman, R.M. and Dannhardt, H.C. *Rev.Sci.Instrum.* **56** 1589 (1985).

[76] Wang, H.P. and Yates, J.T.Jr *J.Catal.* **89** 79 (1984).

[77] Cevallos Candau, J.F. and Conner, W.C. *J.Catal.* **106** 378 (1987).

[78] Campione, T.J. and Ekerdt, J.G. *J.Catal.* **102** 64 (1986).

[79] Ekerdt, J.G. and Bell, A.T. *J.Catal.* **58** 170 (1979).

[80] King, D.L. *J.Catal.* **61** 77 (1980).

[81] Lapinski, M.P. and Ekerdt, J.G. *J.Phys.Chem.* **94** 4599 (1990).

[82] Tinker, H.B. and Morris, D.E. *Rev.Sci.Instrum.* **43** 1024 (1972).

[83] Leyden, D.E. and Murthy, R.S.S. *Trends in Analytical Chemistry* **7** 164 (1988).

[84] Kortüm, G. and Delfs, H. *Spectrochim.Acta.* **20** 405 (1964).

[85] Fuller, M.P. and Griffiths, P.R. *Anal.Chem.* **50** 1906 (1978).

[86] Hamadeh, I.M. and Griffiths, P.R. *Appl.Spectrosc.* **41** 682 (1987).

[87] Niizuma, H.; Hattori, T.; Mori, T.; Miyamoto, A. and Murakami, Y. *J.Phys.Chem.* **87** 3652 (1983).

[88] Kubelka, P. and Munk, F. *Z.Tech.Phys.* **12** 593 (1931).

[89] Schuster, A. *Astrophys.J.* **21** 1 (1905).

[90] Leyden, D.E. and Murthy, R.S.S. *Spectroscopy* **2** 28 (1987).

[91] Hecht, H.G. *Anal.Chem.* **48** 1775 (1976).

[92] Vincent, R.K. and Hunt, G.R. *Appl.Opt.* **7** 53 (1968).

[93] Fuller, M.P. *Ph.D. Thesis* Ohio University, Athens, Ohio, United States 1980.

[94] Brimmer, P.J. and Griffiths, P.R. *Anal.Chem.* **58** 2179 (1986).

[95] Mross, W.-D. *Catal.Rev.Sci.Eng.* **25** 591 (1983).

[96] Yang, P.W.; Mantsch, H.H. and Baudais, F. *Appl.Spectrosc.* **40** 974 (1986).

[97] Messerschmidt, R. *Appl.Spectrosc.* **39** 737 (1985).

[98] Hembree, D.M. and Smyrl, H.R. *Appl.Spectrosc.* **43** 267 (1989).

[99] Spectra-Tech Diffuse Reflectance Accessory, Spectra-Tech, Inc., Stanford, CT, United States.

[100] Brault, J.W. *Phil.Trans.R.Soc.A* **307** 503 (1982).

[101] Golden, W.G.; Saperstein, D.D.; Severson, M.W. and Overend, J. *J.Phys.Chem.* **88** 574 (1984).

[102] Bio-Rad, Digilab Division, Cambridge, MA, United States.

[103] Yang, P.W. and Casal, H.L. *Appl.Spectrosc.* **40** 1070 (1986).

[104] Blitz, J.P.; Murthy, R.S.S.; Leyden, D.E. *Appl.Spectrosc.* **40** 829 (1986).

[105] Holmes, P.D.; McDougall, G.S.; Wilcock, I.C. and Waugh, K.C. *Catal.Today* **9** 15 (1991).

[106] Felder, B. *Helv.Chim.Acta.* **47** 488 (1964).

[107] Holmes, P.D. *Ph.D. Thesis* University of Edinburgh 1992.

[108] Van Every, W.K. and Griffiths, P.R. *Appl.Spectrosc.* **45** 347 (1991).

[109] Fuller, M.P. and Griffiths, P.R. *Appl.Spectrosc.* **34** 533 (1980).

[110] Ross, J.R.H. *Metal Catalysed Methanation and Steam Reforming* in Catalysis (7), Specialist Periodical Reports, Royal Society of Chemistry 1985.

[111] van Veen, G.; Kruissink, E.C.; Doesburg, E.B.M.; Ross, J.R.H. and van Reijen, L.L. *React.Kinet.Catal.Lett.* **9** 143 (1978).

[112] Kruissink, E.C.; van Reijen, L.L. and Ross, J.R.H. *J.Chem.Soc.,Faraday Trans I* **77** 649 (1981).

[113] Zelinsky, N. and Kommarewsky, W. *Chem.Ber.* **57** 667 (1924).

[114] Welcher, F.J. *Analytical Uses of EDTA* pp.234 Van Nostrand, New York 1958.

[115] Puxley, D.C.; Kitchener, I.J.; Komodromas, C. and Parkyns, N.D. in *Preparation of Catalysts III* ed. Poncelet, G.; Grange, P. and Jacobs, P.A.

Elsevier, Amsterdam 1983.

[116] Franklin, K.R. and Lowe, B.M. *Thermochimica Acta* **136** 307 (1988).

[117] Hurst, N.W.; Gentry, S.J.; James, A. and McNicol, B.D. *Catal.Rev.-Sci.Eng.* **24** 233 (1982).

[118] Coenen, J.W.E. *Appl.Catal.* **54** 59 (1989).

[119] Waugh, K.C. *Appl.Catal.* **43** 315 (1988).

[120] Redhead, P.A. *Vacuum* **12** 203 (1962).

[121] Anderson, J.R.; Foger, K. and Breakspere, R.J. *J.Catal.* **57** 458 (1979).

[122] Huang, Y.-J.; Xue, J. and Schwarz, J.A. *J.Catal.* **111** 59 (1988).

[123] Thomas, J.M. and Thomas, W.J. *Introduction to the Principles of Heterogeneous Catalysis* Academic Press, London 1967.

[124] Bartholomew, C.H. and Farrauto, R.J. *J.Catal.* **45** 41 (1976).

[125] Primet, M.; Dalmon, J.A. and Morton, G.A. *J.Catal.* **46** 25 (1977).

[126] Mile, B.; Stirling, D.; Zammitt, M.A.; Lovell, A. and Webb, M. *J.Catal.* **144** 217 (1988).

[127] Montes, M.; Penneman de Bosschey, Ch.; Hodnett, B.K.; Delannay, F.; Grange, P. and Delmon, B. *Appl.Catal.* **12** 304 (1984).

[128] Alzamora, L.E.; Ross, J.R.H.; Kruissink, E.C. and van Reijen, L.L. *J.Chem.Soc.,Faraday.Trans.I* **77** 665 (1981).

[129] Gil, A.; Diaz, A. and Montes, M. *J.Chem.Soc.Faraday.Trans.* **87** 791 (1991).

[130] Tammann, G. *Z.Anorg.Chem.* **149** 67 (1925).

[131] Pannell, R.B.; Chung, K.S. and Bartholomew, C.H. *J.Catal.* **46** 340 (1977).

[132] Bartholomew, C.H. and Pannell, R.B. *J.Catal.* **65** 390 (1980).

[133] Smith, J.S.; Thrower, P.A. and Vannice, M.A. *J.Catal.* **68** 270 (1981).

[134] Ko, E.I.; Hupp, J.M.; Rogan, F.H. and Wagner, N.J. *J.Catal.* **84** 85 (1983).

[135] Benesi, H.A.; Curtis, R.M. and Studer, H.P. *J.Catal.* **10** 328 (1968).

[136] Richardson, J.T. and Cale, T.S. *J.Catal.* **102** 419 (1986).

[137] Cale, T.S. and Richardson, J.T. *J.Catal.* **79** 378 (1983).

[138] Ross, J.R.H.; Steel, M.C.F. and Zeini-Isfahani, A. *J.Catal.* **52** 280 (1978).

[139] Bartholomew, C.H.; Pannell, R.B.; Butler, J.L. and Mustard, D.G. *179th ACS Meeting* Houston 1980.

[140] Chinchen, G.C.; Hay, C.M.; Vandervell, H.D. and Waugh, K.C. *J.Catal.* **103** 7 (1987).

[141] Zielinski, J. *Appl.Catal.* **35** 1 (1987).

[142] Eberly, P.E. and Spencer, E.H. *Trans.Faraday.Soc.* **57** 287 (1961).

[143] Nelson, D.A. and Eggerton, F. *Anal.Chem.* **30** 1387 (1958).

[144] Haywood, D.A. and Trapnell, B.M.W. *Chemisorption* Butterworths, London 1964.

[145] Lee, P.I. and Schwarz, J.A. *J.Catal.* **77** 272 (1982).

[146] Connor, W.C.Jr.; Pajonk, G.M. and Feichner, S.J. *Adv.Catal.* **34** 1 (1989).

[147] Klug, H.P. and Alexander, L.E. *X-ray Diffraction Procedures for Polycrystalline and Amorphous Materials* pp.689 Wiley 1974.

[148] Brunauer, S.; Emmett, P.H. and Teller, E. *J.Am.Chem.Soc.* **69** 309 (1938).

[149] IUPAC Commission on the Colloid and Surface Chemistry including Catalysis, Pure and Applied Chemistry **57** 603 (1985).

[150] Kiselev, A.V. and Yashin, Y.I. *Gas Adsorption Chromatography* Plenum, New York 1969.

[151] Misra, C. *Industrial Alumina Chemicals* ACS Washington 1986.

[152] Beeck, O *Discuss.Faraday Soc.* **8** 118 (1950).

[153] Jenkins, G.I. and Rideal, E. *J.Chem.Soc.Trans* 2490 (1955).

[154] Pliskin, W.A. and Eischens, R.P. *J.Chem.Phys.* **24** 482 (1956).

[155] Morrow, B.A. and Sheppard, N. *J.Phys.Chem.* **70** 2406 (1966).

[156] Morrow, B.A. and Sheppard, N. *Proc.R.Soc.A* **311** 391 (1969).

[157] Lapinski, M.P. and Ekerdt, J.G. *J.Phys.Chem.* **94** 4599 (1990).

[158] Lapinski, M.P. and Ekerdt, J.G. *J.Phys.Chem.* **92** 1708 (1988).

[159] Beebe, T.P.Jr. and Yates, J.T.Jr. *J.Phys.Chem.* **91** 254 (1987).

[160] Mohsin, S.B.; Trenary, M. and Robota, H.J. *J.Phys.Chem.* **91** 254 (1987).

[161] Zhu, X.-Y. and White, J.M. *Catal.Lett.* **1** 247 (1988).

[162] Lehwald, S. and Ibach, H. *Surf.Sci.* **89** 425 (1979).

[163] Bertolini, J.C. and Rousseau, J. *Surf.Sci.* **83** 531 (1979).

[164] Zaera, F. and Hall, R.B. *J.Phys.Chem.* **91** 4318 (1987).

[165] Stroscio, J.A.; Bare, S.R. and Ho, W. *Surf.Sci.* **148** 499 (1984).

[166] Demuth,J.E. and Ibach, H. *Surf.Sci.* **78** L238 (1978).

[167] Skinner, P.; Howard, M.W.; Oxton, I.A.; Kettle, S.F.A.; Powell, D.B. and Sheppard, N. *J.Chem.Soc.Faraday Trans. II* **77** 397 (1981).

[168] Demuth, J.E. and Ibach. H. *Surf.Sci.* **85** 365 (1979).

[169] Oxton, I.A.; Powell, D.B.; Sheppard, N.; Burgess, K.; Johnson, B.F.G. and Lewis, J. *J.Chem.Soc.,Chem.Commun.* 719 (1982).

[170] Andrews, J.; Kettle, S.F.A.; Powell, D.B. and Sheppard, N. *Inorg.Chem.* **21** 2874 (1982).

[171] Evans, J.; McNulty, G.S. *J.Chem.Soc.Dalton Trans.* 79 (1984).

[172] Lee, M.B.; Yang, Q.Y.; Tang, S.L. and Ceyer, S.T. *J.Chem.Phys.* **85** 1693 (1986).

[173] Zaera, F. and Hall, R.B. *Surf.Sci.* **180** 1 (1987).

[174] Chesters, M.A.; McDougall, G.S.; Pemble, M.E. and Sheppard, N. *Appl.Surf.Sci.* **22** 369 (1985).

[175] Ibach, H. and Lehwald, S. *J.Vac.Sci.Technol.* **18** 625 (1981).

[176] Carter, J.L.; Yates, D.J.C.; Lucchesi, P.J.; Elliott, J.J. and Kevorkian, V. *J.Phys.Chem.* **70** 1126 (1966).

[177] Dubois, L.H.; Castner, D.G. and Somorjai, G.A. *J.Chem.Phys.* **72** 5234 (1980).

[178] Steininger, H.; Ibach, H. and Lehwald, S. *Surf.Sci.* **117** 685 (1982).

[179] Koel, B.E.; Bent, B.E. and Somorjai, G.A. *Surf.Sci.* **146** 211 (1984).

[180] Beebe, T.P.Jr.; Albert, M.R. and Yates, J.T.Jr. *J.Catal.* **96** 1 (1985).

[181] Szilágyi, T. *J.Catal.* **121** 223 (1990).

[182] De la Cruz, C. and Sheppard, N. *J.Mol.Struct.* **247** 25 (1991).

[183] Yates, H.T. *Ph.D. Thesis* University of Edinburgh 1992.

[184] Barbier, T.; Churin, E.; Parera, T.M. and Riviere, J. *React.Kinet.Catal.Lett* **29** 323 (1985).

[185] McCarty, J.G.; Hou, P.Y.; Sheridan, D. and Wise, H. *ACS Symp.Ser.* **202** 253 (1982).

[186] McCarty, J.G. and Wise, H. *J.Catal.* **57** 406 (1979).

[187] Lehwald, S.; Erley, W.; Ibach, H. and Wagner, H. *Chem.Phys.Lett.* **62** 360 (1979).

[188] Campione, T.J. and Ekerdt, J.G. *J.Catal.* **102** 64 (1986).

[189] Beebe, T.P.Jr. and Yates, J.T.Jr. *Surf.Sci.* **173** L606 (1986).

[190] Chesters. M.A.; De la Cruz, C.; Gardner, P.; McCash, E.M.; Pudney, P.; Shahid, G. and Sheppard, N. *J.Chem.Soc.Faraday Trans.* **86** 2757 (1990).

[191] Avery, N.R. and Sheppard, N. *Proc.R.Soc.A* **405** 1 (1986).

[192] Bent, B.E.; Mate, C.M.; Crowell, J.E.; Koel, B.E. and Somorjai, G.A. *J.Phys.Chem.* **91** 1493 (1987).

[193] Goursot-Leray, A.; Carles-Lorjou, M.; Pouzard, G. and Bodot, H. *Spectrochim.Acta.A* **29** 1497 (1973).

[194] Haaland, P.D. *Experimental Design in Biotechnology Vol.105 in Statistics:Textbooks and Monographs* Dekker, New York 1989.

[195] Adrion, R.F. et al *Proceedings of the First Carolina Biomedical Engineering Conference* North Carolina Biotechnology Center 1984.

[196] Daniel, C. *Applications of Statistics to Industrial Experimentation* Wiley, New York 1976.

[197] Diamond, W.J. *Practical Experimental Designs* Lifetime Learning Publications, Belmont, C.A. 1981.

[198] Taguchi, G. *Introduction to Quality Engineering : Designing Quality into Products and Processes* Asian Productivity Organisation, Tokyo 1986.

[199] Sneath, P.H. and Sokal, R.R. *Numerical Taxonomy* pp.245 Freeman, San Francisco 1973.

[200] Orton, C. *Mathematics in Archaeology* pp.56 CUP 1975.

[201] Doran, J.E. and Hodson, F.R. *Mathematics and Computers in Archaeology* pp.190 Edinburgh University Press 1975.

6.1 Appendix 1.

Gas and Chemical Purity and Suppliers.

Gases	Purity	Supplier
Hydrogen H_2 (for reduction)	Commercial Grade 99.97%	BOC
Hydrogen H_2 (for adsorption)	CP 99.99%	BDH
Ethene C_2H_4	CP 99.5%	Cambrian
Deuterated Ethene C_2D_4	99.0%	BOC
Propene C_3H_6	Research Grade 99.98%	Union Carbide
Nitrogen N_2 (as carrier gas)	Commercial Grade OFN 99.97%	BOC
Nitrogen N_2 (for adsorption)	99.98%	Union Carbide
Helium He	'A' Grade 99.995%	BOC
Oxygen O_2	'Extra Dry' 99.5%	Cambrian
Argon Ar	'High Purity' 99.98%	BOC
5% Hydrogen in Argon	99.5%	BOC
5% Oxygen in Helium	99.8%	BOC
Carbon Dioxide CO_2	CP 99.998%	BOC
Carbon Monoxide CO	99.5%	BOC
Deuterium D_2	CP 99.8%	Cambrian

Chemical	Purity	Supplier
Nickel Nitrate $Ni(NO_3)_2.6H_2O$	AnalaR 98%	BDH
Aluminium Nitrate $Al(NO_3)_3.9H_2O$	AnalaR 99.6%	BDH
Sodium Carbonate Na_2CO_3	AnalaR 99.9%	BDH
γ-Alumina Al_2O_3	AnalaR 99.7%	BDH
α-Alumina Al_2O_3		ICI
Nickel Oxide NiO	Spec-Pure	Johnson Matthey
Mixed Nickel Oxide NiO/Ni_2O_3	AnalaR	BDH
Silica SiO_2	'Cab-o-sil' M5	BDH

6.2 Appendix 2.

Published Work.

Catalysis Today, 9 (1991) 15–22
Elsevier Science Publishers B.V., Amsterdam — Printed in The Netherlands

Diffuse Reflectance Infrared Spectroscopy of Adsorbates on Supported Metal Catalysts

P.D.HOLMES, G.S.MCDOUGALL*, I.C.WILCOCK

Department of Chemistry, University of Edinburgh,
King's Buildings, West Mains Road, Edinburgh, EH9 3JJ SCOTLAND.

K.C.WAUGH

I.C.I. Chemicals and Polymers Plc., Catalysis Research Centre,
Billingham, Cleveland, TS23 1LB ENGLAND.

* to whom communication should be addressed.

SUMMARY

DRIFTS spectra of ethene adsorbed on a Ni/Al_2O_3 catalyst show excellent sensitivity for adsorbed hydrocarbons across the mid infrared to 1100 cm^{-1}, the blackout of the support. For the Pt/SiO_2 catalyst EUROPT-1, the lower limit of the useful wavelength range in the DRIFTS spectra is 1400 cm^{-1}, compared with 1300 cm^{-1} in transmission. Spectra were recorded as a function of time after exposure of the Ni/Al_2O_3 catalyst to ethene, revealing a very different chemistry on the supported catalyst to that expected from vibrational studies of ethene adsorbed on Ni single crystals. An ethylidyne species forms, rapidly decaying to three other surface fragments. One shows frequencies characteristic of the methyl group, while the others show methylene group vibrations.

INTRODUCTION

The earliest application of both transmission and diffuse reflectance infrared spectroscopies to studies of adsorbates on catalysts date from *circa* 1960 (ref.1,2). Today, however, transmission is by far the more popular sampling method. This is undoubtedly due to the fact that transmission measurements can offer adequate sensitivity for weakly infrared absorbing surface species with comparative ease. The main disadvantage of transmission is the need to press a self supporting wafer of the catalyst material. This process is not only often experimentally tedious, but compressed wafers have poor porosity compared with the original catalyst powder and can limit the usefulness of transmission for *in situ* observation of surface reaction kinetics through diffusion control of reaction rates. This problem is less severe in diffuse reflectance where any mat surface such as pelleted catalysts or catalyst granules can be studied. Best results are normally achieved with finely powdered samples. The low levels of diffusely scattered light and radiation loss by specular reflection are, however, sufficient to make diffuse reflectance still appear unattractive by comparison with transmission.

This low sensitivity can be overcome in part by use of Fourier Transform infrared instrumentation to give the variant of the diffuse reflectance technique known popularly as DRIFTS

0920-5861/91/$03.50

(Diffuse Reflectance Infrared Fourier Transform Spectroscopy). Here we discuss the relative sensitivities of DRIFTS and transmission measurements for the study of ethene adsorption on the standard Pt/SiO_2 catalyst EUROPT-1 (ref.3) and a Ni/Al_2O_3 catalyst.

TRANSMISSION OR DRIFTS ?

In comparing the two techniques it is useful to consider the source of the signal in each case. Figures 1, A and B show single beam spectra of the EUROPT-1 catalyst in transmission and diffuse reflectance respectively. All spectra were collected on a Digilab FTS-40 spectrometer, equipped with a narrow band MCT detector, using standard optics in transmission and a Spectratech diffuse reflectance accessory for the DRIFTS spectra. The spectra are normalised at λ_{max} for ease of comparison. It is important to note that the detected signal integrated over all wavelengths, as measured by the peak to peak signal in the interferogram, might typically differ by a factor of between 10 to 20 from the transmission to the DRIFTS experiment.

In the DRIFTS single beam spectra the signal arises from a combination of three processes. First, the true diffuse reflectance; this is normally considered to be the radiation which has entered the sample and is then scattered over a range of angles by reflection, refraction and diffraction prior to re-emerging. In addition the signal will show components due to simple specular reflection and diffuse specular reflection (ref.4) (i.e. specular reflection from a number of essentially randomly orientated surfaces).

In the transmission spectra the signal will be composed of the true transmission and radiation scattered ('diffusely reflected') in the forward direction. This forward scattered radiation will be rejected in transmission experiments to a greater or lesser degree depending on the instrument design, giving an apparent loss in sample transmittance, particularly at high wavenumber where scattering is most severe. Generally this loss in signal in transmission will give a useful gain in signal in diffuse reflectance and this is evident in the higher relative detector response in the 4000 to 2200 cm^{-1} region of the EUROPT-1 DRIFTS spectrum as compared with the corresponding transmission plot.

The other factor which serves to offset the low optical efficiency of the diffuse reflectance is the high equivalent path length through the sample. For non infrared absorbing samples, effective sampling depths are of the order of 3 mm (ref.5) and the mean path length of the diffusely scattered radiation within the sample is twice the geometric thickness of the sample (ref.5). This gives an equivalent path length of several mm which compares favourably with the small fraction of a mm typical in transmission experiments. For the silica catalyst, where the support is essentially transparent, this high equivalent path length enhances the sensitivity of the DRIFTS experiments for weak adsorbate vibrations. However, where the support has significant absorbance the signal is correspondingly attenuated. This is again evident in Figures 1, A and B where the relative signal level of a given wavelength between 2000 cm^{-1} and 1300 cm^{-1} is at all points lower in the DRIFTS spectrum due to intense absorption by overtone and combination bands of the lattice modes of the silica support.

Below 1300cm^{-1}, where the sample becomes essentially opaque in the transmission single beam, the high apparent transmittance in the DRIFTS spectrum is due to specular or diffuse specular reflection from the silica support.

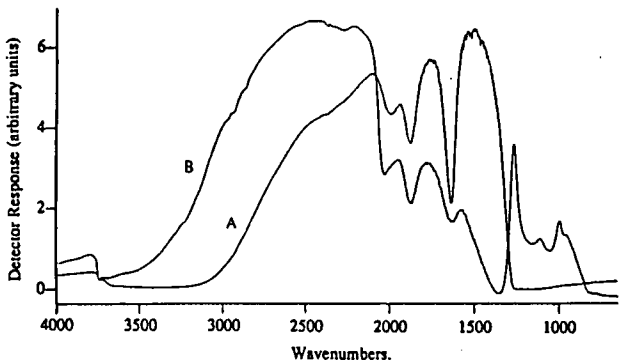

FIGURE 1 A) Single beam spectrum of the Pt/SiO_2 catalyst EUROPT-1 in transmission (ref.6).

B) Single beam spectrum of EUROPT-1 in diffuse reflectance.

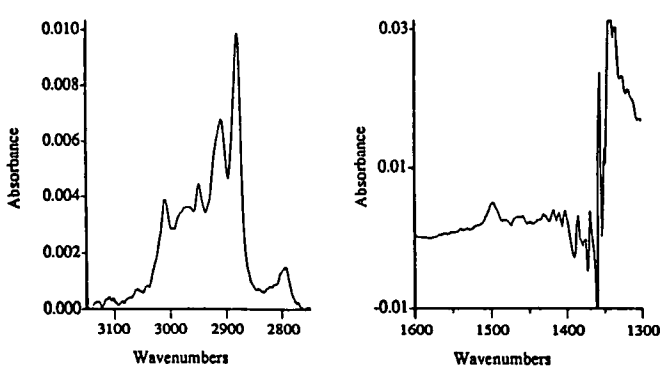

FIGURE 2 A DRIFTS spectrum of ethene adsorbed on EUROPT-1.

An absorbance spectrum is shown in Figure 3. This was generated from two DRIFTS single beam spectra, similiar to Figure 1B, each of 32 scans at 4 cm^{-1} resolution, recorded before and after exposure of the EUROPT-1 sample to saturation coverage of ethene. The noise levels in this spectrum, and so spectral sensitivity, correspond directly to the signal levels in the single beam spectra. The net result of the various factors contributing to the DRIFTS signal is a spectrum of adsorbed ethene which has comparable sensitivity in the C-H stretch region to earlier transmission spectra (ref.6). Signal to noise in the C-H deformation region is acceptable to approximately 1400 cm^{-1}. However, below this value, the noise level in the absorbance spectrum becomes too great to hold out any hope of observing modes due to adsorbed hydrocarbons. From 1300cm^{-1}, noise levels again improve. Since this improvement is due largely to specular reflection from the top surface of the powder, this region carries little useful information on adsorbate vibrations.

A similiar absorbance spectrum for ethene adsorbed on the Ni/Al_2O_3 catalyst is shown in Figure 3. Unlike silica, alumina has no intense absorption features above approximately 1100 cm^{-1} and so the spectrum shows excellent sensitivity across the normal spectral range available in transmission. The particular spectrum shown was recorded at 4 cm^{-1} resolution and 20 scans (15 seconds data acquisition time).

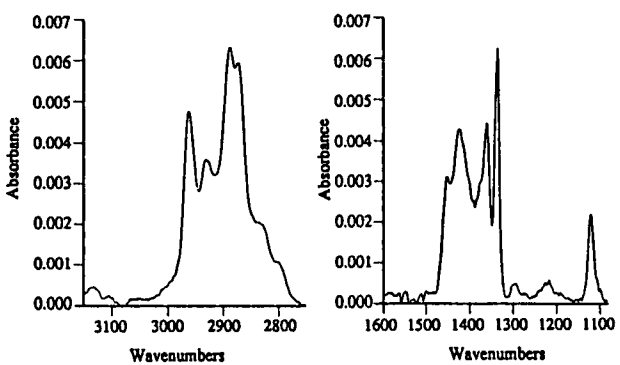

FIGURE 3 A DRIFTS spectrum of ethene adsorbed on Ni/Al_2O_3.

ETHENE ADSORPTION ON Ni/Al_2O_3

The levels of sensitivity achieved with the Ni/Al_2O_3 catalyst make possible *in situ* observation of surface reaction as a function of time following exposure of the catalyst to ethene and during subsequent temperature programming of the sample. The particular Ni catalyst used in these experiments was prepared by conventional co-precipitation of $Ni(NO_3)_2$ and $Al(NO_3)_3$ to give, after reduction at 1000 K, passivation and re-reduction in the DRIFTS environmental cell at 650 K, a catalyst with 25% metal by weight, 200 m^2/g total surface area and 20 m^2/g metal surface area.

Figure 4 consists of a series of spectra showing the evolution of the surface hydrocarbon phase with time following exposure of the catalyst to 3 µmole of ethene. This was injected into a carrier gas stream of He, flowing through the powdered sample in the environmental cell at 15 $mlmin^{-1}$ and $1.5x10^5$ Nm^{-2} (20 psi) backing pressure. The individual spectra represent the co-addition of 20 scans and were recorded at time intervals of 20 seconds. From this series of spectra, and other similiar experiments, it is immediately obvious that the ethene first forms an adsorbed species characterised by the set of bands labelled A in Figure 4. These features are entirely consistent with the wealth of vibrational data available for surface ethylidyne (ref.7) and their assignment is summarized in Table 1 below.

TABLE 1

Absorbance strengths and positions.

Species	Absorption bands	Strength	Assignement	Identification
A	1120-1125 cm^{-1}	medium	$\nu C\text{-}C$	
	1335-1340 cm^{-1}	strong	δCH_{2sym}	Ethylidyne
	2795-2800 cm^{-1}	weak	$2x\ \delta CH_{3as}$	CCH_3
	2870-2875 cm^{-1}	medium	$\nu C\text{-}H_{sym}$	
B	1355-1360 cm^{-1}	strong	δCH_{3sym}	
	2885-2890 cm^{-1}	medium	νCH_{3sym}	
C	1425-1430 cm^{-1}	medium	$\delta CH_{2sym}/\nu C\text{-}C$	
	2925-2960 cm^{-1}	medium	$\nu C\text{-}H_{sym}$	
D	1455-1460 cm^{-1}	strong	$\delta CH_{2sym}/\nu C\text{-}C$	
	2955-2960 cm^{-1}	medium	νCH_{2sym}	

+ gas phase ethane band centred at 2954 cm^{-1} (ν_5 C-H)

The peak marked * is the Q branch of gas phase ethane.

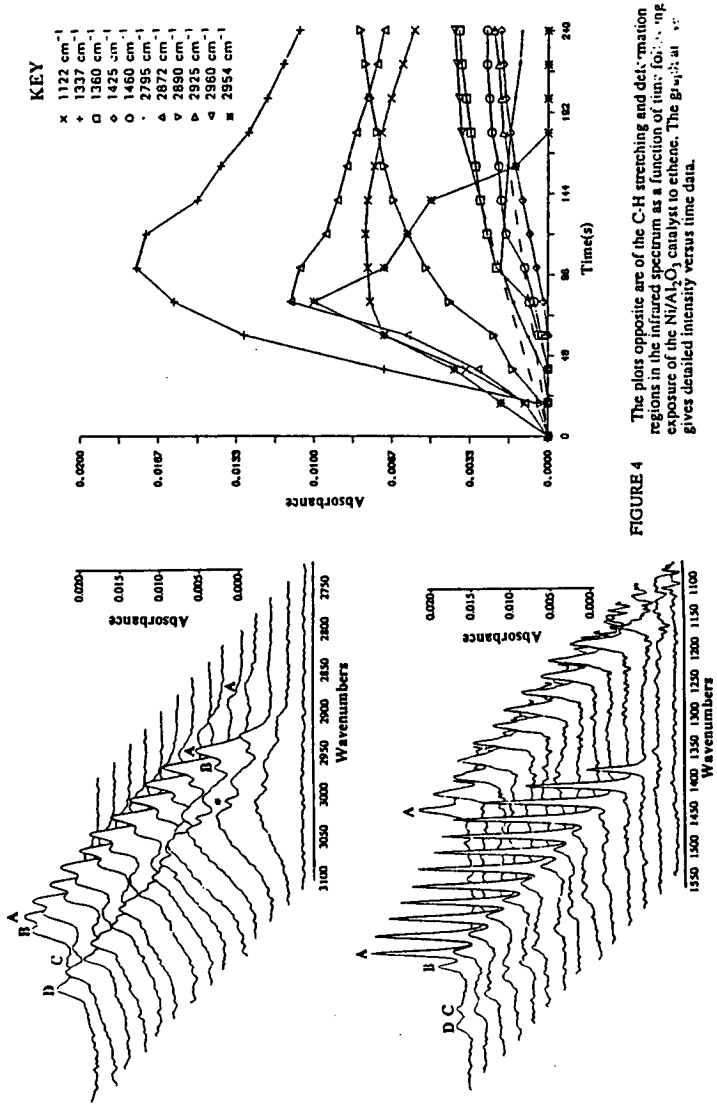

FIGURE 4 The plots opposite are of the C-H stretching and deformation regions in the infrared spectrum as a function of time following exposure of the Ni/Al_2O_3 catalyst to ethene. The graphs also gives detailed intensity versus time data.

Hydrogenation to ethane occurs simultaneously with ethylidyne formation but the extent of hydrogenation is dependent on the degree of outgassing of the sample after reduction (ref.8). This suggests hydrogenation is largely by retained hydrogen rather than self hydrogenation.

The surface ethylidyne species decays to form other surface hydrocarbon fragments. Careful observation of the variation of the band intensities with time (Figure 4) shows three further species to develop each with a characteristic set of frequencies labelled B, C and D in Figure 4 and again summarized in Table 1. The rate of decay of ethylidyne shows a strong dependence on both the coverage of pre-adsorbed hydrogen and surface hydrocarbon deposits (ref.8). However, the decomposition products are always the three hydrocarbon fragments B, C and D. Temperature programmed reaction spectra were recorded and these confirmed the allocation of the bands to species A, B, C and D (ref.8).

The DRIFTS spectra in Figure 4, give clear evidence for the formation of surface ethylidyne and three other surface species together with their relative stabilities at room temperature. The observation of surface ethylidyne is of interest in as much as it differs from either the acetylenic species suggested as the stable room temperature phase on Ni(111) (ref.9) and Ni(100) (ref.10), or the C_2H fragments reported on the Ni(110) plane (ref.7,11). The ethylidyne species has however recently been characterised on a supported Ni catalyst at 228K by transmission infrared (ref.12) and SSIMS studies suggest ethylidyne to form on Ni(111) as a function of the extent of pre-adsorbed hydrocarbon (ref.13).

Although the identity of A as surface ethylidyne is beyond question, an unambiguous assignment of the other fragments, B, C and D is more difficult. All differ totally in their spectral characteristics from the surface acetylenic or C_2H species expected from the room temperature Ni single crystal studies. Similarly there is no obvious relation between the spectral features noted here and those produced by annealing the Ni single crystal room temperature surface species. Comparison of the frequencies associated with B, C and D with a broad range of vibrational data, including all species derived from adsorption of C_2 hydrocarbons on single crystals and a number of organometallic cluster compounds containing C_1 and C_2 hydrocarbon ligands (ref.7), would suggest that fragment B certainly contains a methyl group. The bands at 2890 and 1360 cm^{-1} would be the symmetric CH_3 stretching and deformation vibrations respectively. On the basis of this limited vibrational data it is impossible, however, to discriminate between surface ethyl, ethylidene, methyl or even another form of ethylidyne. A methyl containing C_4 species may also be possible, as originally suggested in the early transmission studies on Ni/SiO_2 catalysts by Morrow and Sheppard (ref.14).

The frequencies associated with both C and D are similiar to those of symmetric CH_2 stretching and coupled symmetric CC stretch/CH_2 deformation vibrations of a methylene group but, once again, one can be no more specific than suggest surface vinyl, vinylidene, methylidene or again surface C_4 fragments. Of these, vinylidene has been implicated in either the formation or decomposition of ethylidyne by several authors (ref.7,15) and observed as a stable fragment from adsorption of ethene on Ru(001) with presorbed atomic oxygen at 350K (ref.16), perhaps making it

intuitively the more likely identity of either C or D.

Although only partly successful in identifying the various species noted, these DRIFTS experiments compare favourably, in terms of sensitivity, with transmission studies of supported metals and surpass reflection infrared or electron energy loss vibrational studies of single crystal substrates. The experiments described here do not however make use of the full potential of the technique by any means. When the DRIFTS cell is operated as a small flow reactor combined with a mass spectrometer for analysis of gas phase then surface reaction mechanisms and the nature of surface intermediates, rates and energetics of individual reactions (when several proceed in parallel) and surface composition of catalysts under reaction conditions should all become experimentally accessible (ref.17).

ACKNOWLEDGEMENTS

This work was supported by the Science and Engineering Research Council and by ICI Chemicals and Polymers Plc. through the CASE studentship scheme.

REFERENCES

1. Eischens, R.P., Francis, S.A. and Pliskin, W.A., J. Phys. Chem. 60, (1956) 194.
2. Kortum, G. and Delfs, H., Spectrochim. Acta 20, (1964) 405.
3. Bond, G.C. and Wells, P.B., Appl. Catal. 18, (1985) 221.
4. Reflectance Spectroscopy, Kortum, G., Springer-Verlag, Berlin, Heidelberg, 1969.
5. Fuller, M.P. and Griffiths, P.R., Appl. Spectrosc. 34, (1980) 533.
6. McDougall, G.S., Ph.D. Thesis, University of East Anglia, Norwich, 1986; De la Cruz, C., Ph.D. Thesis, University of East Anglia, Norwich, 1987; De la Cruz, C. and Sheppard, N., J. Chem. Soc. Chem. Comm (1987) 1854.
7. Sheppard, N., Ann. Rev. Phys. Chem. 39, (1988) 589 and references therein.
8. Holmes, P.D., McDougall, G.S., Waugh, K.C. and Wilcock, I.C., in preparation.
9. Lehwald, S. and Ibach, H., Surf. Sci. 89, (1979) 425; Bertolini, J.C. and Rousseau, J., Surf. Sci. 83, (1979) 531.
10. Zaera, F. and Hall, R.B., J. Phys. Chem. 91, (1987) 4318; Zaera, F. and Hall, R.B., Surf. Sci. 180, (1987) 1.
11. Anson, C.E., Bandy, B.J., Chesters, M.A., Keiller, B., Oxton, I.A. and Sheppard, N., J. Electron Spectros. and Relat. Phenom. 29, (1983) 315.
12. Lapinski, M.P. and Ekerdt, J.G., J. Phys. Chem. 92, (1988) 1708. ; Lapinski, M.P. and Ekerdt, J.G., J. Phys. Chem. 94, (1990) 4599.
13. Zhu, X.-Y. and White, J.M., Catalysis Letters 1, (1988) 247.
14. Morrow, B.A. and Sheppard, N., Proc. Roy. Soc. A 311, (1969) 391.
15. Gates, J.A. and Kesmodel, L.L., Surf. Sci. 124, (1982) 68.
16. Hills, M.M., Parmeter, J.E. and Weinberg, W.H., J. Am. Chem. Soc. 109, (1987) 597.
17. Waugh, K.C., Appl. Catal. 43, (1988) 315.

6.3 Appendix 3.

Scribe Command File.

```
@make(thesis)
@device(postscript)
@use(database="~ercy02/scribex")
@style(leftmargin 4cm, topmargin 2.5cm, rightmargin 2.5cm,bottommargin 3cm, spacing=1.5)
@pagefooting[centre "@value(page)"]
@define(flabel=text, spacing 1, rightmargin 1.5cm, leftmargin 1.5cm)
@libraryfile(postscript), @libraryfile(bib)
@define(abstract=text, spacing 1)
@comment{formats for references}

@form[refpaper={@w[@parm(author)]@imbed[key, def "@tag[@parm(key)]"]@hsp(1.5mm)
@w[@i(@parm(journal))@hsp(2.5mm)@b(@parm(volume))@hsp(1.7mm)
@parm(pages)@hsp(1.7mm)(@parm(year)).@blankspace(1.7mm)]}]

@form[refpapernv={@w[@parm(author)@imbed[key, def "@tag[@parm(key)]"]@hsp(1.5mm)@i(
@parm[journal])]@hsp(1.5mm)@parm(pages)@hsp(1.7mm)(@parm(year)).@blankspace(1.7mm)}]

@form[phdref={@w(@parm(author))@imbed[key, def " @tag[@parm(key)]"]@hsp(1.5mm)
@i(Ph.D. Thesis)@hsp(2.7mm)@parm(uni)@hsp(1.7mm)@parm(year).@blankspace(1.7mm)}]

@form[bkref={@w(@parm(author))@imbed[key, def " @tag[@parm(key)]"]
@hsp(1.5mm)@i(@parm[title])@hsp(3mm)pp.@parm(pages)@hsp(1.7mm)
@parm(pub)@hsp(1.7mm)@parm(year).@blankspace(1.7mm)}]

@form[bkrefed={@w(@parm(author))@imbed[key, def " @tag[@parm(key)]"]@hsp(1.5mm)
in@hsp(1.2mm)@i(@parm[title])@hsp(3mm)ed.@hsp(1mm)@parm(eds)@hsp(1.7mm)
@parm(pub)@hsp(1.7mm)@parm(year).@blankspace(1.7mm)}]

@form[bkrefnp={@w(@parm(author))@imbed[key, def " @tag[@parm(key)]"]@hsp(1.5mm)
@i(@parm[title])@hsp(3mm)@parm(pub)@hsp(1.7mm)@parm(year).@blankspace(1.7mm)}]
@comment{text of chapters}

@chapter[]
@heading(Introduction.)
@include(int.tex)
@chapter[]
@heading(Infrared Spectroscopy.)
@include(c2.tex)
@chapter[]
@heading(Preparation and Characterisation.)
@include(c3.tex)
@chapter[]
@heading(Ethene Adsorption on Ni/Al@-[2]O@-[3].)
@include(c4.tex)
@chapter[]
@heading(Propene Adsorption on Ni/Al@-[2]O@-[3].)
@include(c5.tex)
@chapter[]
@heading(Conclusions and Further Work.)
@include(c6.tex)
@comment{text of bibliography}

@include(bib.tex)
@include(bib2.tex)
@include(bib3.tex)
@include(bib4.tex)
@include(bib5.tex)
@include(bib6.tex)
```

6.4 Appendix 4.

Courses Attended.

Attendance at Catalysis Group Reading Parties, Firbush Point Field Centre, Loch Tay. May 1989 - 1991

Attendance at the following lecture courses;

Surface Science and Catalysis (4th year Chemistry course, 1989).
Catalytic Reaction Mechanisms, Dr.K.C.Waugh 14-15/4/92.
History of Art I, c1500 - present day (Arts Faculty 1st year course, 1989 - 1990).
Recent Advances in Physical Chemistry (Postgraduate lecture series 1989 - 1991).
EMAS/Scribe computing, Computing Centre, 1988.

Attendance at the following conferences;

5th, 6th and 7th Meetings of ICI CASE Students, *Chemical, Physical and Kinetic Aspects of Catalysis*, Catalysis Research Centre, ICI Billingham, May 1989 - 1991.

'Catalysis by Well Characterised Materials' Royal Society of Chemistry - Faraday Division, University of Liverpool, April 1989.

'In - Situ Methods in Catalysis' Royal Society of Chemistry, SURCAT, University of Reading, September 1990.

Royal Society of Chemistry, SURCAT (Scotland) Meeting, University of Glasgow, November 1990.

'Structure and Function in Catalysis' Second Anglo - Dutch Conference on Heterogeneous Catalysis, University of Hull, April 1991.

Royal Society of Chemistry, SURCAT (Scotland) Meeting, University of Edinburgh, July 1991.

Others;

Chemistry Department German Test